Unusual properties of the non-cysteinyl coordinated FeS clusters of IscR, YjdI and the Rieske protein

Vom Fachbereich Chemie der Rheinland-Pfälzischen Technischen Universität Kaiserslautern zur Verleihung des akademischen Grades „Doktor der Naturwissenschaften“ genehmigte Dissertation

DE-386

vorgelegt von

Jessica Candido Soares

geboren in Muniz Freire, Brasilien

Betreuer: **Prof. Dr. Antonio J. Pierik**

Kaiserslautern, 29.11 2024

Unusual properties of the non-cysteinyl coordinated FeS clusters of IscR, YjdI and the Rieske protein

Dissertation approved by the Department of Chemistry of the Technical University of Rhineland-Pfalz Kaiserslautern for the award of the academic degree “Doctor of Natural Sciences”

DE-386

Submitted by

Jessica Candido Soares

born in Muniz Freire, Brazil

Supervisor: **Prof. Dr. Antonio J. Pierik**

Kaiserslautern, November 29th, 2024

The practical part of this scientific work was carried out from February 2021 to September 2024 in the working group of Prof. Dr. Antonio J. Pierik at the Rhineland-Pfalz Technical University of Kaiserslautern-Landau, Department of Chemistry, Biochemistry.

Unusual properties of the non-cysteinyl coordinated FeS clusters of IscR, YjdI and Rieske proteins

Opening of the doctoral process: October 10th, 2024

Presentation and defense day: November 29th, 2024

Doctoral committee:

Chairperson: Prof. Dr. Sabine Becker, Department of Chemistry, Campus Kaiserslautern

First referee: Prof. Dr. Antonio J. Pierik, Department of Chemistry, Campus Kaiserslautern

Second referee: Prof. Dr. Volker Schünemann, Department of Physics, Campus Kaiserslautern

Member: Prof. Dr. Marcel Deponte, Department of Chemistry, RPTU, Campus Kaiserslautern

Eidesstattliche Erklärung

Erklärung über eigenständige Arbeit

Hiermit erkläre ich, Jessica Candido Soares, dass ich diese Arbeit gemäß der Promotionsordnung des Fachbereichs Chemie der RPTU in Kaiserslautern eigenständig verfasst und keine anderen als die angegeben Quellen verwendet habe. Stellen, die sinngemäß oder wörtlich aus anderen Quellen übernommen wurden, sind als solche kenntlich gemacht und im Literaturverzeichnis angegeben.

Kaiserslautern, den 29.11.2024

(Jessica Candido Soares)

Acknowledgements

"If I have seen a little further it is by standing on the shoulders of Giants."

Isaac Newton letter to Robert Hooke, 1675

Like Sir Isaac Newton, I too have been standing on the shoulders of Giants: the scientists that came before me, my mentors, my family and friends – in all aspects of life. Throughout my life, I have met incredible human beings and, while it is impossible to mention everyone that contributed to this thesis, I would like to acknowledge the key contributors to this achievement.

To this country, RPTU and the Department of Chemistry, for providing a safe, inclusive and inspiring environment that fostered a lot of personal and professional growth. The resources I had access to were crucial for the successful completion of this work.

To my PhD supervisor, Prof. Dr. Antonio Pierik, I am grateful for the mentorship, guidance and for the trust you placed in me. Your passion for Science, the extraordinary depth of your knowledge, and your detail-oriented eyes are an inspiration and have helped me see the world from a different perspective. I thank you for sharing and teaching me your expertise and feel fortunate to have had the opportunity to work with you and under your supervision.

To all my past mentors in Lisbon, especially Prof. Ricardo O. Louro, thank you for your continuous encouragement and for always believing in me. I am deeply grateful for our essential discussions, whether about science or life, for your friendship, and for always welcoming me back, no matter how much time has passed since my last visit.

To my lab colleagues and friends, PD. Dr. Daili Netz, Lukas Hewener, Tarik Begic, Lukas Knauer and Laura Leiskau for all the funny times we spent together and for your invaluable help in my project and in all the other aspects of living in a different country. To other members of our lab, especially Alissa Agovic, Nicole Ultes, Gian Franco, Erik Matonia and Doreen Knochenhauer, for all your contribution to my project.

To my collaborators, Ana Lago-Maciel and Dr. Johannes Rebelein; Nicola Sekularac and Prof. Dr. Nicole Frankenberg-Dinkel; Dr. Maxie Roessler and Dr. Alberto Collauto; Dr. Berta Martins; and Lukas Knauer, Prof. Dr. Volker Schünemann and their lab members for the opportunity to work with them in such interesting projects or for accepting the challenge to help me with my project. These collaborations greatly contributed to the expansion of my knowledge beyond my own expertise.

To my friends in Germany, Tallita, Lenine, Vitor, Duda, Andre, Emanoel, Jonas, Florian and my volleyball team for all the support when I thought things were not going well, for all the laughs and for being my family in this country.

To my friends and brother in Portugal, Mariana, Rita, Nuno and Rondi for being those I know I can count on, no matter what. Your friendship has been a source of strength throughout my PhD journey.

And lastly, my deepest gratitude to my mother, Gilceia, for being my greatest supporter. Your sacrifices have made it possible for me to pursue my dreams and your love has been a pillar that held me up through the toughest times. This achievement is as much as yours as it is mine. I am forever grateful for your wisdom and love.

To all of you, I dedicate this thesis

Zusammenfassung

Eisen-Schwefel-Cluster (Fe-S) sind vielseitige Cofaktoren, die in Metalloproteinen vorkommen. Die meisten FeS-Cluster werden ausschließlich durch Cysteinreste koordiniert. Bei einer zunehmenden Zahl von Proteinen konnte jedoch eine Koordination durch Nicht-Cysteinyl-Liganden nachgewiesen werden, deren Zweck jedoch noch nicht vollständig verstanden ist. Mindestens acht weitere Aminosäuren treten als Liganden für FeS-Cluster auf, wobei Histidin die erste identifizierte und möglicherweise auch die häufigste Aminosäure ist, die Cystein ersetzt. Die Koordination durch zwei Histidinreste findet sich in Rieske- und Apd1-ähnlichen Proteinen, während MitoNEET und vermutlich auch das IscR-Protein nur einen Histidinliganden aufweisen. Vorgeschlagene Rollen eines oder mehrerer Histidinreste sind die Modulation des Redoxpotentials, der protonengekoppelte Elektronentransfer (PCET) oder die Feinabstimmung der Clusterstabilität.

In dieser Arbeit wurden die Redox-Eigenschaften des $[2Fe\text{-}2S]^{1+/2+}$-Clusters von *Escherichia coli* IscR und die pK_a-Werte des Histidin-Liganden in beiden Redox-Zuständen untersucht, um zu zeigen, dass PCET stattfindet. Durch Kombination von UV-Vis-, CD-, EPR- und Mössbauer-Spektroskopietechniken mit Redoxtitrationen wurden pK_a-Werte von 8,0 und ~11,1 für den Histidinliganden in der oxidierten bzw. reduzierten Form von IscR ermittelt. Die Redoxpotentiale variieren zwischen -49 und -221 mV bei niedrigen bzw. hohen pH-Werten, mit einer maximalen Steigung von etwa -55 mV/pH-Einheit zwischen den pK-Werten. Darüber hinaus werden die Auswirkungen dieser Ergebnisse auf die physiologische Funktion in der zellulären Umgebung diskutiert.

Eine fehlende Koordination durch ein viertes Cystein kann zu einer Instabilität des Clusters führen, wie bei Aconitase zu sehen ist, bei der es zu einer Umwandlung von [4Fe-4S]- in [3Fe-4S]-Cluster kommt. Im zweiten Projekt wurde das schlecht charakterisierte YjdI-Protein aus *E. coli* charakterisiert. YjdI zeigte g=2,01 und g=12 EPR-Signale, die für einen $[3Fe\text{-}4S]^{1+/0}$-Cluster charakteristisch sind, sich aber bei der Rekonstitution und Reduktion in $[4Fe\text{-}4S]^{1+}$ umwandelten. Weitere Untersuchungen inkl. Mutagenese und Mössbauer Spektroskopie werden erforderlich sein, um den vierten Cluster-Liganden des rekonstituierten YjdI zu ermitteln.

Für Rieske-Proteine wurde PCET ausgiebig untersucht und mit der Funktion des Protonentransports in Verbindung gebracht. Für den reduzierten Zustand von drei verschiedenen Rieske-Proteinen zeigte die Proteinfilmvoltammetrie, dass die beiden pK-Werte identisch sind und über 12 liegen. Trotz der EPR-spektroskopischen Charakterisierung der alkalischen (vollständig deprotonierten) Spezies wurde noch nicht über ein monoprotoniertes Intermediat im reduzierten Zustand berichtet. Die EPR-Spektroskopie des *Thermus thermophilus* Rieske-Proteins konnte bei einer Titration zwischen pH 9,5 und 14 nicht nur die vollständig protonierte und deprotonierte Spezies, sondern auch eine monoprotonierte Spezies mit g=2,03, 1,90 und 1,78 nachweisen. Aufgrund der Nähe der pK_a-Werte wurden nur Mischungen von Spezies gefunden. Auffallend ist, dass das System ein kooperatives Verhalten zeigt: der zweite pK_a-Wert (11,8) ist niedriger als der erste pK_a-Wert (12,1).

Insgesamt vertiefen diese Ergebnisse das Verständnis der Redox-Eigenschaften von IscR, tragen zur Charakterisierung von YjdI bei und zeigen zum ersten Mal im FeS-Forschungsgebiet die Kooperativität aufeinanderfolgender Ligandendeprotonierungen. Diese Ergebnisse unterstreichen die Notwendigkeit weiterer Forschung zu PCET und Eigenschaften von FeS-Proteinen.

Abstract

Iron-sulfur clusters (FeS) are versatile cofactors found in metalloproteins. Most FeS clusters are coordinated exclusively by cysteine residues. However, for an increasing number of proteins the presence of non-cysteinyl coordination has been noted, with a not fully understood role. At least eight other amino acids act as ligands for FeS clusters, with histidine being the first identified and possibly also the most common amino acid to substitute cysteine. Coordination by two histidine residues is found in Rieske and Apd1-like proteins, whereas MitoNEET and presumably also the IscR protein have one histidine ligand. Suggested roles of the histidine residue(s) are tuning of the redox potential, proton-coupled electron transfer (PCET) or modulation of cluster stability.

In this thesis the redox properties of the $[2Fe\text{-}2S]^{1+/2+}$ cluster of *Escherichia coli* IscR and the pK_a values of the histidine ligand in both redox states were investigated to demonstrate that PCET occurs. Combining UV-Vis, CD, EPR, and Mössbauer spectroscopic techniques with redox titrations pK_a values of 8.0 and ~11.1 were determined for the histidine ligand in the oxidized and reduced form of IscR, respectively. The redox potentials varied between -49 and -221 mV, at low and high pH values, respectively, with a maximal slope of approximately -55 mV/pH unit between the pK values. Additionally, the impact of these findings on the physiological function in the cellular environment is discussed.

Lack of coordination by a fourth cysteine can lead to cluster instability, as seen in aconitase, which is subject to [4Fe-4S] to [3Fe-4S] cluster conversion. In the second project the YjdI protein from *E. coli* was characterized. YjdI exhibited g=2.01 and g=12 EPR signals characteristic of a $[3Fe\text{-}4S]^{1+/0}$ cluster but converted to $[4Fe\text{-}4S]^{1+}$ upon reconstitution and reduction. Studies including mutagenesis and Mössbauer spectroscopy will be needed to reveal the fourth cluster ligand of reconstituted YjdI.

PCET has been extensively studied and linked to function in proton translocation for Rieske proteins. For the reduced state of three different Rieske proteins protein film voltammetry indicated that the two pK values are identical and above 12. However, despite EPR spectroscopic characterization of the alkaline (fully deprotonated) species, an intermediate monoprotonated species in the reduced state has not been reported yet. Resorting to a titration between pH 9.5 and 14 of *Thermus thermophilus* Rieske protein EPR spectroscopy revealed not only the fully protonated and deprotonated species, but also a monoprotonated species with g=2.03, 1.90 and 1.78. Due to the proximity of the pK_a values only mixtures of species were found. Strikingly, the system exhibited cooperative behavior: the second pK_a (11.8) is lower than the first pK_a (12.1).

Overall, these findings deepen the understanding of the redox properties of IscR, contribute to the characterization of YjdI, and demonstrate cooperativity of consecutive ligand deprotonations for the first time in the FeS field. These findings emphasize the need for further research into PCET and properties of FeS proteins.

Table of contents

List of Figures

Abbreviations

Amp – ampicillin

APS – ammonium persulfate

bp – base pair

BSA – bovin serum albumin

CAPS – 3-(Cyclohexylamino)-1-propanesulfonic acid

CD – Circular Dichroism spectroscopy

CHES – *N*-cyclohexyl-2-aminoethane-1-sulfonic acid

CODH – carbon monoxide dehydrogenase

CV – column volume

DNA – deoxyribonucleic acid

dNTP – deoxynucleotide triphosphate

DOC – deoxycholate

DTT – dithiothreitol

E. coli – *Escherichia coli*

EMSA – Electrophoretic mobility Shift assay

EDFS – Echo-Detected Field-Swept

EPR – Electron Paramagnetic Resonance

ENDOR – Electron-nuclear double resonance spectroscopy

FAC – ferric ammonium citrate

Fdx – Ferredoxin

FeS – iron-sulfur

Fur – ferric uptake regulator

HEPES – 4-(2-hydroxyethyl)-1-piperazineethanesulfonic acid

HiPIP – High Potential Iron-sulfur Protein

HYSCORE – Hyperfine Sublevel Correlation

IPTG – Isopropyl β- D-1-thiogalactopyranoside

ISC – Iron sulfur cluster biogenesis machinery

IscR – iron-sulfur cluster regulator

LB – lysogeny broth/ Luria-Bertani

LCPL - left circularly polarized light

M9 – minimal medium

MES – 2-(*N*-morpholino)ethanesulfonic acid

NaDT – sodium dithionite

OD – optical density

ORF – open reading frame

PAGE – polyacrylamide gel electrophoresis

PCET – proton coupled electron transfer

PCR – *polymerase chain reaction*

PIPES – 1,4-Piperazinediethanesulfonic acid

PLP – pyridoxal-5′-phosphate

PMS – phenazine methosulfate

PMSF – phenylmethylsulphonyl fluoride

RCPL – right circularly polarized light

Rnr – respiratory nitrate reductase

ROS – Reactive Oxygen Species

rpm – revolutions per minute

RT – room temperature

SAM – *S*-adenosyl-L-methionine

SDS – sodium dodecyl sulphate

SDS-PAGE – sodium dodecyl sulphate-polyacrylamide gel electrophoresis

SHE – Standard hydrogen electrode

SUF – sulfur mobilization system

TAPS – *N*-[tris(hydroxymethyl)methyl]-3-aminopropane-1-sulfonic acid

TCA – trichloroacetic acid

TEMED – *N,N,N',N'*-Tetramethylethylendiamine

Tris – tris(hydroxymethyl)aminomethane

TtRp – *Thermus thermophilus* Rieske protein

UV – ultraviolet

UV-Vis – UV-Visible spectroscopy

v/v – volume per volume

Vis – visible

w/v – weight per volume

Chapter I. FeS clusters in metalloproteins

1. Metalloproteins

Metalloproteins are a class of proteins characterized by the presence of one or more metal ions fully or partially coordinated by the side chain of amino acids from the polypeptide backbone. As described by Malmström and Neilands[1], metal coordination must be stable enough so that, at physiological pH, temperature values and in the absence of chelating molecules, the metal does not dissociate from the protein in an equilibrium with solution.

Metalloproteins are necessary for the viability of life. They are estimated to compose a quarter to a third of all known proteins in cells and are present in all six Enzyme Commission classes[2]. They take part in vital reactions such as cellular respiration and photosynthesis[3] – the most fundamental biological processes involved in energy transfer and carbon cycling between organisms and their environment. They are also involved in other relevant pathways such as nitrogen assimilation, nitrogenases[4] being one of the best known and studied metalloproteins, and in the metabolism of molecular hydrogen by hydrogenases[5].

There are numerous metal cofactors that are primarily differentiated by the metallic element they contain. Specific metal ions are usually associated with the specific type of reactions they catalyze[6]. For instance, even though magnesium is the most abundant metal ion in metalloproteins, copper, iron and molybdenum are more abundant in oxidoreductases than magnesium[6]. This occurs because these metals are chemically more suited to perform such reactions than magnesium. Reviews by Waldron and colleagues[2,6], as well as by Foster and colleagues[7], give insights into metal preference, the process of metallation, sensing and metal management in the cell. A summary of the distribution of metals in proteins within each Enzyme Commission class is shown in Figure 1.

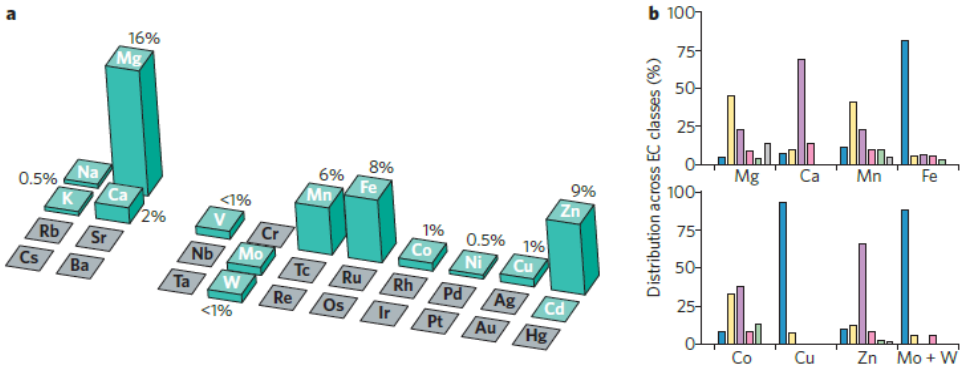

Figure 1. Periodic system of selected metal ions occurring in metalloproteins (A) and their proportion in different classes of enzymes (B). Reproduced from Waldron *et al.*[6]. In Panel B oxidoreductases are shown in blue, transferases in yellow, hydrolases in purple, lyases in pink, isomerases in green and ligases in grey.

Iron-containing cofactors are among the most extensively studied, with four main forms of iron-based cofactors identified: hemes[8], FeS clusters[9,10], diiron centers[11–13] and non-heme iron[13] centers. The FeS cofactors will be further explored in Section 2.

2. FeS clusters in Nature and their physical properties

Iron-sulfur (FeS) clusters are widely spread and ubiquitous in Nature. Discovered in the early 1960's by Beinert and Sands (1960)[14], they are known as one of the most ancient components of living matter on Earth. The number of identified FeS cluster-containing proteins has been steadily increasing in the past 60 years. These clusters are present in all Domains of life, and in viruses, taking part in a variety of processes that are vital to life[15,16].

2.1. Cluster structures

FeS clusters consist of high spin Fe^{2+} and Fe^{3+} ions coordinated in a tetrahedral geometry by inorganic sulfide (S^{2-}) ions and two or more ligands from the protein. There is a wide variation in FeS cluster composition and ligands. Amongst the most common ones are $[4Fe\text{-}4S]^{1+/2+}$ (frequently called cubanes), $[3Fe\text{-}4S]^{0/1+}$ and $[2Fe\text{-}2S]^{1+/2+}$ clusters, in which the cluster ligands are usually cysteine residues from the polypeptide chain[9,17]. Clusters with full cysteine coordination are often referred to as canonical. These clusters are represented in Figure 2.

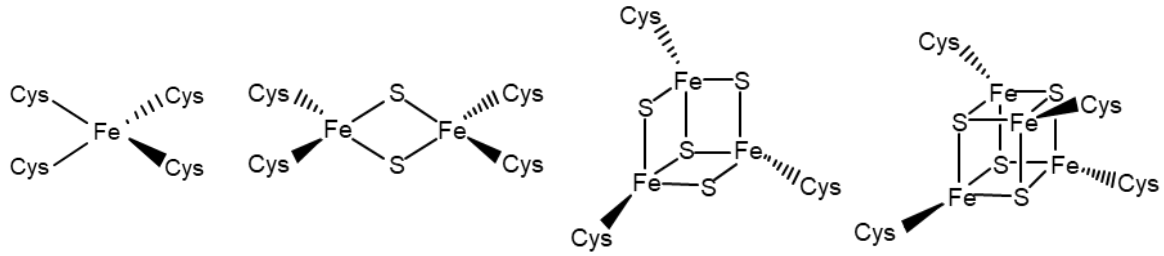

Figure 2. Rubredoxin $[Fe(Cys)_4]$ and the three most common FeS clusters in Nature. All clusters represented are canonical, *i.e,* with full cysteine coordination.

Even though the $[Fe(Cys)_4]$ from rubredoxins are formally not considered to be part of the FeS clusters class due to the lack of inorganic sulfides in the core, it provides a good starting point to understand their structure. Rubredoxins are small proteins of approximately 50 amino acids that contain one Fe ion coordinated by four cysteine residues from the polypeptide chain of the protein[18]. Involved in various electron transfer processes such as alkane hydroxylation and also present as a domain in flavodiiron proteins, rubredoxins could be one of the most ancient FeS cluster structures due to their low complexity when compared to other FeS clusters[18].

Various other types of clusters have been identified. However, they comprise a small fraction of those found in nature. Some examples of the clusters mentioned below are represented in Figure 3. Among these variations are the P-clusters [8Fe-7S], composed of two [4Fe-4S] clusters that share a central μ6-sulfur (S) atom[19,20], the FeMo cofactor $[MoFe_7S_9C]$ that contains eight metal ions, including a molybdenum, with a central carbide and bridged by nine sulfides[20]. Both clusters are extensively researched as they are found in nitrogenase enzymes.

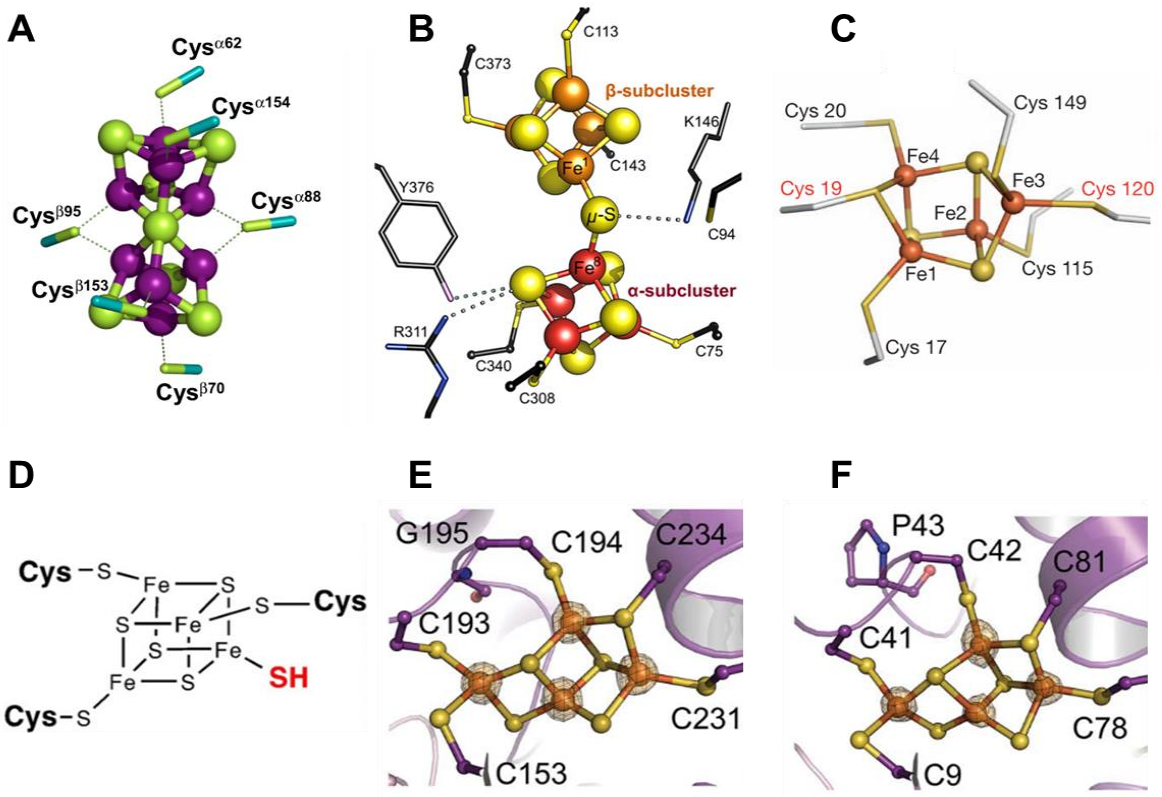

Figure 3. Examples of variations in FeS clusters' structures. (A) P-cluster [8Fe-7S] from nitrogenase from *A. vinelandii*; (B) [8Fe-9S] cluster from a 2-hydroxyacyl-CoA dehydratase *from C. hydrogenoformans* Z-2901; (C) oxygen resistant [NiFe]-hydrogenase from *R. eutropha* H16; (D) [4Fe-5S] cluster from a thiouracil desulfurase from *Aeromonas*; (E) and (F) two non-cubane [4Fe-4S] clusters present in a methanogenic heterodisulfide reductase from *M. thermolithotrophicus*. Figures reproduced from references 19-24.

In some 2-hydroxyacyl-CoA dehydratases, as described by Jeoung and Dobbek, 2018[21], an [8Fe-9S] cluster is present. This cluster corresponds to two [4Fe-4S] clusters linked together by an inorganic sulfide ion, but unlike P-clusters that have a bridging μ6-sulfur [8Fe-7S], this cluster contains a μ2-sulfur (an extra sulfide) coordinating and consequently linking both full [4Fe-4S] clusters.

In 2011, Fritsch and coworkers[22] reported a novel [4Fe-3S] cluster. This cluster, present in an oxygen-tolerant [NiFe] hydrogenase from *Ralstonia eutropha* H16, was shown to be coordinated by six cysteine residues. According to their model, this cluster was thought to act as an electronic switch accepting electrons for H_2 oxidation and delivering electrons in the presence of O_2.

Another variation of a [4Fe-4S] cluster, a [4Fe-5S] cluster was reported for a thiouracil desulfidase by Zhou and coworkers in 2021[23]. This cluster was reported to be coordinated by three cysteine residues only and, upon incubation with substrate, bind an inorganic sulfur at the fourth iron position, generating a [4Fe-5S] cluster. That shed a light on the enzyme's mechanism and defined the intermediate generated in the reaction.

In 2017, two non-cubane [4Fe-4S] clusters present in the heterodisulfide reductase HdrB subunit were described by Wagner and colleagues[24]. These clusters can be envisaged as a fusion of a [3Fe-

4S] and a [2Fe-2S] cluster and are coordinated and stabilized by five cysteine and two histidine residues, respectively.

Another subtle structural variation occurs in the High Potential Iron-sulfur Proteins (HiPIPs) that, despite sharing their core structure with the $[4Fe\text{-}4S]^{1+/2+}$ clusters, physiologically shuttle between the $[4Fe\text{-}4S]^{2+}$ and $[4Fe\text{-}4S]^{3+}$ states at a much higher redox potential[25,26]. This example shows that not only ligands, but also hydrogen bonds and the environment of the cluster critically contribute to redox properties.

2.2. Canonical FeS clusters: redox properties and their associated role

Reduced FeS clusters are often inherently sensitive to molecular oxygen as they usually contain at least one ferrous, Fe (II), ion. Molecular oxygen (O_2), as the most physiologically relevant and abundant oxidizing molecule, tends to readily oxidize ferrous ions to ferric, Fe (III), ions, thus leading to cluster oxidation[27]. The detrimental effect of O_2 is especially pronounced for reduced, low redox potential clusters[28].

Molecular oxygen, upon reaction with FeS clusters, also tends to generate Reactive Oxygen Species (ROS), such as hydrogen peroxide (H_2O_2) and the superoxide anion ($O_2^{\bullet -}$). These ROS tend to react with other not yet damaged cluster-containing molecules generating further oxidative damage[27]. The presence of H_2O_2 in solutions containing ferrous ions released from FeS clusters can also lead to the Fenton reaction[29], as follows:

$$Fe^{2+} + H_2O_2 \rightarrow Fe^{3+} + HO^- + \bullet \mathrm{OH}$$

The hydroxyl radical, a product of this reaction, is a highly reactive molecule that will join the cascade of oxidative damage generated by O_2 in the proximities of FeS clusters[30]. Apart from that, the presence of molecular oxygen on Earth's atmosphere significantly decreases iron availability, leading to the necessity of incorporating new metals to the system[28].

Under anaerobic conditions, FeS clusters with a full set of protein ligands (*i.e.* 4 cysteine residues for [2Fe-2S] and [4Fe-4S] clusters) are quite stable and participate in various redox reactions. Due to their flexibility in alternating between oxidation states, they are ideally suited to perform electron transfer within a protein or between molecules thus facilitating redox reactions. This flexibility also enables their redox state to be used as a switch or regulatory mechanism for a specific function[26]

In biological systems, the redox potential of canonical FeS clusters tend to fall in very characteristic ranges. Their coordination by cysteine side chains, with their negatively charged sulfur, plays an important role for their redox potentials[31,32]. The sulfur atoms act as strong nucleophiles, thus stabilizing the cluster and drastically decreasing their redox potential.

Their typically rather low potentials are especially important for the function in anaerobic electron-transport chains where potentials close to H_2/H^+ or $NADH/NAD^+$ are involved. Canonical FeS clusters are often associated with electron cascades where an electron travels through a long path of clusters, with intercluster distances in the range of 10-14 Å[33]. A notable example is the hydrophilic arm of the NADH dehydrogenase, which harbors a chain of eight FeS cluster, represented in Figure 4, A[34]. For this path to be energetically favorable there must be an overall redox potential gradient, where the electron travels from clusters with a more negative redox potential to clusters or cofactors with a more positive redox potential. If a similar or a slightly uphill redox potential occurs, even equilibrium could play a role.

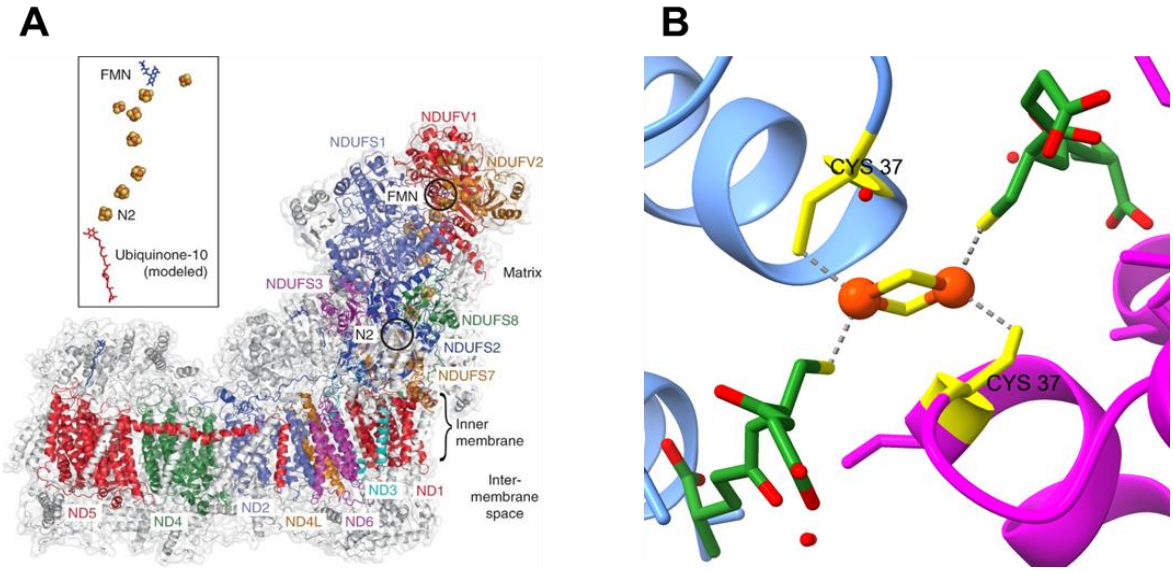

Figure 4. Examples of redox active FeS clusters. (A) Cryo-EM structure of the NADH dehydrogenase complex and the schematic representation of the cofactors involved in the electron cascade; (B) [2Fe-2S] cluster with a double GSH coordination from the dimeric human glutaredoxin 2 (PDB: 2HT9). Panel (A) was reproduced from Agip *et al*.[34] and Panel (B) made with ChimeraX from the PDB structure published by Johansson *et al*. [37]

Ferredoxins (Fdx) are well-known for containing canonical FeS clusters, with each protein harboring one or more canonical clusters. They are small globular proteins that participate in electron transfer processes such as those found in photosynthesis and nitrogen fixation and are classified into bacterial or plant type. Bacterial ferredoxins are usually associated with $[4Fe\text{-}4S]^{1+/2+}$ clusters whereas the plant type generally contains $[2Fe\text{-}2S]^{1+/2+}$ clusters. Ferredoxins can also constitute a fused domain as it happens in hydrogenases[35] and in the respiratory nitrate reductase (Rnr)[36]. These proteins are usually related to electron cascades with redox potentials varying from -600 to -300 mV relative to the standard hydrogen electrode (S.H.E) [28,33].

Another example of a redox active FeS cluster is the one present in the mitochondrial glutaredoxin 2 (GLRX2) that, despite being coordinated by four sulfur atoms, is not coordinated by four cysteine residues from the polypeptide chain. Glutaredoxins are small proteins often associated with redox processes and signaling. GLRX2, found in the human mitochondria, was also linked to redox sensing

in the mitochondria and apoptosis. It was described as a dimer protein which bridges a [2Fe-2S] cluster coordinated by Cys 37 of each monomer and two molecules of glutathione[37] as shown in Figure 4, B.

2.3. Canonical FeS clusters: sensing and catalysis

FeS cluster containing proteins can also act as sensors in the cell. As discussed previously, FeS clusters are redox and oxygen (and its byproducts, ROS) sensitive[38,39]. Sensing oxygen, ROS, and redox conditions in general, is fundamental for cellular adaptation and survival. A good example is the superoxide response (SoxRS) system[40]. This system is constituted by two proteins, SoxR and SoxS, that act consecutively to activate a cellular response against oxidative stress in the cell[41]. SoxR contains a canonical [2Fe-2S] cluster that is necessary for the activation of SoxS, which is its only known target[38]. On another hand, SoxS is a transcription factor that activates approximately 15 genes related to redox homeostasis. The production of SoxS is SoxR-dependent and SoxS is readily degraded to keep oxidative stress response dependent on SoxR[41–45].

Finally, some canonical FeS clusters present a catalytic role in which the cluster actively participates in the reaction. Two examples are represented in Figure 5. An interesting example of redox catalysis mediated by an FeS cluster is the *S*-adenosyl-L-methionine (SAM)-dependent enzymes. These enzymes contain a $[4Fe\text{-}4S]^{1+}$ cluster that binds the SAM cofactor and, through a reductive cleavage, produces methionine and a highly reactive 5′-deoxyadenosyl radical species. This radical will then be used to perform energetically challenging reactions such as hydrogen atom subtraction[25,32].

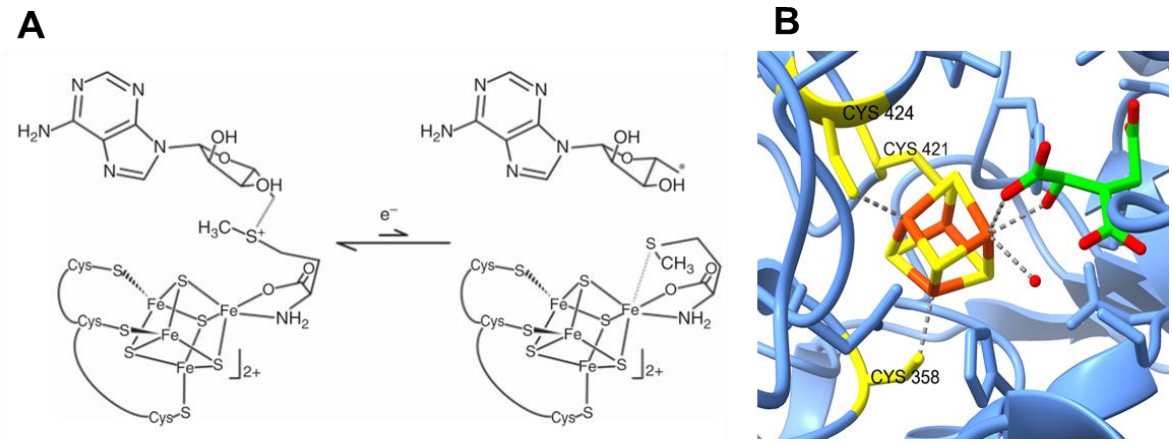

Figure 5. Examples of catalytic active FeS clusters. (A) Cleavage of the SAM cofactor from a [4Fe-4S] cluster resulting in the 5′-deoxyadenosyl radical species. (B) Aconitase [4Fe-4S] cluster from *Bos taurus* bound to isocitrate, its substrate (PDB: 8ACN); Panel (A) was reproduced from Nicolet *et al.*[25] and Panel (B) made with ChimeraX from the PDB structure published by Lauble *et al.*[49]

The incorporation of different metals into FeS clusters also plays a role in redox catalysis. This is the case for carbon monoxide dehydrogenase (CODH) that catalyzes the reversible interconversion of CO to CO_2 and contains a Ni-Fe-S cluster[25] and the widely known nitrogenase with their FeV or FeMo catalytic clusters[46].

Another, and perhaps the best known, example of a non-redox catalytic FeS cluster is the [4Fe-4S] cluster of mitochondrial aconitase. This enzyme is a part of the Krebs cycle catalyzing the conversion of citrate to isocitrate. In this cluster, the “fourth” Fe ion lacking cysteinyl coordination is used for catalysis and, while in the resting state, this corner is occupied with a water or hydroxide molecule. Upon loss of the “fourth” iron ion aconitase converts to its inactive state, forming a $[3Fe\text{-}4S]^0$ cluster[25,47–49].

2.4. Non-Cys ligated FeS clusters: properties and biological role

Canonical FeS clusters, ligated by four cysteine residues, are the most prevalent type of FeS clusters. However, alternative types of cluster coordination have been garnering interest lately. These clusters appear to serve a variety of purposes and have different physicochemical properties in comparison to canonical clusters[50].

FeS clusters coordinated by molecules, such as citrate, SAM or glutathione will not be considered as they were included in the previous section. FeS clusters coordinated by amino acids that are part of the protein polypeptide chain but are not cysteines, such as histidine and aspartate residues will be discussed in this section.

2.4.1. Properties of non-cysteinyl ligated FeS clusters

The presence of non-cysteinyl ligands can change several properties. First, the tuning of the, generally very low, redox potential in FeS clusters by non-cysteinyl coordination is a very important phenomenon. It can be exemplified by the ~700 mV upward shift of the redox potential in the Rieske center in comparison with plant type ferredoxins[51]. Second, again exemplified by the Rieske center, proton-coupled electron transfer (PCET)[50] can be gained. Third, especially relevant for regulatory purposes, changes in cluster stability can be introduced[52].

Tuning of the redox potential can be achieved by changing the nucleophilicity and electronegativity of the atoms coordinating the cluster. For example, in histidinyl coordination, the increased electronegativity of the nitrogen when compared to the sulfur atom will lead to an increased electron density towards the nitrogen atom. This will then cause an electron deficiency in the cluster. Adding to the electronegativity effect, the presence of the nitrogen atom in an aromatic imidazole ring will add up to this effect as its increased electron density can then be delocalized through the ring. This will then contribute to an even lower electron density in the cluster itself. This electron depletion will in turn contribute to the increase of the redox potential of the cluster, a well-studied consequence of cysteine substitution by one or two histidine residues in [2Fe-2S] and [4Fe-4S] centers[50,53].

The presence of a protonable amino acid, such as histidine residues, as cluster ligands introduces another component to the properties of non-cysteinyl ligation in FeS clusters. In comparison to the negatively charged cysteinyl ligand an uncharged protonated histidine decreases the negative charge in the vicinity of the cluster, and it becomes thermodynamically more favorable to introduce a negative

charge (electron). Thus, an increase of the cluster's redox potential occurs when a nearby protonation accompanies a redox process. This process is the so-called PCET and it has been mainly found in biological FeS systems with histidine coordination, though it has also been found in Fe/S model compounds[54,55] and in other redox processes[56].

Another phenomenon related to non-cysteinyl coordination is the change in cluster stability. The most stable ligands for FeS clusters are undoubtedly cysteine residues. Their thiolate anions are ideal to form stable and geometrically optimal bonds. When ligands are changed, the ideal conditions provided by cysteines are not fully met. It has been suggested that non-cysteinyl coordination may intentionally reduce cluster stability. In MitoNEET the $[2Fe\text{-}2S]^{2+}$ half-life of the H87C variant is 30-fold longer[57], a property which for regulatory or biosynthetic purposes might be essential to perform its function[14].

2.4.2. Types of non-cysteinyl coordination and their biological roles

Non-cysteinyl coordination in [2Fe-2S] clusters, in which one or two cysteine ligands of the cluster are replaced by histidine residues, is the most common substitution found in nature[50]. Ligands replacing a single cysteine can be aspartate, glutamate, glutamine, threonine or arginine residues. It is worth noting that the histidine coordination of FeS clusters is often highly conserved among organisms while coordination by other amino acids is not[50].

Several coordination schemes can be found in nature with the substitution of one or two cysteine ligands by other amino acids. The most common substitutions are shown in Figure 6 and will be shortly described in this section.

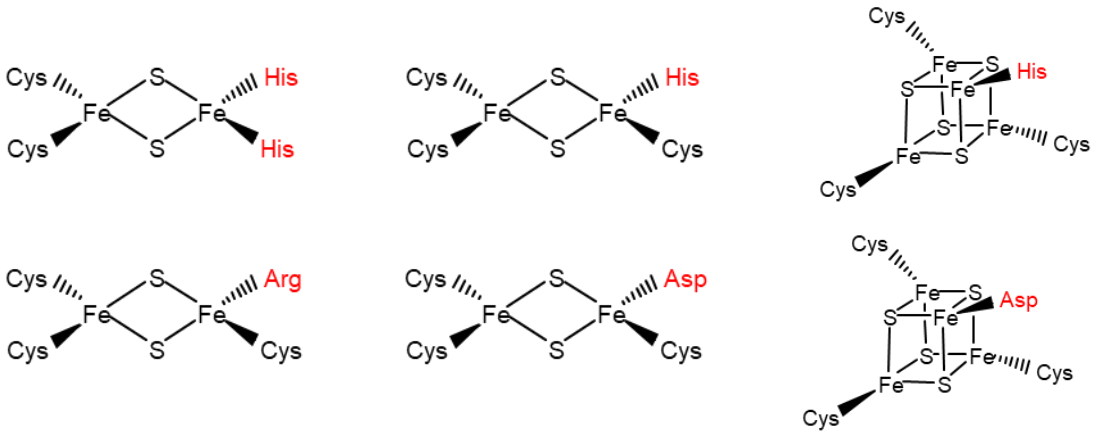

Figure 6. Most common types of non-cysteinyl coordination of [2Fe-2S] and [4Fe-4S] clusters.

2 Cys – 2 His coordination of [2Fe-2S] clusters

In the class of [2Fe-2S] clusters with non-cysteinyl ligands, the Rieske proteins are certainly the best studied case. Rieske proteins can be divided into high and low potential types. Both can be found in

many electron transfer chains in all three Domains of life. The high potential Rieske centers are present in the respiratory and photosynthetic electron transfer chains of many organisms, in the bc_1 and b_6f complexes, respectively[58,59]. Low potential Rieske clusters are found in Rieske type ferredoxins of dioxygenases and dioxygenases[60,61]. In both types they present a [2Fe-2S] cluster with a 2-Cys and 2-His coordination[59]. Another class of proteins containing a Rieske cluster are arsenite oxidases. They do not seem to fit either class mentioned previously, but still share the cluster coordination[61]. Rieske proteins will be discussed in more detail in Chapter V.

Other proteins with the same coordination were described in literature but classified as Rieske-like/non-Rieske clusters. This is the case for the GrxS14-BolA1 from *Arabidopsis thaliana* where structural modelling and spectroscopy indicate a Rieske-like cluster in a non-Rieske fold protein complex[62]. Another example is Apd1, a cytosolic yeast protein extensively studied in this working group. It contains a non-Rieske [2Fe-2S] cluster with bis-histidinyl coordination and displays PCET behavior. Even though Apd1 is thought to be a part of the cellular detoxification system, its role is still not fully understood[63].

2 Cys – 1 His- 1 Asp/Glu coordination of [2Fe-2S] clusters

Studies carried out in our group by Dr. Catharina Blinn for her PhD thesis characterized an Apd1 protein homolog from the bacterium *Thermomonospora curvata* and demonstrated that this protein contains a $[2Fe\text{-}2S]^{1+/2+}$ cluster coordinated by 2-Cys, 1-His and 1-Asp residue[64].

In 2019, a study by Volbeda and colleagues[65] presented the structure of the Redox sensitive response Regulator (RsrR), a member of the Rrf2 family of transcription regulators. The protein was present in solution as a dimer and contained two [2Fe-2S] clusters in the interfaces between monomers. These clusters were coordinated by 2-Cys residues from one subunit and 1-His and 1-Glu from the other. Its function and DNA binding ability are associated with the oxidation state of the clusters via conformational changes.

3 Cys – 1 His coordination of [2Fe-2S] clusters

Cluster coordination by one histidine and three cysteine residues is a common coordination scheme in non-cysteinyl coordinated clusters, appearing in several proteins. Among those, the *CDGSH* proteins are a class of proteins characterized by the presence of the name-giving amino acid sequence, known to be a part of the primary structure responsible for [2Fe-2S] cluster binding. This motif appears in several proteins that are claimed to regulate iron and ROS metabolism, and in which the clusters are coordinated by 3-Cys and 1-His residue[66,67]. They are divided into Class I and II, containing one and two [2Fe-S] clusters, respectively. The most studied protein in this family is the human MitoNEET whose function is still unclear. It was found that MitoNEET is intimately related to diabetes, cancer and neurodegeneration in humans[68].

Another protein that shows this cluster coordination scheme is the iron-sulfur cluster regulator (IscR). This protein is known to regulate the transcription of the ISC and Suf pathways of FeS cluster biogenesis regulating the production of FeS clusters in *E.coli*[69–71], and will be discussed in detail in Chapter III.

IscU, another protein encoded in the ISC pathway, serves as a scaffold protein for FeS clusters before their final incorporation in the destination protein. It also contains a [2Fe-2S] cluster with a 3-Cys 1-His coordination. Through the crystal structure, the cluster was shown to be buried between three subunits, but exclusively coordinated by amino acids from subunit B[72].

Mono-histidinyl coordination can also be studied in the non-naturally occurring His-to-Cys mutants from Rieske proteins and Apd1. A study by Kounosu[73] and coworkers produced two 3-Cys 1-His mutants, H44C and H64C, of the Rieske-type [2Fe-2S] ferredoxin from *Sulfolobus solfataricus*. The study of these mutants revealed that H44C mutant contained a highly unstable cluster whereas mutant H64C harbored a stable [2Fe-2S] cluster. The determination of the redox potential of the cluster from mutant H64C by dye-mediated redox titrations yielded a redox potential in the range of -400 ± 60 mV. The decrease in the redox potential caused by the mutation of one histidine residue was approximately 350 mV when compared to the wild type with a redox potential of -52 ± 4 mV.

A similar study was conducted in our working group by Stegmaier and colleagues[63] for the Apd1 protein. Both H255C and H259C mutants were stable enough for spectroscopic studies contrarily to the Rieske protein mentioned above. As observed for the Rieske protein, the substitution of a ligating histidine by a cysteine led to a ~200 mV decrease in the redox potential from −203 mV to −415 mV (H255C) and −395 mV (H259C).

Another interesting coordination scheme is described for the heterodimers formed with yeast glutaredoxins, Grx3 and 4. In 2009, Li and coworkers[74] reported that the yeast proteins Grx3 and 4 interact with the Fe repressor of activation-2 (Fra2). It was reported that, in the absence of Fra2, Grx3/4 would form a dimer bridged by a [2Fe-2S] cluster coordinated by two cysteine residues and two glutathione molecules. However, upon addition of Fra2, the Grx3/4 dimer would dissociate and a heterodimer of Grx3/4 and Fra2 would form, also containing a bridging [2Fe-2S] cluster but with a different coordination scheme. The new cluster's coordination was described to be composed of 1-Cys (from Grx3/4), one glutathione molecule, 1-His (from Fra2) and a fourth unknown ligand[74]. Li and colleagues[75] reported a follow up analyzing a putative interaction between the human glutaredoxin (Glrx3) and BolA2, the human homologue of yeast Fra2. A titration of Glrx3 with BolA2 yielded relevant changes in spectroscopic data that allowed the identification of a histidinyl coordination as observed for Grx3/4 and Fra2[75].

3 Cys – 1 Arg coordination of [2Fe-2S] clusters

Biotin synthase is an *E. coli* protein that catalyzes the last step in the production of biotin from dethiobiotin through the insertion of a sulfur atom. It contains a [2Fe-2S] cluster coordinated by 3 cysteine residues and 1 arginine residue and a radical SAM-dependent [4Fe-4S] cluster that generates the 5'-deoxyadenosyl radical. Reaction occurs through hydrogen atom abstraction of dethiobiotin that generates a dethiobiotin radical. Interestingly, it has been shown that the radical reacts with a sulfide from the [2Fe-2S] cluster[16] that, after the reaction, dissociates from the enzyme and is replaced every turnover. The role of the arginine residue is currently not known, but it seems non-essential for catalysis as mutant proteins still showed activity[32]. However, a mutation from arginine to cysteine significantly lowers the activity indicating that this might be a case of ligand substitution to facilitate sulfur donation, decrease cluster stability and enhance cluster dissociation[76].

3 Cys – 1 Asp coordination of [2Fe-2S] clusters

Succinate-ubiquinone oxidoreductase (SQR), or succinate dehydrogenase, is a bacterial enzyme, analogous to complex II in mitochondria. It is a part of the Kreb's cycle catalyzing the reversible oxidation of succinate ($2e^-$) to fumarate and the two step reduction of ubiquinone ($2x\ 1e^-$). It is a partially membrane-bound enzymatic complex composed of four subunits (ABCD) that possesses one FAD cofactor, one [2Fe-2S], one [4Fe-4S], one [3Fe-4S] cluster and a quinone binding pocket. Even though the *E. coli* [2Fe-2S] cluster of SQR has a 3-Cys 1-Asp coordination[77] most SQR and menaquinol:fumarate oxidoreductases (QFR) harbor canonical [2Fe-2S] clusters[78]. Literature on the role of the variation is Asp/Cys ligation in *E.coli* SQR is very scarce.

Additionally, the NADH-dependent reduced ferredoxin:NADP oxidoreductase (NfnAB), from *Thermotoga maritima* is another case of three Cys/ one Asp coordination. Associated with an electron bifurcation pathway in the cytosol of anaerobic bacteria and archaea, this protein contains two [4Fe-4S] clusters, one canonical and one non-canonical, and a [2Fe-2S] cluster with a non-cysteinyl coordination. Besides that, two FAD molecules also participate in the electron bifurcation pathway. The presence of the NfnA [2Fe-2S] aspartate ligand was linked to a possible decrease of the cluster redox potential in comparison to the canonical cluster from the bacterial dihydroorotate dehydrogenase (Dodh) with a high sequence similarity (-212 mV)[79].

3 Cys – 1 Ser coordination of [2Fe-2S] clusters

Several studies have been conducted on the substitution of ligating cysteines to serine residues in the human[80], plant-[81] and bacterial-type[82] ferredoxins . Even though no naturally occurring cluster has been shown to contain a 3-Cys 1-Ser coordination scheme, the chemical similarity between cysteine and serine residues make serine mutants highly relevant for the understanding of FeS cluster coordination. In all cases it was concluded that these ferredoxins can tolerate the mutation of at least one cysteine to serine[80–82].

3 Cys – 1 Asp/Glu/Gln coordination of [4Fe-4S] clusters

The fumarate and nitrate reduction (FNR) protein, an oxygen-sensor in the facultative aerobic *Bacillus subtilis*, was found to contain a [4Fe-4S] cluster with an aspartate coordination, besides the three cysteine residues. This protein is a transcription factor that regulates the transcription of genes related to anaerobic metabolism. Even though this cluster coordination is not conserved among species (*E. coli* and *Aliivibrio fischeri* contains an FNR with full cysteinyl coordination[83]), the substitution of cysteine by an aspartate[84] residue is thought to be related to the tuning of the redox potential. This substitution, when compared to the cysteine mutant showed a slightly higher redox potential that presumably allows for the reversibility of the reaction[84].

In the NO sensor NsrR from *Streptomyces coelicolor*, a dimeric protein associated with regulation of gene expression in the presence of nitric oxide (NO), a [4Fe-4S] cluster is present. This cluster is coordinated by three cysteine residues from monomer A and by an aspartate residue from monomer B. In this case, the presence of NO displaces the aspartate residue leading to a progressive cluster breakdown required for protein function[85].

In *Thermosynechococcus elongatus*, a dark operative protochlorophyllide oxidoreductase (DPOR) (composed of subunits ChlL, ChlN, and ChlB) catalyzes the production of chlorophyllide by a two-electron reduction process. The heterotetramer (ChlN/ ChlB)$_2$ contains two [4Fe-4S] clusters coordinated by one aspartate, from ChlB, and three cysteine residues, from ChlN. Interestingly, this aspartate residue does not appear to be conserved as other homologous proteins, namely enzymes from the nitrogenase-like family, contain a cysteine residue in the fourth coordination site[86].

Another protein containing a 3-Cys 1-Asp coordination is the F420 reducing [NiFe] hydrogenase from *Methanothermobacter marburgensis*. This protein is organized in a dodecameric mega complex of 1.25 MDa with a $(\alpha\beta\gamma)_4$ spatial configuration. The heterotrimer is composed of monomers A, B and G. A [NiFe] cluster is present in monomer A, an FAD binding site and a [4Fe-4S] cluster are present in monomer B and three [4Fe-4S] clusters in monomer G. The proximal cluster of monomer G shows a 3-Cys 1-Asp coordination, which was correlated with the dislodgment of a glutamate residue in the vicinity and that, due to this replacement, forms a hydrogen bond with a histidine residue. Besides that, it was hypothesized that a redox potential shift could be another consequence of this substitution[87].

The IspG protein, involved in the production of universal isoprenoid precursors and structurally characterized in 2010 by Lee and coworkers was shown to contain a [4Fe-4S] cluster with a 3-Cys 1-Glu coordination. In this study, the substitution of the glutamate residue by an aspartate resulted in almost complete loss of activity whereas the mutant protein where the glutamate was substituted by a cysteine could not be expressed at all. However, upon its substitution by a glutamine residue the

protein presented 28% of remaining activity. The authors then concluded that the glutamate residue possibly plays a role in stabilizing the cluster against the loss of the fourth iron ion[88].

The same electron bifurcation mechanism previously mentioned in the section on 3-Cys 1-Asp coordination of [2Fe-2S] clusters also contains a [4Fe-4S] cluster with a 3-Cys 1-Glu coordination. Located in NfnB subunit, contrarily to its other non-cysteinyl coordination that is in NfnA, the glutamate ligand was also associated with decreased redox potential when compared to the usual cysteinyl ligand[79]. A similar protein, dihydropyrimidine dehydrogenase (DpdH) shows a glutamine in its coordination shell instead of a glutamate residue[79,89].

3 Cys – 1 His coordination of [4Fe-4S] clusters

Hydrogenases are well studied proteins that catalyze the reversible conversion of molecular hydrogen (H_2) into protons ($2H^+$) and electrons ($2e^-$). They are divided into [FeFe] and [NiFe] hydrogenases based on the metals present in their catalytic cluster (H-cluster). Besides the catalytic cluster, hydrogenases contain other FeS clusters that function as an electron transfer chain. In the [FeFe] hydrogenase from *Clostridium pasteurianum I*, besides the H cluster, three [4Fe-4S] and one [2Fe-2S] clusters are present. The distal [4Fe-4S] cluster, close to the surface, was shown to have a 3-Cys and 1-His coordination. The cubane is coordinated by the N_ε atom of the histidine residue[90]. A similar coordination, though with the N_δ nitrogen atom, is found for the solvent exposed distal [4Fe-4S] cluster in the structure of [NiFe][91] and [NiFeSe] hydrogenases[92]. In these cases, the histidine mutation to a cysteine still allowed cluster formation although it drastically decreased protein activity. It was then hypothesized that the presence of a histidine ligand could be a tuning mechanism for the redox potential[5].

The cytoplasmic membrane-bound quinol-nitrate oxidoreductase (nitrate reductase A, Nar) is an *E. coli* enzyme that catalyzes the conversion of nitrate to nitrite coupled to a proton-motive force generation. This complex enzyme is composed of three subunits (NarGHI), harboring a Mo-bisMGD, five FeS clusters and two hemes. From the five FeS clusters, four are in subunit H, and one in subunit G. The latter, named FS0 and the closest to the molybdenum cofactor is the one showing a three cysteine and one histidine coordination. In 1998, Magalon and coworkers carried out site directed mutagenesis studies on the coordinating histidine from subunit G. It was reported that histidine mutation to either a cysteine or a serine residue impaired the cells ability to grow anaerobically on nitrate or in minimum media. The enzyme had a heavily decreased activity and changed substrate specificity. In this study, it was concluded that, even though the histidine residue does not coordinate the molybdenum ion, it was necessary for the correct functioning of the cell possibly through hydrogen bonds in the cluster vicinity[93]. Later, in 2003, Bertero and colleagues showed through the crystal structure that the [4Fe-4S] cluster near the molybdenum cofactor was the cluster coordinated by histidine residue (N_δ)[94].

NADH dehydrogenase, or Complex I, is an important enzyme involved in the respiratory chain. It is composed of eight subunits with a total of nine FeS clusters, being two [2Fe-2S] (N1a and N1b) and seven [4Fe-4S] clusters (N2, 3, 4, 5, 6a, 6b and 7). Cluster N5, was described by Sazanov and colleagues[95] as containing a non-cysteinyl coordination, having 3-Cys 1-His (N_ε) residues as ligands in the study of the soluble part of Complex I from *Thermus thermophilus*. The authors discuss that, for other proteins, this coordination has been shown to tune the redox potential and yield specific spectroscopic features. They then compare the N5 cluster coordination with similar ones, as in the [FeFe]-hydrogenase[90] and the nitrate reductase A[94], but do not hypothesize on the role played by the histidine beyond questioning whether cluster N5 is only a "stepping stone" of the electron transfer pathway.

The 4-hydroxybutyryl-CoA dehydratase from *Clostridium aminobutyricum* is a part of the acyl-CoA dehydratase family involved in fermentation. This enzyme was shown to contain a [4Fe-4S] cluster coordinated by three cysteine and one histidine (N_ε) and to be present at approximately 7 Å of distance from an FAD. In this case, the substrate binds in between the cofactors, both necessary for catalysis to occur. It was shown that the cluster's redox potential increases around 200 mV upon substrate binding and was associated with possible solvent protection. The shift of the redox potential was explained by the protonation of the histidine ligand[96].

3 Cys – 1 Ser/Thr coordination of [4Fe-4S] clusters

The 3-Cys 1-Thr coordination scheme, though not common in Nature, can be found in the dissimilatory sulfite reductase (dSir) from *Archaeoglobus fulgidus*. This protein catalyzes the reduction of sulfite to S^0, an important process in the sulfur biogeochemical cycle. To catalyze such a complex reaction, the protein, organized as a heterotetramer $(\alpha\beta)_2$, contains two siroheme-[4Fe-4S] units, one in each αβ catalytic dimer. Schiffer and colleagues[97] showed that, surprisingly, it appears that only one siroheme-[4Fe-4S] cluster is catalytically active. The crystallographic structure shows that the catalytically active cluster is coordinated by 3-Cys and 1-Thr residues. In contrast, the non-active one and the cofactor reported for the assimilatory Sir, a phylogenetically similar protein, are coordinated by four cysteine residues. However, the authors argue that, though the distance between the cysteine sulfur and the cluster (3 Å) is quite large, conformational changes could lead to a replacement of the threonine residue by cysteine.

The 3-Cys 1-Ser coordination of [4Fe-4S] clusters has not yet been reported for naturally occurring clusters. However, several mutagenesis studies have been published, as for [2Fe-2S] clusters. This is mostly due to the structural similarity between cysteine and serine residues that only differ in the side chain final functional group (thiol to hydroxyl).

In 1996, Babini and coworkers[98] carried out studies on the mutation of cysteine 77 to a serine residue in the High Potential Iron-Sulfur Protein (HiPIP) from *Chromatium vinosum*. A 25 mV cluster redox

potential decrease was reported. According to the authors, the overall stability of the cluster change was barely significant, both in the reduced and oxidized states.

Two similar studies were conducted by Brereton and colleagues in 1998[99] and 1999[100]. In one of these studies (1999), the 7.5 kDa ferredoxin from *Pyrococcus furiosus*, containing a $[4Fe\text{-}4S]^{1+/2+}$ cluster with a 3-Cys 1-Asp *in vivo* coordination, was subjected to several site-directed mutagenesis experiments to produce proteins containing clusters with full cysteinyl as well as 3-Cys 1-Ser coordination. The authors observed similar cluster stability when compared to the wild type, but different paramagnetic properties. The canonical cluster and one of the serine mutants showed homogeneous S=1/2, but the others presented a mix of S= 1/2 and 3/2 states. The redox potentials decreased only slightly by 49 and 78 mV in two serine mutants[100].

In the experiments carried out in 1998, the coordinating aspartate residue was substituted by a cysteine, serine, histidine, asparagine, valine, and tyrosine residues and the mutant protein expressed in *E. coli*. The authors observed that the mutant proteins coordinated by serine and cysteine residues still contained a $[4Fe\text{-}4S]^{1+/2+}$ cluster, whereas the remaining mutants presented a $[3Fe\text{-}4S]^{0/1+}$ cluster. The authors also showed a pH-dependent behavior for the $[3Fe\text{-}4S]^{0/1+}$ wild type and histidine coordinated cluster, associated with the protonation of the amino acids' sidechain. For the $[4Fe\text{-}4S]^{1+/2+}$ protein, a pH dependence was also observed for the aspartate to serine but not for the aspartate to cysteine mutant[99].

3. FeS cluster biogenesis

Sensing cellular levels of iron, oxygen, ROS and redox active molecules triggers cellular responses, as previously discussed. One of the most important responses of the cell is the restoration of the lost FeS clusters. There are three main FeS cluster biogenesis pathways in prokaryotes – the Nitrogen fixation (Nif), the Iron-Sulfur cluster (ISC) and the Sulfur-formation (Suf) pathways. The Nif system was the first FeS biogenesis pathway identified[101], followed by the ISC[102] and the Suf pathways[103]. All systems are based on the presence of a dedicated cysteine desulfurase (NifS, IscS and SufS), that removes sulfur atoms from L-cysteine and transfers it to a scaffold protein (NifU, IscU, and SufBCD), where a [2Fe-2S] cluster is assembled[104]. It was also recognized, that in eukaryotes mitochondria have an ISC system[105], which is responsible for maturation of mitochondrial FeS proteins as well as for Cytosolic Iron-sulfur cluster Assembly (CIA) machinery. This pathway will only be briefly mentioned in this section as this work focuses on prokaryotes.

3.1. Nitrogen fixation (Nif) pathway and nitrogenase

In 1989, Jacobson and others first described the Nif system, discovered in *Azotobacter vinelandii*[106]. This system is composed of the genes that encode proteins directly connected to the production and maturation of the nitrogenase proteins, that convert N_2 into NH_3 in nitrogen-fixing bacteria. There are three types of nitrogenase enzymes described for *Azotobacter vinelandii* – a molybdenum, a vanadium and an iron-containing protein. They were designed *nif*, *vnf* and *anf*, respectively, the latter two are sometimes referred to as alternative nitrogenases (*anf*). These proteins are genetically distinct but play the same role and require a similar set of proteins for their complete maturation[15,107].

The molybdenum protein, which is the preferred version when metal availability conditions allow, is the catalyst reacting with N_2. It is organized as dimer of heterodimers $(\alpha\beta)_2$ $(Nif(DK)_2)$ and contains two clusters – a P-cluster, with an arrangement of two [4Fe-4S] clusters sharing one inorganic sulfide in the center (Fe_8S_7)[19]; and a FeMo cofactor (Mo-Fe_7-S_9-C-homocitrate)[107,108]. For catalysis, the MoFe protein requires electrons that are provided by the Fe protein, also designated as nitrogenase reductase, composed of a homodimer $(\alpha)_2$ ($NifH_2$) bridging a [4Fe-4S] cluster, that is Mg^{2+} and ATP dependent[107].

The *nif* gene cluster is composed of genes encoding the protein catalytic subunits $(\alpha\beta)_2$ (*nifD* and *nifK*) and the Fe-protein (*nifH*). Also present in the *nif* gene cluster are the genes encoding the auxiliary proteins, such as *nifE*, *nifN* and *nifB*, essential for FeMoco biosynthesis and maturation and *nifV*, which encodes a homocitrate synthase[107].

3.2. Iron-Sulfur Cluster (ISC) biogenesis pathway

The iron-sulfur cluster pathway, encoded by the operon *iscRSUA-hscBA-fdx-iscX*, represented in Figure 7, is considered the housekeeping FeS cluster biogenesis pathway in Eubacteria[109]. The *E. coli* system, first described in 1998 by Zheng and coworkers[110], has been extensively studied. This operon contains eight genes directly related to FeS cluster biogenesis in the cell and is highly conserved eubacteria and eukaryotes (mitochondria)[111].

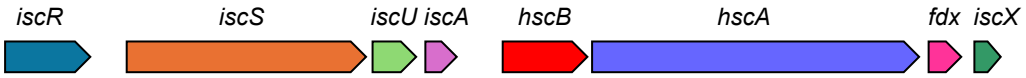

Figure 7. *isc* operon from *E. coli*. Adapted from Romsang *et al.*[111]

At the 5' end of this operon, the *iscR* gene encodes the iron-sulfur cluster regulator (IscR), which contains a [2Fe-2S] cluster itself. This protein regulates DNA transcription by alternating between holo and apo forms, regulating its own cluster content by a negative feedback loop[112]. This protein will be further discussed in detail in Chapter III. Following *iscR* comes *iscS* and *iscU*, homologous to *nifS* and *nifU*, respectively[109,113].

IscS, a pyridoxal-5′-phosphate (PLP)-dependent cysteine desulfurase, has as main role to remove sulfur atoms from L-cysteine residues, forming L-alanine. These sulfur atoms will then be delivered to a variety of metabolic pathways and scaffold proteins, including IscU[114].

IscU is a scaffold protein of the ISC pathway. *In vivo*, it forms a heterotetramer with IscS to receive inorganic sulfides. IscU presents 3 conserved cysteine residues (37, 63 and 106, *E. coli* numbering[115]) in a three-dimensional space consistent with cluster coordination[72]. This FeS cluster binding site was shown to be at the interface with IscS in the $(\alpha\beta)_2$ complex. Upon purification, IscU does not present any cofactors, however, in the mutants of a critical aspartic acid or upon anaerobic reconstitution with Fe^{3+} and S^{2-} it shows the presence of a [2Fe-2S] cluster[72]. Other studies were also able to detect a sequential mechanism where, initially, IscU binds a [2Fe-2S] cluster per dimer followed by the identification of two [2Fe-2S] clusters per dimer and a final species containing one [4Fe-4S] cluster per dimer. The lack of a constitutive cluster in IscU strongly supports the hypothesis of a role as a scaffold protein. It was also found that IscU interacts with the protein product of the genes *hscA* and *hscB*, Hsc66 and Hsc20, respectively[116]. *HscA* encodes a specialized bacterial molecular chaperone, also known as Hsc66, while *HscB* encodes a co-chaperone, also known as Hsc20. HscA is known for participating in the assembly of FeS cluster containing proteins and interacts with IscU. The interaction between HscA and IscU is facilitated by HscB, that binds to both proteins bringing them together enough to bind, or at least interact[117].

IscA is the following in the ISC operon. IscA is part of the A-type carrier group of proteins. It is known to form a protein complex with and transfer clusters to the electron transferring [2Fe-2S] ferredoxin (*fdx*) also encoded in the ISC operon. IscA is organized in solution as dimer of homodimers (non-

equivalent monomers for the first dimer as in $(\alpha_1\alpha_2)_2$). Upon purification the protein is in its apo form, but when anaerobically reconstituted it harbors a [2Fe-2S] cluster with full cysteinyl coordination in the interface between the four monomers[118].

Fdx encodes a ferredoxin that is necessary for electron transfer processes required for the maturation of various other FeS cluster containing proteins. It harbors a regular [2Fe-2S] cluster coordinated by four cysteine residues (42, 48, 51, and 87, *E.coli* numbering). It has been described as the electron donor for the reduction of S^0 to S^{2-} in IscS and is involved in the coupling of two [2Fe-2S] clusters in IscU.

YfhJ, also called ORF3 or IscX, is a small protein encoded by *IscX*, the last gene in the ISC operon. Its function is not known, but it is thought that it might be involved in Fe transport for FeS cluster production due to its highly acidic character (pI = 3.7). Similar acidic residue-containing pockets are very characteristic of Fe storing and transporting proteins, such as ferritins[119].

3.3. Sulfur Formation (Suf) biogenesis pathway

The sulfur formation (Suf) pathway, discovered in 1999[103], is another biogenesis pathway present across all domains of life. While not as prevalent as the ISC pathway, the Suf pathway is of extreme importance and holds intriguing functions in different organisms.

The Suf operon, *sufABCDSE*, encodes six proteins organized in two complexes and one protein. The complex sufSE is composed of SufS, a PLP-dependent desulfurase that removes sulfur atoms from L-cysteine residues; and SufE, that acts like a scaffold accepting sulfur atoms from SufS and donating it to SufA afterwards. In some organisms, however, SufE is replaced by SufU. SufU presents a higher similarity with IscU in terms of primary structure but performs the same function of SufE. Though *sufU* and *iscU* were shown to not be equivalent, successful complementation of *B.subtilis* Δ*sufSU* with the *E. coli sufSE* and vice versa was achieved by Yokoyama and coworkers[120,121].

The SufBCD complex, composed of four cytosolic monomers – one SufB, two SufC and one SufD – is an ATPase and a member of the ABC transporter family. It is a scaffold protein where FeS clusters are assembled prior to their final incorporation into the target proteins[121]. The *suf* operon is represented in Figure 8.

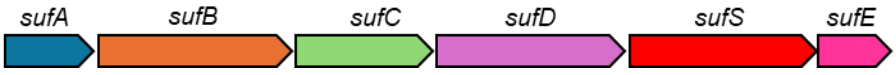

Figure 8. *suf* operon from *E. coli*. Adapted from Johnson *et al*.[122]

The role played by the Suf pathway in each type of organism appears to be highly dependent on the characteristics of this organism. In Enterobacteria, the Suf pathway is a stress-induced biogenesis mechanism. It is activated by apo-IscR and performs more effectively than the ISC pathway upon oxidative stress and under iron starvation conditions. Under normal conditions it is repressed by the

ferric uptake regulator (Fur), a protein that regulates iron homeostasis in bacteria[122]. The Suf pathway is also thought to act as an emergency “fight or flight” response. It only produces and inserts FeS clusters into proteins that are absolutely necessary for the correct functioning of the cell or that are related to overcoming the transient redox stress situation[123].

In plant chloroplasts and cyanobacteria, on the other hand, the Suf pathway is known to be the constitutive FeS biogenesis pathway[124]. It has been hypothesized that the nature of photosynthetic and non-photosynthetic organisms, and their characteristic habitats, might favor different FeS biogenesis pathways. Cyanobacteria are sometimes found under iron starvation conditions in metal-poor seawater. A further source of stress is the oxygen production in cyanobacteria by photosynthetic pathways that will inevitably lead to the continuous production of ROS in the cells. The oxygen production by photosystem II explains why the Suf system is employed in plant chloroplasts[125].

3.4. Cytosolic Iron-sulfur Assembly (CIA) biogenesis pathway

Cellular compartmentalization is one of the most prominent differences between prokaryotic and eukaryotic cells. In Bacteria, the lack of cellular compartments allows for molecules to move through the cell in a less constrained way when compared to eukaryotic cells. This might also reflect on the type of FeS cluster biogenesis machineries required to produce and incorporate FeS clusters in each type of cells[16,126–128].

Eukaryotic cells contain FeS cluster proteins in the mitochondrial space, cytosol, and nucleus. Inside the mitochondria, FeS cluster biogenesis is managed by the ISC pathway, while in the cytosol, this role is taken over by the CIA machinery. It is believed that the mitochondrial ISC pathway is inherited from a bacterial ancestor involved in the endosymbiotic event. This pathway was then confined to a reducing environment, likely similar to early Earth's conditions[16,126–128].

The CIA machinery operates in a tightly regulated and coordinated way with the mitochondrial ISC pathway, accepting an unknown precursor from mitochondria, possibly a [2Fe-2S] cluster coordinated by glutathione[129].The whole eukaryotic FeS pathway is more complex than their bacterial analogues and consists of seventeen proteins regulated/encoded by the mitochondrial ISC pathway, three from the ISC export machinery and eleven proteins from the CIA machinery[16,126–129]. Given its complexity and limited relevance to the work presented in this thesis, it will not be further discussed.

4. Spectroscopy of FeS clusters

4.1. Ultraviolet-Visible spectroscopy

Ultraviolet-Visible (UV-Vis) spectroscopy is the simplest and most cost-effective spectroscopy. It is widely used for a series of purposes in all areas, including the field of biochemistry. This method is based on the absorption of discrete wavelengths in the ultraviolet and visible region, from approximately 200 to 750 nm[130].

In biochemistry, UV-Vis spectroscopy can be used to determine the concentration of biomolecules, especially proteins and their cofactors, as well as conformational changes, protein-protein interactions, protonation and deprotonation processes, kinetic studies, among others.

It is dependent on the sample concentration, pathlength and the nature of the sample under study. This dependence can be calculated using the Lambert-Beer law, described in Equation 1[131].

$$A = \varepsilon c b \qquad \text{Equation 1}$$

Where A is the absorbance directly measured by the UV-Vis spectrophotometer with no units and ε is the extinction coefficient, in $M^{-1}cm^{-1}$, characteristic of the sample under study. c and b are the concentration of the sample, in M, and the pathlength, in cm, respectively.

The UV-Vis spectrophotometer is composed of a light source, usually a tungsten and a deuterium lamp, that emit light in the entire visible and UV range, respectively. The light is then focused on a monochromator and passes through the sample. The radiation is partially absorbed by the sample while the radiation that was transmitted reaches a photocell that acts as detector and generates electric current. The electric current is amplified, and the data are processed converting the electrical signals into a graphic display of absorbance versus wavelength, the so-called UV-Vis spectrum[132].

The use of UV-Vis is especially necessary in this project due to the high sensitivity of the technique in the study of FeS clusters and their ligands. These clusters generally act as chromophores that absorb light in the ultraviolet-visible range and yield a characteristic signal allowing its identification based on the spectra obtained. For FeS clusters, the ligand-to-metal charge transfer (LMCT) absorption bands are specific for each type of cluster, sensitive to redox state, to the ligands and their protonation states.

4.2. Circular Dichroism spectroscopy

Circular Dichroism (CD) spectroscopy is an important tool to analyze biomolecules. Due to the intrinsic chirality of the amino acids, this spectroscopy is of paramount importance in the structural studies of proteins. It is based on the differential absorption of left and right circularly polarized light (LCPL and RCPL, respectively) by chiral molecules. It provides important structural information on the molecule under study, such as protein secondary structure, DNA and protein interactions. By

recording melting curves CD spectroscopy contributes to our understanding of protein folding and stability[133].

When a chiral molecule absorbs LCPL and RCPL differently, this difference in absorption is measured. This phenomenon is called circular dichroism. This difference in absorption, given the same pathlength and sample concentration, is related with the changes in the extinction coefficient, a measure of the standard absorption of a 1 M solution in a 1 cm path length. The CD spectra are then recorded as Δε (ε_{left}- ε_{right}), or molar circular dichroism, at each wavelength. Instead of Δε, the intensity of the signal is more commonly reported as molar ellipticity (θ), which is related to the Δε by a factor of 3298.2[134]. Peaks at specific wavelengths indicate specific electronic transitions in the chiral molecule[133].

In the far UV range, typically between 180 and 250 nm, the bands in a CD spectrum can give insight into protein secondary structure. These bands arise from the absorption of light by the peptide bonds in the chiral protein backbone. α-Helices tend to show two negative (around 222 and 208 nm) and one positive (near 190 nm) band, while β-sheets tend to present only one negative band (close to 218 nm) and one positive (around 195 nm). Random coils present a single negative band around 195 nm. Apart from specific proteins mainly composed of one type of secondary structure, most proteins present a mixture of secondary structural elements. To derive information, a deconvolution of the spectra is done by minimization of residuals between experimental and a calculated mixture of species. This calculation allows the description of the secondary structure[135].

In visible CD spectroscopy, typically ranging from 300 to 750 nm, it is possible to obtain insights into the chromophores and metallocentres, including FeS centers. These peaks arise from the LMCT as observed in UV-Vis spectroscopy[136]. It can be used to study cluster ligands and changes that might happen in the vicinity of the cluster, such as protonation and deprotonation or amino acids, as well as to gain insight into cluster stability over time, pH or temperature.

In the visible range, CD spectroscopy has been used in the study of FeS cluster containing proteins for several purposes. These include the determination of cluster oxidation state and its electronic changes upon site-directed mutagenesis, as performed for MitoNEET wild type and its H87C mutant[137]. Additionally, protein-protein interaction and its influence on cluster structural properties can be assessed, as described for the interaction between Fra2 and Grx3[74]; or to follow cluster formation, as described for the ISU1 protein[138,139].

Magnetic CD spectroscopy is also often used in the study of FeS cluster containing proteins due to the clusters' intrinsic magnetic properties. It consists of measuring the circular dichroism effect in the presence of a strong applied magnetic field in parallel to the path of light at low temperatures[4].

A protocol published by Greenfield for the study of protein's secondary study with circular dichroism summarizes useful information on buffer and cuvette choice, as well as protein preparation and data

analysis[135]. Additionally, a review by Miles and colleagues[140] supplies more information on CD data analysis.

4.3. Paramagnetic Resonance: Continuous wave and pulsed EPR spectroscopy

Electron Paramagnetic Resonance (EPR), also referred to as Electron Spin Resonance (ESR), is a widely used technique for the study of paramagnetic species. It can detect electronic transitions of unpaired electrons, usually with a good signal to noise ratio in the micromolar (μM) range for proteins. Biochemists are particularly interested in EPR spectroscopy due to the wide range of metallocofactors occurring in proteins in Nature. Metallocofactors can frequently undergo reduction and/or oxidation and typically have at least one EPR-active form. EPR spectroscopy provides valuable information on aspects such as cluster identification, redox states, ligands and catalytic processes. Among the EPR-active species are most transition metals and radicals[141–143].

Single unpaired electrons in Nature have a spin (S) of ½ and spin magnetic quantum number (m_s) of ± ½. Each number corresponds to a specific *eigenstate*[a]. In the absence of a magnetic field, the *eigenstates* characterized by m_s = ± ½ are degenerate, or possess the same energy. However, in the presence of a magnetic field, this degeneracy is lifted as the electron spin can align in parallel with or against the magnetic field. This splitting is known as Zeeman splitting and is the basis for EPR spectroscopy. By convention, it is said that the unpaired electron under a magnetic field mostly occupies the m_s = -½ spin magnetic quantum level, which possesses lower energy[141–143].

When the unpaired electron under a magnetic field is irradiated with electromagnetic radiation with an energy corresponding to the difference of energy between m_s levels -½ and +½ the resonance condition is fulfilled. That way, the electron absorbs an electromagnetic radiation photon and transitions to the m_s = +½ state. EPR spectra can be measured with a wide range of microwave frequencies. The most used are S-Band (~3 GHz), X-Band (~9 GHz), Q-Band (~35 GHz) and W-Band (~90 GHz)[141–143].

The difference between levels (ΔE) is directly proportional to the magnetic field applied and can be quantified with the formula

$$\Delta E = h\nu = g\mu_B B \qquad \text{Equation 2}$$

where h is the Planck's constant (6.6261×10^{-34} J.s), ν is the electromagnetic radiation frequency (Hz), μB is the Bohr magneton ($9.2740154\ 10^{-24}$ J.T^{-1}) and B is the magnetic field (T). g is the so-called Landé factor, usually just expressed as *g*-value, a property of the electron under analysis and an important parameter to be calculated in EPR spectroscopy as it contains most the information on the

[a] *Eigen* is the German word for "one's own". An *eigenstate* or *eigenvalue*, in this case is a defined quantum state characteristic of and populated by a single electron.

electron and its surroundings[141–143]. A simplified schematic view of the Zeeman effect is shown in Figure 9.

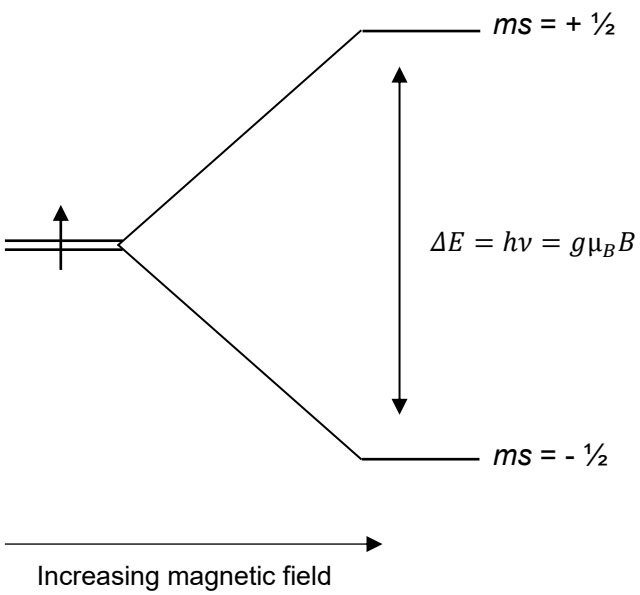

Figure 9. The Zeeman effect and the resonance condition in EPR spectroscopy.

As the resonance condition is dependent on the magnetic field, any other particle that possesses a magnetic moment present in the environment around the unpaired electron will contribute to the variation of the energy between the energy levels. That gives rise to other phenomena that will contribute to variations of the *g*-values of a given unpaired electron.

The main interactions observed are spin-orbit coupling (μ_L), spin-nucleus (hyperfine, μ_N) coupling and spin-spin (electron-electron, μ_{Sn}) coupling. Spin-orbit coupling gives rise to *g*-value anisotropy, observed as a deviation of the *g-value* away from the free electron value of 2.0023. Since most samples have random orientation of molecules a sum of EPR spectra corresponding to all orientations is observed. If due to *g*-anisotropy the three main orientations differ, a rhombic EPR spectrum is obtained; if two main orientations are similar/equal, an axial spectrum can be seen; or if the three orientations are equal, an isotropic EPR signal appears. The (super)hyperfine interaction leads to symmetric splitting of the absorption bands that are separated by the (super)hyperfine constant (A, in MHz), characteristic of the nucleus. The electron-electron interaction, that occurs in systems with multiple unpaired electrons, gives rise to the zero field splitting and to a total spin that corresponds to the sum of all spins. Thus, it is possible to have a sample with an $S \neq ½$. The spin magnetic quantum number m_s take values from -*S* to *S* in one-unit steps[141–143].

EPR spectroscopy can be divided into two main modes: continuous wave (cw EPR) and pulsed EPR. Pulsed EPR is less commonly used than cw EPR mostly due to its higher complexity when it comes to data processing and equipment required. Besides that, cw EPR is more sensitive eliminating the

need for highly concentrated samples and for [2Fe-2S]$^{1+}$ clusters not requiring as low temperatures as pulsed EPR[141–143].

In cw EPR, the sample is continuously irradiated by an electromagnetic radiation with a fixed frequency and the magnetic field is swept in the chosen range. It is then possible to observe all the resonances that were fulfilled in that range of magnetic field and frequency. In pulsed EPR the spectra are recorded by irradiating the sample with a large frequency range along with a single microwave-frequency pulse at a constant magnetic field[141–143].

The EPR spectrometer is composed of: 1) a microwave bridge, that contains the microwave source and the detector; 2) an electromagnet or a superconducting magnet, that generates the magnetic field; 3) a microwave resonator, also known as cavity, that will resonate with the microwave frequency and detune in case there is absorption of radiation by sample, returning a corresponding signal back to the bridge to the detector[143].

In pulsed EPR, there are many techniques that can be used according to the pulse type and the electronic interactions under study. The most common are Davies and Mims Electron Nuclear Double Resonance (ENDOR), Electron Spin Echo Envelope Modulation (ESEEM), Double Electron-Electron Resonance (DEER) and Hyperfine Sub-level Correlation (HYSCORE)[142,143].

ENDOR is an important technique in pulsed EPR as it allows the observation of electronic and nuclear transitions. This experiment is based on the total saturation of the electronic transitions leading to an almost equal population of the electronic states. Posteriorly, a radio frequency (RF) pulse is applied to partially saturate the nuclear transitions, leading to a small desaturation of the, previously saturated, electronic transitions as nuclear transitions begin to happen. Davies and Mims are two distinct and complementary variants of ENDOR spectroscopy. While Davies is most used for strongly coupled nuclei, Mims is used for weakly coupled nuclei around the paramagnetic species of interest. Although their pulse sequence differs significantly, each offers unique details in the study of paramagnetic species[142,144].

HYSCORE spectroscopy is also a pulsed EPR technique. However, unlike ENDOR, it provides information by varying both correlation times, τ_1 and τ_2, thus generating a two-dimensional spectrum. This technique is often used to resolve hyperfine couplings that could not be resolved by ENDOR spectroscopy. The peak positions and shapes give indications on which nucleus is being observed, the hyperfine couplings and the presence of quadrupolar interactions (for nuclei with $I > 1/2$)[144].

4.4. Mössbauer spectroscopy

Iron is the most abundant transition metal in biological systems. It is part of a series of cofactors vital to life, including FeS centers. ^{57}Fe Mössbauer spectroscopy is one of the most suitable techniques in the study of iron in biological systems. It is based on the recoilless absorption of γ-rays emitted by a

source. The source, initially radioactive ^{57}Co, decays, by electron capture, to ^{57}Fe in an excited state with a nuclear spin quantum number (I) of $^{5}/_{2}$. This excited state rapidly decays to, mostly, $I=^{3}/_{2}$, but also, $I=^{1}/_{2}$. The next decay, from $I=^{3}/_{2}$ to $I=^{1}/_{2}$ corresponds to the γ-rays emission absorbed by the ^{57}Fe atom present in the sample, corresponding to the Mössbauer effect[145].

Due to the differences in the environment around the Fe atoms when comparing the source with the sample, it is necessary to apply the Doppler effect to slightly shift the frequency of the emitted frequency until it matches the energy of the nuclear transition in the sample. This is achieved by moving the source back and forth in the same direction of γ-ray propagation at velocities of up to 10 mm/s[145].

The Mössbauer spectra are mainly characterized by the isomer shift (δ, in mm/s) and the quadrupole splitting (ΔQ, in mm/s). The isomer shift relates to the shift in the γ-ray radiation when compared to the source, arising from the difference between their s-electron densities and reflects properties such as oxidation state, electronic configuration and environment in general. The quadrupole splitting is created due to interactions with an electric field gradient that is generated by an asymmetric distribution of the electronic charge around the nucleus, thus providing information about the symmetry of the local electronic environment. Other parameters such as linewidth and the magnetic hyperfine splitting also contain relevant information that contribute to a better understanding of the system under study[145].

4.5. X-ray crystallography

X-ray Crystallography (XRC) is a crucial tool for studying structural biology. While spectroscopic methods provide significant insights into protein and their metallocofactors, understanding the entire protein requires a detailed analysis of its structure[146,147].

XRC is widely used and allows for the determination of a three-dimensional structure of a protein or other biomolecules. This technique is based on the crystallization of a pure and homogeneous protein under known and optimized conditions. The optimization process can involve pH, temperature, protein concentration, precipitant agent and its concentration, amongst others[146,147].

The most common crystallization method is the vapor diffusion. A phase transition process will be achieved upon placing a droplet of protein with precipitant agent, either sitting on a bridge or hanging, in a reservoir with precipitating agent. Phase transition happens due to water molecules diffusing towards the outside of the protein droplet leading to the formation of a supersaturated protein solution. The distance between protein molecules in solution decreases as direct consequence of the volume reduction and the formation of a supersaturated solution, leading to the creation of nucleation sites. This process can lead to the formation of a highly organized state, or a crystal. These crystals are then collected and exposed to an X-ray beam[146,147], either in the laboratory with Cu Kα radiation, or at a various wavelengths at a synchrotron.

Upon crystal irradiation, a diffraction pattern is observed giving partial information to resolve the protein structure. The phase problem (*i.e.* the lack of information of the phase in the diffraction pattern) can be solved by techniques such as Molecular Replacement (MR), Sigle/Multiple Anomalous Dispersion (SAD/MAD) or Single/Multiple Isomorphous Replacement (SIR/MIR)[146,147].

4.6. Spectroscopic methods in the characterization of FeS clusters

Spectroscopic and structural methods are of extreme importance in the study of FeS clusters containing proteins. They facilitate the understanding of the properties that make these proteins so valuable for life.

Spectroscopic and structural methods are rarely applied alone as they can report on electronic, structural and dynamic properties thus providing complementary information on different parameters of the same system. Numerous articles combine spectroscopic and structural data, exemplifying this synergy. A notable example is the review "The Spectroscopy of Nitrogenases" by Van Stappen and coworkers (2020)[4].

Using UV-Vis spectroscopy, one can identify species present in solution, determine their redox states, and observe specific electronic transitions. Adding CD spectroscopy can provide insights into protein secondary structure and cluster stability. EPR spectroscopy can reveal the nature of the cluster and spin distribution, while Mössbauer spectroscopy can complement EPR data by providing information on the properties of individual Fe ions. Other spectroscopies might also play a role in the study of FeS clusters, such as Fourier Transform Infra-Red (FTIR)[148], Nuclear Magnetic Resonance (NMR)[149], Magnetic Circular Dichroism[150], Resonance Raman spectroscopy[151,152], among others. Utilizing these techniques in a complementary manner provides high-quality and reliable data and enhances our understanding of new mechanisms in nature.

Chapter II. Methodology

1. Materials

All materials used in this practical work can be found in the tables below. They include machines, laboratory equipment, software and chemicals, cells, plasmids and primers used in Chapters III to V.

1.1. Lab equipment

Table 1. Laboratory equipment used in this work.

Equipment	Brand
Anaerobic chamber	Vinyl anaerobic chambers, Coy Laboratories
Autoclave	LVSA 40/60, Zirbus
Biofreezer	VIP™ SERIES -86 °C, Sanyo
CD spectrophotometer	Chirascan™ V100, Applied Photophysics
Centrifuge	Avanti J-26S XP, Beckman Coulter, (Rotor: JLA 8.1000)
Chromatography system	ÄKTA Start, GE Healthcare
EPR	Bruker Elexsys E580-10/12 X band spectrometer with a 4122HQE resonator. Measurements were done with a Bruker ER 167 FDS-Q liquid nitrogen finger dewar or an Oxford Instruments ESR900 helium flow cryostat, cryocooled by a Stinger (Cold Edge Technologies, Allentown, Pennsylvania, USA) linked to helium compressor (Sumitomo F-70).
French Press	Thermo Spectronic French Pressure Cell Press Model FA-078, SLM Aminco, with FA-032 cell
Gel imager	New-Line ECL ChemoSTar Image, Intas
Plate incubator (30ºC and 37ºC)	Heratherm IGS 100, Thermo Scientific Heratherm IMC 18, Thermo Scientific
Mössbauer and cryo system	Wissel GmbH and Oxford Intruments
Nanodrop	NanoDrop ONE^{C}, Thermo Scientific
Nanopure water	Arium H_2Opro-UF-T, Sartorius
Orbital incubator	Multitron Pro MP5050-SCSC, Infors
pH-meter	InLab Micro, Mettler Toledo
Pipette boy	Rudolf Grauer AG Swiss Boy 110
Pipetting robot (Crystallization)	OryxNano, Douglas instruments, UK
Potentiometer	Seven Excellence Multiparameter, Mettler Toledo
Sterile bench	MSC-Advantage, Thermo Scientific
Thermocycler	Hybaid, Limited PCR Sprint Thermal
Thermomixer	Thermomixer comfort, Eppendorf
Ultracentrifuge	LE 80K Ultracentifuge, Beckman Optima™, (Rotor: 45 Ti)
UV-Vis spectrophotometer	UV-1900 UV-VIS, Shimadzu Genesys 10uv Scanning, Thermo Scientific

1.2. Software

Table 2. Software used in this work.

Software	Producer
Chromas	Technelysium
Clustal Omega	EMBL-EBI
EasySpin	Stefan Stoll, Arthur Schweiger[153]
ExPASy	SIB Swiss Institute of Bioinformatics
GeeStrain5	W.R. Hagen [143]
MatLab	The MathWorks, Inc. (2023) 9.14.0.2489007 (R2023a) Update 6
Unicorn	GE Healthcare
Vinda	H. P. Gunnlaugsson[154]
VISIONlite	Thermo Fischer Scientific
Xepr	Bruker

1.3. Lab materials, kits and consumables

Table 3. Lab materials and consumables used in this work.

Lab material	Brand
Agarose gel apparatus	Biostep® HU10
Common laboratory glass	Duran
Cuvette (plastic)	Polystyrene cuvettes, Ref: 67.742, Sarstedt
Cuvette (quartz)	High Precision Cell, Art:104-10-40, Hellma Analytics
EPR tubes	Quartz, (3.0 mm inner diameter, 3.8 mm outer diameter, 180 mm length), Ilmasil PS, QSIL GmbH Ilmenau, Langewiesen, Germany
Heparin column	HiTrap Heparin HP, Cytiva
Miniprep kit	NucleoSpin® Plasmid (NoLid), Macherey-Nagel
PCR-Clean-Up-Kit	Nucleo Spin ® Gel and PCR clean up, Macherey-Nagel
PD10 desalting column	Cytiva
Petri dishes	Sarstedt Petri dishes, 92 x 16 mm
pH-electrode	Mettler Toledo, InLab®Easy-Electrode Mettler Toledo, InLab®Micro-Electrode
Pipettes	Eppendorf, Research Plus 10 µL, 20 µL,100 µL, 200 µL and 1000 µL.
Protein concentrator	Amicon 10.000 MWCO
Redox electrode	InLab Redox Micro, Mettler Toledo

Screw cap vials	ROTILABO ®, short screw-top vials ND9, D-76185, Roth
SDS-PAGE apparatus	Bio Rad, Mini Protean IITM
Sterile filter, 0.2 µm	Ultrapore

1.4. Chemicals

Table 4. Chemicals used in this work.

Chemicals	Brand	Reagent Number
Acetone	Honeywell	32201-1L
Acrylamide/bisacrylamide 30% (37.5:1)	Sigma Aldrich	A3699-100ML
Agar-agar	Roth	5210.2
Agarose	Biozym	840004
Ammonium acetate	AppliChem	131114.1210
Ammonium chloride ^{15}N enriched	Cambridge Isotope Laboratories Inc.	NLM-467-10
Ammonium persulfate	AppliChem	M3007.0100RG1
Ammonium sulfate	AppliChem	131140.1211
Ampicillin	AppliChem	A0839.0100
Anthraquinone 2-sulfonic acid sodium salt monohydrate	Sigma-Aldrich	123242-100G
L-Ascorbic acid	Sigma-Aldrich	A5960-25G
Benzylviologen dichloride	Sigma-Aldrich	251845-250MG
Bicine	Sigma-Aldrich	B3876-100G
Biotin	IBA Lifesciences	2-1016-005
Bradford Reagent	Bio-Rad	500006
Bromophenol blue	Serva	15375.01
Calcium chloride dihydrate	Sigma-Aldrich	C3306-500G
CAPS	Roth	9168.2
CHES	Sigma-Aldrich	C2885-25G
Coomassie Brilliant blue G250	Sigma-Aldrich	B-1131
L-Cysteine hydrochloride monohydrate	Roth	T203.1
DEPC	Roth	K028.1
Deuterium oxide	Deutero	00507-100ML
Dipotassium phosphate	AppliChem	131512.1211
DMPD	Fluka Analytical	07770-256
DNase I	AppliChem	A3778,0100
dNTP mix	New England Biolabs	N04475
DpnI	New England Biolabs	R0176S
DOC	Sigma-Aldrich	D6750

DTT	AppliChem	A2948,0010
Ethanol absolute	ChemSolute	2246.2500
Ferene	Sigma-Aldrich	P4272-5G
Ferric ammonium citrate	Sigma-Aldrich	F5879
Ferrous ammonium sulfate (Mohr's salt)	ThermoScientific	040751.14
Forming gas	Air Liquide	Arcal™ F5
Gel loading dye purple	New England Biolabs	B7024A
GelRed (Roti®- GelStain)	Roth	3865.1
D-Glucose monohydrate	Roth	6780.1
Glycerol	Roth	3783.2
Glycine	Roth	HN07.3
HEPES	Roth	9105.3
Hydrochloric acid 37% (v/v)	VWR Chemica	20252.335
Hydrogen peroxide 30% (v/v)	AppliChem	A1134,0250
2-Hydroxy-1,4-naphtoquinone	Sigma Aldrich	H46805-10G
Indigo carmine	Sigma-Aldrich	57000-25G-F
IPTG	Gerbu Biotechnik	1043
Iron (II) chloride ^{57}Fe enriched	Donated by Lukas Knauer/Prof. Schünemann	
Iron(III) chloride hexahydrate	Roth	P742.1
LB-medium mix	Roth	X968.2
Lithium disulfide	Sigma-Aldrich	213241
Lysozyme	Roth	8559.2
Magnesium chloride hexahydrate	Roth	HN03.2
Magnesium sulfate	AppliChem	131404.1211
β-mercaptoethanol	Merck	805740
MES	Roth	4256.2
Methyl Phenazine Methosulfate	Fluka BioChemika	68600-1G
Methylene blue	Merck	1283-25G
Methylviologen dichloride hydrate	Sigma-Aldrich	856177-1G
MOPS	Roth	6979.4
Neutral Red	Sigma-Aldrich	N4638-1G
PageRuler™ Prestained Protein Ladder	Thermo Scientific	26616
pH standard solutions	Mettler Toledo	-
Phenosafranin	Sigma-Aldrich	199648-1G
PIPES	Roth	9156.2
PMSF	AppliChem	A0999.0005
Potassium chloride	Roth	P017.1
Potassium chloride 3M AgCl saturated	Mettler Toledo	-
Potassium dihydrogen phosphate	Roth	P018.2
Potassium ferricyanide	Sigma-Aldrich	60299-100G-F

Potassium hydroxide	JT Baker	19002008
Q5 polymerase	New England Biolabs	M04915
Q5 reaction buffer	New England Biolabs	B90275
Quinhydrone	Sigma-Aldrich	282960-25G
Resorufin	Sigma-Aldrich	424455-1G
Safranin O	Sigma-Aldrich	84120-25G
SDS	Roth	8029.2
Sodium hydroxide	Sigma-Aldrich/ Roth	06203-1KG/ 9356.1
Sodium chloride	Roth	3957.2
Sodium deoxycholate	Sigma-Aldrich	D6750-25G
Sodium dihydrogen phosphate monohydrate	AppliChem	131965.1211
Sodium dithionite	Thermo Scientific	33381
Sodium hydrogen phosphate dihydrate	Honeywell	30435-1KG
Sodium pyrophosphate	Sigma-Aldrich	P8010-500G
TAPS	Roth	6982.2
TEMED	AppliChem	A1148.0100
Tetracycline	Roth	0237.1
Trichloro acetic acid	Roth	3744.1
Tris	AppliChem	A2264,1000
Zinc acetate	Sigma-Aldrich	96459-250G

1.5. Cells

Table 5. Cellular strains used in this work.

Cells	Genotype
***E.coli* BL21 (DE3)**	*fhuA2 [lon] ompT gal (λ DE3) [dcm] ΔhsdS λ DE3 = λ sBamHIo ΔEcoRI-B int::(lacI::PlacUV5::T7 gene1) i21 Δnin5*
***E.coli* NEB10β**	*Δ(ara-leu)7697 araD139 fhuA ΔlacX74 galK16 galE15 e14- φ80dlacZΔM15 recA1 endA1 nupG rpsL (StrR) rph spoT1 Δ(mrr-hsdRMSmcrBC)*
***E.coli* NEB5α**	*fhuA2Δ(argF-lacZ)U169 phoA glnV44 φ80Δ(lacZ)M15 gyrA96 relA1 endA1 thi-1 hsdR17*

1.6. Plasmids

Table 6. Plasmids used in this work.

Plasmids	Brand	Reference
pET-duet1	Novagen	Cat number: 71146-3
pRKISC	-	Nakamura *et al.*[102]

pPR-IBA101	IBA BioTAGnology	Cat number: 2-3690-000
pPR-IBA101 Esccol IscR	Twist	This work
pPR-IBA101 Esccol YjdI	-	This work
pPR-IBA102 Esccol YjdI	-	This work

1.7. Primers

Table 7. Primers used in this work. SDM- Site Directed Mutagenesis.

Primer	**Purpose**	**Sequence (5`→ 3`)**
pET-DUET1 up1	Sequencing	ATGCGTCCGGCGTAGA
pET-DUET down1	Sequencing	GATTATGCGGCCGTGTACAA
IBA101 up	Sequencing	TAATACGACTCACTATAGGG
IBA101 reverse	Sequencing	TAGTTATTGCTCAGCGGTGG
H107C forward	SDM	TGCCTGACCTGCGCGCTGTGGCGTGATTTGAGC
H107C reverse	SDM	CCACAGCGCGCAGGTCAGGCATTTATCGCCGCC
H107D forward	SDM	TGCCTGACCGACGCGCTGTGGCGTGATTTGAGC
H107D reverse	SDM	CCACAGCGCGTCGGTCAGGCATTTATCGCCGCC
H107E forward	SDM	TGCCTGACCGAGGCGCTGTGGCGTGATTTGAGC
H107E reverse	SDM	CCACAGCGCCTCGGTCAGGCATTTATCGCCGCC
L136* forward	SDM	CCAGGAAGTGTAGGATGTGTCTGGTCGTCAGCATAC
L136* reverse	SDM	ACACATCCTACACTTCCTGGTTATTAACCAGTTCG
H143* forward	SDM	GGTCGTCAGTAAACTCACGACGCGCCACGC
H143* reverse	SDM	GTCGTGAGTTTACTGACGACCAGACACATCC
D146* forward	SDM	CATACTCACTAGGCGCCACGCACCCGCACACAAG
D146* reverse	SDM	CGTGGCGCCTAGTGAGTATGCTGACGACCAGAC
R149* forward	SDM	CCACGCACCTGAACACAAGACGCGATCGACG
R149* reverse	SDM	GTCTTGTGTTCAGGTGCGTGGCGCGTCGTGAG
***iscrb* reverse**	Type 1 DNA primer for annealing	GACATTCCCGAGTAAAATGGTCAACTATTT
***iscrb* forward**	Type 1 DNA primer for annealing	AAATAGTTGACCATTTTACTCGGGAATGTC
***hya* reverse**	Type 2 DNA primer for annealing	CACAAAACAATACAAACTGTGTGGATTTAT

***hya* forward**	Type 2 DNA primer for annealing	ATAAATCCACACAGTTTGTATTGTTTTGTG
EcYjdI_IBA101_EcoRI	Cloning	ATGGTAGAATTCATGAATCAGGCGCTACTGGACGG
EcYjdI_IBA101_PstI	Cloning	TACCATCTGCAGTTTATGACGGTATTTCAGCGC
EcYjdI_IBA102_EcoRI	Cloning	ATGGTAGAATTCGATGAATCAGGCGCTACTGGACGG
EcYjdI_IBA102_PstI	Cloning	TACCATCTGCAGTTATTTATGACGGTATTTCAGCGC

2. Experimental procedures used in Chapter III

2.1. Plasmid cloning, sequencing and isolation

Plasmid cloning is possibly one of the most important techniques used in biochemistry and molecular biology. It lifted most of the necessity of purifying protein from native organisms and incredibly increased protein yield by allowing controlled overexpression in different and simpler hosts. In this practical work, recombinant plasmids produced by previous members of the working group through cloning with restriction enzymes were used. Further and more extensive information on cloning can be found in the review article from Fakruddin and coworkers[155].

A pETDuet-1 vector with the IscR encoding gene (*iscR*) was cloned by M. Sc. Dominique Bechtel in our working group. Cloning was done in multiple cloning site 1 (MCS1). NcoI and SalI were used as restriction enzymes. The His-tag at the N-terminal side of MCS1 was purposely not included because IscR is a DNA binding protein that can be efficiently purified by Heparin affinity purification. By choosing NcoI as restriction site for the cloning at the 5' side, the His-tag encoding DNA is removed.

A pET-29b(+) plasmid containing the gene encoding IscR (*iscR*) was also used in this practical work. However, cloning was not done in our working group as the plasmid (vector + *iscR* gene) was bought from Twist. This plasmid encoded IscR with a Twin-Strep tag at the C-terminus, cloned in the MCS. Both vector maps can be consulted in the supplementary information (S.1.).

To start this project, the pETDuet-1 plasmid encoding IscR was sequenced by EuroFins genomics. Plasmid sequencing was done using the primers pETDuet-1 up1 and pETDuet-1 down1 due to the gene placement in MCS1. Pipetting scheme was as shown in Table 8. Data analysis was performed by alignment between the sequencing results and the plasmid sequence as intended, using Chromas and Clustal Omega.

Table 8. Sample preparation for sequencing.

	Sequencing 1	**Sequencing 2**
Primer (10 µM)	2.5 µL pETDuet-1 down1	2.5 µL pETDuet-1 up1
Plasmid (109 ng/ µL)	3.67 µL	3.67 µL
MilliQ water	3.83 µL	3.83 µL

After confirming that the plasmid was correct, 2 µL of the plasmid (218 ng DNA) were added to 100 µL of *E.coli* NEB10 competent cells and incubated at 4 ºC for 30 minutes. The cells were then heat shocked for 30 seconds at 42ºC followed by 2 minutes at 4 ºC. Then, 1 mL of sterile lysogeny broth (LB) medium was added to the solution and the culture was incubated at 37 ºC for 1 hour. After incubation, 100 µL of the cell culture was plated onto an LB-agar plate containing 100 µg/mL ampicillin. The plate was incubated overnight at 37 ºC.

One overnight grown colony was inoculated in 10 mL LB medium and grown at 37 ºC, 150 rpm, overnight. The cells were then harvested by centrifugation and the DNA purified. DNA purification was performed according to the protocol available for low copy plasmids from a mini prep kit. The protocol can be found in the supplementary information (S.2.). After plasmid isolation, the DNA concentration was determined by Nanodrop.

2.1.1. NanoDrop

NanoDrop, a microvolume UV-Vis spectrophotometer, is an important tool in a molecular biology laboratory. It allows the measurement of reduced volumes, as low as 1 µL samples on a pedestal. As a UV-Vis spectrophotometer, it is based on the absorption of light at a specific wavelength, but in contrast to UV-Vis spectrophotometers, it takes advantage of smaller pathlengths, that can go from 1 to 0.05 mm, to mensurate sample absorbance from small volumes. This pathlength is achieved without the need of a cuvette to contain the sample. Upon sample loading on the pedestal, the arm is closed and, due to surface tension, a sample column is formed between both components. The pathlength is then optimized by the machine. This is particularly useful for molecular biology due to the low volumes with relatively high absorbance obtained after DNA purification, but also due to the higher throughput, faster scans and the easiness to clean when compared to UV-Vis[156].

This technique can be used to measure DNA/RNA or protein concentrations at the wavelengths of 260 and 280 nm, respectively. It also yields information on sample purity from the ratio of absorbance at various wavelengths and thereby detect contaminants[156].

In this work, NanoDrop was used to quantify the DNA after purification described in the previous topic. To quantify it, double strand nucleic acid mode was selected, 1 µL of the DNA solution was loaded onto the NanoDrop pedestal, the arm was closed, and the absorbance was measured. The machine automatically calculates the DNA concentration from the information available on the sample and its absorbance at each wavelength.

2.2. Site-directed mutagenesis

The production of protein mutants has been used for a long time. It allows the determination of the function of a specific or several combined amino acids and is an important tool to the current field of biochemistry and molecular biology. It is used to determine changes in catalytic activity, folding, stability, among others by introducing an intentional amino acid mutation into proteins[157].

Several mutants were prepared in this study. To produce IscR mutant proteins, the pETDuet-1 plasmid encoding IscR wild-type was used as a template for the mutagenesis. The site-directed mutagenesis process to obtain the mutants was done through linear amplification, in a process similar to the Polymerase Chain Reaction (PCR) technique. It required primers that would introduce the mutation to the new strand being amplified. The primers used in this study can be found in section 1.7. The process started with the mix of the components in PCR tubes, as described in Table 9

Table 9. Site directed mutagenesis sample preparation.

Reagent	Batch A	Batch B	Control
Sterile water	35 µL	35 µL	37.5 µL
5 x Q5 Buffer	10 µL	10 µL	10 µL
Plasmid of interest (30 ng)	1 µL	1 µL	1 µL
Primer 1 (10 µM)	2.5 µL	0	0
Primer 2 (10 µM)	0	2.5 µL	0
dNTP-Mix (2.5 mM each nucleotide)	1 µL	1 µL	1 µL
Q5 polymerase (ca. 2 U/ µL)	0.5 µL	0.5 µL	0.5 µL
Total volume	50 µL	50 µL	50 µL

The mixtures were then placed in a thermocycler followed by the steps shown in Table 10.

Table 10. Thermocycler cycle used for amplification of mutated DNA.

Segment	Cycles	Temperature (ºC)	Time
1	1	98	30 s
2	8	98	15 s
		55	30 s
		72	4 min
3	1	4	hold

Subsequently, batches A and B were mixed (25 µL each) and 0.5 µL fresh Q5 polymerase was added to the mix. The same amount of Q5 polymerase was also added to the control tube (50 µL) lacking the plasmid. The tubes were then again placed in the thermocycler and underwent the steps outlined in Table 11.

Table 11. Thermocycler cycle used for annealing of the mutated DNA.

Segment	Cycles	Temperature (ºC)	Time
1	1	98	30 s
2	18	98	15 s
		55	30 s
		72	4 min
3	1	72	10 min
4	1	4	hold

Afterwards, 1 µL of DpnI was added to the samples which were incubated for 1 h, at 37 ºC. DpnI is an endonuclease that cleaves methylated and hemimethylated DNA. DpnI digestion only targets the original plasmid that served as template and that does not carry the intended mutation since the

original strands are the only methylated DNA present in solution. The digestion with DpnI has been widely used for site directed mutagenesis as it is a simple way to eliminate non-mutated DNA[158].

Finally, a PCR-Clean-Up-Kit was used following the manufacturer's instructions for DNA purification, also described in detail in the supplementary information (S.3.). The resulting DNA was used to transform *E. coli* NEB5α competent cells and to isolate and sequence the mutated DNA as described in section 2.1.

2.3. Transformation and pre-culture

The DNA obtained in the previous sections, either in the pET-Duet1 or pET29b(+), containing the gene encoding IscR, was then transformed into *E.coli* BL21 pRKISC cells for protein overproduction. *E.coli* BL21 pRKISC cells are *E. coli* BL21 competent cells which had been first transformed with the pRKISC plasmid from Nakamura *et al*.[102] and were suitable for overproduction of FeS cluster containing proteins. The pRKISC plasmid consists of a pRK-415 plasmid in which more restriction sites were added, as well as the *iscS-iscU-iscA-hscB-hscA-fdx-ORF3* genomic DNA fragment from *E. coli*. This fragment encodes the *isc* operon which is the machinery for FeS cluster production, but lacks *iscR*, the regulator[102].

Initially, 100 µL of competent cells were thawed in ice, and gently mixed with 100 ng of DNA. The mixture was then incubated for 30 min at 4ºC, heat shocked in a water bath at 42 ºC for 30 seconds and then placed at 4ºC for 2 more minutes. 1 mL of sterile LB media was then added to the solution and the mixture was incubated for 1 h at 37 ºC and 150 rpm. To ensure double selection, cells were plated onto LB-agar plates containing either 100 µg/mL ampicillin (pET-Duet1 plasmid resistance) or 30 µg/µL kanamycin (pET29b(+) plasmid resistance). Additionally, all plates contained 10 µg/mL tetracycline (pRKISC plasmid resistance). Plates were incubated overnight at 37 ºC and then stored at 4 ºC for no longer than a week. Ultimately, pET-Duet1 plasmid was chosen for protein production in this project, so further references to IscR wild type or mutant growth conditions will mention 100 µg/mL ampicillin and no kanamycin in the medium.

For pre-culture preparation, three colonies from the overnight grown plates were be picked and inoculated into 40 mL of sterile LB-medium containing 100 µg/mL ampicillin and 10 µg/mL tetracycline and incubated overnight at 37 ºC, 150 rpm.

2.4. Cell growth

A 40 mL pre-culture, prepared as described previously, was used to inoculate 2 L of LB medium containing 100 µg/mL ampicillin and 10 µg/mL tetracycline in a 5 L Erlenmeyer flask and grown at 37 ºC, 150 rpm. The optical density ($OD_{600\ nm}$) was measured hourly, and the growth curve was plotted. At OD 0.4 the temperature was lowered to 30 ºC. At OD 0.5, cells were induced with 0.5 mM IPTG and supplemented with 100 µM ferric ammonium citrate (FAC) and 100 µM L-cysteine, final

concentration. The cells were grown overnight at 30 ºC, 150 rpm. To create a microoxic environment, parafilm was wrapped around the flask opening, restricting influx of air.

2.5. Growth with isotope enrichment

Isotope enriched samples were necessary for some experiments performed in this study. Samples enriched with ^{57}Fe are necessary for Mössbauer spectroscopy and ^{15}N samples were prepared for pulsed EPR.

Isotope enriched cell cultures were grown in minimal media (M9) which is composed of minimal required nutrients for bacterial growth: a source of carbon, nitrogen, sulfur, phosphorous, metals and salts. For ^{57}Fe enrichment, the source of Fe ions was changed from FAC (with Fe in its natural abundance) to $^{57}FeCl_2$. For 15N enrichment, the source of nitrogen was changed from NH_4Cl with natural abundance of nitrogen to $^{15}NH_4Cl$. Media composition can be found in **Error! Not a valid bookmark self-reference.**.

Table 12. Minimal media (M9) composition.

Reagent	Volume
$CaCl_2$ (1 M)	200 µL
$MgSO_4$ (1 M)	2 mL
Glucose (20 %)	40 mL
Pre-culture	40 mL
M9 Salts 5x	400 mL
Ampicillin (100 mg/mL)	2 mL
Tetracycline (10 mg/mL)	2 mL
ddH_2O	Up to 2 L

M9 salts 5x were composed of 37.6 g $Na_2HPO_4.2H_2O$, 30.7 g $KH_2PO_4.7H_2O$, 2.5 g NaCl, 5.0 g NH_4Cl dissolved with ddH_2O in a total volume of 1000 ml. Besides growing in minimal media instead of a rich medium and the substitution of the sources of Fe or N, no other changes were applied between growth protocols.

2.6. Cell harvesting and lysis

Cells were harvested by centrifugation at 4000 rpm, for 20 min, at 4 ºC. The centrifuge Avanti J-26S XP and rotor JLA 8.1000 were used for this purpose. Cell pellet was then resuspended in 25 mL 20 mM HEPES, 30 mM KCl, 5% (v/v) glycerol, pH 8.0 and centrifuged once again, under the same conditions, to remove any residual media. The cells were weighed, shock frozen in liquid nitrogen and stored at -80 ºC until cell opening and protein purification.

The cells containing the overexpressed protein of interest were thawed in ice for approximately 30 min and resuspended in 23 mL buffer 20 mM HEPES, 30 mM KCl, 5% (v/v) glycerol, pH 8.0. After full resuspension, 30 mg of DNase and 15 mg of phenylmethylsulphonyl fluoride (PMSF) dissolved in 1 mL 20 mM HEPES, 30 mM KCl, 5% (v/v) glycerol, pH 8.0 and in 1 mL ethanol absolute, respectively, were added and the solution was incubated at 4 ºC for 20 min.

The cells were then placed in a 30 mL French Press pressure cell. The pressure cell was placed in the hydraulic press and the cells were then opened in one cycle at 1000 psi pressure according to the manufacturer's instruction. The lysate was then centrifuged at 45000 rpm, for 1.5 hours, at 4 ºC, in an Optima™ LE-80K Ultracentrifuge with a Ti 45 rotor. After cell disruption, the lysate was anaerobically filtered with an Ultrapore sterile 0.2 µm filter in an anaerobic chamber where the purification process was then carried out.

2.7. Protein purification

The filtered lysate was loaded onto a 5 mL Heparin column, previously equilibrated with 100 mM HEPES, 150 mM KCl, 10% (v/v) glycerol, pH 8.0 (buffer 1), using an ÄKTA start. The column was then washed with 10 column volumes (CV) of buffer 1. The protein of interest was subsequently eluted with buffer 2, corresponding to buffer 1 but containing 660 mM KCl instead of 150 mM. Sample loading and elution were done at a flow rate of 1 mL/min and the washing step at 2 mL/ min.

Protein elution yielded between 5-8 mL of highly concentrated protein with ~0.7 M KCl in solution. After elution the protein was subjected to buffer exchange from buffer 2 to buffer 1 through a PD10 desalting column. After buffer exchange, the resulting protein was split into approximately 200 µL samples and shock frozen in screw cap vials using liquid nitrogen. Samples were stored at -80 ºC until further use.

2.8. Protein, iron and sulfur quantification

The determination of protein, iron and acid-labile sulfur content in biological samples is of paramount importance. Besides helping cofactor identification, it allows the determination of metal and clusters incorporation. There are several methods for protein, iron and acid-labile sulfur determination. Here, three colorimetric methods were used.

2.8.1. Micro Biuret method for protein determination

The determination of the protein concentration was performed using the Micro Biuret colorimetric method. The Micro Biuret method is a rapid and sensitive technique for the quantification of protein concentrations in biological samples. This method is based on the biuret reaction, which involves the complexation of copper ions with the peptide bonds of proteins, leading to a color change that can be detected spectrophotometrically[159–161].

In the micro biuret method, after trichloroacetic acid/sodium deoxycholate (TCA/DOC) precipitation, the protein pellet is dissolved in 1 % (w/v) sodium hydroxide solution, followed by addition of copper sulfate/sodium potassium tartrate solution, which induces the biuret reaction. The absorbance of the purple complex formed is then measured at 545 nm using a UV-Vis spectrophotometer[159–161].

Compared to other protein quantification methods, such as the Lowry and Bradford assays, the micro biuret method, when combined with TCA/DOC precipitation, is more tolerant to common interfering substances, such as detergents and reducing agents, which in other protein assays can lead to spurious results[159–161].

Even though the micro biuret method has its own limitations, including its relatively low sensitivity, this method is a useful and convenient technique that can be applied to a wide range of biological samples and especially known for performing well for Fe-S and other cofactor containing proteins. Additionally, the response is not so dependent on the amino acid composition and thus gives a reliable absolute protein concentration.

The method involves the utilization of a standard protein with a known concentration to build a calibration curve. Bovine Serum Albumin (BSA) 2 mg/mL (standardized by measurement of the absorbance at 279 nm) was used in this work. The full protocol can be found in the supplementary information (S.4.).

2.8.2. Iron determination

The determination of the concentration of Fe^{2+}/Fe^{3+} in the protein was also performed by colorimetry. This method is based on the complexation of 3-(2-pyridyl)-5,6-bis(5-sulfo-2-furyl)-1,2,4-triazine, disodium salt trihydrate (Ferene) with Fe^{2+} in solution. Quantification is based on a calibration curve of a solution with known concentration of iron[162].

Initially, hydrochloric acid is added to the protein sample to release the iron ions, and the solution is neutralized by the addition of ammonium acetate. The Fe^{3+} ions present in solution are reduced to Fe^{2+} by the addition of ascorbic acid while protein precipitates are complexed with sodium dodecyl sulphate (SDS). Ferene is then added to the solution and chelation with Fe^{2+} occurs, yielding a blue complex. The complex absorbance at 593 nm is directly proportional to the concentration of Fe^{2+} in solution[162]. The full protocol can be found in the supplementary information (S.4.).

2.8.3. Acid-labile sulfur determination

This method is based on the denaturation of the protein in an alkaline solution containing zinc hydroxide leading to the release of labile sulfide that is precipitated as ZnS. Upon medium acidification, precipitated ZnS is dissolved and forms H_2S. H_2S reacts with *N*,*N*'-dimethyl-*p*-phenylenediamine (DMPD), under oxidizing conditions ($FeCl_3$) forming methylene blue that can be spectrophotometrically measured at 670 nm. Lithium sulfide is used as standard. This technique takes

advantage of the reaction first described by Fogo and Popowski in 1949[163] and was later adapted to biochemical purposes[162]. The method only detects acid labile sulfide, sulfur from cysteine and methionine residues does not produce color. The full protocol can be found in the supplementary information (S.4.).

2.9. SDS-PAGE

In this work, sodium dodecyl sulphate-polyacrylamide gel electrophoresis (SDS-PAGE) was used to assess the protein's purity and efficacy of production. This technique is used to, within a certain degree of resolution, determine the purity of the protein sample. It is based on the premise that proteins are charged, and they will migrate in an electric field according to it.

By loading these proteins in a matrix with pores that have a diameter in the same order of magnitude of the protein size, it is possible to separate and resolve proteins in a complex protein mixture mainly based on their masses. The size of the pores will facilitate the passage of smaller proteins and delay the passage of the larger proteins. This matrix is made of a mixture of acrylamide and bis-acrylamide[164].

Combining the matrix and the electric field it is possible to estimate the migration pattern of a given protein based on its size, shape and charge. Since the protein shape and charge play a very important role for the migration, SDS is used to denature the protein and disrupt non-covalent interactions. The addition of SDS linearizes the protein and confers an evenly distributed negative charge throughout the protein, which is proportional to the length of the polypeptide. The addition of a reducing agent, e.g. β-mercaptoethanol or dithiothreitol (DTT), is necessary to break disulfide bridges[164].

All the SDS-PAGE gels run in this study were in the presence of β-mercaptoethanol for a complete reduction of the disulfide bridges. All samples were heated at 95 ºC for at least 5 minutes prior to loading the gel. PageRuler™ Prestained Protein Ladder (Thermo Scientific) 10–180 kDa was used as molecular mass marker. The recipes for preparation of the gel and the buffers necessary for electrophoresis can be found in the supplementary information (S.5.).

2.10. Electrophoretic Mobility Shift Assay (EMSA)

Electrophoretic mobility shift assay (EMSA) is a rapid and sensitive method to study protein-nucleic acid interactions. This method is based on the principle that, upon binding, the size, shape and charge of the complex changes in comparison to the protein or the DNA or RNA individually. It requires, as for SDS-PAGE, a matrix with pores that sort proteins, nucleic acids and their complexes based on their sizes and shape and an electric field that will lead to migration according to its charge. The charge is strongly determined by the negatively charged nucleic acids. Since the objective of this technique is the study of physiological interactions, it is required that the protein is natively folded and

not denatured by SDS. Unlike SDS-PAGE, this technique uses the so-called native PAGE that does not have SDS[165].

In this study, EMSAs were used to obtain insights on the binding of the IscR to type 1 and type 2 promotor regions (double stranded DNA) and its stoichiometry. All gels run in this study were free of SDS and β-mercaptoethanol. All samples were prepared aerobically, with protein as isolated and at room temperature. Other proteins, such as the *E. coli S*-adenosylmethionine synthase (MetK), the inorganic pyrophosphatase (IPP) from yeast (both MetK and IPP were donated by Tarik Begic 2022, Synthese und Isolation von ß-Lysin mit der Lysin 2,3-aminomutase, Master thesis, TU Kaiserslautern, 2022)[166] and a putative flavoprotein cytochrome B5 reductase (Pga3, donated by Kristin Hansen 2023 Expression, Reinigung und Charakterisierung von fünf potenziellen Fe- oder Fe/S-Proteinen der Bäckerhefe, Bachelor thesis, RPTU Kaiserslautern-Landau)[167] from yeast with a known molecular mass were used as possible standards.

2.11. Ultraviolet-Visible spectroscopy

In this work, UV-Vis spectroscopy was used to identify the cluster type, to determine the pK_a in the oxidized and reduced states of the IscR protein and to obtain insights into the stability of the cluster. In all experiments the baseline was set beforehand as air/empty cuvette holder. Spectra of a cuvette filled with buffer were used for subtraction and protein concentrations are given for IscR dimer.

2.11.1. UV-Vis spectra of IscR

To record the UV-Vis spectra of wild-type IscR and mutants, a 1 cm path length quartz cuvette was used. The spectra were recorded between 250 and 750 nm, with a scan rate of 3 nm/s and a resolution of 1 nm/point.

The cuvette was filled with 950 µL of buffer 1. A UV-Vis spectrum was recorded. Then, 50 µL of protein was added to the cuvette, properly homogenized by inversion and another spectrum was recorded. Most of the samples were prepared as described above, however, to obtain the best signal to noise ratio, the absorbance at 280 and 420-460 nm was always set to be as high as possible without compromising the linearity range of the technique. To avoid spectrophotometric artefacts, appropriate dilutions were employed to have a maximal absorbance at 280 nm of 1 and are specified in each UV-Vis spectrum.

2.11.2. IscR pH titration in the oxidized and reduced states

pH titrations were carried out to determine the pK_a. Contrary to the praxis for stable chemical compounds, the high sensitivity of a protein to local denaturation by strong acids and bases required to perform such titrations in a different way. Individual protein solutions at discrete pH values were prepared. This preparation consisted of gently adding the protein as purified (pH 8), to an excess of buffer from the buffer set with a different pH value. This avoided dilution of the protein during a

continuous titration. Usually, the pH shift obtained upon mixing was close to the intended pH, with a small deviation towards pH 8. The real pH value was always measured with a micro pH electrode to ensure maximum precision.

Sample preparation was done by adding 50 µL of IscR in Buffer 1 (pH 8) as purified, to 950 µL of 100 mM Good's buffer, containing 100 mM KCl and 10% (v/v) glycerol from pH 5.5 to pH 10.5 in 0.5 pH units steps, yielding 11 samples.

Buffer preparation was done by making a stock solution of 200 mM Good's buffer mix as presented in Table 13. Then, 25 mL of stock solution, 1.66 mL of 3 M KCl and 5 mL of glycerol (v/v) were added to 11 falcon tubes. The pH values were adjusted, and H_2O was added up to 50 mL.

Table 13. Good's buffer mix for 500 mL of a 200 mM stock solution.

Component	Buffering range	Mass (g)
MES	5.5-6.7	9.76
HEPES	6.8- 8.2	11.92
TAPS	7.7-9.1	12.16
CHES	8.6-10.0	10.36
CAPS	9.7- 11.1	11.1
H_2O	-	up to 500 mL

Additionally, two samples were prepared to determine signal reversibility upon pH shift. These samples consisted of a 5-fold dilution of IscR as isolated (750 µM IscR dimer, 200 µL) in 50 mM Good's buffer, containing 100 mM KCl and 10% (v/v) glycerol, at pH 5.5 and 10.5 (800 µL). Their UV-Vis spectra were recorded, followed by measurement of the real pH value (6.1 and 10.2 for samples diluted into pH 5.5 and 10.5 buffers, respectively). To assess reversibility, it was necessary to shift the pH value back to pH 8. For that, after a 20-minute incubation, 200 µL of the sample at pH 6.1 was diluted 5-fold with pH 8.5 buffer, while 200 µL of the sample at pH 10.2 was diluted 5-fold with pH 7.5 buffer. The final pH values measured were 7.9 and 8.1 and another UV-Vis spectrum was recorded for each sample.

2.12. Redox titrations

The midpoint potential of an FeS cluster gives valuable insights into the cluster's function and redox partners in the cell. Redox potentials can be determined through dye-mediated redox titrations where redox dye mediators, which are mostly organic dyes with known properties, are used to stabilize the redox potential in solution upon adjustment of the potential by addition of a reductant or oxidant. They act by reversibly oxidizing and/or reducing the cofactor of the protein until a redox equilibrium is reached and a sample can be taken[168].

In this study, redox titrations were used to determine the redox potential of the [2Fe-2S] cluster in IscR. A protein sample is then titrated with a reducing or oxidizing agent through a wide range of redox potentials. At regular intervals a sample is taken from the solution, loaded into an EPR tube, followed by freezing in liquid nitrogen and EPR measurement. For this cluster, the expected redox active species are the $[2Fe\text{-}2S]^{1+/2+}$ states. The reduced (1+) species is paramagnetic (*S*=1/2) and therefore EPR active, while the oxidized (2+) species is diamagnetic (*S*=0), thus EPR inactive. The transition between species can be monitored by EPR spectroscopy and the fraction of reduced/oxidized clusters can be calculated according to the amplitude of the signal corresponding to the reduced species. A plot of EPR amplitude versus the redox potential at which the sample was collected is a sigmoid curve with a slope that depends on the number of electrons being transferred. The fraction of reduced species in solution is described by the Nernst equation:

$$E = E^0 - \frac{RT}{nF}\ln Q \qquad \text{Equation 3}$$

in which, E is the reduction potential, E^0 is the standard redox potential, R is the universal gas constant, T is the temperature in Kelvin, n is the number of electrons involved in the process, F is the Faraday constant, and lnQ is the natural logarithm of the reaction quotient. At the midpoint potential, the quotient Q is 1 (fraction of reduced and oxidized species are 0.5 each) and the reduction potential (E) is equal to the standard redox potential (E^0). It is necessary to have a cocktail of redox mediators with redox potentials throughout the range of interest. The mediators used here are shown, along with their redox potentials at pH 7[169,170], in Table 14.

Table 14. Redox mediators used in this work.

Mediator (5 mM)	Volume used for mix	Midpoint potential (mV)
N,*N*,*N*',*N*'-tetramethyl-*p*-phenylenediamine (TMPD)	200 µL	+276
2,6-Dichlorophenolindophenol (DCPIP)	200 µL	+217
Phenazine methosulfate (PMS)	200 µL	+80
Methylene Blue (MB)	200 µL	+11
Resorufin*	400 µL	-51
Indigo Carmine (IC)	200 µL	-125
2-Hydroxy-1,4-napthaquinone	200 µL	-145
Sodium anthraquinone 2-sulfonate	200 µL	-225
Phenosafranin	200 µL	-252
Safranin O	200 µL	-280
Neutral red	200 µL	-340
Benzyl viologen	200 µL	-350
Methyl viologen	200 µL	-440

*2.5 mM

In this study, the titrations were started with the anaerobic preparation of the solution composed of 100-200 µM IscR dimer, 40 µM mediator mix and completed with buffer at a specific pH value. A total volume of solution between 2400 and 3000 µL would be used depending on the number of points desired in the titration (300 µL of solution required per point). The solution was gently and constantly stirred with a mini magnetic stirrer in a short assay tube, and the redox potential was uninterruptedly measured. With the sequential addition of small volumes (1-3 µL) of 1.5-100 mM sodium dithionite (NaDT) prepared in 100 mM Tris, pH 9, the redox potential decreases in small and controlled steps. The redox potential of the solution was measured with an InLab Argenthal microelectrode (Ag/AgCl, E=+207 mV versus H_2/H^+, with combined Pt counter electrode). It was calibrated with a quinhydrone saturated pH 7 reference buffer solution (E=+285 mV versus H_2/H^+ at 25°C). At a given potential a 300 µL sample would be collected from the solution, loaded into an EPR quartz tube, shock frozen in liquid nitrogen and stored at 77 K until measurement. Redox titrations were carried out at several pH values.

Due to the known pH shift with temperature, temperature independent buffers were prepared. A list of temperature-independent buffers (TIB), adapted from Le Breton and coworkers[171], is available in Table 15. However, the only temperature-independent buffers found in literature had pH values between 6 and 9. Above pH 9 and below pH 11.5 the Good's buffer mix described in section 2.11.2 were used.

Table 15. Temperature independent buffers (TIB).

Buffer (all with 150 mM NaCl and 30% (v/v) glycerol)	pH
4 mM Na_2HPO_4, 96 mM HEPES	6.0
25 mM Na_2HPO_4, 75 mM HEPES	6.5
55 mM Na_2HPO_4, 45 mM HEPES	7.0
70 mM Na_2HPO_4, 30 mM HEPES	7.5
90 mM Na_2HPO_4, 10 mM HEPES	8.0
23 mM $Na_4P_2O_7$, 27 mM Bicine	8.5
36 mM $Na_4P_2O_7$, 14 mM Bicine	9.0

Few biological-compatible buffers are available above pH 11.5. Thus, above pH 11.5 100 mM potassium phosphate buffer (pK_{a3}=12.3) containing 150 mM KCl and 10% (v/v) glycerol at pH 12, 12.5 and 13 were used.

2.13. Circular Dichroism spectroscopy

In this work, CD spectroscopy was used to determine the secondary structure of the protein, to determine the pK_a values, both in the oxidized and in the reduced state and to study the cluster stability as a function of time and temperature. All protein concentrations refer to the IscR dimer.

2.13.1. Secondary structure determination

To study the secondary structure of a protein, it is necessary to analyze the shape of the CD spectra in the far UV wavelength region (180-250 nm). Depending on the secondary structure of the protein different transitions are observed for the peptide bonds resulting in distinct CD spectra[133].

Preparing samples for far UV CD spectroscopy imposes certain restrictions, such as using low concentrations of suitable UV-transparent buffers and avoiding specific components such as chloride ions. The buffer used in this experiment was 10 mM phosphate pH 7.8 containing 200 mM KCl and 10% (v/v) glycerol. The CD conditions used in this experiment were a compromise due to the instability of IscR at low buffer and salt concentration. A higher concentration of KCl and lower concentration of buffer was chosen due to a lower interference from chloride salts in comparison to the buffer. The spectra were recorded at room temperature between 195 and 250 nm, with a scan rate of 2 nm/s and a resolution of 1 nm/point.

Initially, a baseline was set with the empty cuvette holder purged with nitrogen gas. Then 200 µL of buffer were added to a 1 mm pathlength quartz cuvette and a spectrum was recorded. 5 µL of ~500 µM protein (13 µM final) was then added, homogenized, and another spectrum was recorded. The data were corrected in Microsoft Excel by subtracting the buffer contribution from the sample with protein.

2.13.2. pK_a value determination in the reduced and oxidized states

To determine the pK_a value of IscR in the oxidized and reduced states, the visible range was used. The change in pH was achieved by mixing the protein at pH 8 with an excess of a buffer at a specific pH value. The real pH value could be accurately determined for each sample by measurement with a pH micro electrode after collection of the CD spectral data. The recordings were done at room temperature between 340 and 700 nm, with a scan rate of 2 nm/s and a resolution of 1 nm/point. The choice of the wavelength range was based on the high extinction coefficient of sodium dithionite below 340 nm. Each sample was subjected to six scans, each lasting approximately 3 minutes. This number of scans was chosen to determine whether changes observed in the spectral data were due to time dependent protein degradation/cluster breakdown or if they were indeed related to protonation and deprotonation phenomena.

To start, the baseline was set with an empty cuvette holder of the CD spectrometer purged with nitrogen. For oxidized IscR, 800 µL of buffer were loaded into a 5 mm pathlength quartz cuvette and a buffer spectrum was recorded. Then, 200 µL of ~500 µM IscR dimer (100 µM final concentration) were added to the cuvette and the spectra were recorded. For reduced IscR, 600 µL of buffer were loaded into a 5 mm pathlength quartz cuvette and a buffer spectrum was recorded. Then, 500 µL of ~750 µM IscR dimer (~340 µM final concentration) and 33 µL of 100 mM sodium dithionite (~3 mM final concentration) were added to the cuvette and the spectra were recorded. Samples in the oxidized

state were prepared aerobically and samples in the reduced state were prepared anaerobically. For anaerobic samples, the cuvettes were filled in the glove box, homogenized and sealed with parafilm, while avoiding mixing the head space outside the tent.

The high protein concentration led to good signal to noise ratios. Thus, buffer subtraction, which would have deteriorated the signal to noise, was not necessary for analysis of the data. Data treatment was done in Microsoft Excel by plotting the ellipticity versus wavelength for all pH values analyzed in these experiments.

2.13.3. Cluster stability as a function of time and temperature

For several experiments, including redox titrations and pH dependence of UV-Vis and CD spectroscopic features, cluster stability is of paramount importance. Understanding cluster stability at different temperatures allows for correlation between the data collected *in vitro* (20 °C) with cluster and protein function *in vivo* (37 °C for *E. coli*).

To evaluate cluster stability the same wavelength range used for the pK_a determinations were used (340-700 nm). Spectral data were acquired with a scan rate of 2 nm/s and a resolution of 1 nm/point and the baseline was set for the instrument purged with nitrogen. First, 800 µL of 100 mM HEPES pH 8.0, containing 150 mM KCl and 10 % (v/v) glycerol were loaded into a 5 mm quartz cuvette and a CD spectrum of the buffer was recorded. Then, 200 µL of protein were added to the cuvette and the spectrum was recorded. The samples were prepared anaerobically in the reduced and oxidized state and temperature stability was measured at 20 and 37 ºC. To follow spectral changes with time at two different temperatures, 40 spectra were recorded for each sample.

2.14. Mössbauer spectroscopy

Mössbauer samples were prepared by growing *E. coli* cells in a ^{57}Fe-enriched medium and performing protein purification as described in sections 2.5-2.7. Then, the ~8 mL of protein purified with an estimated concentration ranging between 400 and 600 µM of dimer, around 14-21 mg/mL, would be concentrated to approximately 500 µL - 1 mL to a final concentration between 120 and 330 mg/mL. These would then be distributed to Mössbauer sample holders and mixed with buffers at different pH values (see Table 16). The resulting pH was measured with a pH micro electrode. The samples were aerobically frozen with a metal block previously cooled with liquid nitrogen. Samples were stored at 77 K until measurement. To avoid loss of valuable samples protein, iron and acid-labile sulfide determinations were not carried out. The concentrations were estimated based on the average protein yield obtained upon purification from cells grown with natural abundance iron.

The buffers referred to as Good's buffers are the same as described in section 2.11.2 at different pH values. Additionally, some samples were prepared by a direct addition of different volumes of 1M HCl or 1 M NaOH, followed by a rapid homogenization and pH measurement in a time sensitive process (Table 16).

Table 16. Mössbauer sample preparation at several pH values with two different protein preparations.

Oxidized ^{57}Fe wild type IscR 1		
Protein (µL)	**Buffer**	**pH measured**
160	40 µL Good's buffer pH 6	7.9
	40 µL Good's buffer pH 8	7.0
	40 µL Good's buffer pH 10	8.9
100	50 µL Good's buffer pH 11 + 25 µL Good's buffer pH 9	10.0

Oxidized ^{57}Fe wild type IscR 2		
Protein (µL)	**Buffer**	**pH measured**
100	25 µL 1 M HCl	5.7
	15 µL 1 M HCl	6.4
	15 µL 1 M NaOH	11.1
	20 µL 1 M NaOH	11.5
	30 µL 1 M NaOH	12.1
	40 µL 1M NaOH	12.5

Mössbauer spectra were recorded in transmission geometry with a conventional spectrometer from Wissel GmbH with a liquid N_2 bath cryostat (Oxford Instruments). The isomer shifts are given relative to α-Fe at room temperature. A closed-cycle cryostat equipped with a superconducting magnet (CRYO Industries of America Inc.) was used to perform high-field, low-temperature measurements. The field was applied parallel to the γ rays. The spectra were analyzed with the program Vinda. The spectra were simulated by least-square fits using Lorentzian line shapes. For the high-field measurements, the magnetically split spectra were simulated with the spin Hamiltonian formalism[154,172].

2.15. Electron Paramagnetic Resonance (EPR) spectroscopy

As discussed in Chapter I, EPR spectroscopy is a widely used technique in the study of metalloproteins. In this experimental work, continuous wave (cw) and pulsed EPR were used to unravel properties of the [2Fe-2S] cluster present in IscR.

2.15.1. CW EPR spectroscopy

cw EPR spectroscopy was vastly used here to obtain insights on cluster coordination, determine its redox potential, assess changes upon DNA binding, understand the effects of DEPC modification and to determine the pK_a of the coordinating histidine in the reduced state.

For cw EPR, sample preparation varied according to the purpose of the experiment. However, all measurements were performed with a 4122HQE resonator attached to a Bruker Elexsys E580-10/12

X band spectrometer, with a Bruker ER 167 FDS-Q liquid nitrogen finger dewar or with an Oxford Instruments ESR900 helium flow cryostat, which was cryocooled by a Stinger (Cold Edge Technologies, Allentown, Pennsylvania, USA) linked to helium compressor (Sumitomo F-70). Quartz for the EPR tubes were from Ilmasil-PN, Quarzschmelze Ilmenau GmbH, Langewiesen). The tubes have a wall thickness of 0.45 ± 0.05 mm, an outer diameter of 4.7 ± 0.2 mm and a length of approx. 13 cm. For anaerobic samples the tubes were connected with Latex tubing (inner diameter 3 mm, outer diameter 7 mm, length approx. 3 cm), and capped with round acrylic sticks (diameter 5 mm).

Cluster and ligand identification

Sample preparation for cluster identification was done by mixing 100 µL of protein after purification with 194 µL of buffer 100 mM HEPES pH 8.0, containing 150 mM KCl and 10% (v/v) glycerol in an Eppendorf tube, anaerobically. Then, 6 µL of 100 mM buffered sodium dithionite were added to the protein solution, homogenized and incubated at room temperature for three minutes. The sample was then transferred to a quartz EPR tube and shock frozen anaerobically. Samples were kept at 77 K until measurement. Sample measurements were carried out between 320 and 380 mT, at 77 K, at 2 mW microwave power, 1 mT modulation amplitude and 100 kHz modulation frequency.

Determination of the redox potential

After sample preparation as described in section 2.2.13, EPR spectra were recorded between 320 and 380 mT, at 77 K, at 2 mW microwave power, 1 mT modulation amplitude and 100 kHz modulation frequency. Due to the lower protein concentration when compared to the previous experiment, an average of six scans were recorded for each sample to improve signal to noise ratio.

DNA binding and redox titration in the presence of DNA

To analyze the cluster properties when the protein was bound to DNA it was necessary to produce EPR samples at a relatively low protein concentration. This adjustment was required because double stranded DNA was only available in sub micromole quantities, due to the very high cost of commercially available oligonucleotides. The samples were therefore produced by dilution of wild type IscR to a final concentration of 10 µM in TIB at pH 8 in a short assay tube. Then, 3 µL of a 6 mM solution (10 µM final concentration) of a 32 bp fragment of DNA corresponding to the *iscrb* promotor region, made by annealing (explained in detail section 2.16.4) of two complementary synthetic *iscrb* oligonucleotides, was added to the protein solution, along with 173 µL of a 416 µM mediator mix containing dyes with an E_m from +55 to -449 mV from Table 14. The mixture was incubated for 10 minutes at room temperature for redox potential stabilization under mild stirring with a mini magnetic stirrer. The total volume of the solution was 1.8 mL, and it was then titrated with 1-3 µL of 1.5-100 mM sodium dithionite in small and controlled steps. This titration yielded five samples at redox potentials of -194, -155, -98, -46 and +2 mV, versus S.H.E, which were transferred to quartz EPR tubes and anaerobically shock frozen in liquid nitrogen.

Spectral data were acquired between 320 and 380 mT, at 20 K, at 2 mW microwave power, 1 mT modulation amplitude and 100 kHz modulation frequency.

Histidine pK_a determination in the reduced state

[2Fe-2S] clusters are EPR- inactive in the oxidized state since they are diamagnetic. Thus, by EPR spectroscopy only the pK_a of the reduced EPR active state can be determined.

Several samples were prepared at different pH values and in different buffers. From pH 6 to 9 the temperature independent buffer system (see section 2.12) was employed. From pH 9 to pH 11.5 the Good's buffer mix (see section 2.11.2) was used. Two NaOH solutions (200 and 50 mM) containing 150 mM KCl and 10% (v/v) glycerol were used to prepare samples at pH 12.9 and 12.1, respectively.

In this experiment, sample preparation was done anaerobically by adding 100 µL of IscR (275 µM final dimer concentration) to 298 µL of buffer and 8 µL of buffered 100 mM sodium dithionite (2 mM final concentration). The solution was gently homogenized and incubated for 3 minutes prior to the transfer of 300 µL to an EPR tube. The remaining 100 µL were used to measure the sample pH value. Samples were anaerobically frozen in liquid nitrogen and kept at 77 K until measurement. Spectral data were acquired between 320 and 380 mT, at 77 K, at 2 mW microwave power, 1 mT modulation amplitude and 100 kHz modulation frequency.

DEPC modification

Diethyl pyrocarbonate (DEPC), typically used in laboratories to deactivate RNases, is known to form covalent adducts with the side chains of the amino acids histidine, and to a lesser extent, lysine, tyrosine and cysteine, as well as chemical compounds with primary and secondary amines. Upon reaction, carbethoxylation occurs and CO_2 and ethanol are released. It has been used in the past to modify histidine residues of metalloproteins, particularly the Rieske protein[173], leading to an almost irreversible adduct that, in case of reaction with the other nitrogen atom of a cluster bound histidine ligand, can be detected by EPR spectroscopy.

DEPC can react with either nitrogen atom of the histidine imidazole ring. However, it can only react with a deprotonated nitrogen. If one of the two nitrogen atoms of histidine is coordinated to a metal ion or a cluster, DEPC modification can only occur at the non-coordinating nitrogen when it is deprotonated, or a substantial deprotonated population is present (i.e. at a pH value close to the pK). DEPC modification is therefore a suitable technique to assess the pK_a of the histidine ligand. However, the spontaneous hydrolysis of DEPC especially at alkaline pH, the reaction with buffers (Tris) and the adduct hydrolysis can be a challenge in these experiments.

Four different experiments were conducted with DEPC. In these experiments a mixture of two buffers was used to vary the pH value. The actual pH value of the samples, which slightly deviated from the pH of the buffer, was always measured with a micro pH electrode. The buffers used in this experiment

were 50 mM Good's buffer mix, containing 200 mM KCl and 10% (v/v) glycerol, pH 5.5 (buffer A) and pH 10.6 (buffer B). Experiments were carried out in an anaerobic glove box at an average temperature of 22 °C. All samples were anaerobically shock frozen in liquid nitrogen and measured by EPR at 77 K, 2 mW microwave power, 1 mT modulation amplitude and 100 kHz modulation frequency. Five averaged scans were recorded for each sample to obtain a better signal to noise ratio. All DEPC solutions were freshly prepared in absolute ethanol.

Initially, 11 samples at different pH values between 6.5 and 10.5 were prepared, with constant protein concentration (100 μM IscR dimer) and constant DEPC concentration (100 μM). Sample preparation pipetting scheme is shown in Table 17. Buffer total volume was fixed at 185 μL and the values described in the Table are percentages from this volume. All samples were incubated anaerobically with DEPC for 5 minutes prior to the addition of sodium dithionite. Additionally, three control samples were prepared at pH values 6.9 (90% buffer A, 10% buffer B), 8.3 (60% buffer A, 40% buffer B) and 9.4 (30% buffer A, 70% buffer B) with a total buffer volume of 194 μL, corresponding to the 185 μL used in the samples combined with the 9 μL of DEPC used in the samples.

Table 17. Sample preparation for the pH dependency of DEPC modification (before dithionite reduction).

Buffer A %	Buffer B %	Sample measured pH value	Protein	DEPC (3.3 mM)	NaDT (100 mM)
100	0	6.47	100 μL	9 μL	6 μL
90	10	7.04			
80	20	7.57			
70	30	7.97			
60	40	8.30			
50	50	8.66			
40	60	8.97			
30	70	9.33			
20	80	9.70			
10	90	10.08			
0	100	10.45			

A second experiment was carried out to assess IscR modification by DEPC at different pH values and redox states. For that purpose, nine samples were prepared at three different pH values: 7.31, 8.35 and 9.31. Three times 900 μL of 120 μM IscR dimer were prepared at each pH value by dilution of 180 μL of IscR as isolated in 720 μL of buffers (75, 50 and 25 % buffer A and 25, 50 and 75% buffer B to make solutions pH 7.3, 8.4 and 9.3, respectively).

For each pH value, three 300 μL samples were prepared by a) reducing the protein with sodium dithionite (2 mM final concentration) without DEPC; b) 5 minute DEPC treatment (1 mM final concentration) of the protein in the as isolated state, presumably mainly oxidized, followed by reduction for 3 minutes with sodium dithionite (2 mM final concentration); c) reduction by sodium

dithionite for 3 minutes (2 mM final concentration) followed by 5 minutes incubation with DEPC (1 mM final concentration).

The effect of the DEPC concentration was assessed in a third experiment where DEPC concentrations were varied between 100 and 1000 µM at a fixed IscR dimer concentration of 50 µM. Here, 300 µL IscR (600 µM dimer) was diluted in 3000 µL buffer (50% buffer A, 50% buffer B, pH 8.3) yielding a protein concentration of 54.5 µM. Eleven Eppendorf tubes were then filled with 275 µL of the 54.5 µM IscR solution. Five samples were treated with 1.8, 3.6, 7.3, 14.6 and 18.2 µL of DEPC (16.5 mM in ethanol), resulting in samples that would then have 100, 200, 400, 800 and 1000 µM of DEPC final concentration, respectively. These samples were incubated for 5 minutes, then reduced with sodium dithionite (2 mM final concentration, 3 minutes incubation) and the remaining volume was filled with buffer up to 300 µL. Another five samples were prepared by reversing the order of the DEPC and sodium dithionite addition steps. Again 3 minutes was allowed for dithionite reduction and 5 minutes for DEPC modification. The last sample was only treated with 6 µL 100 mM sodium dithionite, filled with buffer up to 300 µL, and incubated for 3 minutes.

Lastly, a fourth experiment similar to the second experiment was conducted. In this experiment, however, samples not at three (pH 7.3, 8.4 and 9.3) but at five pH values in a wider range were prepared. These buffers were again composed of a mix of buffers A and B at the ratios 100:0, 75:25, 50:50, 25:75 and 0:100 and the pH values obtained for 1000 µL of protein solution (250 µL IscR and 750 µL buffer mix) were 6.6, 7.6, 8.5, 9.4 and 10.3, respectively. EPR samples were prepared as previously described with 276 µL IscR (~138 µM dimer, final concentration), 18 µL 3.3 mM DEPC (~200 µM final concentration) and 6 µL of sodium dithionite (2 mM final concentration). For the non-DEPC-treated sample a final volume of 300 µL was achieved by buffer addition.

Cluster stability with time at different redox states

In this experiment, three samples were prepared: fully reduced, an air-oxidized and a ferricyanide-oxidized sample. Both reduced and air oxidized samples were prepared at the same time, with protein from the same batch, except that the reduced protein was prepared anaerobically in an anaerobic chamber and the air oxidized prepared aerobically. For each, 500 µL of 500 µM IscR dimer were added to two assay tubes and diluted with 1200 µL and 1166 µL TIB at pH 8.5 to prepare the oxidized and reduced states, respectively. 34 µL of 100 mM buffered sodium dithionite was also added to reduce the second sample. Both samples were incubated at room temperature and mildly stirred. At times 0, 30 min, 2 hours, 6 hours and 24 hours 300 µL samples were taken from each main solution, loaded into EPR tubes and shock frozen in liquid nitrogen. The samples incubated in air were treated with 2 mM of sodium dithionite (final concentration) prior to freezing to reduce the clusters that remained intact (since EPR measurements only yield signals for a reduced [2Fe-2S] cluster). All samples were stored at 77 K until measurement.

In a second experiment IscR from the same batch was first oxidized with 2 mM final concentration of anaerobic potassium ferricyanide, incubated for 5 minutes and buffer exchanged in a Sephadex PD10 column to remove the excess oxidant. The solution was then submitted to the same procedure followed for the oxidized sample mentioned above, except it was performed anaerobically. Due to a low amount of protein from the same batch available only samples at times 0 min, 30 min and 2 hours could be prepared.

2.15.2. Pulsed EPR spectroscopy

Pulsed EPR was employed in this work due to its ability to resolve and inform on proton couplings with metal centers. Here, samples for pulsed EPR were prepared to investigate the protonation of the histidine ligand at two pH/pD values (8 and 12) in H_2O and D_2O buffers.

Additionally, pulsed EPR can also inform on the nitrogen couplings. ^{14}N, the most abundant isotope of nitrogen, has an I=1. This nuclear spin in proximity with the $[2Fe\text{-}2S]^{1+}$ cluster will give rise to three splittings in the EPR spectra in contrast with two for a I= ½ ^{15}N atom. To unequivocally identify the origin of the pulsed EPR signal by comparing the differences observed in the quadrupolar splitting, ^{15}N labelling by growth of *E. coli* expressing IscR on minimal medium with $^{15}NH_4Cl$ was also performed

Sample preparation started with the purification of ^{15}N labelled protein as described in section 2.7. Then, the 6.3 mL of ^{15}N labelled IscR obtained and 8 mL of IscR grown with naturally abundant nitrogen were equally split (two 3.15 mL and two 4 mL) and handled as described in Figure 10.

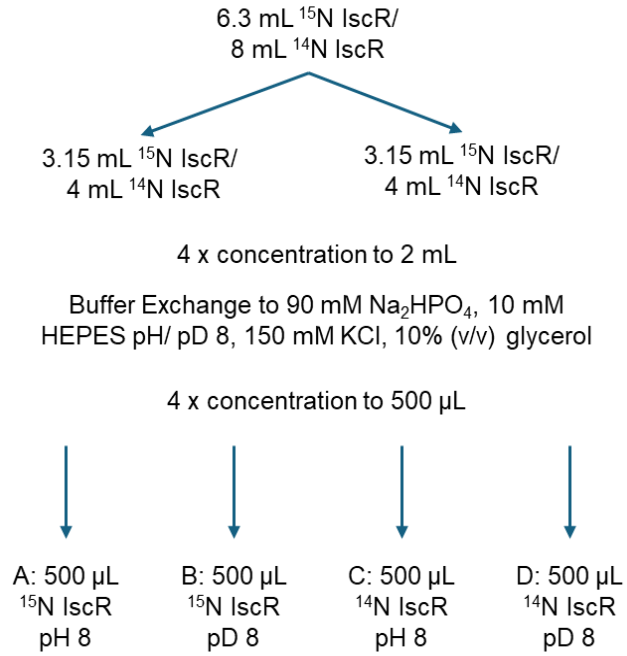

Figure 10. Schematic representation of initial steps in sample preparation for pulsed EPR.

Samples A to D were split in screw cap vials in two 100 µL and one 300 µL aliquots, totalizing 12 samples, eight of 100 µL and four of 300 µL. The eight 100 µL samples were then shipped in dry ice to the Molecular Science Hub in London for further preparation and pulsed EPR.

Cluster content was then determined by UV-Vis spectroscopy using a $\varepsilon_{420\ nm}$= 6600 $M^{-1}cm^{-1}$ for $[2Fe–2S]^{2+}$ and the samples were prepared according to Table 18 to obtain a final cluster concentration of 500 µM per sample and 4 mM of sodium dithionite.

Table 18. Pulsed EPR sample preparation.

Sample	Buffer + 6 µL NaDT 100 mM	Protein
^{14}N pH 8	111 µL buffer 3	33 µL 2.3 mM ^{14}N IscR pH 8
^{14}N pD 8	85 µL buffer 4	59 µL 1.27 mM ^{14}N IscR pD 8
^{14}N pH 12	111 µL buffer 3	33 µL 2.3 mM ^{14}N IscR pH 8
^{14}N pD 12	85 µL buffer 4	59 µL 1.27 mM ^{14}N IscR pD 8
^{15}N pH 8	105 µL buffer 5	39 µL 1.94 mM ^{15}N IscR pH 8
^{15}N pD 8	112 µL buffer 6	32 µL 2.37 mM ^{15}N IscR pD 8
^{15}N pH 12	105 µL buffer 5	39 µL 1.94 mM ^{15}N IscR pH 8
^{15}N pD 12	112 µL buffer 6	32 µL 2.37 mM ^{15}N IscR pD 8

The buffers used for sample preparation in London were 90 mM Na_2HPO_4, 10 mM HEPES, containing 150 mM KCl and 10% (v/v) glycerol at pH 8 (buffer 3), and pD 8 (buffer 4). For samples at high pH buffers 100 mM Na_2HPO_4, containing 150 mM KCl and 10% (v/v) glycerol at pH 12 (buffer 5) and pD 12 (buffer 6) were used.

2.16. X-ray Crystallography

Crystal structures for IscR are currently available, however, these structures are in fact from a triple cysteine to alanine mutant prepared specifically to obtain a structure of the apo protein. It was attempted to obtain a crystal structure of holo IscR by collaboration with Dr. Berta Martins, at the Humboldt-University in Berlin with sample preparation as described below. All the protein samples that were purified in Berlin were stored in screw cap vials and all samples but one vial of each fraction were frozen in liquid nitrogen and stored at -80 ºC overnight. The samples that were not frozen were kept in the anaerobic chamber overnight, at room temperature, to assess cluster breakdown and, in case no breakdown was detected, the possibility of using the non-frozen protein for crystallization.

2.16.1. Screening with previously purified protein

88.3 µL of IscR wild type 630 µM in 100 mM HEPES, pH 8.5, 10% (v/v) glycerol, 660 mM KCl were used per screening condition. The initial screens were ProPlex, MemGold and MemGold2 using 1.8 µL of protein per drop and 80 µL of precipitating agent per reservoir. The protein and the precipitating

agent were mixed in a 1:1 proportion. The screening contents can be found in the supplementary information (S.6.).

2.16.2. Screening with protein purified from a frozen cell extract

The protein was purified as described in section 2.2.8, except that during elution the protein was separated into two fractions – the first 3 mL and the remaining 6 mL. Concentrations were estimated by NanoDrop measurement.

The first 3 mL (named IscR 1-1) was determined to have a concentration of approximately 720 µM of IscR dimer with a cluster incorporation of approximately 40%. The second fraction (6 mL, named IscR 1-2) was concentrated to approximately 1 mL using a 15 mL Amicon with a 10 kDa cut-off. It contained a higher protein concentration (2-fold when compared to IscR 1-1) but a similar cluster concentration, indicating a lower cluster content per protein.

2.16.3. pRKISC cells containing overexpressed IscR opened by sonication

For the cells opened by sonication the resulting protein was also separated into two fractions – the first 2 mL and the remaining 6 mL. Concentrations were estimated by NanoDrop measurement.

The first 2 mL (named IscR 2-1) had a protein concentration of approximately 1 mM IscR dimer, but the estimation of cluster content was 16%. The second fraction (6 mL, named IscR 2-2) was concentrated to approximately 1 mL using a 15 mL Amicon with a 10 kDa cut-off. Due to spectroscopic artefacts the protein and cluster concentration could not be properly determined on the purification day.

2.16.4. Primer annealing and crystallization with *iscrb* DNA

***iscrb* (promoter type 1) double strand DNA preparation**

The oligonucleotides corresponding to complementary single stranded-DNA (see Table 7 in section 1.7) were dissolved in water to a final individual concentration of 6 mM. A program for primer annealing was created in the thermocycler. This program consisted of a steady temperature decrease of -0.1 ºC/6 seconds, from 95 ºC to 25 ºC, 1 min at 25 ºC and stand-by at 4 ºC. The program lasted 70 minutes.

Protein and DNA mix for crystallization

An analysis of the cluster and protein content of the frozen and non-frozen protein samples was carried out the following day. The frozen protein batch IscR 2-1 was chosen for the crystallization since it had the lowest ratio$_{A280/A420}$ ($A_{280\ nm}$ =0.729, $A_{420\ nm}$ =0.102, 40-fold dilution, ratio$_{A280/A420\ nm}$ = 7.2) in the UV-Vis spectrum. Additionally, it had not been concentrated and thus, possibly, more homogeneous. The calculated concentration of the homodimer in that batch was 910 µM. For 100 µL of this protein, it would be needed 15.2 µL of double strand DNA 6 mM to have approximately 790

μM of protein and DNA. To prepare a volume of 215 μL of 500 μM protein + DNA each, 18 μL of 6 mM DNA was added to 118.42 μL of 0.91 mM protein and 79.3 μL of 100 mM HEPES pH 8.0, containing 150 mM KCl and 10% (v/v) glycerol.

DNA + protein complex crystallization

The DNA+protein mixture was then used for two crystallography screenings: ProPlex and JBScreen B1/C1/B4/C10. These screenings and protein concentrations were chosen based on the literature data from apo IscR. They contained similar precipitant solutions, and the same protein concentration was used. The droplet size was, once again, 1.8 μL, using 86.4 μL of DNA+protein mixture and 86.4 μL of precipitant solution for each screen.

Around 40 μL of protein + DNA complex was left and 12 μL of this solution was used for another crystallization plate. In this crystallization plate protein from batch IscR 2-1 was also used in some wells (shown below in Table 18). This crystallization plate was not a part of a commercial screening. It was handmade and its components were chosen based on Rajagopalan *et al.* 2012[70].

For this plate, 100 μL of precipitating agent was in each reservoir. 2 μL of protein + DNA mixture or protein without DNA was pipetted on the crystallization bridge followed by 2 μL of the precipitating agent from the corresponding well. The schematic was as shown in Table 19.

Table 19. Composition of the screening used in the crystallization of IscR with *iscrb* DNA.

	Ammonium sulfate concentration			**Glycerol concentration**		
IscR without DNA	2.0 M	2.1 M	2.2 M	15%	20%	25%
	Glycerol concentration constant: 20%			Ammonium sulfate concentration constant: 2.1 M		
IscR with DNA	0.15 M	0.2 M	0.25 M	15%	20%	25%
	Glycerol concentration constant: 20%			Ammonium sulfate concentration constant: 0.2 M		

3. Experimental procedures used in Chapter IV

Most of the experimental procedures employed in this project are identical or similar to those described in this Chapter, Section 2. Therefore, this section will feature a simpler version and the differences in protocols when compared to those described before. For details not covered here, refer to Section 2 of Chapter II. This project was performed by the bachelor student Alissa Agovic under my direct supervision.

3.1. Plasmid cloning, transformation and pre-culture

IBA-101 and 102 plasmids cloned with the *YjdI* gene were made by the technical assistant Doreen Knochenhauer with EcoRI and PstI restriction enzymes. IBA101, containing YjdI fused to a twin streptag at the C-terminus, was then transformed in BL21(DE3) and BL21(DE3) pRKISC cells by heat shock and platted in LB-agar plates with antibiotic that corresponded to their resistance – 100 µg/mL ampicillin for BL21(DE3) and 100 µg/mL ampicillin and 10 µg/mL tetracycline for pRKISC cells. After overnight incubation at 37ºC, three pRKISC colonies were picked and separately inoculated in an Erlenmeyer flask containing 120 mL of LB medium and the same antibiotic composition. Pre-cultures (25 mL) were grown overnight at 37 ºC, 150 rpm.

3.2. Cell growth and protein overexpression

Four times 25 mL of overnight grown pre-culture were inoculated in four Erlenmeyer flasks containing 2 L of LB-medium and the same antibiotic composition. These cultures were grown as described previously, without parafilm to seal the bottle necks. ^{57}Fe labelled cells were also grown for Mössbauer spectroscopy. This, together with cell harvesting, disruption and ultracentrifugation were also performed as previously described in Chapter II, except that cells were resuspended in 20 mM Tris HCl pH 8, 30 mM NaCl 2 % glycerol

3.3. Protein purification

Due to the presence of a twin streptag in the overexpressed protein, the purification process was done with a 5 mL Strep Tactin XT 4-FLOW gravity column. The 25 mL of soluble fraction resulting from the ultracentrifugation process were filtered with a 0.2 µm filter and loaded onto the column previously equilibrated with 10 CV of 100 mM Tris HCl pH 8, 150 mM NaCl 10% glycerol (Buffer 1). The column was posteriorly washed with 10 CV of Buffer 1. Afterwards, the protein was eluted with 10 mL of elution buffer, 100 mM Tris HCl pH 8, 150 mM NaCl 10% glycerol 50 mM biotin (Buffer 2). Finally, to remove biotin from solution, the buffer was exchanged back to 100 mM Tris HCl pH 8, 150 mM NaCl 10% glycerol through a PD10 column by 2 mL loading and eluting steps until all the protein was biotin free. All the protein was then pooled together, homogenized, split into screw cap vials in 300 µL samples, shock frozen in liquid N_2 and stored at -80 ºC until further utilization. The purification

process was performed entirely under anaerobic conditions. Protein, iron and sulfur determination was performed as described previously.

3.4. SDS-PAGE

All SDS-PAGEs run for YjdI were 15% in acrylamide:bisacrylamide with a 6% stacking gel. Gel preparation and running was done as described previously. Sample preparation was performed according to Table 20.

Table 20. YjdI SDS-PAGE sample preparation

Sample	Content	Volume loaded (µL)
Before induction (BI)	Pellet of 1 mL of cells before induction + 50 µL of buffer 1 + 50 µL of sample buffer	7
After induction (AI)	Pellet of 1 mL of cells after induction + 50 µL buffer 1 + 50 µL sample buffer	4
Soluble fraction (SF)	10 µL soluble fraction + 30 µL sample buffer	4
Pellet (P)	~10 mg of pellet + 100 µL buffer 1 + 100 µL sample buffer	3
Flowthrough (FT)	10 µL flowthrough + 20 µL sample buffer	4
Wash step (W)	20 µL wash step + 20 µL sample buffer	4
Molecular Marker	-	6
YjdI 1:40	2.2 µL YjdI 1:40 + 5 µL sample buffer + 17.8 µL buffer 1	18
	6.5 µL YjdI 1:40 + 5 µL sample buffer + 13.5 µL buffer 1	18
	13 µL YjdI 1:40 + 4 µL sample buffer + 7 µL buffer 1	18

3.5. UV-Visible spectroscopy

3.5.1. UV-Vis absorption spectrum of YjdI

For the study of YjdI by UV-Vis spectroscopy, the absorption UV-Vis spectrum was measured between 250 and 800 nm with a disposable UV cuvette. Protein dilution was 1:20.

3.5.2. UV-Vis titration of YjdI with potassium ferricyanide

For this titration, the spectrum of 933 µL of Buffer 1 was measured first between 250 and 800 nm. Subsequently, 67 µL of YjdI protein was added to the solution, and another spectrum was recorded. Following this, 10 µL of 1 mM potassium ferricyanide was added to the solution, mixed thoroughly, and measured. This process was repeated ten times, resulting in a total of ten spectra. This titration was repeated with a total of 15 spectra recorded. The experiment was carried out under anaerobic conditions.

3.5.3. UV-Vis time stability assay

The stability of YjdI's cluster was also assessed by UV-Vis spectroscopy, also performed anaerobically. For this assay, the spectrum of 933 µL of buffer 1 was measured between 250 and 800 nm followed by the addition of 67 µL of YjdI, homogenization and measurement. 75 scans of approximately 3 minutes per scan were measured.

3.6. EPR spectroscopy and dye-mediated redox titrations

3.6.1. As isolated, reduced and oxidized samples

Initially, three samples of YjdI were prepared to be measured by EPR. They were YjdI as isolated, dithionite reduced and ferricyanide oxidized. The sample as isolated was prepared by loading 300 µL of the protein as isolated in an EPR tube. The reduced and oxidized samples were prepared by incubating the 296 and 288 µL of protein with 6 and 12 µL of 100 mM sodium dithionite and potassium ferricyanide, respectively. All protein samples were shock frozen in liquid nitrogen and stored at 77K until measurement.

3.6.2. Dye-mediated redox titrations

For the reductive redox titration, a mediator mix was prepared covering a redox range from -449 to +217 mV, with a final concentration of mediators of 385 µM. All but the first (+276 mV) mediators found in Table 14 were used in this mediator mix (mediator mix 1). For the oxidative redox titration only mediators from +276 mV to -51 mV, N,N,N',N'-tetramethyl-p-phenylenediamine to resorufin, were used to prepare a mediator mix with a final concentration of 833 µM (mediator mix 2).

In the reductive titration, 1220 µL of 100 mM Tris HCl pH 8, containing 150 mM NaCl 10% glycerol, 1200 µL protein and 280 µL of 385 µM mediator mix 1 (final concentration 37 µM) were added to a test tube with a magnetic stirrer under anaerobic conditions. Posteriorly, the redox titration was carried out with the addition of small volumes of 1-100 mM of sodium dithionite and the shift in redox potential was evaluated. Seven 300 µL samples were collected between 0 and -688 mV, measured with an Ag/AgCl electrode (-207 mV when compared to the S.H.E), along the titration.

For the oxidative titration, 1200 µL of protein, 1365 µL 100 mM Tris HCl pH 8, containing 150 mM NaCl 10% glycerol and 135 µL of mediator mix 2 (final concentration 42 µM) were added to a test tube with a magnetic stirrer and under anaerobic conditions. The solution was titrated with small volumes of 1-100 mM of ferricyanide from approximately -200 to 0 mV. All samples were shock frozen in liquid nitrogen immediately after their collection and stored at 77 K until measurement.

3.6.3. Cluster reconstitution

Anaerobic cluster reconstitutions were attempted in this practical work. In the first cluster reconstitution 400 µL of 506 µM YjdI protein was added to an Eppendorf tube. Afterwards, 20 µL of 2.4 mM Mohr's salt was added and slowly homogenized and incubated for 1 minute. This procedure

was repeated five times. No changes in protein appearance were observed. Posteriorly 10 µL of 2 mM sodium dithionite was slowly added to the solution, homogenized and the solution was incubated for 4 minutes. A 300 µL EPR sample was collected. To the remaining solution 10 µL of 2 mM sodium dithionite was added once more, the sample was incubated for 30 minutes and then transferred to an EPR tube. Samples were shock frozen in liquid nitrogen immediately after their preparation and stored at 77 K until measurement.

In the second cluster reconstitution, three samples were prepared. Initially, 153 µL of 506 µM protein were pipetted in each Eppendorf tube. Posteriorly, 20 µL of 100 mM Tris HCl pH 8, containing 150 mM NaCl 10% glycerol, 20 µL of 2.8 mM Mohr's salt and 20 µL of 5.6 mM Mohr's salt were pipetted in each Eppendorf tube. The three samples were incubated for 30 minutes. 6 µL of 100 mM sodium dithionite was then added to each sample and they were, once more, incubated for 30 minutes. After the incubation time, the solutions were transferred to EPR tubes, shoch frozen and stored at 77 K until further measurements.

3.7. Circular Dichroism spectroscopy

CD spectroscopy was used in this experimental work to analyze the protein's secondary structure, by UV CD, and cluster features, by visible CD. All experiments here described were performed aerobically.

3.7.1. Ultraviolet CD spectroscopy

UV CD spectra were measured between 197 and 250 nm in 10 mM phosphate NaOH pH 8, containing 200 mM NaCl 10% glycerol. 900 µL of buffer were loaded into a 5 mm quartz cuvette, and 30 spectra were recorded as baseline. Posteriorly, 100 µL of protein as isolated were added to the solution and homogenized. However, due to the high protein concentration this solution was then diluted 1:10 in the same buffer and 30 scans were recorded.

3.7.2. Visible CD spectroscopy

Visible CD spectra were recorded between 250 and 800 nm in of 100 mM Tris HCl pH 8, containing 150 mM NaCl 10% glycerol. Initially, 900 µL of buffer was loaded in a 5 mm quartz cuvette and 30 5-minute scans were recorded as baseline. Posteriorly, 100 µL of protein as isolated were added to the solution and homogenized and 30 5-minute scans were recorded.

4. Experimental procedures used in Chapter V

This project was conducted by the bachelor student Erik Matonia under the supervision of the PhD student Lukas Knauer. Consequently, only the EPR spectroscopy performed in collaboration with me is included in this section.

Thirteen samples were anaerobically prepared at pH values ranging from 10.6 to 13.9. Initially, 3.5 mL of a 635 µM protein solution was reduced using 65 µL of 175 mM sodium dithionite, resulting in a final concentration of 3 mM. The reduced protein was then distributed into thirteen Eppendorf tubes, with each tube containing 250 µL of the sample. 250 µL buffer/alkaline solution with a given pH value was added to each Eppendorf tube to shift the solutions pH value. 300 µL of the samples were then loaded into quartz EPR tubes, shock frozen in liquid nitrogen and stored at 77 K until measurement. The remaining protein was used to measure the real pH value. For sample preparation, buffer solutions were prepared according to Table 21. X-Band continuous wave EPR measurements were carried out using a commercial Bruker Elexsys EMX E580 at 18 K, between 250 and 450 mT, 10 G modulation, and 100 kHz frequency modulation.

Table 21. EPR sample preparation at different pH values for the Rieske protein from *Thermus thermophilus*.

Sample pH	Reduced protein (µL)	Buffer (µL)
10.6	250 µL	250 µL100 mM CAPS 200 mM KCl pH 10.7
10.9		250 µL100 mM CAPS 200 mM KCl pH 11.0
11.0		250 µL 8 mM NaOH 50 mM KCl
11.1		250 µL 100 mM CAPS 200 mM KCl pH 11.3
11.4		250 µL 100 mM CAPS 200 mM KCl pH 11.7
11.6		250 µL 100 mM CAPS 200 mM KCl pH 11.9
11.8		250 µL 16 mM NaOH 50 mM KCl
12.1		250 µL 40 mM NaOH 50 mM KCl
12.6		250 µL 120 mM NaOH 50 mM KCl
13.0		250 µL 130 mM NaOH 50 mM KCl
13.3		Titrated with 1M NaOH to the desired pH value
13.6		Titrated with 1M NaOH to the desired pH value
13.9		Titrated with 1M NaOH to the desired pH value

Chapter III. Redox and spectroscopic properties of the *E. coli* regulator IscR

1. Introduction

As seen in the previous Chapter, FeS clusters are ubiquitous and ancient cofactors playing an essential role in life. These clusters have a wide range of geometries and ligand compositions and play a wide variety of roles. Their biogenesis is tightly regulated[15,126,174], which in *E. coli* involves the Iron-sulfur cluster Regulator (IscR), a transcription factor regulating the ISC pathway[69]. IscR is the subject of this chapter and will be discussed in detail.

E. coli IscR is a member of the Rrf2 family of transcription regulators, and its structure contains a helix-turn-helix (HTH) DNA-binding motif[70], like other proteins from the same family. It is found in solution as a homodimer (α_2) and each monomer, composed of six α-helices and two small β-sheets, has 176 amino acids, a molecular mass of 17.35 kDa[71], and a calculated isoelectric point of 6.5. IscR coordinates one [2Fe-2S] cluster per monomer and is encoded by the *iscR* gene at the 5' end of the ISC operon, regulating its own production via a negative feedback loop process[175].

IscR is known to regulate around 40 genes in *E. coli*[112], including its own gene, and the mechanism of regulation of the ISC pathway is thought to be related to the fraction of IscR in the holo and apo states, [2Fe-2S]-bound and not bound, respectively. The current proposed mechanism is that IscR in its holo form binds to its own promotor region known as "Type 1" DNA. Upon binding, transcription of the *isc* operon is repressed, decreasing the production of FeS clusters through the ISC biogenesis pathway. Holo IscR is also known for binding to Type 1 promotor regions of the *yhgI* and *yadR* genes and to "Type 2" DNA promotor regions, among which are those of *sufA*, encoding the activator of the Suf pathway, and of *hya*, encoding a NiFe hydrogenase subunit[112]. Type 1 and Type 2 DNA consensus sequences are shown in Table 22.

Table 22. Consensus sequence of Type 1 and Type 2 DNA binding motifs. Adapted from Giel, 2006[112]. R and Y represent purine and pyrimidine, S is G or C, W is A or T, K is T or G, M is A or C.

Promoter DNA	Sequence
Type 1	5′- ATASYYGACTRWWWYAGTCRRSTAT-3′
Type 2	5′- AWARCCCYTSNGTTTGMNGKKKTKWA-3′

However, under oxidative stress or when FeS clusters are depleted in the cell, IscR's [2Fe-2S] cluster dissociates, and IscR loses its ability to bind to Type 1 DNA causing the protein to be released from the ISC promoter region. This release allows transcription to begin, consequently initiating the production of FeS clusters through the ISC pathway. In its apo form, IscR is known to bind only Type 2 DNA sequence[176], which was shown by a combination of *in vivo* and *in vitro* experiments on *iscR*,

sufA, *hya*, *ydiU*, *napF*, and *hybO* promoter regions Nesbit and colleagues[176]. A scheme representing IscR's variable function according to the presence or absence of cluster is shown in Figure 11.

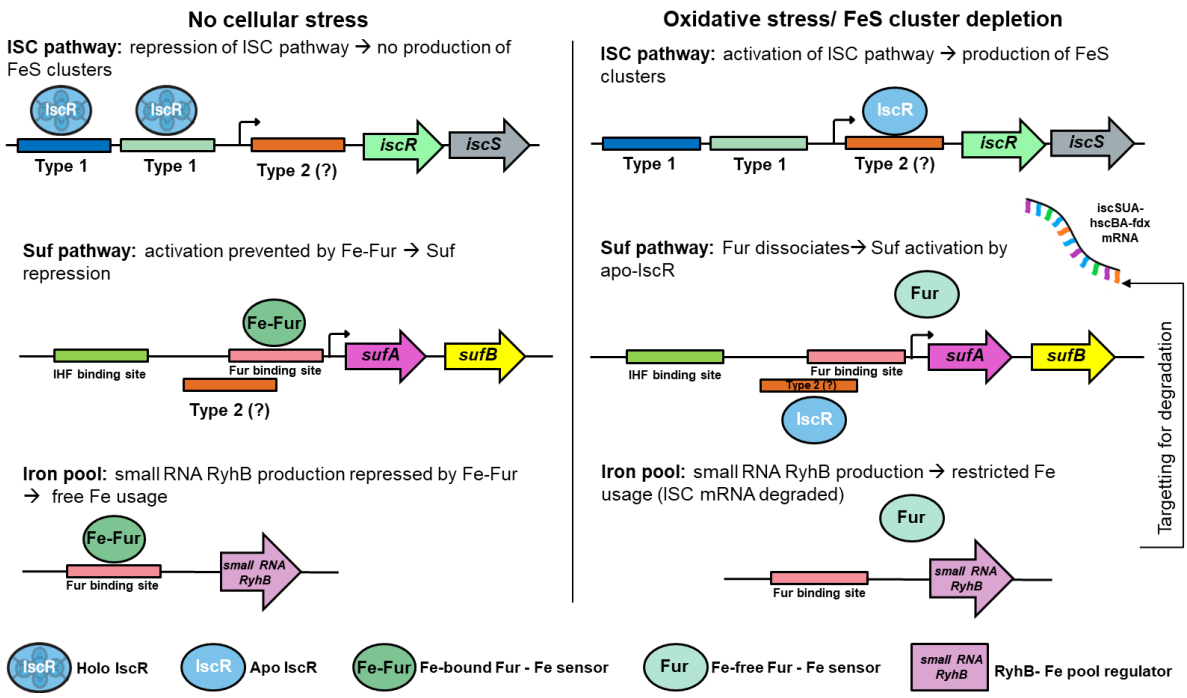

Figure 11. Apo and holo IscR effects on the ISC and Suf pathways under regular (left) and cellular stress (right) conditions. Adapted from Romsang *et al.*[111], Giel *et al.* [112] and Mettert *et al.*[113].

Currently there are four crystal structures of *E. coli* IscR with resolutions of 1.9 to 3.0 Å. The three structures by the Phillips and Kiley groups published in 2013 are of a triple cysteine to alanine mutant (C92A/C98A/C104A, abbreviated as IscR C3A) to obtain the structure of the apo protein[70]. These three structures are of (A) apo-IscR C3A without DNA; (B) apo-IscR C3A bound to the 29 base pair DNA fragment corresponding to the *hya* promoter, a Type 2 DNA sequence; and (C) apo-IscR C3A E43A bound to the same promoter. In this study, it was identified that glutamate 43 is essential for IscR's binding properties to Type II, but not for Type I promoters. One of the three crystal structures (4HF1) of IscR is shown in Figure 12, the others can be found in the PDB repository with codes 4HF0 (apo-IscR C3A without DNA) and 4HF2 (apo-IscR C3A E43A mutant bound to DNA)[70]. A year later, together with the structure of a *Thermincola potens* apo-IscR "C3S" mutant (PDB 4CIC, 36 % amino acid sequence identity with *E. coli* IscR), the structure of a complex of the *E. coli* apo-IscR "C3S" mutant with a 26 base pair *hya* promoter fragment (PDB 4CHU) was published[177]. Recently, the crystal structure of a regulator described as "IscR" from *Dinoroseobacter shibae* was released (PDB 7ZPN). Despite its 42% amino acid sequence identity with *E. coli* IscR the region containing the three cysteine residues was less conserved, and moreover not visible in the 1.9 Å resolution structure.

In none of the four structures it was possible to determine an accurate structure in the vicinity of the cluster, though in PDB 4CIC and 4CHU only the first cysteine residue (serine in the mutant) was

missing. Mutation of essential residues, leading to removal of the cluster, possibly led to the creation of a flexible zone that could not be well resolved by X-ray crystallography.

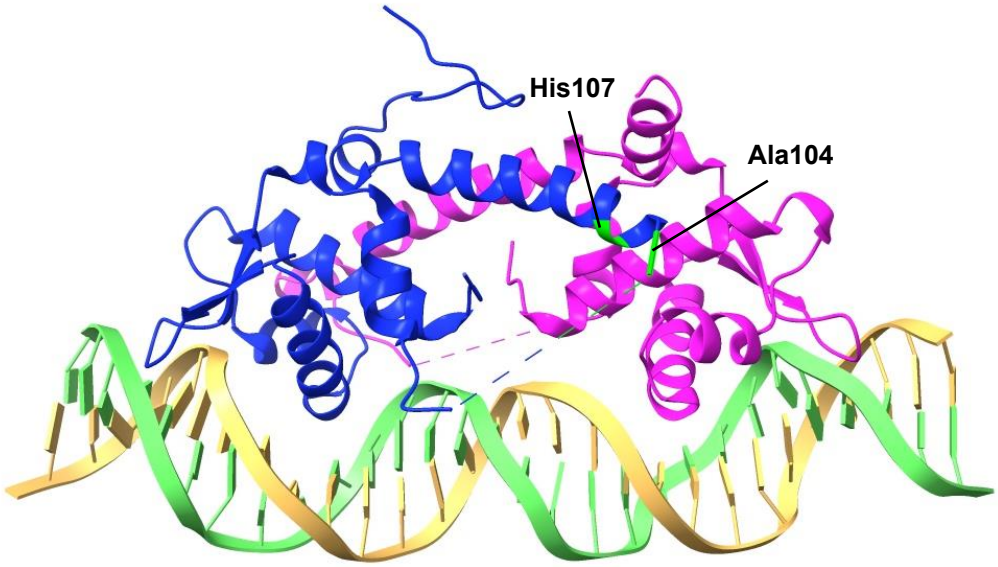

Figure 12. *E. coli* Apo-IscR 3CA bound to the *hya* promoter. Residues Ala107 and His107 are identified in the figure, but residues Ala98 and Ala92 could not be resolved. PDB code: 4HF1. Figure made in ChimeraX from the structure published by Rajagopalan *et al.*[70]

The C-terminus of IscR contains many positively charged amino acids that could be used to target DNA. However, due to disorder in the structures or possibly through proteolysis, the last 20-30 amino acids of IscR could not be resolved.

IscR's [2Fe-2S] cluster has a non-cysteinyl coordination since the primary structure only contains 3 cysteine residues[69] and the three cysteine residue containing regions in the C3A mutants are too far away from each other for a cluster bridged protein.[70] It is currently thought that the presence of a histidine as a cluster ligand could lower the cluster stability, an important prerequisite for IscR's function, switching between the apo and holo forms. For the His87Cys variant of MitoNEET its cluster stability is increased[137]. Thus, the decrease in cluster stability by histidine coordination could be the reason why IscR can act as a sensor for the FeS cluster concentration in the cell[71]. While extensive research has been published on apo IscR and its DNA binding properties, less is known on structural and spectroscopic properties of holo IscR. Early work by Schwartz and coworkers in 2001[69] provided the first insights by demonstrating that holo IscR bound a redox active $[2Fe\text{-}2S]^{2+/1+}$ cluster. In 2012, Fleischhacker and coworkers published the currently still most comprehensive article on the spectroscopic properties of IscR, including Mössbauer, Raman and Nuclear Magnetic Resonance (NMR) spectroscopies[71].

Regarding potential histidine coordination in IscR, another phenomenon comes to mind. As discussed in Chapter I, the presence of a histidine residue as a cluster ligand, especially in [2Fe-2S] clusters, is

often associated with tuning of the redox potential of the cluster and PCET[50,54,60,63,178,179]. To understand whether that plays a role in IscR's function, an in depth characterization of the pK_a values and the study of the redox chemistry of IscR is necessary. These data are currently not available for IscR except for a claimed pK_a in the reduced state of approximately 7.2 determined by NMR spectroscopy of the Markley group as published in Fleischacker *et al*.[71]. This value does not seem to agree with values for similar proteins such as Rieske[60] and Apd1[63], both with double histidine coordination, and MitoNEET[51], with single histidine coordination. All these systems exhibit pK_a values in the reduced state above pH 12, whereas the pK_a values in the oxidized states are usually about 4 pH units lower and are in the physiological range of pH values. Except for the observation by Mössbauer spectroscopy that IscR appears to be present in its reduced form in *E. coli* cells[71] no data is available on the redox chemistry of IscR. The *in vivo* reduced redox state of IscR suggests a relatively high potential in comparison with the cytosol of *E. coli* cells that is usually between -250 and -300 mV vs the Standard Hydrogen Electrode (S.H.E)[180].

In this Chapter, the determination of the pK_a values of *E. coli* IscR in the reduced and oxidized state, as well as the determination of the midpoint potentials of its cluster at various pH values will be described and discussed. Evidence for histidine coordination from DEPC modification at different pH values and redox states will be presented, which supplies independent support for histidine coordination as no structure is available for holo IscR. Additionally, the role for the redox chemistry of IscR's cluster will be explored.

2. Results and discussion

2.1. Biochemical characterization of IscR

Initially, the expression and production of holo IscR was non-reproducible. Therefore, several experimental conditions were tested varying the *E. coli* strain, temperature after induction, concentration of inducing agent and supplements (iron and sulfur sources) and media. Under many of the conditions employed the purified IscR had a low cluster content. Thus, purification of apo IscR did not seem to be the problem. Employing a microaerobic or even anoxic environment by using a larger volume than the standard 2 L of media in a 5 L Erlenmeyer flask was tested together with variation of the orbital speed, variation of the IPTG concentration; and variation of the temperature after induction. Figure 13 shows the resuspended *E. coli* cells overexpressing a non-tagged version of IscR, which were obtained under the four conditions mentioned. It is worth noting that the color of the cells changes among conditions. This is likely related to the amount of IscR holo protein present in the cell since this form is expected to be reddish/brownish. One can clearly observe that growing the cells at 20 ºC does not lead to the production of holo protein, whereas growing the cells in an anoxic environment seems to have a positive effect on cluster incorporation.

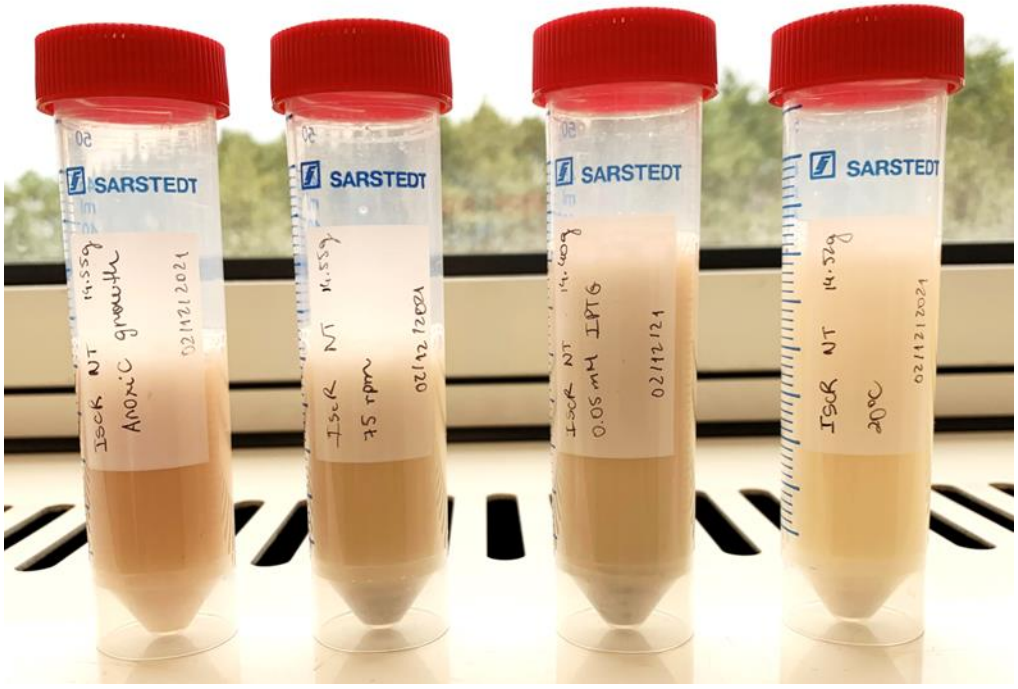

Figure 13. IscR-overexpressing *E. coli* cells grown under different conditions. From left to right the parameters that were varied in each growth when compared to a standard *E.coli* growth protocol: anoxic growth by growing 3 L of cells in a 5 L Erlenmeyer flask, 75 rpm, 0.05 mM IPTG induction, 20 ºC after induction.

Even more holo IscR was finally obtained upon sealing the aluminum foil on the Erlenmeyer flask neck with parafilm. Aluminum foil is oxygen impermeable, however the space between the foil and the Erlenmeyer flask is enough for some diffusion of air into the 5 L flask, especially when incubated in an orbital shaker. It is hypothesized that, although oxygen permeable, the layer of parafilm would allow for the formation of a microaerobic environment throughout the overnight incubation. This method led to a significant improvement, already observable upon visible inspection of the cells (Figure 14). Although the wet weight of *E. coli* cells was considerably lower using parafilm, due to a slower growth rate, it is possible to see the color of holo IscR in the cells, indicating that isolation of holo IscR would be possible, and its yield would be higher. With the aluminum foil/parafilm method, production of holo IscR at a reasonable scale and with a good quality became reproducible, enabling biophysical studies requiring large amounts of holo IscR.

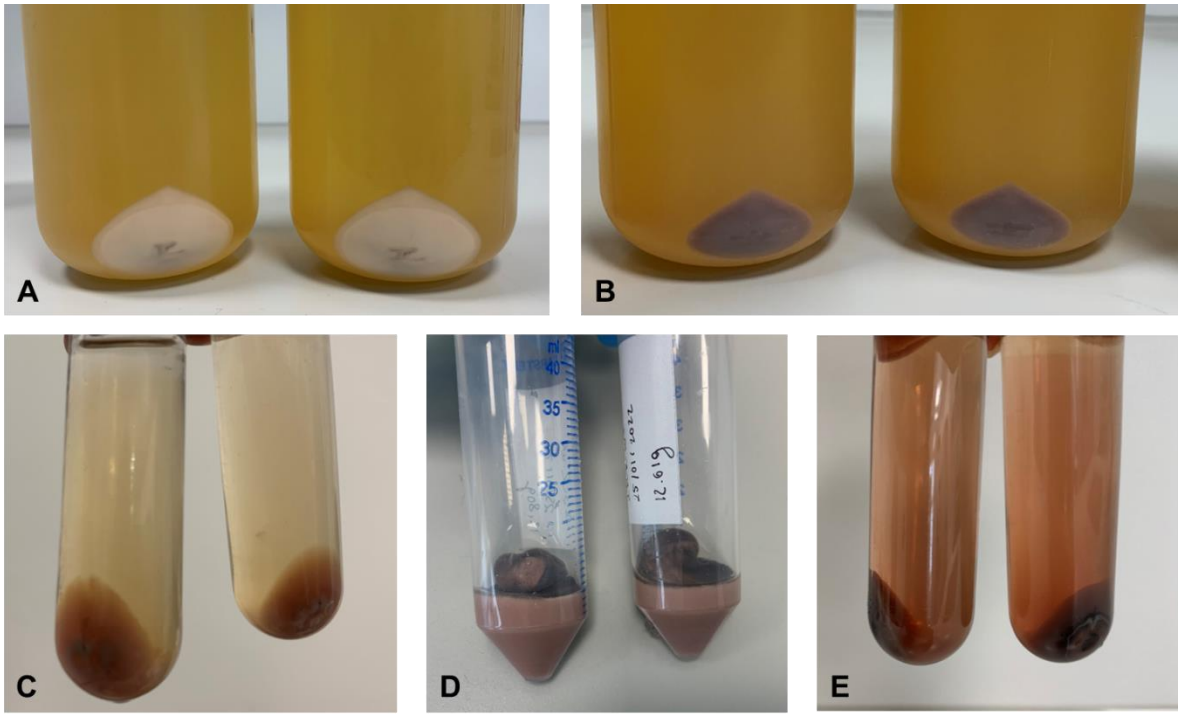

Figure 14. Overexpression of IscR in *E. coli* cells transformed with pRKISC plasmid without and with wrapping with parafilm. Panels show harvested cells (A, B) and soluble fractions after disruption and ultracentrifugation (C, E) of cells grown without (A,C) and with (B, E) parafilm capping. Panel (D) shows the cells grown with parafilm after a wash with buffer and before cell disruption.

Because expression of the untagged version of the IscR, in opposition to the protein tagged with a Twin-Strep-tag, resulted in higher protein yields, purification was carried out with a Heparin-Sepharose column. This column mimics DNA negative charges through its highly sulfated polysaccharide surface and has successfully been used for the purification of DNA binding proteins[181], including *E. coli* IscR[69]. The procedure, performed as described in the methodology, yielded at least in part holo protein based on the brownish/ reddish color. To avoid dilution and cluster loss, IscR was typically block eluted by application of 650 mM KCl in buffer. A brownish color is typically found in

[2Fe-2S] cluster containing proteins. However, the reddish tone was the first indicator of a histidinyl coordination as opposed to the typical brownish color observed for proteins containing canonical clusters, as shown by Stegmaier *et al.* for Apd1 and its cysteine mutants[63]. Figure 15 illustrates these findings on the soluble fraction, IscR protein bound onto the heparin column and after elution in a screwcap vial.

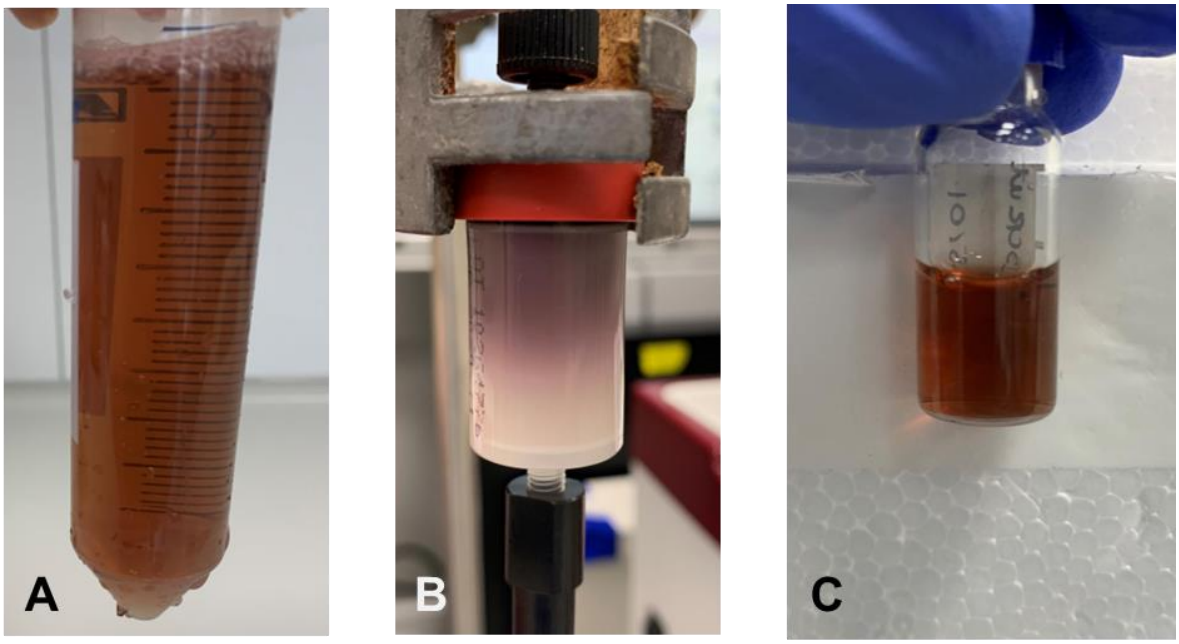

Figure 15. Purification of holo IscR. (A) Soluble cell extract fraction after membrane filtration; (B) Holo IscR attached to the heparin column; (C) Holo IscR after purification.

To assess the success of the overexpression process and protein purification, the purity of IscR was analyzed by SDS-PAGE. For this purpose, samples were collected after individual steps. These samples were cells after induction, soluble fraction, pellet, flow through, wash step and the eluted IscR fraction. The resulting Coomassie stained SDS-PAGE gel is shown in Figure 16.

IscR was detected in the SDS-PAGE gel as thick band, present in all wells, at or slightly above the marker protein corresponding to 15 kDa. In the well corresponding to the sample after induction (AI) it is already possible to observe a clear band at the position corresponding to purified IscR, indicating that a substantial fraction of *E. coli* protein after induction is IscR. After cell lysis, the protein band is observed both in the soluble fraction (SF) and in the pellet (P). During purification, little protein is observed in the flowthrough (FT), but a significant amount of protein can be observed in fractions of the wash step (WS). Intriguingly, the wash fraction might contain (more) apo-IscR as it did not show a strong reddish color. After purification (lanes at the right), it is possible to observe minor contaminants, but these were not considered an issue for spectroscopic studies due to their relatively low abundance.

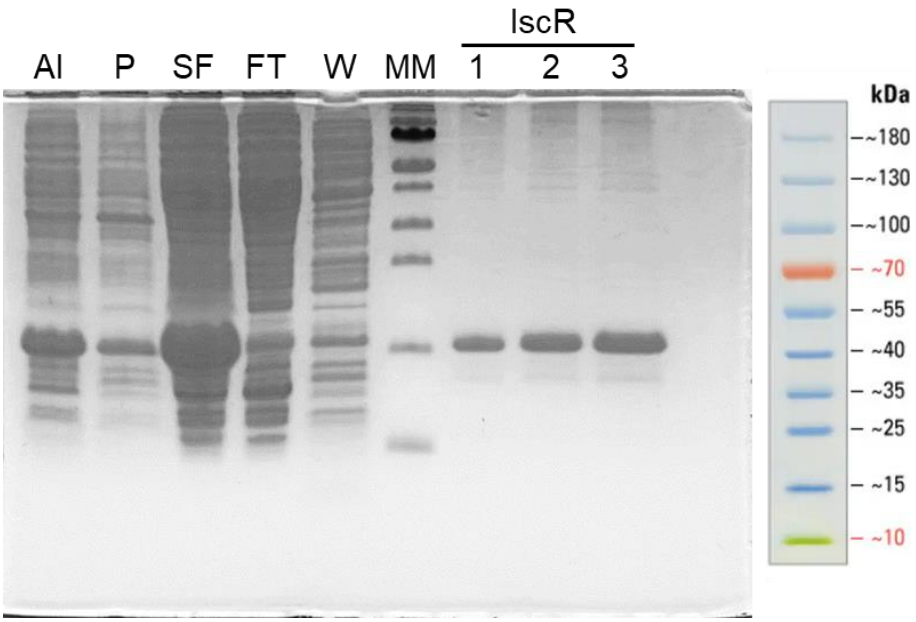

Figure 16. 15% SDS-PAGE of samples collected during the growth and purification of holo IscR. AI – cells after induction; SF – soluble fraction; P – pellet; FT – flowthrough; WS – wash step; MM – molecular mass marker; IscR 1, 2 and 3 – 1, 2 and 3 µL of protein after purification.

Protein, iron and acid-labile sulfur content were determined after assessing protein purity by SDS-PAGE. Their determination was done through colorimetric assays within the technique's linear range. Table 23 exemplifies the results obtained in all the quantifications performed in this practical work.

Table 23. Example of four protein and iron quantifications and two acid-labile sulfur through colorimetric methods.

	Preparation 1	**Preparation 2**	**Preparation 3**	**Preparation 4**
Protein dimer (mM)	0.66	0.76	0.67	0.61
Iron (mM)	0.65	1.13	0.55	0.44
Acid labile sulfur (mM)	2.26	1.45	-	-
Fe/protein dimer	0.98	1.49	0.82	0.71
S^{2-}/ protein dimer	3.42	1.91	-	-

Due to an often unreliable estimation of acid-labile sulfur quantification, most cluster incorporation assessments were performed through iron quantification only. Another method that proved to be reliable, easier and faster to perform than the colorimetric methods was a direct comparison between protein preparations through the ratio A_{280nm} /$A_{420\ nm}$ from UV-Vis spectra. Determining the ratio A_{280nm} /$A_{420\ nm}$ gives indications on cluster incorporation as a protein with 100% cluster incorporation would present a ratio of 2.7 and a preparation with 25% cluster incorporation, a ratio of 7.8. These ratios were determined under the premise that cluster contribution to the absorption at 280 nm is equal to its contribution at 420 nm and using the extinction coefficients described in the next section. IscR

preparations typically showed ratios A_{280nm} /$A_{420\ nm}$ between 4.5 and 7.5 indicating that the protein typically presented between 27 and 49% of cluster incorporation.

Typically, between 180 and 230 mg of IscR could be isolated from approximately 5 g of wet weight cells (3x 2 L culture). Table 23 shows that especially the very reliable iron contents by the Ferene method and the less reliable and variable acid-labile sulfur content by the methylene blue method were not as high as expected for one [2Fe-2S] cluster per monomer. However, a lower Fe and S content is often observed since FeS clusters are known for being labile oxygen sensitive cofactors that often dissociate from the protein during handling. Besides that, for IscR itself, as a transcription factor whose function inherently involves switching between holo and apo protein in the cell, it would not be logical to assume that all IscR protein in *E. coli* would exclusively be in the holo form.

2.2. UV-Visible spectroscopy

2.2.1. Spectral characterization of IscR by UV-Vis

UV-Vis spectroscopy was extensively used in this work to determine the cluster type, its quality and infer the occupancy of the [2Fe-2S] cluster in IscR through another method other than the colorimetric assay for protein, iron and acid-labile sulfur quantification.

IscR spectra were always measured between 250 and 800 nm. This wavelength range allows for the identification of multiple possible components in the solution. Among these are DNA (maximum absorbance around 260 nm)[182], since IscR binds to DNA and could have been co-eluted with it; aromatic amino acids (maxima around 279 nm)[183], a known indicator for protein quantification mainly due to π-π* transition of the sidechain of tryptophan, and, in the visible range (300- 700 nm), the features corresponding to the ligand to metal charge transfer bands, very characteristic of FeS clusters and other metallocofactors[184]. Though the absorbance above 700 nm is not negligible, measuring up to 800 nm provides a baseline for spectral data correction. An example of an UV-Vis spectrum of IscR at pH 8 is represented in Figure 17.

IscR, as a small protein, contains in its primary structure only three tyrosine, two phenylalanine and one tryptophan residue per monomer. These residues are known to absorb, to different extents, around 280 nm. To accurately determine the protein content based on the 280 nm absorbance, the extinction coefficient of IscR based on its amino acid sequence was calculated in Protparam[185]. The calculated value ($\varepsilon_{280\ nm}$ = 9970 $M^{-1}cm^{-1}$, per monomer, assuming all cysteine residues are reduced) is based on the amino acid content only. For this specific spectrum, calculating the protein concentration with the extinction coefficient and the Lambert-Beer law, for an absorbance of 0.89 at 280 nm, yielded a monomer concentration of approximately 89 μM (or 45 μM dimer), or 1785 μM monomer (or 890 μM dimer) correcting for the 20-fold dilution. This value seemed to be overestimated upon comparison with protein determination obtained with the Micro biuret technique(~600 μM IscR dimer). It does not seem likely that this overestimation could be explained by the presence of

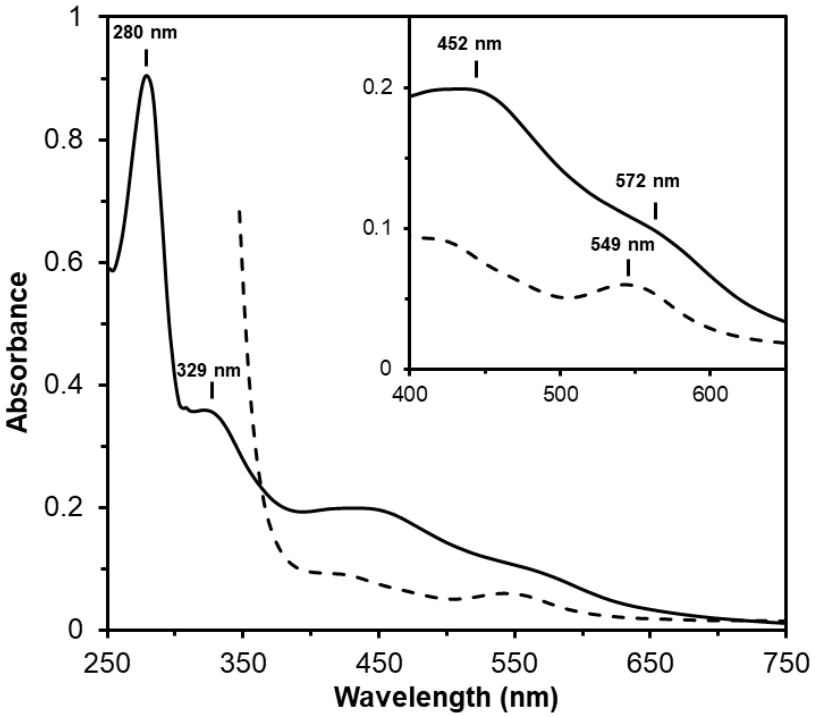

Figure 17. UV-Vis spectrum of holo IscR pH 8 in the as isolated (full) and dithionite reduced (dashed) states. The inset is an expanded view between 400 and 650 nm. The main peaks are identified with their corresponding wavelength.

tryptophan-rich protein contaminants. A better explanation is that due to absorption at 280 nm by the [2Fe-2S] cluster the extinction coefficient is much higher than that calculated based on the aromatic amino acid content. A publication by Motomura and coworkers on the ferredoxin 2 from *Thermosynechococcus vestitus* BP-1 also shows a high absorbance at 280 nm by the [2Fe-2S] cluster. This protein, containing only four tyrosine and no tryptophan residues, shows an extinction coefficient at 280 nm that is almost equal to the one in the visible range, emphasizing the high absorbance of the [2Fe-2S] cluster in the UV range. Thus, [2Fe-2S] clusters presumably absorb almost as much at 280 nm as in the visible range[186].

A theoretical calculation with the absorbance at 280 nm (0.89) minus the cluster absorbance (0.197) in the visible range would yield an IscR dimer concentration of approximately 35 μM in the cuvette and 695 μM before dilution. This value agrees with the determined by Micro biuret colorimetric assay.

UV-Vis spectroscopy was also used to estimate the cluster concentration. The extinction coefficient for [2Fe-2S] clusters is reported to be between 8000 and 10000 $M^{-1}cm^{-1}$ for all cysteine coordinated canonical clusters[187], whereas for non-cysteinyl coordination it is lower, typically between 5300 and 6300 $M^{-1}cm^{-1}$ [115,188]. Using an average ε_{460} of 5800 $M^{-1}cm^{-1}$ it was possible to calculate a total cluster concentration of 680 μM, that considering two clusters per protein, would be 340 μM of fully occupied and functional holo protein. Calculating cluster incorporation with those values, without accounting for protein contamination and the absorbance of FeS clusters at 280 nm, a final average incorporation

(for this preparation) of [2Fe-2S] clusters in holo IscR would be around 49%. In IscR's UV-Vis spectrum there is no peak with a maximum at 260 nm, contrarily the absorbance smoothly goes down from 280 nm to 250 nm, indicating that no DNA co-eluted with IscR. Presumably, if any DNA was bound to IscR before chromatography, it was replaced by Heparin upon binding to the column.

The peaks present at 329, 452 and 572 nm are typically found in non-cysteinyl coordinated oxidized [2Fe-2S] cluster[10,189]. Peaks around 330 nm are often associated with LMCT, mainly the electronic transitions between the sulfide ligands (S^{2-}) to the iron atoms (Fe^{3+}). In canonical $[2Fe\text{-}2S]^{2+}$ clusters the peak present around 420 nm is mainly attributed to electronic transitions from the iron ions (Fe^{3+}) to the cysteine-S ligand σ* (* refers to antibonding) orbitals, or metal to ligand charge transfer (MLCT). However, upon histidine substitution these transitions are now summed with the MLCT from iron ions (Fe^{3+}) d-orbital to the antibonding π* orbitals in the nitrogen imidazole ring, which has a different energy due to the different nature of the transition [130,184,190]. Consequently, a shift of the UV-Vis band to around 450-460 nm is observed instead. The specificity of this transition is what makes this peak the fingerprint for histidinyl coordination in [2Fe-2S] clusters.

No data could be found in literature on oxidized [2Fe-2S] or [4Fe-4S] clusters coordinated by four cysteine residues presenting the broad shoulder around 570 nm. This shoulder is often associated with d-d transitions between metal ions. The presence of non-cysteinyl ligands can alter the crystal field environment around the iron atoms, affecting the energy levels of the d-orbitals and thus the position of the absorption peaks. In summary, the information obtained by UV-Vis spectroscopy seems to indicate that IscR is purified mainly in the oxidized state and that its cluster content is about one $[2Fe\text{-}2S]^{2+}$ per dimer.

2.2.2. pK_a determination by UV-Vis

UV-Vis spectroscopy was also used to determine the pK_a of the histidinyl ligand in IscR's [2Fe-2S] cluster in the oxidized and reduced states. The rationale behind this experiment was that, upon protonation and deprotonation of the histidine sidechain, MLCT electronic transitions would change energy due to a different chemical environment in one of the ligands and shift the peak at 452 nm. Samples were prepared at several pH values as described in the methodology section. The resulting pH titration is shown in Figure 18, Panel A.

Small spectral variations were observed as samples were prepared individually and not slowly "titrated" with acid or base over time. This method of sample preparation was chosen due to IscR's sensitivity to extreme pH values and cluster lability as a function of time. To correct these small variations the standard deviation of the absorbances at different pH values were calculated and plotted against their respective wavelength. This plot allowed the identification of a wavelength with the smallest standard deviation (457 nm), which was chosen for spectral correction. Spectral correction was performed under the assumption that the observed phenomena correspond to a

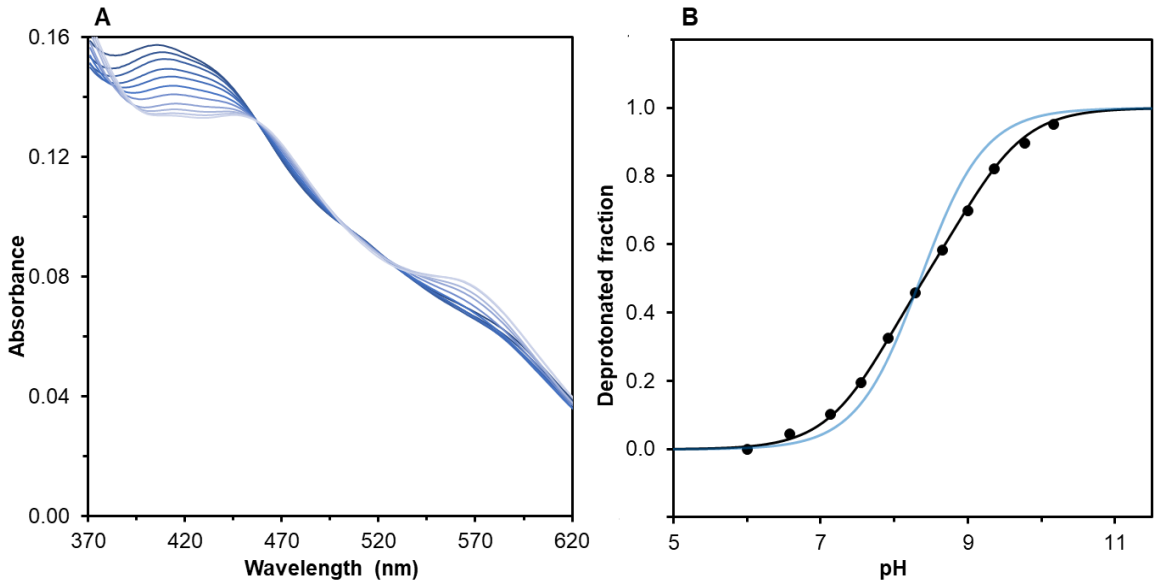

Figure 18. Deprotonation of oxidized wild type holo IscR as a function of the pH value. (A) UV-Vis absorbance at different pH values between 6 and 10.5. pH variation is depicted as a color gradient from higher (dark blue) to lower (light blue) pH values and data were corrected for an isosbestic point at 457 nm. (B) deprotonated fraction as a function of the pH value fitted with one and two pK_a, values. These pK_a values were 8.3 (blue) and 7.9 and 9.1 (black).

simple conversion of one species to another without intermediates (deprotonated to protonated histidine). This process can give rise to isosbestic points, at wavelengths at which the absorbance is identical for both species. The spectral correction was performed by dividing each absorbance value by its corresponding absorbance at 457 nm, and then multiplying it by the average absorbance at 457 nm across all pH values.

By analysis of the spectra of IscR at several pH values it becomes clear that a transition between species is taking place. At low pH values, the main peak observed has a maximum at approximately 457 nm. A gradual shift of the maximum to 407 nm is observed upon increase of the pH. This transition was attributed to the deprotonation of the non-coordinating nitrogen atom of the histidine residue coordinating the $[2Fe\text{-}2S]^{2+}$ cluster in IscR.

In the standard deviation plot previously mentioned, the highest shift or largest standard deviation was observed at 422 nm. The determination of the pK_a was done by subtracting the constant absorption at the isosbestic point, 457 nm, from the wavelength with the highest observable change, 422 nm. Shown in Figure 18, Panel B, the change of absorbance ($\Delta A = A_{422\ nm} - A_{457\ nm}$) was normalized between 0 and 1 and plotted as a function of the pH of the sample. The data were then fitted with the Henderson–Hasselbalch equation

$$pH = pK_a + log_{10}\frac{[A^-]}{[AH]} \qquad \text{Equation 4}$$

where pH is the pH value of the solution, pK_a is the pH value at which a 50 % fraction of protonated and deprotonated species occur and [A^-] and [AH] are the concentrations of base and acid, respectively.

Two potential protonation curves were calculated. The first curve, shown in blue in the figure, represents the fit of the experimental data using a single pK_a value of 8.3. However, the fit is not perfect, as the experimental curve has a slightly less steep slope than the calculated one. This discrepancy may be due to the influence of protonatable residues in the surrounding environment, which could have a weaker but significant effect. The second curve, depicted in black, suggests the presence of two pK_a values: 7.9 and 9.1. These values are close enough that they do not appear as distinct steps but result in a smaller slope, making it impossible to fit the curve with just one pK_a. In this case, the pK_a of 7.9 would be attributed to the deprotonation of the histidine whereas the pK_a of 9.1 would be attributed to another protonable amino acid in the surroundings.

The pK_a values obtained with both curves for IscR, 7.9 and 8.3, are in the physiological range and are consistent with literature data for similar clusters with 3-Cys 1-His coordination such as MitoNEET($pK_{a,\,ox}$ = 6.7)[51], as well as for 2-Cys 2-His coordination, as Apd1 ($pK_{a1,\,ox}$=7.9)[63] and Rieske proteins (RsRp and TtRp, $pK_{a1,\,ox}$= 7.6 and 7.9, respectively)[60].

The same experiment was performed under anaerobic conditions in the presence of 2 mM sodium dithionite, to keep the [2Fe-2S] cluster of IscR in the reduced state. Figure 19 summarizes the experimental data. In this experiment it was impossible to determine a pK_a in the reduced state since the experimental data did not fit to the Henderson–Hasselbalch equation like for IscR in the oxidized state. It appears that the absorbance at 545 nm decreases with the increase in pH value, but no correlation could be found with a deprotonation process. Due to the low absorbance of the reduced

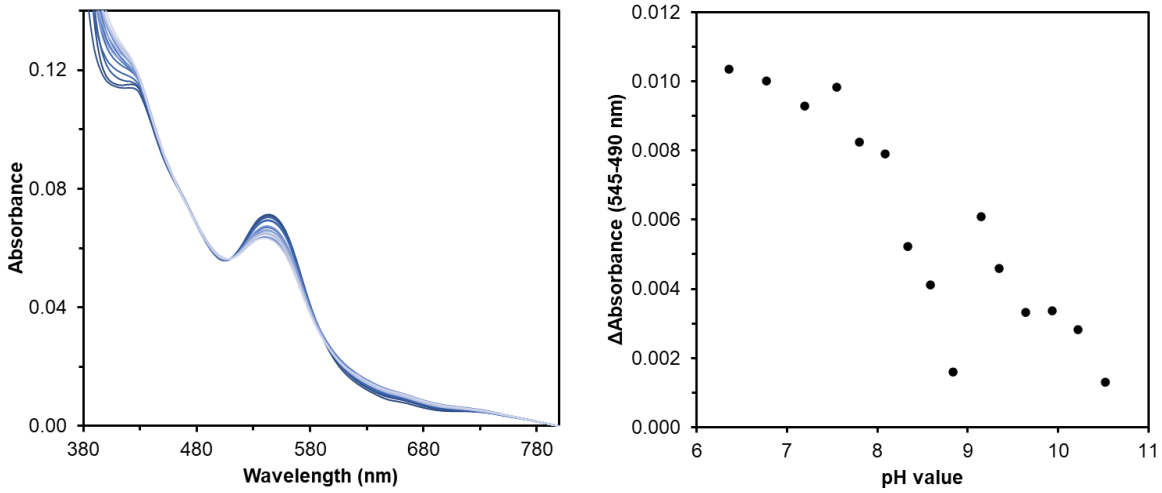

Figure 19. pH titration of reduced wild type holo IscR. (A) UV-Vis absorbance at different pH values between 6 and 10.5. pH variation is depicted as a color gradient from higher (light blue) to lower (dark blue) pH values and data were corrected for an isosbestic point at 510 nm. (B) Difference in absorbance between 545 and 490 nm as a function of the pH value.

IscR cluster, combined with the lack of samples at high pH values (*i.e.* above 10.5), it was not possible to determine a reliable pK_a in the reduced state. The pK_a in the reduced state could be determined by CD spectroscopy (section 2.4).

Additionally, experiments were carried out to determine whether the peak shifts observed were in fact corresponding to reversible deprotonation/protonation effects. Concentrated IscR (as isolated in pH 8 buffer) was diluted into buffers with pH 5.5 and 10.5 to cause a pH shift, and a UV-Vis spectrum was recorded at time "zero", corresponding to the addition of buffer and homogenization of the solution, and at 20 minutes. The pH shift obtained was checked by measurement with a pH electrode as 6.1 and 10.2, for the samples diluted into pH 5.5 and 10.5 buffer, respectively. Then these solutions were diluted again with buffer to return the pH to 8 and another UV-Vis spectrum was recorded for each sample. The measured pH values were 7.9 and 8.1 for the samples with a previous pH of 6.1 and 10.2, respectively. Figure 20 summarizes these results.

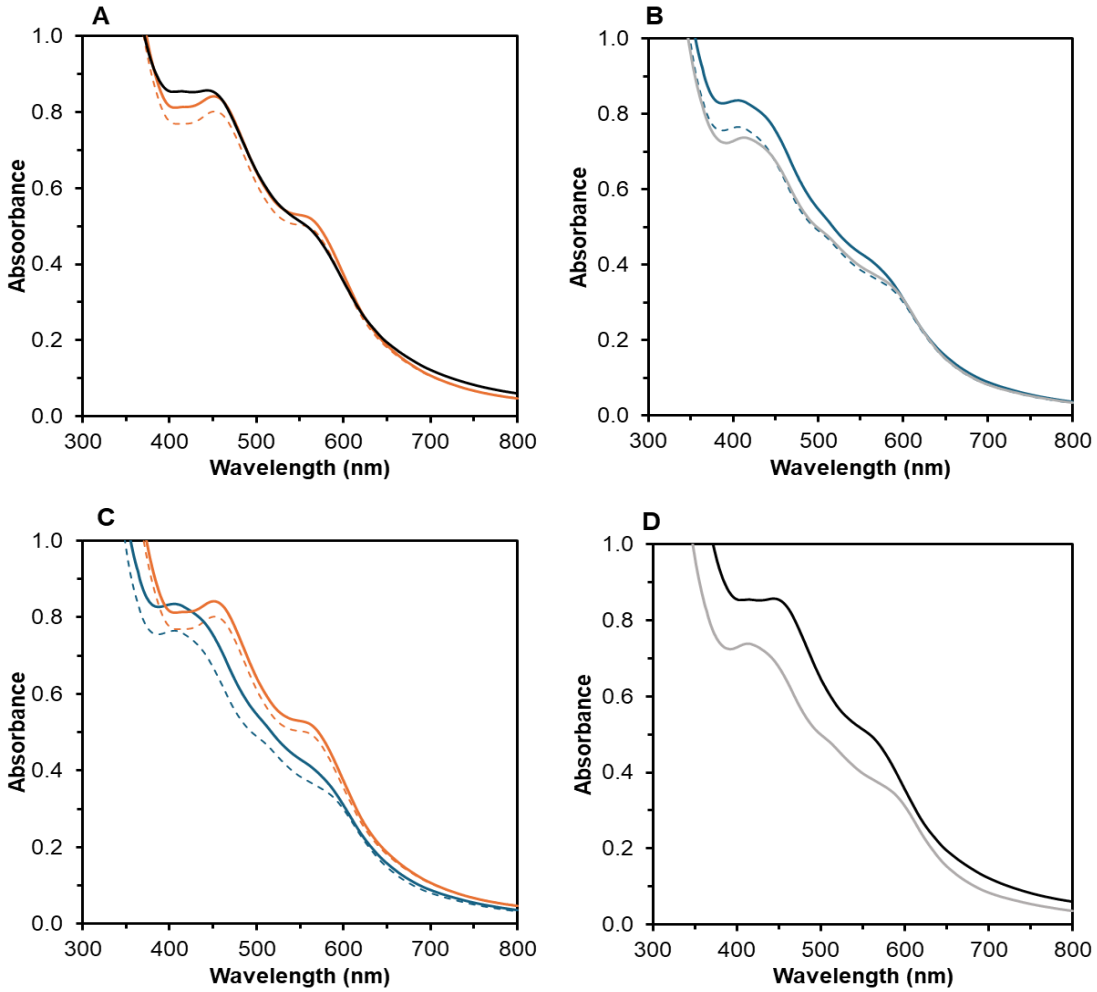

Figure 20. pH reversibility assay of the as isolated wild type IscR. (A) Shift to low pH reversibility assay; (B) Shift to high pH reversibility assay; (C) high and low pH IscR; (D) IscR pH reversed to around pH 8. Legend: Black is IscR pH 7.9 shifted from pH 6.1 and grey is IscR pH 8.1 shifted from pH 10.2, data are multiplied by 5 to compensate for dilution; Orange is IscR pH 6.1; Blue is IscR pH 10.2. Dashed line corresponds to IscR after 20 minutes incubation time at room temperature.

Examining the UV-Vis spectra of IscR at pH 6.1 and 10.2, directly compared in Figure 20, panel C, reveals the same behavior observed in the previous experiment. At high pH values the maximum of the spectra is centered around 415 nm while at low pH values this peak is present around 457 nm. Incubating the sample at room temperature for 20 minutes led to a decrease in absorption throughout the whole wavelength range, but the overall shape remained the same. This result was attributed to a mild cluster breakdown of approximately 10 %.

In Panel A, it is possible to observe that, upon return of the pH back to approximately pH 8, the sample previously shifted to pH 6.1 shows an overall increase in absorbance and a specific increase in intensity around 420 nm and a slightly decreased absorbance around 550 nm. This spectrum agrees with data shown for IscR pH 8 before brief exposure to pH 6.1, indicating full or almost full reversibility in histidine protonation state between pH 6 and pH 8.

In Panel B, however, shifting the from pH 10.2 back to 8.1 does not restore the initial spectrum intensity and an almost insignificant shift is observed between 420 and around 445 nm is observed. It is also possible to observe that around 595 nm the spectrum remained the same upon pH shift. In this experiment, to test whether it would take more time to restore the histidine protonation state, another spectrum of this sample was recorded after 20 minutes, but nothing besides a decrease in intensity with the same overall shape was observed. These results seem to indicate that the deprotonation of the histidine residue is not completely reversible in the oxidized state.

2.3. Electrophoretic mobility shift assay (EMSA)

Electrophoretic mobility shift assays were used to assess DNA binding by holo IscR, which was important for experiments in the presence of DNA such as redox titration and crystallography. Performing spectroscopic experiments in the presence of DNA can give insights into whether the properties of the cluster are impacted upon DNA binding.

Initially, the behavior of IscR in a native PAGE was assessed. To analyze the electrophoretic migration profile of IscR without SDS, a 6% acrylamide gel was run with several proteins. Together with IscR, other native proteins supplied by members of the working group, such as the *E. coli* *S*-adenosylmethionine synthase (MetK), *E. coli* inorganic pyrophosphatase (IPP) and a putative flavoprotein cytochrome b_5 reductase (Pga3) from yeast were loaded in the gel to try and find a suitable standard protein for this experiment. Commercial BSA was also loaded in the gel. Besides that, a protein mix with all the above proteins was prepared. This gel is shown in Figure 21, Panel A. A second gel, run with MetK, IscR without DNA and IscR plus the *hya* promoter DNA, a Type 2 promoter, is represented in Figure 21, Panel B.

Considering homogeneity of these proteins in the first gel, MetK was chosen as reference due to its single sharp band. This protein is found in solution as a homotetramer (α_4) in which each subunit has a molecular mass of approximately 42 kDa.

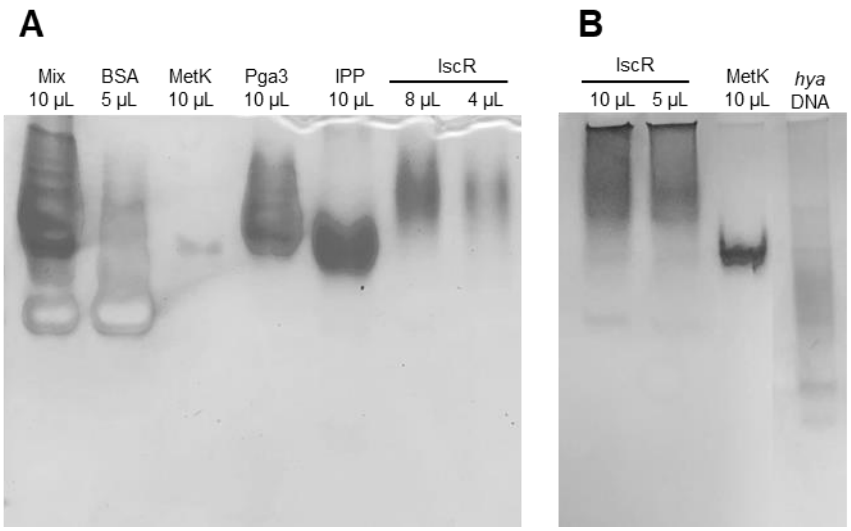

Figure 21. Coomassie stained 6% Native PAGE of IscR. (A) Native PAGE including BSA, MetK, Pga3, IPP, a protein mix and IscR; (B) Native PAGE with IscR, MetK and IscR + *hya* promoter DNA. In panel B the gel was cut to omit the lanes with IscR H107C that will be further discussed in another section.

It is worth emphasizing that, due to the absence of SDS in a native PAGE experiment, this experiment cannot be used for estimation of molecular masses. A variety of factors comes into play, such as the isoelectric point of the proteins, their shape and the nature of the interactions they establish with other molecules. MetK is merely an indicator that for a homogeneous protein a sharp band can be obtained under the conditions used and supply a marker of protein mobility between different gels. In case there is a doubt whether a different migration pattern was observed for IscR, MetK served as a reliable indicator.

Analyzing Figure 21, it is notable that IscR did not migrate well and presented unsharp bands unlike IPP and MetK. It seemed to be stronger on the outer limits of the lane and faint in the middle, not showing a reliable electrophoretic behavior. It also appeared unusual that IscR had migrated less than MetK, though MetK has a larger native mass of 168 kDa, compared to 35 kDa for the IscR dimer. An explanation could be the formation of multimeric complexes of IscR dimers. MetK's isoelectric point, estimated to be between 4.5 to 5.0, is significantly lower than IscR's (6.5). This could cause IscR to be less negatively charged at pH 8.5 than MetK at the pH of the gel, thus leading to slower migration.

In the gel represented in Figure 21 panel B it is interesting to note that the migration behavior of IscR changed when compared to panel A, presenting an aggregated smear at the top of the gel as well as some faint bands below the band corresponding to MetK. It is not clear why this happened since the protein came from the same preparation. The lane containing IscR and the *hya* promoter, however, showed a significant change in migration pattern. Though IscR still showed some smear in the middle of the gel, the position in comparison to IscR in absence of *hya* DNA changed. This is a clear indication that DNA binding took place, with a corresponding shift resulting from the increase of negative

charges in the molecule (DNA phosphate groups). It was not possible to determine the ratio of protein to DNA due to the faint and poorly defined bands, so other EMSA assays focusing on detection of the DNA were run.

Upon observing DNA binding in the previous gel, an EMSA assay was attempted. The gel is shown in Figure 22 of which, like in Figure 21, some lanes were cut off as they correspond to IscR's mutant H107C, that will be discussed later. In this gel (DNA is detected from fluorescence of the Gel red dye in the transilluminator) it is possible to see that in the first lane, without IscR, only a single band for the *hya* DNA is present. Upon IscR addition, the formation of new bands is seen, indicative of IscR-DNA complexes. Interestingly, two resolved bands and a smear are seen contrarily to a single band. Inspection of the literature revealed that IscR has been observed to form a dimer of dimers upon DNA binding in a cooperative way[176]. It is not clear whether this tetramer relates to the ratio protein/DNA or to environmental conditions

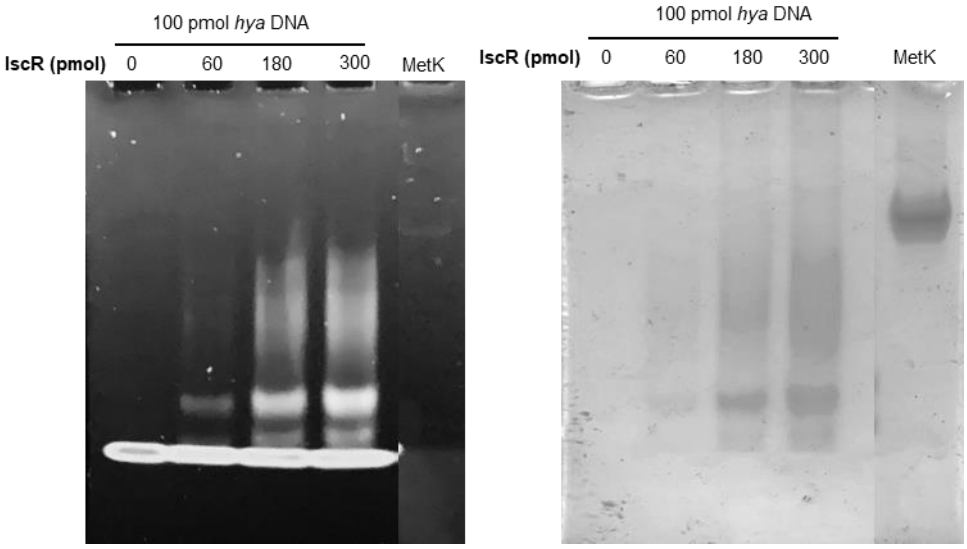

Figure 22. EMSA assay of variable masses of IscR and a constant amount (100 pmol) of hya promoter DNA. The gel on the left was recorded by UV illumination, detecting DNA by Gel red fluorescence with an imager, while the gel on the right was stained with Coomassie Blue for protein detection. Gels were cut to omit bands corresponding to IscR H107C mutant.

Three hypotheses then arose – (1) the bands corresponded to one (lower band) and two (top band) monomers bound to DNA and the smear to a possible homotetramer bound to DNA; (2) the bands corresponded to the dimer (lower band) and the homotetramer (top band) whereas the smear would be a type of mega complex with DNA or (3) the two bands and the smear correspond to dimeric apo, semi-holo and holo IscR. Considering that the typical quaternary structure of IscR is a dimer, it seems more likely that the stronger band (top) would correspond to the dimer conformation bound to DNA, or hypothesis (1), but it could not be determined whether the migration depended on cluster incorporation. Monomeric IscR has not been reported thus far. A fourth hypothesis could be related to a C-terminus degradation of IscR, also observed by SDS-PAGE. In case a C-terminus degradation

did not prevent DNA binding, it would be possible that the bottom band could correspond to IscR that suffered C-terminus degradation bound to DNA and thus possesses a lower mass, as well as the fact that IscR's C-terminus contains several positively charged amino acids. Their removal would lower the protein's net charge leading to a faster migration.

To study whether the different bands were related to different complexes the ratio IscR/DNA was varied and further EMSA assays were performed. In the EMSA assay, shown in Figure 23, an IscR excess in comparison to DNA was tested. DNA (25 pmol) was incubated with 0-900 pmol IscR dimer. The gel was first observed in the fluorescence imager for DNA visualization and then stained with Coomassie Blue for protein visualization. In this gel, it is possible to see a similar behavior to the gel depicted in Figure 22, which is the presence of two bands and a smear above them, up to around 420 pmol of protein, a ratio IscR dimer to DNA of 17. It is interesting to note that, when compared to MetK, these bands show a higher mobility. However, above 420 pmol IscR, the mobility of these smears decreases, and the IscR-DNA complex starts to migrate slower than MetK. Interestingly, this migration pattern is similar to what was observed for IscR initially, but in the left gel (DNA visualization) it is clear that DNA also migrated less than it did without protein and that it sits precisely where the protein is (right gel). This could be a combination of the decrease in the total negative charges of the sample, due to the high amount of protein when compared to DNA and could also indicate that IscR could possibly create larger complexes with DNA.

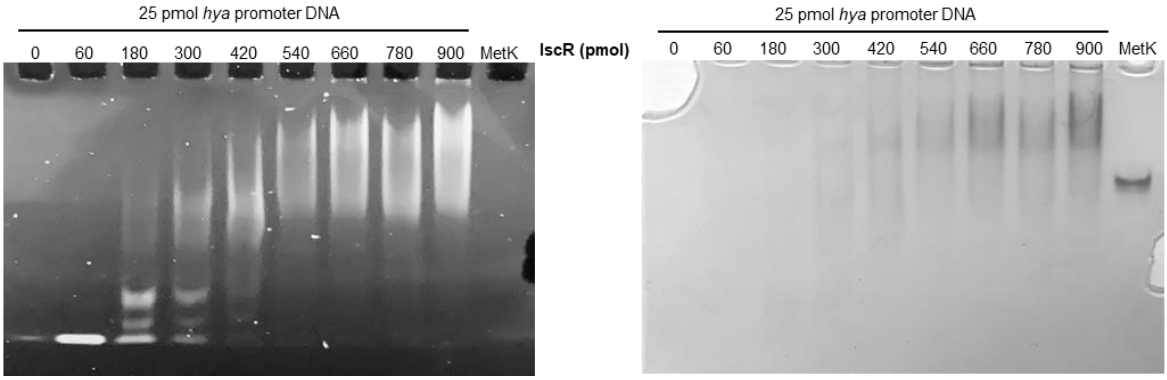

Figure 23. EMSA assay of IscR-*hya* promoter binding profile at different DNA/protein ratios (0 to 36 fold). The gel on the left observed with a fluorescence DNA imager while the gel on the right was stained with Coomassie Blue for protein observation.

Two other gels were run with lower ratios for IscR/DNA. The DNA fluorescence image is shown in Figure 24. As expected, at lower protein/DNA ratios no clear complex formation is observed. However, it is interesting to note that the optimum ratio for the formation of discrete bands is an interval from a 1:1 to 5:1 IscR dimer to DNA. This result is similar to the described by Nesbit and coworkers[176] and shows that partially holo wild type IscR indeed binds to the *hya* promoter construct prepared here. However, it is not clear whether the binding was preferential for holo, semi-holo or apo IscR since the protein obtained was never fully occupied with cluster.

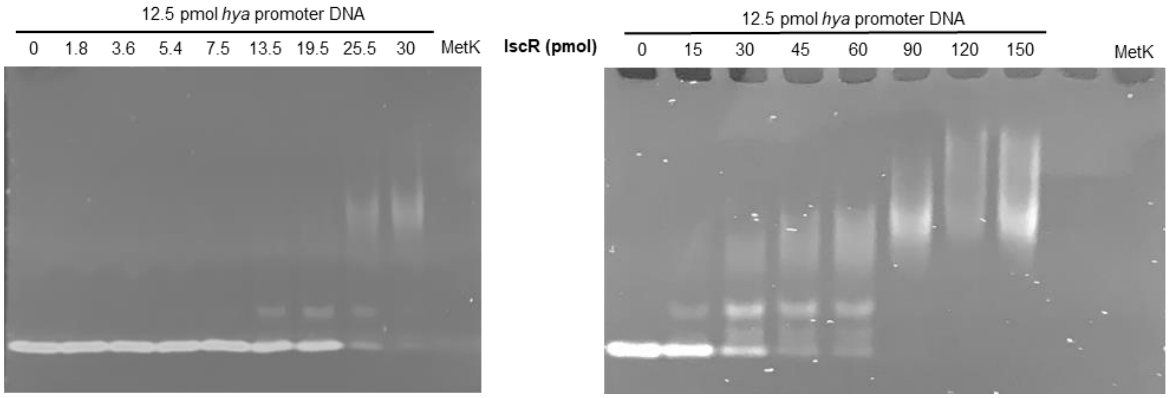

Figure 24. EMSA assay of IscR-*hya* promoter binding at different DNA/protein ratios (0 to 12 fold). Both images, left and right, were taken under UV irradiation, visualizing DNA by Gel-red fluorescence.

To finalize the EMSA assays for IscR wild type, the binding of IscR to *iscrb*, a Type 1 promoter, was assessed by EMSA. Gels were run to determine the optimal ratio of protein to DNA as done for the Type 2 DNA promoter. The binding of partially occupied IscR to *iscrb*, can be seen in Figure 25. For *iscrb*, protein binding could also be observed, however, it lacked the two bands observed in the previous EMSA assays with the *hya* promoter, showing only the smear in the middle of the gel, also present in the previous experiments. In this gel, DNA binding by IscR is detectable above a ratio of 2:1 IscR to DNA. Because apo IscR should not bind *iscrb*, this raises the question of whether in the previous gels the bands corresponded to apo IscR present in the preparation and the smear corresponded to holo or semi-holo IscR.

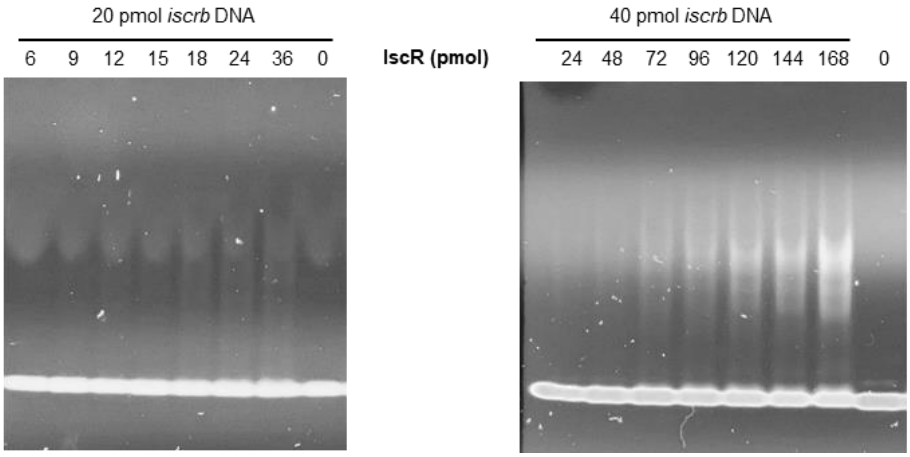

Figure 25. EMSA assay of IscR-*iscrb* promoter binding profile at different protein/DNA ratios(0 to 4.2 fold). Both images, left and right, were taken under fluorescent light for DNA visualization only.

2.4. Circular Dichroism spectroscopy

CD spectroscopy was used here to determine IscR's secondary structure and to determine the protein's melting temperature. More extensively CD spectroscopy was applied to determine the cluster stability as a function of temperature and to determine pK_a values.

2.4.1. UV CD spectroscopy: detecting elements of secondary structure

The far UV spectra of IscR for the study of protein secondary structure at different pH values, represented in Figure 26, were recorded between 195 and 280 nm. However, due to buffer interference below 205 nm the spectra are shown and analyzed only between 205 to 280 nm.

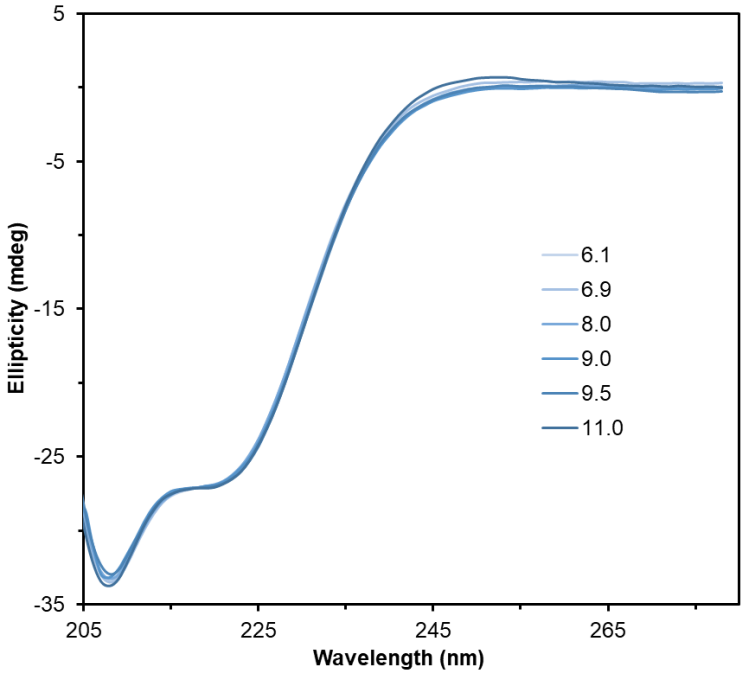

Figure 26. Far UV CD spectra of holo IscR at several pH values.

Two minima can be observed in the CD spectra at 208 nm and approximately 220 nm, characteristic of α-helices[135], which agrees with the crystal structure obtained by Rajagopalan and coworkers[70]. In IscR's crystal structure, only two short β-sheets are observed, and seven α-helices compose most of the protein's secondary structure. The secondary structure of IscR based on CD spectroscopy did not change in the pH range between 6 and 11.

A protein titration with an *iscrb* DNA fragment was a second experiment performed by far UV CD spectroscopy. In this experiment, a total of 24 μM of *iscrb* Type 1 DNA was slowly titrated (2 μM steps) into 13 μM of IscR dimer. A spectrum was recorded after each DNA addition to assess possible changes in secondary structure elements. The CD spectra and the correlation between the ellipticities and DNA volume is shown in Figure 27.

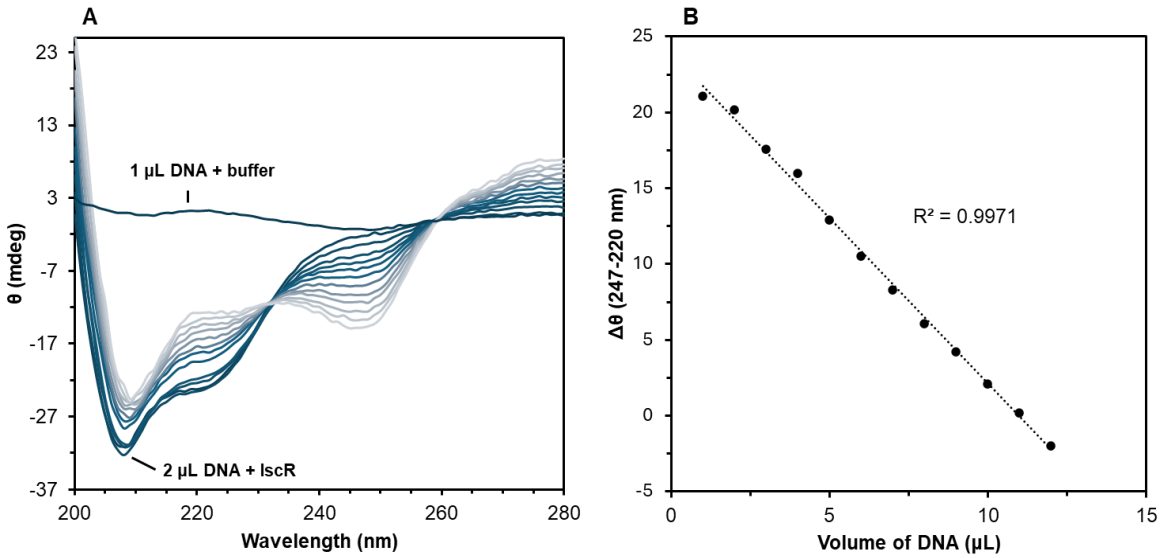

Figure 27. Far UV CD spectroscopy of holo IscR with upon step addition of *iscrb* DNA Type 1 promotor. (A) CD spectra of IscR plus *iscrb*, smaller volumes of *iscrb* are represented in dark blue and higher volumes in light blue. (B) Difference in ellipticities between 247 and 220 nm versus DNA volume. Experimental data were fitted with a linear regression.

Due to the strong contribution of double stranded DNA in the UV region to the CD spectrum, major changes in the spectra were observed upon the stepwise additions of DNA. The effect of DNA was then determined by the difference of the ellipticity at 247 nm minus the ellipticity at 220 nm versus the volume of DNA. It does not appear that secondary structure changes occur in IscR upon DNA addition as a linear change is seen in Figure 27, panel B. A linear relation between the DNA volume and the ellipticity difference is anticipated in case the changes were caused by DNA absorption only. Contrarily, a more complex pattern would emerge as the sum of a linear contribution from DNA, changes from bending of DNA upon IscR binding and a non-linear contribution from IscR secondary structural changes. This behavior can be explained by a lack of interaction between DNA and protein leading to spectra that correspond to the sum of both individual components in solution, or more likely that DNA binding by the protein does not cause sufficient structural changes to be detected by CD spectroscopy.

It is quite interesting to note that a minor change could have taken place at low concentrations of DNA and high relative concentrations of protein, namely in the sample with 2 µL of DNA (4 µM) as this is the only sample that presents a slight increase in ellipticity at 208 nm upon DNA addition. Comparing the results obtained by CD with those obtained by EMSA, the hypothetical formation of a protein-DNA complex seen by CD spectroscopy would have happened at a ratio of 3.2: 1 protein to DNA, whereas by EMSA it reached its peak at about 4.2:1 protein to DNA. With the decrease of the ratio protein to DNA by EMSA no complexes were observed, whereas by CD the contribution of DNA itself appears to be the dominant factor for the changes observed in the CD spectra.

2.4.2. Visible CD spectroscopy: detecting cluster properties

To corroborate the pK_a determination by UV-Vis spectroscopy CD spectroscopy in the visible region was applied. In such experiments, as for UV-Vis, a shift in peaks was expected upon pH change due to variations around the chiral cluster environment. These changes around the cluster lead to variations in the energy necessary for the electronic transitions to occur. This experiment was performed both for the as isolated, mainly oxidized, and for the dithionite reduced protein.

For the protein as isolated, the resulting CD spectra as a function of pH and the derived fits to the Henderson-Hasselbalch equation for a single deprotonation step and are represented in Figure 28. IscR's CD spectra in the visible range show similarities with those described in literature for Rieske[191] and MitoNEET[137], although they do not entirely match. IscR's CD spectra present two minima (371 and 560 nm) and four maxima (316, 456, 519 and 615 nm). At higher pH values, a decrease in peak intensity and a mild shift in the wavelength of the maxima at 316 to 313 nm and at 615 to 605 nm is observed (Figure 28, Panel A). Initially, the decrease in intensity associated with the increase in pH was thought to be related to cluster breakdown. However, as done for UV-Vis, each sample was prepared individually under the same conditions. Additionally, six 3-minute scans were recorded for each sample to assess spectral changes within the same sample and thus infer the stability of that sample over time, at a specific pH value. The six scans recorded did not show any significant decrease in ellipticity with time indicating that cluster breakdown was not playing a role in this experiment and that any decrease in signal intensity could be attributed to protonation/deprotonation at different pH values.

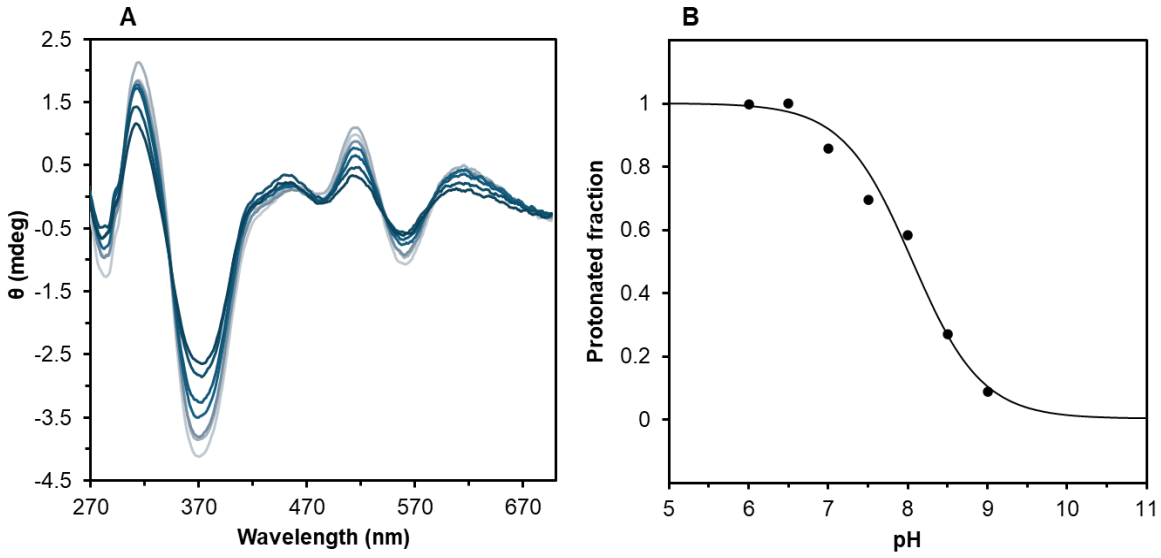

Figure 28. CD visible pH titration of the as isolated holo IscR. (A) CD spectra of holo IscR (first spectrum from six recorded) at different pH values between 6 (light blue) and 9 (dark blue). (B) Variation of protonated fraction with pH value.

For the determination of the pK_a in the as isolated state, presumably oxidized, the wavelengths 316 and 371 were chosen. The ellipticity at 371 was subtracted from the ones at 316 nm and plotted as a

function of the pH value. From this plot, the pK_a was estimated to be 8.1. This value is very similar to the average pK_a in the as isolated state obtained by UV-Vis (pK_a = 8.3), or the first pK_a value (7.9), if a fit for two pK_a values is used.

Along the same line IscR reduced with sodium dithionite under anaerobic conditions at various pH value was subjected to CD spectroscopy. The resulting spectra and pK_a determination can be found in Figure 29. Spectra were recorded between 340 and 700 nm due to the high absorption of sodium dithionite below 340 nm.

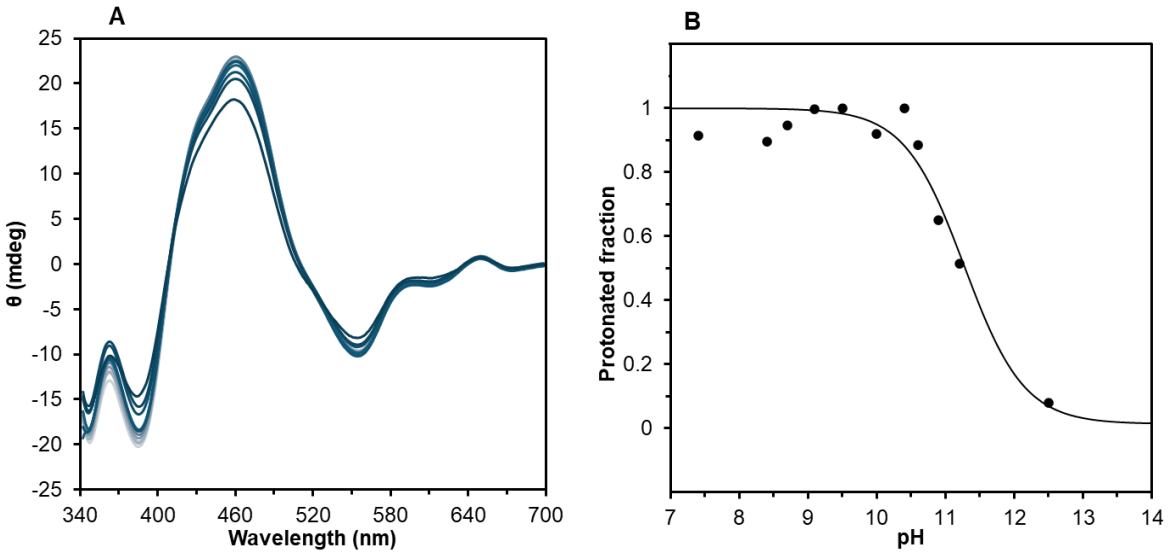

Figure 29. CD visible pH titration of the reduced holo IscR. (A) CD spectra of holo IscR (first spectrum from six recorded) at different pH values between 7.4 (light blue) and 12.5 (dark blue). (B) Variation of protonated fraction with pH value.

In the reduced state, holo IscR presents three minima (347, 385 and 556 nm) and two maxima (461 and 652 nm). Little information is available in literature on CD spectroscopy for reduced non-cysteinyl coordinated [2Fe-2S] clusters. Amazingly, the CD signal of reduced IscR is very intense in opposition to the decreased absorbance observed for protein in the reduced state by UV-Vis spectroscopy. Even though protein concentration was higher in the reduced state (*ca.* 3.4 fold when compared to the oxidized sample), signal intensity was around seven-fold higher in the reduced state. Similar to the as isolated protein, at higher pH values a decrease in ellipticity is observed. Again, six 3-minute scans were recorded to demonstrate that the reduced cluster was stable, and breakdown was not responsible for the decrease in ellipticity. It is clear that in the as isolated state intensity changes started at lower pH whereas in the reduced state the major decrease of intensity started above pH 10. This could be an indication that spectral intensity decreases could indeed be related to deprotonation effects. However, in sample pH 12.5, contrarily to the observed for all the other samples, a signal intensity decrease was observed with time. In six three-minutes scans the ellipticity decreased from 17 to 14.5 mdeg at the maximum 461 nm. Assuming complete cluster breakdown would correspond to 0 mdeg, this would indicate a 15% cluster breakdown in around 15 minutes.

Contrarily to the as isolated state, no significant peak shifts were observed for the titration in the reduced state. Due to sample preparation by dilution in buffer at a different pH value, other samples at pH values could not be prepared as sample at pH 12.5 was prepared by dilution in buffer pH 13. For the determination of the pK_a in the reduced state, the ellipticity at 527 nm was subtracted from the ellipticity values at 461 nm and plotted versus the corresponding pH value. From this plot, the pK_a was estimated to be 11.3, which is deemed to be less reliable than the pK_a of the oxidized cluster due to the onset of cluster breakdown. This value is similar to the pK_a values in the reduced state for non-cysteinyl coordinated [2Fe-2S] clusters, such as the Rieske[60], Apd1[63] and mitoNEET[51] proteins.

Additionally, cluster stability in the reduced state as a function of time was assessed with CD spectroscopy at two different temperatures, 20 and 37 ºC. These temperatures were chosen to mimic the *in vitro* and *in vivo* temperatures, respectively. The experiment was performed by recording forty 3-minute scans between 340 and 700 nm. Figure 30 shows the spectral data for reduced holo IscR

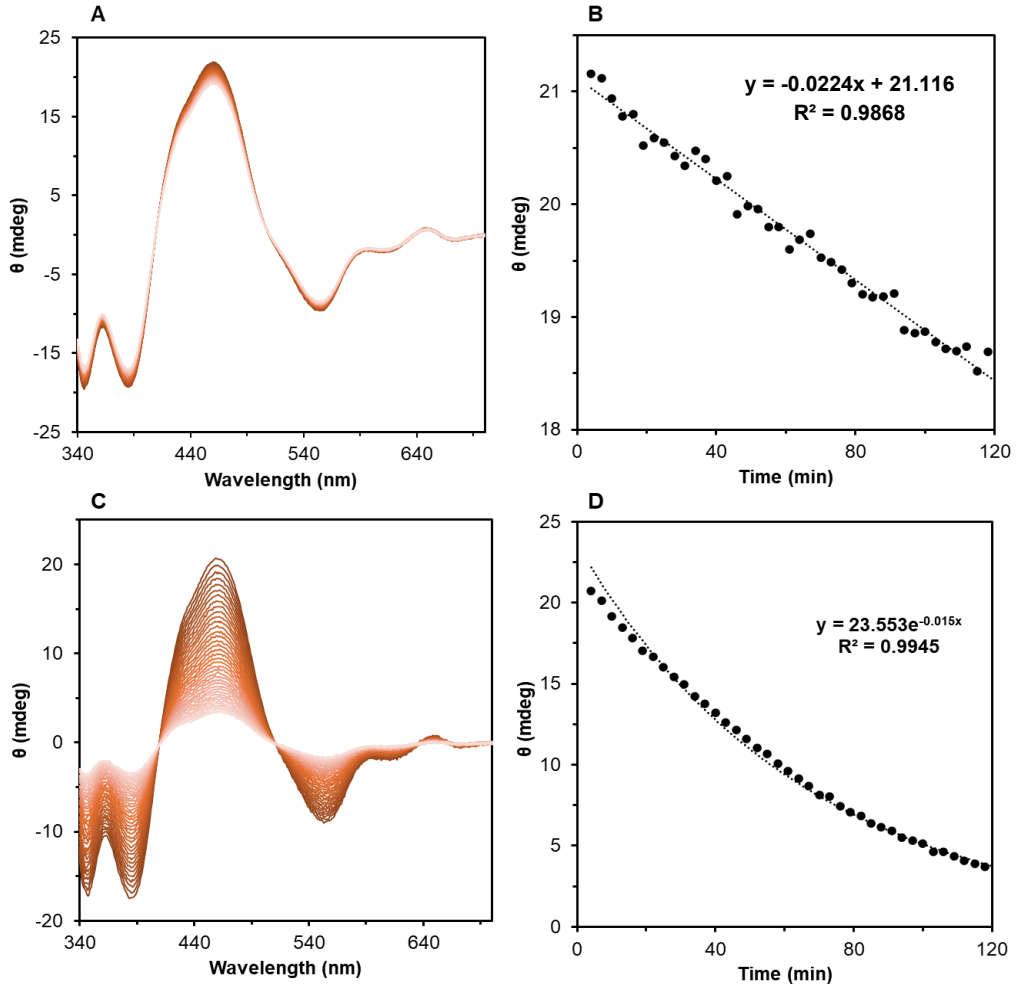

Figure 30. Reduced holo IscR CD Visible spectra at different times, and at two different temperatures. (A) CD spectra at 20 ºC, 40 3-minute scans; (B) Cluster breakdown determination at 20 ºC; (C) CD spectra at 37 ºC, 40 3-minute scans; (D) Cluster breakdown determination at 37 ºC. Data were recorded between 4 (dark orange) and 121 min (light orange). All times were corrected by 4 minutes to account for sample preparation.

over time (Panel A) and the difference between the ellipticities at 460 and 507 nm plotted as function of incubation time at 20 ºC to calculate the cluster breakdown rate (Panel B). In Panels C and D, the same analysis was repeated for reduced holo IscR at 37 ºC.

In this experiment, it is interesting to note the different behavior the samples present. The initial ellipticity is roughly the same for both samples, at 20 and 37 ºC, however, cluster breakdown seems to occur by different processes. At 20 ºC cluster breakdown proceeds in a linear manner, with a large dispersion between the data points. The data were fitted with a linear regression with a slope of -0.0224 mdeg per minute, corresponding to cluster loss of 1% per minute. This could also represent the early part of an exponential breakdown, which would require experiments with longer measurement time. At 37 ºC the decrease of ellipticity does not seem to follow a linear pattern, instead it seems that an exponential equation is the best fit to the experimental curve.

This behavior indicates that the cluster breakdown mechanism is influenced by temperature in a complex way. At lower temperatures it appears to be slow, while at 37 ºC the half-life of approximately 45 minutes could play a physiological role.

2.5. Continuous-wave EPR spectroscopy

Electron paramagnetic resonance was used to determine the cluster's redox potential, the pH dependency thereof and the pK_a of the reduced IscR at alkaline pH. Additionally, EPR spectra of IscR were recorded with DNA to assess whether DNA binding would affect the properties of the cluster and to study the deprotonation process of the histidine ligand. Pulsed EPR Davies and Mims ENDOR as well as HYSCORE were measured to try and resolve the hyperfine interactions between the coordinating nitrogen atom and protons in the vicinity of the cluster, including the proton at the non-coordinating nitrogen atom. X-Band and Q-Band were measured to identify spectral features that would give insights on the type of cluster present in IscR. The X and Q- Band EPR spectra are shown in Figure 31.

The EPR spectra of reduced IscR shows a rhombic shape, typically found in $[2Fe\text{-}2S]^{1+}$ clusters. *g*-values were determined to be 1.980, 1.930 and 1.872. These values are characteristic of a [2Fe-2S] cluster in which one of the iron atoms is in the ferric (Fe^{3+}, S= 5/2, oxidized) and the other is in the ferrous state (Fe^{2+}, S= 2, reduced). The iron atoms are antiferromagnetically coupled resulting in a total spin (S) of 1/2. The cluster's asymmetric structure combined with spin-orbit coupling lead to an unequal distribution of electron density resulting in three different *g*-values. These values agree with the previous data published on IscR (g= 1.99, 1.93 and 1.88)[69] and on the MitoNEET [2Fe-2S] cluster with 3Cys/1His coordination (g= 2.005,1.937, 1.895)[192]. Even though the *g*-values are similar, IscR's cluster is the only reported so far that presents all three *g*-values below 2.

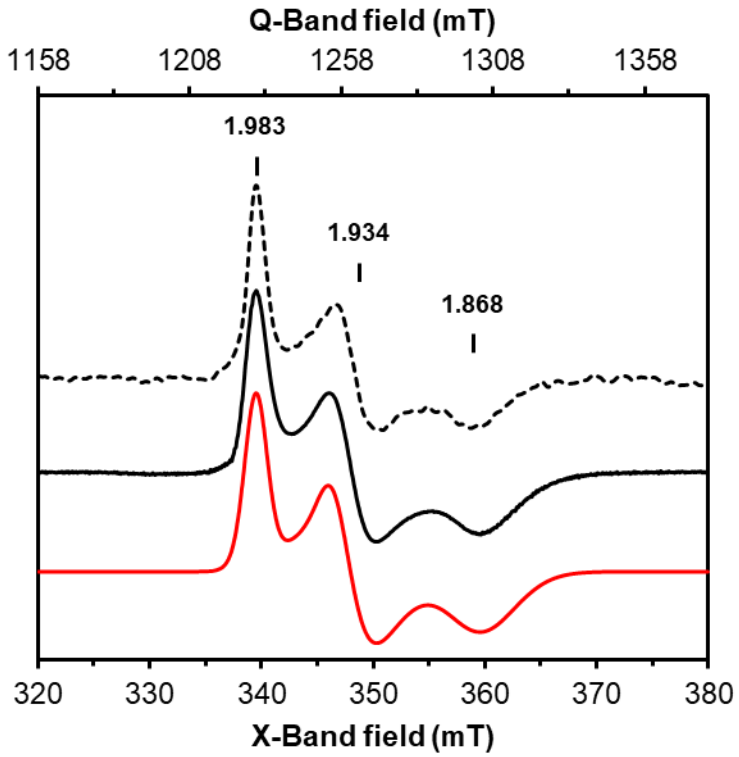

Figure 31. X-(black full) and Q-Band (black dashed) EPR spectra of dithionite reduced IscR with the *g*-values determined for this cluster. A spectral simulation carried out with GeeStrain5 is shown in red. EPR conditions – Microwave frequency: 9.43 GHz, T: 77K (X-Band); microwave frequency: 34.12 GHz; T: 20 K (Q-Band). Microwave power: 2 mW, modulation amplitude: 10 G, modulation frequency: 100 kHz. Simulation parameters: *g*-values: 1.983, 1.934 and 1.868; Residual broadenings (w-0): 0.0065; Linewidth (W): 0.0016 (xx), 0.0100 (yy) and 0.0000 (zz); *g*-strain (w): 0.000 (xy), 0.010 (xz) and 0.009 (yz).

2.5.1. pK_a determination in the reduced state

After establishing optimal conditions for EPR spectroscopy, a pH titration was carried out. In this titration, several IscR samples at different pH values were prepared and reduced with excess sodium dithionite (2 mM) at a protein concentration of 275 µM IscR dimer. IscR spectra at different pH values is shown in Figure 32.

In these spectra, recorded between pH 6.5 and 12.9 it is possible to observe the subtle changes in spectral shape. Below pH 9, the spectral shape is invariant and identical to the one shown in Figure 31. Between pH 9 and pH 12, even though the *g*-values are unchanged, it is possible to observe the broadening of the third *g*-value (at high field). This could be indicative of mild changes in the environment surrounding the cluster. Above pH 11 it is possible to see clearer changes in the second and third *g*-values as they converge with an increase of the pH, indicating that a change in rhombicity is occurring. This most prominent change is attributed to the deprotonation of the histidine ligand, as this would likely invoke the strongest structural and electronic change of the cluster. The decrease of

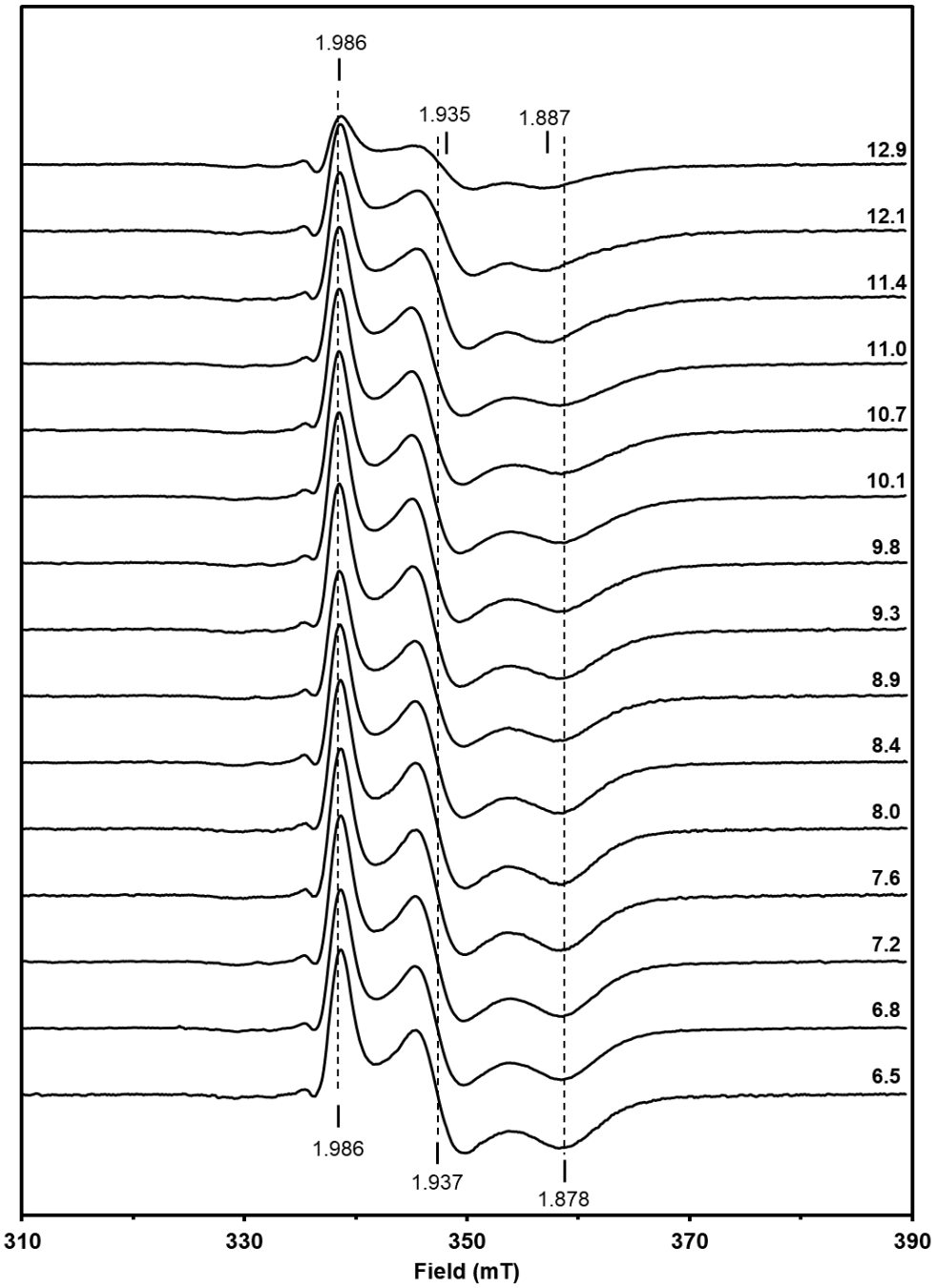

Figure 32. X-Band EPR spectra of reduced IscR at different pH values. Frequency: 9.41 GHz, 77 K, microwave power: 2 mW, modulation amplitude: 10 G, modulation frequency: 100 kHz.

signal amplitude was attributed to cluster breakdown at extreme pH values during sample preparation as showed by the double integral as a function of pH shown in Figure 33.

The determination of a pK_a in the reduced state based on the EPR spectra was done by analysis of the g_y zero crossing. For this purpose, a linear regression between the field and the amplitude of

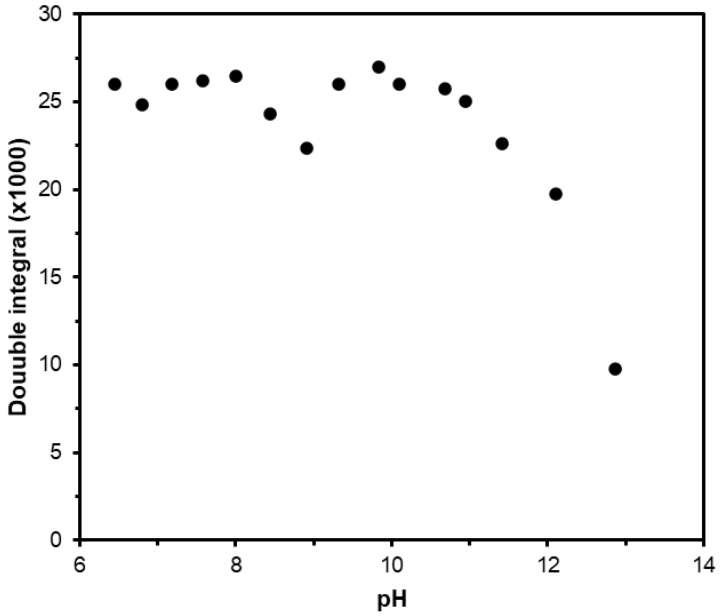

Figure 33. Double integral of the EPR spectra of wild type IscR calculated between 300 and 800 G.

seven data points around the zero crossing of each spectrum was calculated. The field at which the amplitude was zero was calculated from the equation and the exact *g* value at that point was calculated for each pH value using the field, previously calculated, and the microwave frequency. The calculated *g*-values were then plotted against the pH value and are shown as experimental data in Figure 34.

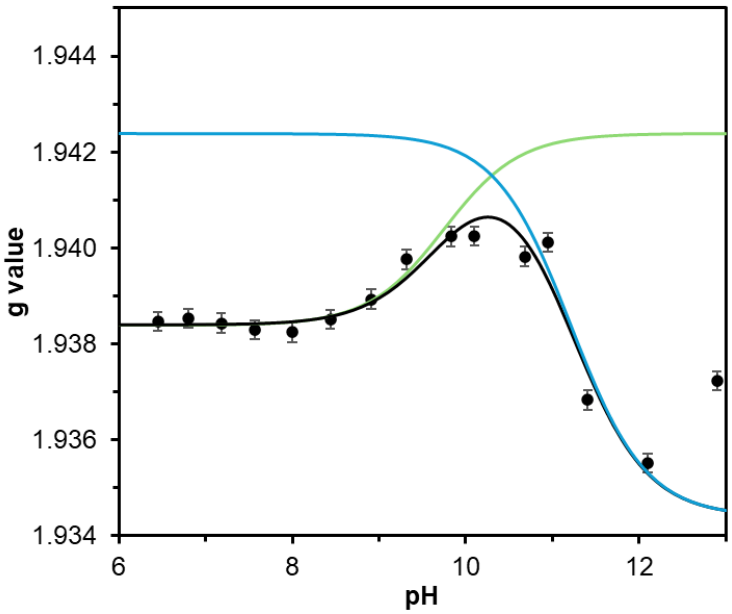

Figure 34. Histidine pK_a determination in the reduced state. The sum of the fits is shown in black, and its components are shown in green (pK_a=9.7) and blue (pK_a=11.2).

Surprisingly, two pK_a values could be determined. The first, fitted as 9.7, plays a role up to approximately pH 10 and leads to a ~0.002 shift towards higher *g*-values. This value agrees with the second pK_a determined by UV-Vis in the oxidized state (pK_a ~9.1) and indicates that there might be a protonable group that is spatially close enough to the cluster to influence its spectral properties, but that has a pK_a that is independent from the redox state of the cluster since it is not a ligand. The second, fitted as 11.2, starts to play a role above pH 10. It appears that the first pK_a of 9.7 could correspond to the same species observed by UV-Vis (pK_a=9.1) that is independent of, or perhaps less affected by, the oxidation state of the cluster. The second pK_a of 11.2 associated with a much larger downward shift of g_y of 0.008 is more likely related to the histidine deprotonation when the cluster is in the reduced state. This value is also compatible with the value determined by CD (Figure 29) and with literature data obtained for Rieske[60], Apd1[63] and MitoNEET proteins[51], but contrary to the pK_a determined by Fleischacker and coworkers[71] of approximately 7.2. It is also worth noting that the last experimental point seems to not fit the curve, which can possibly be explained by the onset of cluster breakdown at this pH value. For better visualization, Figure 35 shows the direct comparison between reduced IscR at pH 8.0 and pH 12.1 in which the *g*-value shift and signal broadening are easier to observe.

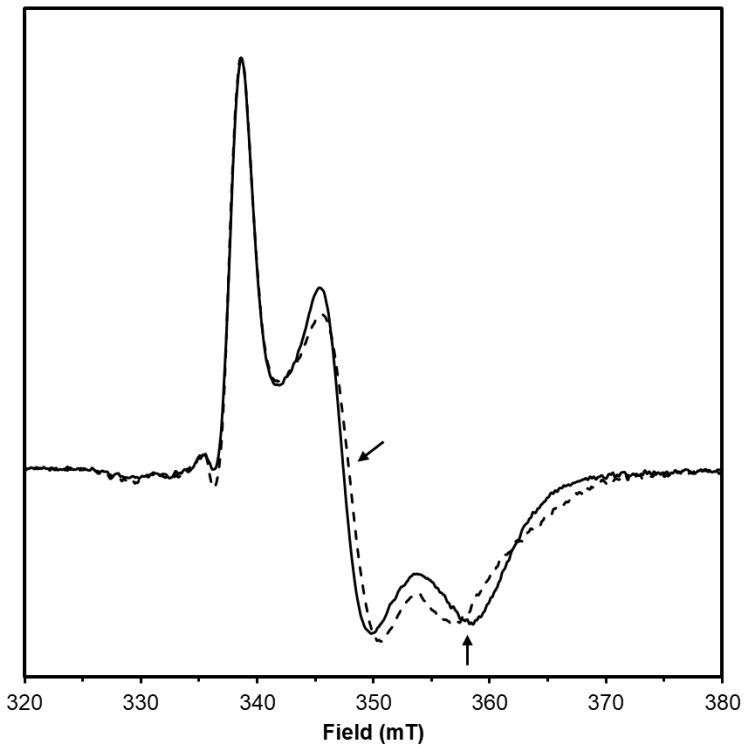

Figure 35. X-Band EPR spectra reduced IscR at pH 8.0 (full) and pH 12.1 (dashed). Frequency: 9.41 GHz, 77 K, microwave power: 2 mW, modulation amplitude: 10 G, modulation frequency: 100 kHz.

2.5.2. Redox potential determination at different pH values

An important aspect of the biophysical studies on IscR was to uncover whether the observed pK_{ox} and pK_{red} values for the cluster indeed relate to a proton-coupled electron transfer process of the [2Fe-2S], as thus far has only been observed in the MitoNEET, Rieske and Apd1 proteins.

Currently, no information is available on the redox midpoint potential of the $[2Fe\text{-}2S]^{1+/2+}$ cluster of IscR, possibly because the partial occupancy and the inherent instability posed a challenge for experimentalists. But, with knowledge on the stability of IscR and the efficient production of large quantities of IscR the redox potential of IscR through redox titrations, at variable pH values, could be determined. Due to its characteristic conversion between an EPR silent *S*=0 species, Fe^{3+}/Fe^{3+} in the oxidized state, to an EPR active *S*=1/2 species in the Fe^{2+}/Fe^{3+}reduced state, this transition could very conveniently be used to evaluate the cluster's redox potential. The midpoint potential of the cluster corresponds to the redox potential at which EPR signal intensity is 50%. Redox mediators (40 µM each) were used in all titrations to facilitate electron transfer, stabilize the solution potential, and to give a stable reading of the combination electrode. Figures 36 and 37 show the mediated EPR monitored redox titrations for determination of the redox potential of IscR between pH 6.0 and pH 11.0. All redox potentials referred to in this thesis are versus the S.H.E.

In the titrations at pH 11 and 11.5, not enough data points could be obtained below what was estimated to be 50% reduction. Due to the extensive time of approximately 60-90 minutes necessary to perform a redox titration, no titrations could be done above pH 11.5, since cluster breakdown and reduction/oxidation processes become intermingled towards the end of titrations.

The midpoint potentials obtained appeared to demonstrate a redox potential dependence on the pH value. At the lowest pH measured (pH 6) the midpoint potential obtained was -38 mV vs. H_2/H^+, whereas at the highest pH value, pH 11.5, the estimation was -215 mV. The midpoint potential difference between pH values below the pK_{ox} and above the estimated pK_{red} is very comparable with that reported by Zuris and coworkers in 2010 for MitoNEET[51] (approximately +40 mV at pH 6, and -150 mV at pH 11). The data strongly indicate that in IscR proton-coupled electron transfer occurs, though a function related to DNA binding is not obvious. A summary of the midpoint potentials obtained for each pH value is shown in Table 24.

Due to the occurrence of further reduction below -200 mV, observed in various redox titrations at pH 8 and above (Figure 36 and 37, red data points, except for pH 11.5), two dedicated ten point redox titrations were carried out at pH 8. These titrations, performed as the previous ones, were carried out with the same batch of protein and the same mediator mix, with a 50 mV interval. The double integral of each spectrum was calculated and plotted as a function of the redox potential (Figure 38). In this experiment two very well defined transitions were observed: the first reduction, corresponding to 64% of the EPR-active species, shows a midpoint potential of -67 mV consistent with that observed for

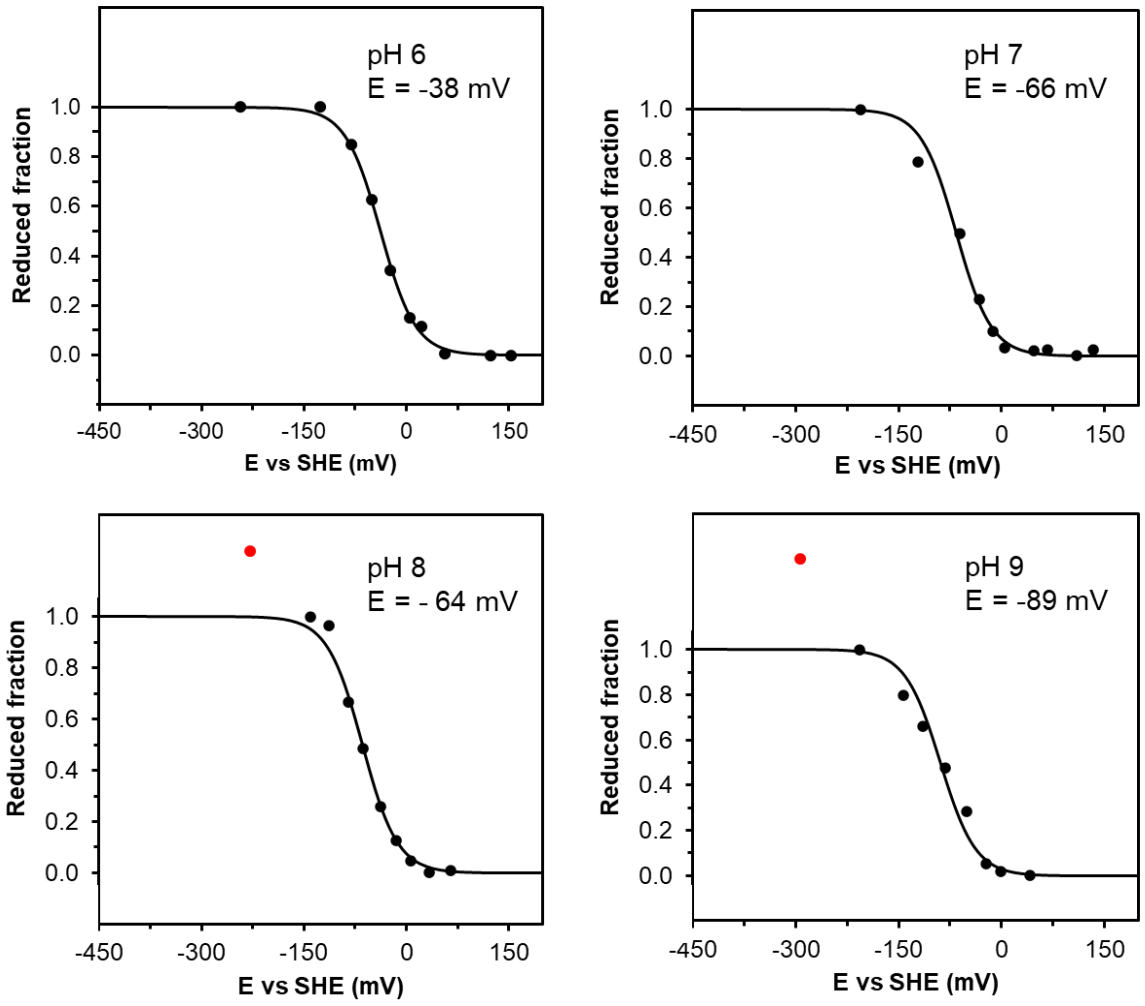

Figure 36. Determination of the midpoint potential of the $[2Fe\text{-}2S]^{2+/1+}$ cluster of IscR at pH 6, 7, 8 and 9. EPR amplitude (max-min at g_y) data were normalized between zero and one.

IscR at pH 8 in the previous experiment; the second reduction, corresponding to 36% of the EPR-active species, shows a midpoint potential of -245 mV. The first transition appears to fully agree with the high potentials previously reported for [2Fe-2S] clusters with histidinyl coordination. Literature on [2Fe-2S] clusters coordinated by histidine residues report midpoint potentials of +25 mV for MitoNEET[51], -164 mV for Apd1[63], -150 mV for Rieske dioxygenases[60,193], and +300 mV for cytochrome bc_1/b_6f Rieske clusters[60,193]. However, the second potential obtained here is lower than the reported in literature for similar coordination. The experimental data represented in red in Figure 38 were outliers (like in Figure 37, pH 11.5), possibly deriving from cluster breakdown.

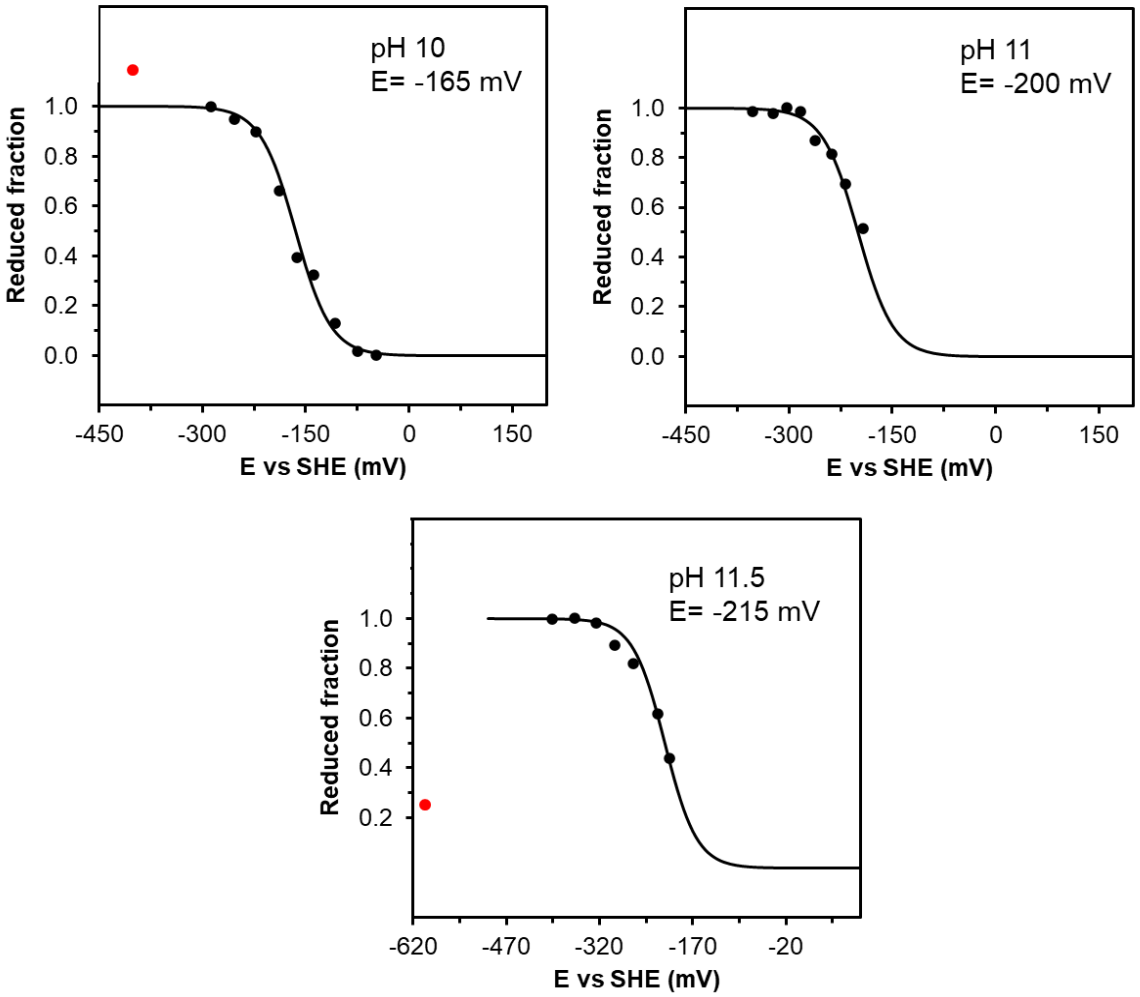

Figure 37. Determination of the midpoint potential of the $[2Fe\text{-}2S]^{2+/1+}$ cluster of IscR at pH 10, 11 and 11.5. EPR amplitude (max-min at g_y) data were normalized between zero and one. The red data point in the titration pH 11.5 presumably relates to cluster breakdown.

Table 24. Midpoint potentials (duplicates) determined by dye-mediated redox titrations at several pH values.

pH	Experiment 1 Midpoint potential (mV)	Experiment 2 Midpoint potential (mV)
6.0	-43	-38
7.0	-59	-66
8.0	-66	-64
9.0	-100	-89
10.0	-168	-177
11.0	-200	-193
11.5	-215	-

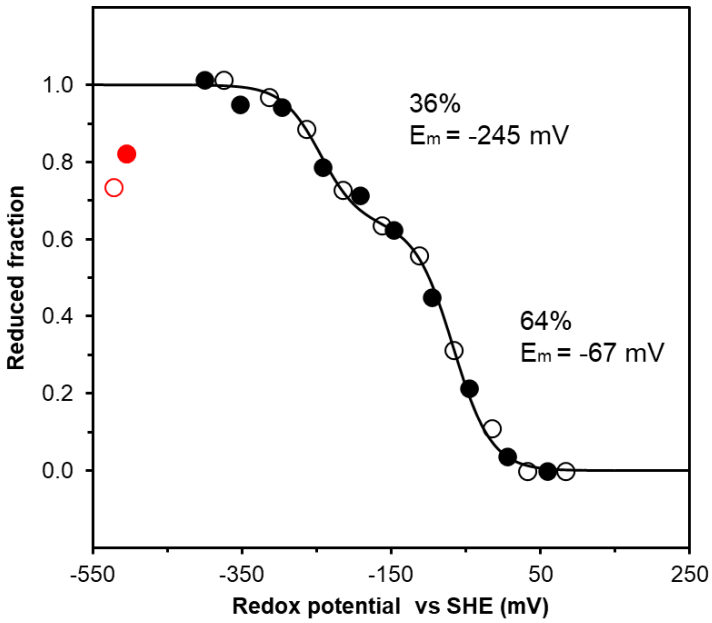

Figure 38. Dye-mediated redox titrations of holo IscR at pH 8. Full and empty circles represent different titrations performed under the same conditions. Data points correspond to spectra double integral corrected among titrations with a factor of 0.87. Red experimental points were considered outliers and not accounted for in the fit.

Two hypotheses were raised to explain this behavior. The first hypothesis was that each midpoint potential corresponded to one cluster in a bis-holo IscR dimer. However, as bis-holo IscR is, presumably, a symmetric homodimer with equivalent cluster environment, the midpoint potentials should necessarily be the same. Since different potentials can only occur if the clusters' environments were not identical, protein conformational changes would be necessary. However, such differences in midpoint potentials would require significant structural changes. The second hypothesis was that the first redox potential (-67 mV) could correspond to an IscR dimer containing a single [2Fe-2S] cluster and that the second redox potential (-245 mV) corresponds to both clusters of a symmetrical bis-holo IscR dimer.

Another important question was whether the IscR's midpoint potential changes upon DNA binding. For this purpose, a single titration in the presence of *iscrb* Type 1 DNA promoter was carried out at pH 8. The excessive costs of µmol quantities of synthetic oligonucleotides prevented multiple experiments. EPR spectra corresponding to the titration and the determination of the midpoint potential are shown in Figure 39.

From this titration it can be concluded that DNA binding does not exert a major change of the midpoint potential of IscR. The potential obtained was -88 mV at pH 8, compared with -66 mV at pH 8 in the absence of DNA. The difference between these values (22 mV) is two-fold larger than the biggest

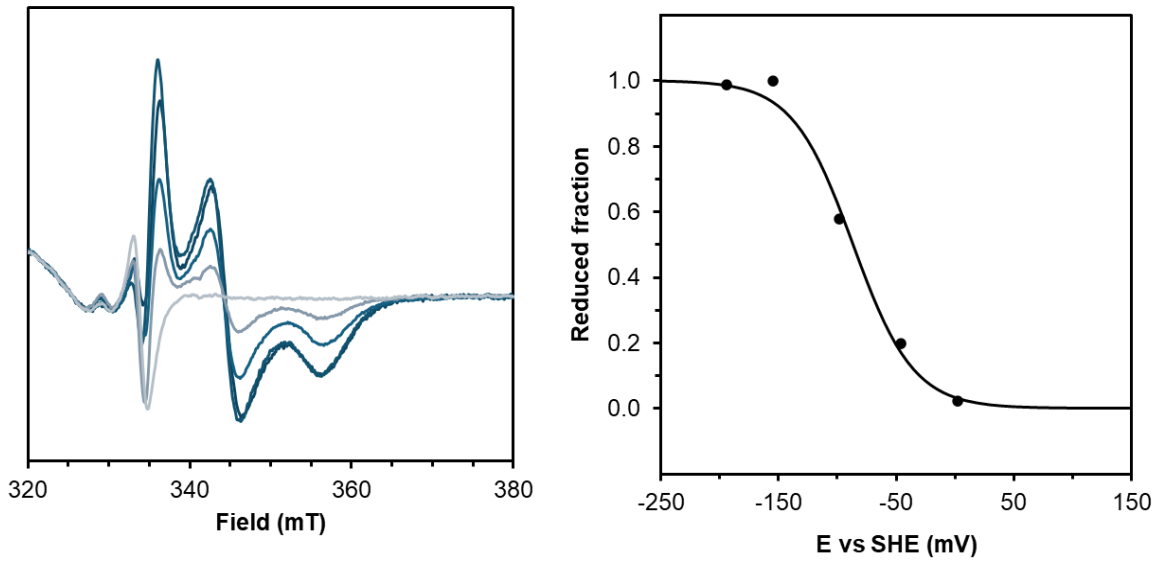

Figure 39. Midpoint potential determination of IscR in the presence of *iscrB* Type 1 DNA promoter. EPR conditions: Frequency: 9.35 GHz, T: 20 K, microwave power: 2 mW, modulation amplitude: 10 G, modulation frequency: 100 kHz.

difference between duplicates (Table 24). The similarity between redox potentials, with and without DNA, seems to indicate that changes around the cluster upon DNA binding are not pronounced enough to drastically change its redox potential, possibly due to the distance between the DNA binding region and the cluster.

Cluster stability was also assessed by EPR spectroscopy and is represented in Figure 40. Initially, sodium dithionite reduced and air oxidized samples were prepared under mild stirring. Their cluster integrity was assessed after 0 min, 30 min, 2 hours, 6 hours and 24 hours incubation. Upon measurement of their EPR spectra it was clear that, like most FeS clusters, IscR's cluster is also oxygen sensitive. It was observed that in an anaerobic environment in the reduced state at pH 8 under stirring IscR's cluster is quite stable showing slightly less than 50% of cluster content after 24 hours at room temperature. Air-oxidized IscR however, did not show such stability, losing over 90% of its cluster content upon aerobic incubation at room temperature for 30 minutes.

A question was then raised whether the lack of stability of the cluster in the oxidized state would be related to exposure to air (particularly its 21 % O_2) or if it would be related to the oxidized state of the cluster. Therefore, an experiment was carried out in which three samples of protein oxidized with ferricyanide under anaerobic conditions were prepared. These samples were collected under the same conditions as the previously mentioned. Protein from the same batch was sufficient for preparation of samples at 0 min, 30 min and 2 hours. From these samples it was possible to observe that, even though the rate of cluster breakdown is more pronounced than that observed for the reduced state, it is much lower than for the "air-oxidized" samples. After 2 hours the cluster content reached 50%, indicating that IscR's cluster can indeed survive for a significant amount of time in the

oxidized state, but only under anaerobic conditions. This indicates that a combination of both factors, the redox state and the presence of oxygen (in air) play a role in cluster breakdown.

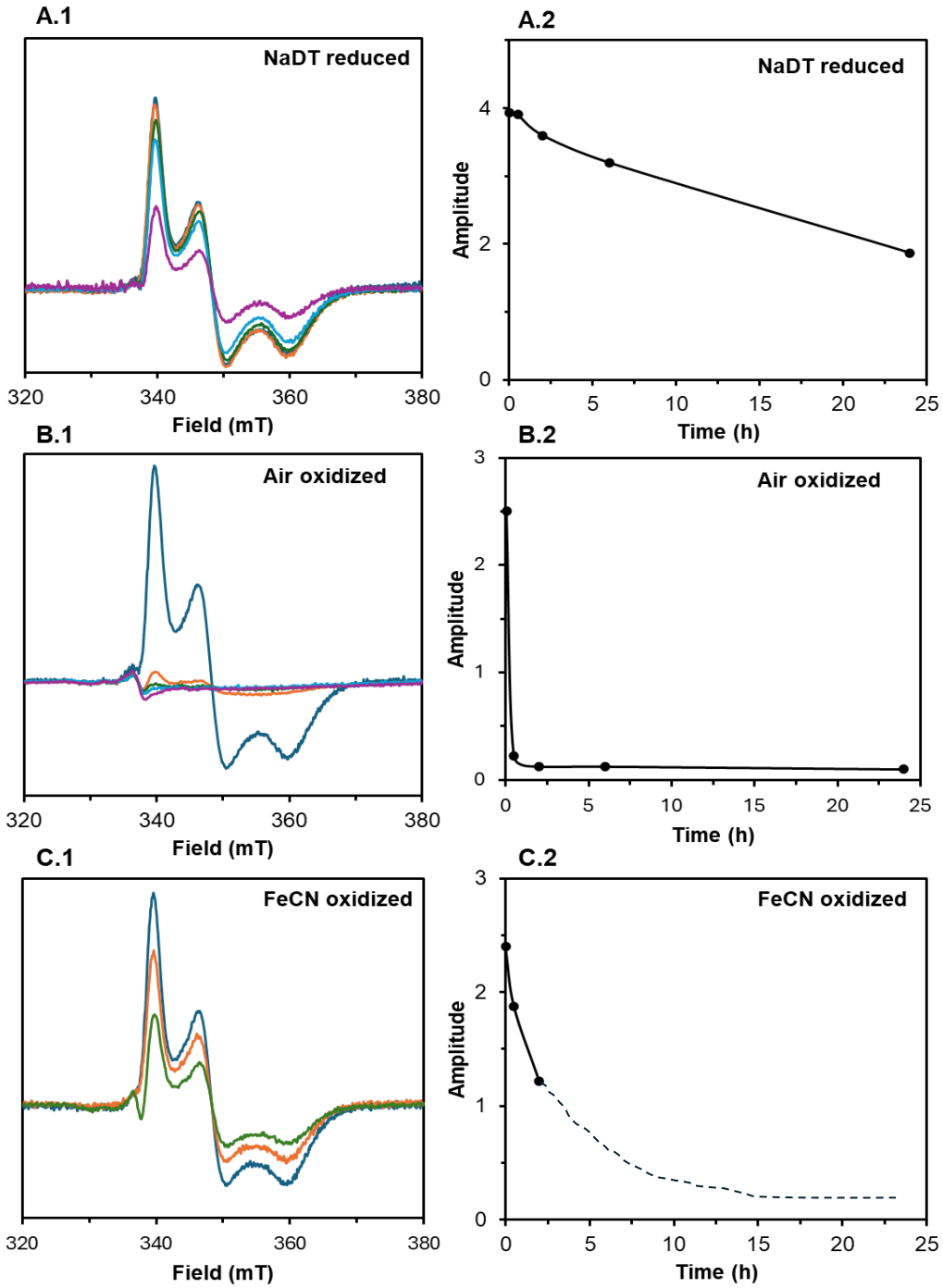

Figure 40. Cluster stability after different incubation times under reducing, air-oxidizing and anaerobic ferricyanide oxidizing conditions. (A) dithionite reduced protein; (B) air oxidized protein and (C) ferricyanide oxidized, and afterwards dithionite reduced IscR. Panels on the left correspond to the samples EPR spectra, a times 0 (dark blue), 30 min (orange), 2 hours (dark green), 6 hours (light blue) and 24 hours (purple). Panels on the right correspond to the intensity of the middle *g*-value as maxima minus minimum. Dashed line in C corresponds to a possible pattern of breakdown progression not experimentally determined. EPR conditions: Frequency: 9.35 GHz, T: 77 K, microwave power: 2 mW, modulation amplitude: 10 G, modulation frequency: 100 kHz.

This experiment raised another question: Could IscR's function as a transcription factor be related to its ability to sense oxygen or other oxidants through the oxidation and breakdown of its cluster? If IscR acts as an oxidant sensor, its clusters might dissociate at varying rates in response to each type of oxidation state, thereby influencing DNA binding according to the level of oxidative stress. It is important to note, however, that the above experiments were performed at 22 °C under anaerobic conditions and perhaps, as observed by CD spectroscopy, the outcome could differ at other temperatures.

2.5.3. DEPC modification of the histidine ligand

Histidine modification by DEPC has been used to characterize FeS clusters with histidinyl coordination as previously reported for the Rieske protein from bovine heart by Ohnishi and coworkers in 1994[173], for the *Thermus thermophilus* Rieske protein by Konkle *et al*.[194] and its mutants by Karagas and colleagues[195]. Additionally, DEPC modification was used in the study of the non-Rieske bis-histidinyl coordinated [2Fe-2S] cluster of Apd1[64] in our working group.

In a first experiment eleven samples of 100 µM of IscR dimer as isolated were incubated with one equivalent of DEPC, followed by reduction with 2 mM sodium dithionite. The resulting spectra are shown in Figure 41. Three parallel IscR samples at three different pH values lacking DEPC were prepared to provide a reference for the EPR signal and its intensity.

At pH values above the pK_a of the oxidized state histidine deprotonation takes place. Thus, DEPC modification is in principle expected to be more efficient at higher pH values as the deprotonated fraction increases. However, in this experiment two findings indicate a higher complexity: 1) DEPC modification appears to lead to the generation of a more axial signal (convergence of g_2 and g_3 values) that reached its maximum at pH 8.3 instead of higher pH values; 2) Signal intensity, particularly at low pH, is not constant indicating that cluster breakdown occurs. The first observation can be explained either by the rapid spontaneous hydrolysis of DEPC at elevated pH, effectively leading to a lower DEPC concentration or by instability or the hydrolysis at high pH values of the formed DEPC-histidine adduct. DEPC modification seems to be most efficient at pH 8.3. Despite being close to the pK_a (~8.1) not all histidine ligands are deprotonated and re-equilibration of the protonated and deprotonated fractions must occur for a (complete) conversion. At low pH values, besides the certainly lower modification rate due to the predominance of the protonated state species, it appears that DEPC in solution leads to cluster breakdown. The breakdown was assessed by the calculation of the double integral of each spectrum from Figure 41. Figure 42 shows that above pH 8.5 the double integral is constant, but that cluster breakdown occurs at low pH values. It is also important noting that even though no extensive cluster breakdown appears to occur above pH 8.5, the EPR species present is mainly the unmodified more rhombic form indicating removal/hydrolysis of the DEPC adduct. The double integral of the DEPC treated samples was always lower than the untreated samples.

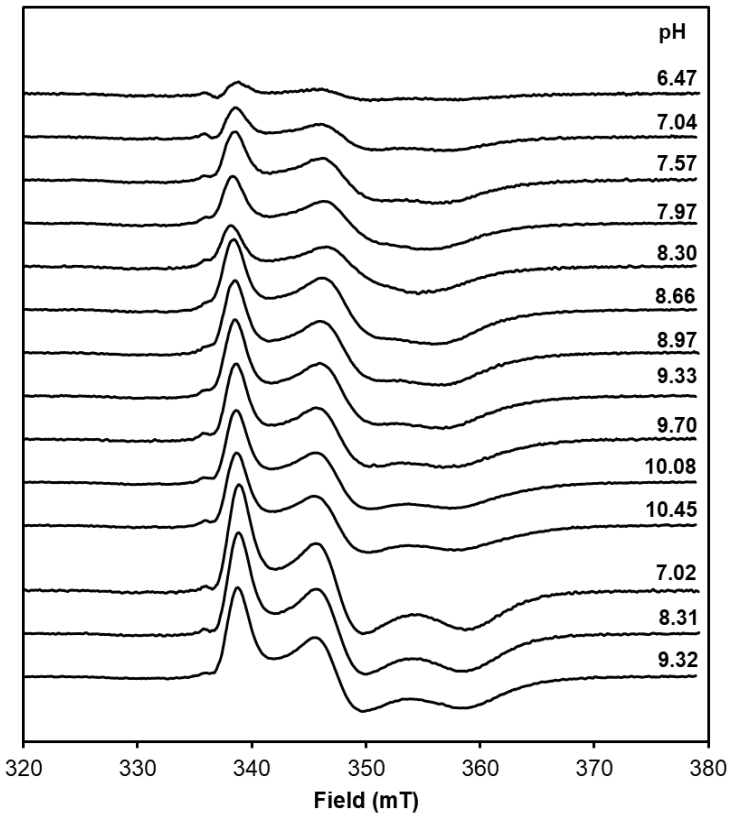

Figure 41. pH dependence of the DEPC modification of the histidinyl ligand of the [2Fe-2S] cluster from IscR. Top eleven spectra correspond to DEPC modified samples; bottom three spectra correspond to the non-modified IscR samples. EPR conditions: Frequency: 9.4 GHz, T: 77 K, microwave power: 2 mW, modulation amplitude: 10 G, modulation frequency: 100 kHz.

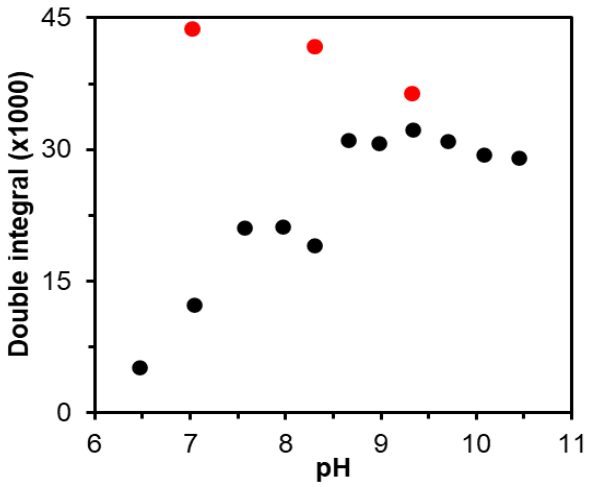

Figure 42. Double integral of the EPR spectra of the DEPC modified IscR. Double integral calculated between 335 and 370 mT. Black corresponds to the DEPC modified samples; Red corresponds to the three control samples.

A second experiment was carried out to determine the optimal ratio of DEPC to protein. Again, a constant concentration of IscR dimer (100 µM) at pH 8 was used, but now the DEPC equivalents were varied between 1 and 10 (100 - 1000 µM) and DEPC treatment was tried also after dithionite reduction. The resulting EPR spectra are represented in Figure 43.

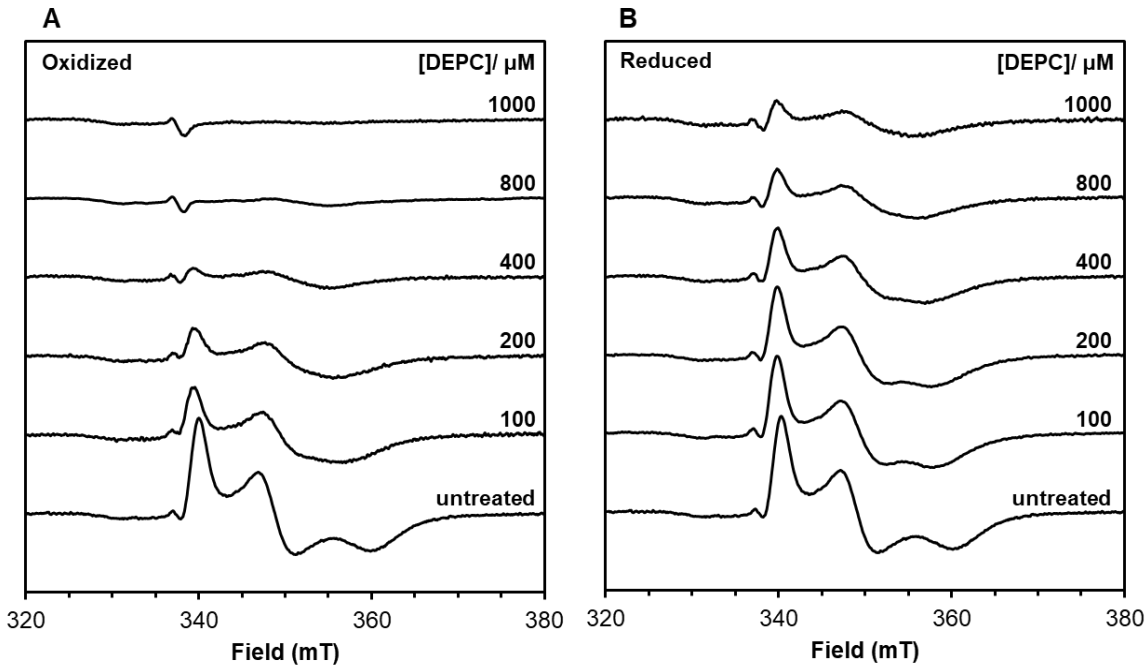

Figure 43. DEPC modification of IscR in the oxidized (A) and reduced states (B) with several DEPC concentrations. EPR conditions: Frequency: 9.4 GHz, T: 77 K, microwave power: 2 mW, modulation amplitude: 10 G, modulation frequency: 100 kHz.

These results show that oxidized IscR at pH 8 showed a maximal DEPC modification at a ratio of 1:1 DEPC to monomer IscR (2:1 DEPC to IscR dimer). Below this ratio modification appears incomplete, as a mixture of EPR species is present. Above this ratio cluster breakdown led to a rapid loss of the more axial, DEPC modified, EPR signal. Contrarily, IscR in the reduced state at pH 8 did not seem to react with DEPC as readily as the oxidized form does. This is in full agreement with the experimentally observed pK in the reduced state. Instead, the results indicate that it is necessary to use an excess (ratio of 8:1 of DEPC to IscR monomer) to have maximal modification in the 5 minutes DEPC incubation time. But, as for the oxidized form, it appears that high concentrations of DEPC also lead to cluster breakdown. A direct comparison between the EPR spectral features of untreated samples and samples treated with a 1 to 1 ratio of DEPC in the oxidized and reduced states is shown in Figure 44. Under identical conditions DEPC treatment in the oxidized state, followed by reduction, is more efficient in comparison to reduction, followed by DEPC treatment.

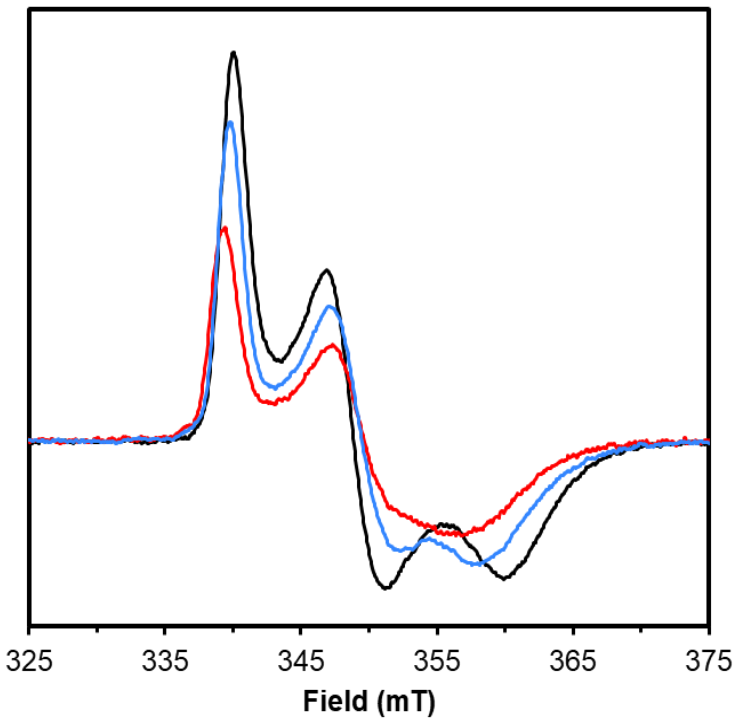

Figure 44. DEPC modification of IscR at a 1:1 proportion of DEPC and IscR dimer. Black – untreated reduced protein; blue – DEPC treated after reduction; red – DEPC treated before reduction.

A third experiment was performed to assess DEPC modification in the oxidized and in the reduced states, but now including pH variation. Fifteen samples were prepared: five dithionite-reduced but untreated, five DEPC treated then reduced and five reduced and then DEPC treated probes. In each series five pH values (6.59, 7.63, 8.50, 9.35, 10.26) were tested. The resulting spectra are shown in Figure 45.

As expected, the untreated samples remained almost unchanged, showing the same EPR spectrum as previously shown in Figures 32 and 41. The DEPC treated samples, however, showed a different extent of modification as revealed by the increase of the axial signal. In the samples treated in the oxidized state the axial species associated with DEPC modification appeared to be the exclusive species. For the samples treated with DEPC in the reduced state a mixture of signals appeared. In both experiments with DEPC treatment at low pH values extensive cluster breakdown was seen. This time, however, modification even at high pH values was observed. This could result from the slightly higher DEPC to protein ratio compared to the previous experiment (~1.5 versus 1.0 equivalent per dimer). In summary, the modification of the EPR spectrum of IscR by DEPC treatment agrees with histidine as a ligand, with a pK value which is substantially lower in the oxidized state.

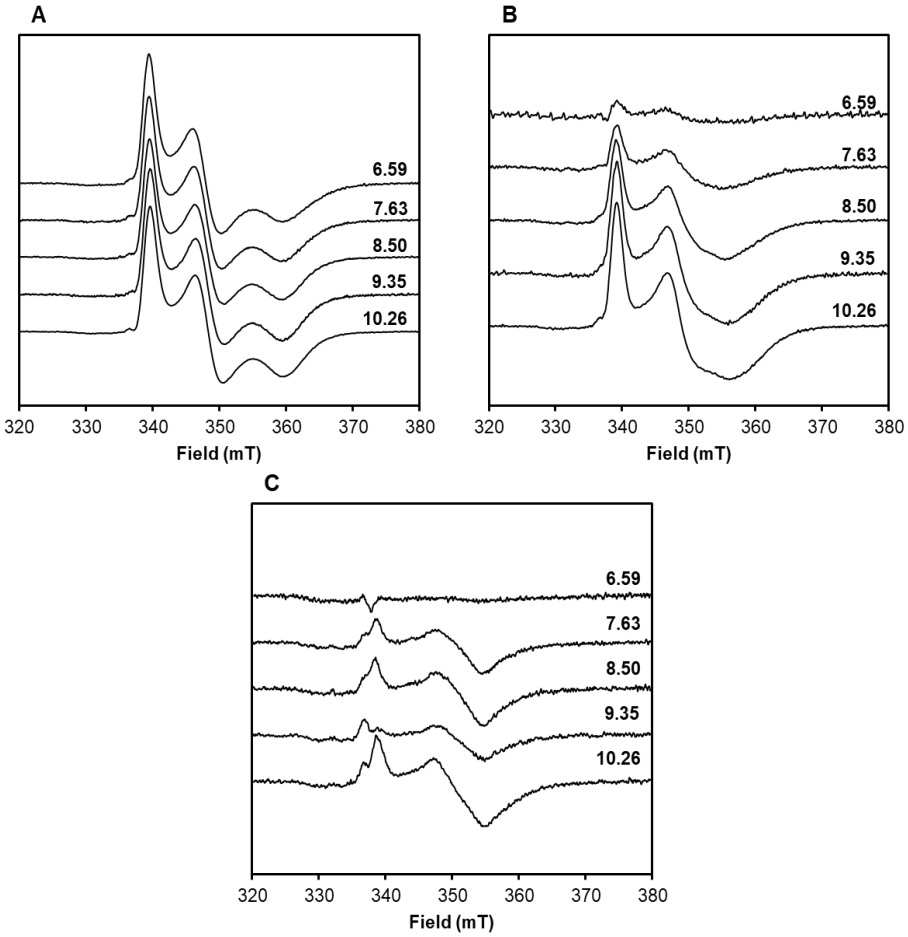

Figure 45. DEPC modification of IscR at a 1.5:1 proportion of DEPC and IscR dimer; (A) Unmodified IscR; (B) Reduced IscR treated with DEPC; (C) As isolated IscR treated with DEPC and then reduced. EPR conditions: Frequency: 9.4 GHz, T: 77 K, microwave power: 2 mW, modulation amplitude: 10 G, modulation frequency: 100 kHz.

2.6. Pulsed EPR spectroscopy

In this study, Q-Band (34 GHz) Davies and Mims ENDOR as well as X- (9.5 GHz) and Q-Band HYSCORE spectroscopies were used. Pulsed EPR was done in collaboration with Dr. Alberto Collauto and Dr. Maxie Roessler, at the Centre for Pulse EPR Spectroscopy (PEPR), Molecular Sciences Research Hub, Imperial College of London, London, UK. Data acquisition and treatment were performed by Dr. Alberto Collauto, who strongly contributed to the description of the spectral methods and the features in this Chapter.

Pulsed EPR was used to independently assess deprotonation of the histidine residue at high pH values in the reduced state. Pulsed EPR can probe nuclear transitions by either making use of a second radiofrequency (RF) field (ENDOR experiments) or taking advantage of the so-called ‘forbidden’ nuclear transitions (ESEEM and HYSCORE experiments). The obtained spectrum gives insights into the hyperfine couplings, yielding information on the cluster environment and surrounding nuclei. ^{14}N, the most naturally abundant nitrogen isotope, possesses a nuclear spin (I) of 1, leading

to quadrupolar splitting, whereas ^{15}N has an $I = 1/2$, lacking quadrupolar splitting. The latter isotopes were exploited through the preparation of samples with and without ^{15}N enrichment, thereby leading to a simplification of the energy levels and consequently of the nuclear spectrum.

Samples were also prepared in $^{1}H_2O$- and $^{2}H_2O$ (D_2O)-based buffers. The protons/deuterons present in solution are in constant exchange with the exchangeable protons of IscR, as is the proton present at the non-coordinating nitrogen atom of the imidazole ring of the histidine ligand. The presence of a proton or a deuteron in the proximity of the cluster can give rise to different signals due to the large difference of the gyromagnetic ratios of ^{1}H and ^{2}H. pH/pD variation between 8 and 12 would then lead to deprotonation and loss of signals of protons/deuterons allowing the characterization of these four states.

2.6.1. Q-Band Davies and Mims ENDOR spectroscopy

Q-Band Davies ENDOR

The Q-Band Davies ENDOR[196] spectra of the ^{14}N samples at pH and pD 8 and 12 were recorded to investigate whether the histidine deprotonation could be detected upon pH shift. Under the weak-coupling condition ($|\nu_I| > |A/2|$, where ν_I is the nuclear Larmor frequency, $\nu_I = B_0 \cdot \gamma/(2\pi)$, and A is the hyperfine coupling, ENDOR spectra are symmetric with respect to the nuclear Larmor frequency and provide a direct readout of the magnitude of the hyperfine coupling. The Larmor frequency depends on the static magnetic field (B_0) and on the gyromagnetic ratio (γ) of the nucleus coupled to the unpaired electron. ^{1}H and ^{2}H have very distinct $\gamma/(2\pi)$ values of 42.58 MHz/T and 6.54 MHz/T, respectively[197,198]. For B_0 = 1.252 T, corresponding to a microwave frequency of 34 GHz and a *g-value* of 1.94 (g_y of IscR), the ^{1}H nuclear Larmor frequency is around 53.3 MHz whereas the ^{2}H nuclear Larmor frequency is around 8.2 MHz. Such a difference between the two different isotopes allows focusing on the one of interest by choosing a suitable radio frequency (RF).

Davies ENDOR spectra and difference spectra thereof are represented in Figure 46, panels A and B. In this experiment, the bulk of protons present around the $[2Fe\text{-}2S]^{1+}$ cluster of IscR under physiological conditions is represented by the sample at pH 8, which has the most intense signal due to detection of all protons surrounding the cluster. Upon pH increase to pH 12, it is expected that several proton containing groups around the cluster deprotonate, leading to a general decrease of the ENDOR signal intensity, which is observed in the dark orange spectrum in Figure 46, Panel A.

In the sample at pD 8, however, the exchangeable protons are exchanged by deuterium and cannot be detected around the ^{1}H nuclear Larmor frequency for the reasons mentioned above. Thus, the obtained signals correspond solely to protons that are not readily exchangeable, such as those from the protein backbone and from the sidechain of most amino acids. Additionally, in the sample at pD 12, as observed for the sample at pH 12, the protonated groups can deprotonate; and due to the impossibility to observe deuterons around the ^{1}H nuclear Larmor frequency, the spectra of the pD 8

and pD 12 samples are expected to appear almost identical. This is also experimentally observed (see Figure 46, Panel A, traces in light orange and blue).

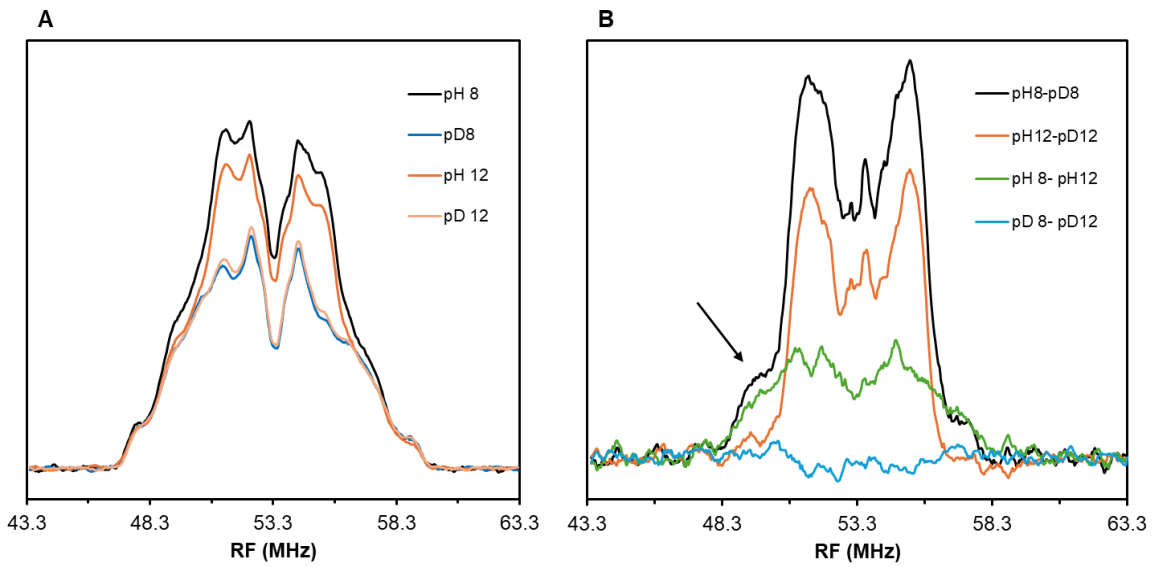

Figure 46. Q-Band Davies ENDOR experiment of wild type IscR centered in the Larmor frequency of ^{1}H at B_0 = 1.252 T. (A) spectra of IscR pH 8 (black), pD 8 (blue), pH 12 (dark orange) and pD 12 (light orange). (B) Difference spectra between samples pH 8 and pD 8 (black), pH 12 and pD 12 (orange), pH 8 and pH 12 (green) and pD 8 and pD 12 (blue). These spectra were smoothed with a 7 data point moving average. Measurement conditions: g_2 field position, corresponding to the maximum of the EDFS-EPR spectrum; T: 20 K, π_{MW} = 100 ns, π_{RF} = 16 µs, 50(π/2)-400(τ)-100(π) detection sequence with an integration gate of 400 ns; single-shot detection with stochastic acquisition, 2-step phase cycle applied to the π/2 microwave pulse. Data acquisition by Dr. Alberto Collauto.

Knowing that the samples have the same cluster concentration and what each signal represent in each spectrum allows to calculate, within some degree of certainty, difference spectra to unravel signals that are specifically produced by the couplings of interest. In Figure 46, panel B, four difference spectra are shown. The spectrum of all the exchangeable protons can be obtained by subtracting the spectrum of the sample at pD 8 (only non-exchangeable protons) from the sample at pH 8 (all protons). A maximum of 5% rescaling was performed and chosen based on the best flat baseline obtained. This trace shows a shoulder around 4 MHz below the central frequency, corresponding to a coupling of approximately 8 MHz; this has been attributed to the histidine proton. Additionally, the spectrum of the protons that were lost upon pH increase can be obtained by subtracting the spectrum of the sample pH 12 from the one of sample pH 8, which interestingly also shows the shoulder previously mentioned. If IscR's cluster-coordinating histidine underwent deprotonation upon pH shift from 8 to 12, the shoulder could indeed be associated with this coupled transition. It is not clear, however, why the spectra are not as symmetrical as they were expected to be.

The difference spectrum pH 12 minus pD 12 presents a minor signal in the shoulder region, attributed to the protonatable groups that did not undergo deprotonation at high pH values. Upon comparison with previously shown EPR data on the $pK_a \approx 11.1$ in the reduced state, the faint presence of a shoulder in this difference spectrum could be explained by the incomplete deprotonation of the

histidine residue at pH ~12. Lastly, the difference spectrum between pD 12 and pD 8 does not show any specific features indicating that, as previously mentioned, deuterons are not shown in this frequency range and the non-exchangeable protons are similar in both samples.

The histidine residue would be approximately 90% deprotonated at pH 12, and with a $pK_a \approx 11.1$ in the reduced state. Assuming that the intensity of the shoulder feature in the pH 8 - pD 8 spectrum is 100% of the exchangeable protons, their shoulder relative intensity in both pH 8 - pH 12 and pH 12-pD 12 could give some insights into the percentage of deprotonated and protonated histidine residues, respectively. This analysis performed with the intensities at 49.7 MHz, where the shoulder is observed, resulted in approximately 80 and 15% of histidine in the deprotonated and protonated states, respectively.

Q-Band Mims ENDOR

Mims ENDOR[199] was also used in this experimental work. Its pulse sequence differs from Davies ENDOR and is characterized by higher sensitivity when compared to the latter mostly because hard (short, high-power) microwave pulses are used instead of soft (long, low power) ones.

Concerning the ability to detect hyperfine couplings of different magnitude, Davies ENDOR makes use of a soft microwave π preparation pulse which is selective with respect to the magnitude of the hyperfine coupling and generates therefore a non-equilibrium population across the nuclear spin transitions. This makes it suitable for the detection of large couplings ($A \geq 7$ MHz for a 100 ns microwave π pulse[200]), however the signals from smaller couplings are partially suppressed as in this case the microwave π preparation pulse can invert both EPR transitions (namely, in the α and β nuclear spin manifolds). Mims ENDOR, on the other hand, relies on a $\pi/2 - \tau - \pi/2$ preparation sequence to generate a polarization grating across the EPR line and has a response function characterized by so-called 'blind spots', namely values of the hyperfine coupling for which the ENDOR efficiency is zero[200]. These occur at integer multiples of $1/\tau$, namely $A \cdot \tau = 0, 1, 2, \ldots$. As the shortest τ value that can be achieved experimentally is limited by the dead-time of the EPR spectrometer, usually ≈130 ns, large hyperfine features are strongly distorted by the mentioned blind-spot behavior. Features near the nuclear Larmor frequency of the investigated nucleus are instead enhanced, making Mims ENDOR the technique of election to resolve weak hyperfine couplings. Davies ENDOR, however, is more often used for strongly coupled systems.

In this work, to harness the sensitivity gain offered by Mims ENDOR over Davies ENDOR whilst retaining undistorted line shapes a variant of the former technique, known as refocused Mims ENDOR (ReMims)[201], has been used. In ReMims ENDOR an additional π pulse is used to refocus the stimulated echo generated by the three π/2 pulses, bringing the signal outside of the spectrometer dead-time even for very short τ values.

As in cw EPR most of the changes occurred at two *g*-values, the field value chosen for Davies ENDOR, at g_y or 12513 G, could perhaps not correspond to the direction where most changes could be observed. The higher sensitivity offered by (Re)Mims ENDOR was leveraged to collect spectra across the whole EPR line, more specifically at nine different field values for ^{14}N wild type IscR pH 8 and twelve for ^{14}N wild type IscR pH 12 . The corresponding Echo-Detected Field-Sweep (EDFS) EPR spectrum highlighting the magnetic field positions chosen to record the ReMims spectra and the spectra obtained at each magnetic field are shown in Figures 47 and 48, respectively.

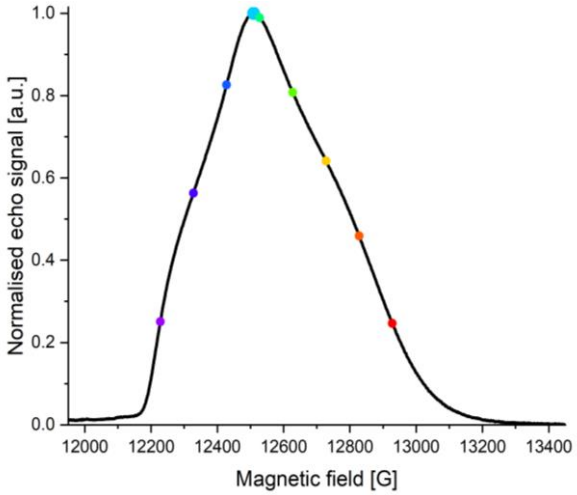

Figure 47. EDFS-EPR spectrum of ^{14}N IscR pH 8. The colored dots indicate the field positions used to record the spectra represented below. Data acquisition, treatment and Figure by Dr. Alberto Collauto.

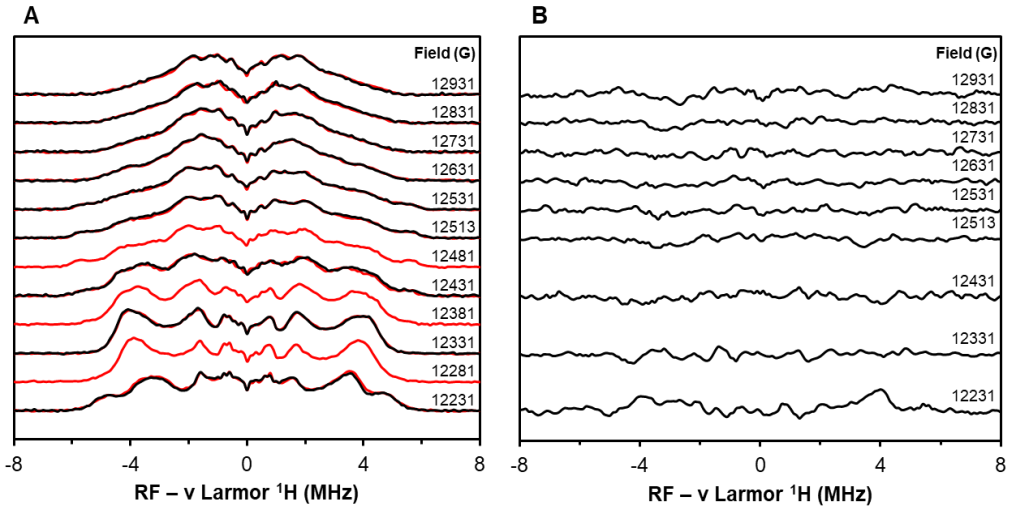

Figure 48. ^{14}N wild type IscR pH 8 and pH 12 ReMims ENDOR spectra at nine and twelve different field values, respectively. (A) Mims spectra pH 8 (black) and pH 12 (red) and (B) difference spectra between pH 12 and pH 8 at similar field values. Measurement conditions: T: 20 K, τ = 50 ns, $\pi/2_{MW}$ = 6 ns, π_{RF} = 16 µs, T_2 = 160 ns for the stimulated echo refocusing, 18 ns integration gate; single-shot detection with stochastic acquisition, 2-step phase cycle applied to the first $\pi/2$ microwave pulse. Data acquisition by Dr. Alberto Collauto.

Surprisingly, the spectra observed for samples at pH 8 and pH 12 are almost identical at the different field values. The difference spectra between pH 12 and pH 8 were calculated at each field value and only showed mild differences at a field of 12231 G. However, the signal intensity was expected to be higher at pH 8 than pH 12. The significance of these results is not clear, however the difference in sensitivity between ReMims and Davies ENDOR in this work could be related to the use of longer and more selective pulses in Davies ENDOR.

2.6.2. X- and Q-Band HYSCORE

X- Band HYSCORE experiments were also performed to study both the exchangeable protons and the nitrogen atoms that present a coupling with the [2Fe-2S]$^{1+}$ cluster of IscR. In these experiments the ^{14} and ^{15}N samples were compared in the nitrogen region whereas the deuterated and non-deuterated samples were compared in the hydrogen region.

X-Band HYSCORE provided valuable information on the coordination of the [2Fe-2S] cluster in IscR. The individual and overlaid spectra of $^{14/15}$N IscR at pH 8 are shown in Figure 49. HYSCORE detects the presence of a strongly coupled nitrogen atom to the [2Fe-2S] cluster of IscR, shown by the signals observed in the left quadrant of Panels A and B. In the ^{14}N sample (Panel A) it is possible to observe intense double quantum (dq, at or near the red lines in Figure 49, Panel A) and single quantum (sq, at or near the black lines in Figure 49, Panel A) transitions in the left quadrant in agreement with a strong coupling. These transitions are characteristic quadrupolar interactions occurring due to an I=1 from the ^{14}N atom. In the right quadrant, it is also possible to observe some less intense signals originating from weak couplings with ^{14}N atoms in the surroundings. ^{15}N labelling of IscR allowed the acquisition of simpler spectral data (Figure 49, Panel B), by the enrichment with ^{15}N (I=1/2), due to the absence of quadrupolar splitting of ^{14}N, present in the previous samples. In this spectrum it is also possible to observe a strong coupling in the left quadrant, as well as weak couplings in the right quadrant. Comparing these results with the HYSCORE data published by Iwasaki and coworkers in 2009[192] for the mono-histidinyl coordinated [2Fe-2S] cluster of rat MitoNEET it becomes clear that IscR and MitoNEET present a similar, if not identical, coordination. However, it was not possible to determine which nitrogen atom, δ or ε, is the coordinating nitrogen as observed for MitoNEET.

The overlaid X-Band HYSCORE spectra of ^{14}N and ^{15}N IscR in the nitrogen region is represented in Figure 50. The determination of hyperfine couplings for the ^{14}N and ^{15}N samples and the evaluation of the proton region for deuterated versus non-deuterated samples are still ongoing. Due to its smaller hyperfine couplings, the proton region must be carefully analyzed to pinpoint subtle changes and attribute couplings.

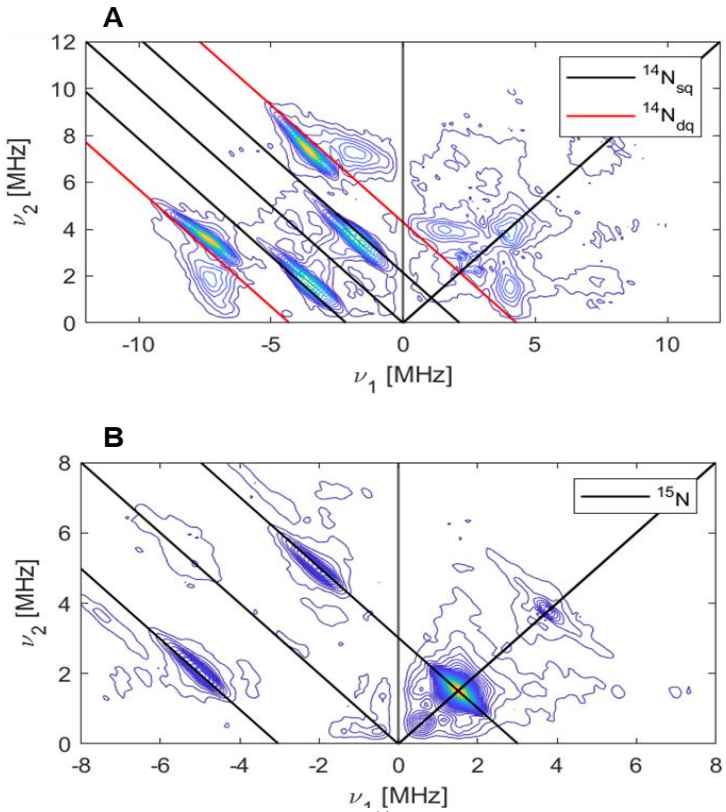

Figure 49. X-Band HYSCORE of ^{14}N (N/A, 99.63%) and uniformly labelled ^{15}N IscR at pH 8. Data was acquired at gy corresponding field. (A) ^{14}N IscR; (B) ^{15}N IscR. Microwave frequency and magnetic field value were 9.5169 GHz and 3493 G, and 9.5292 GHz and 3499 G for the samples in ^{14}N and ^{15}N, respectively. T: 10 K, τ:134 ns, π/2=π=12 ns. The echo was integrated over a 6 ns gate centered at the echo maximum. Data acquisition, treatment and Figure by Dr. Alberto Collauto.

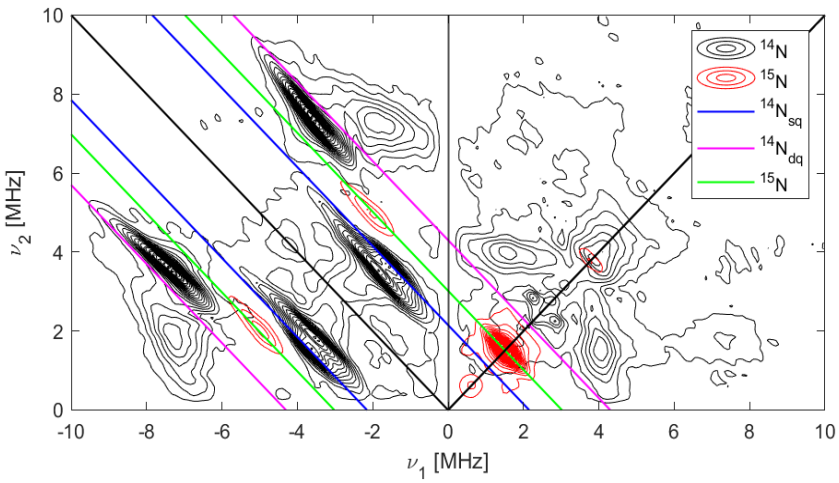

Figure 50. Overlaid X-Band HYSCORE spectra of ^{14}N and ^{15}N IscR. Parameters as described in Figure 49. Data acquisition, treatment and Figure by Dr. Alberto Collauto.

2.7. Mössbauer spectroscopy

Mössbauer spectroscopy is an important technique for analyzing Fe-containing proteins, such as IscR. Mössbauer spectroscopy was used here to confirm whether the previously determined histidine's pK_a in the oxidized would fit the observed spectra. Additionally, Mössbauer was used to study IscR's cluster *in vivo* behavior upon cell treatment with hydrogen peroxide at low concentrations as a mild oxidizing agent. Sample preparation was conducted with the assistance of PhD student Lukas Knauer, who was also responsible for measuring the spectra and performing all data treatment including spectral simulation.

Initially, several samples of as isolated IscR were prepared at several pH values. These samples were measured by Mössbauer at 77 K in the absence of an applied field. The spectra confirmed that the protein was purified in the oxidized state. Mössbauer spectra and their simulations are shown in Figure 51. In these spectra, the experimental data were simulated with three main components. The first component, corresponding to the iron atom ligated by two cysteine residues and two acid-labile sulfur atoms, was kept constant throughout all simulations and was simulated with an isomer shift δ of 0.26 mm/s and a quadrupole splitting ΔE_Q of 0.48 mm/s. This component was fixed at 50 % of contribution for all spectra. Component 2, with a δ of 0.28 mm/s and a ΔE_Q of 0.65 mm/s, and component 3, with a δ of 0.30 mm/s and a ΔE_Q of 0.80 mm/s, correspond to the iron atom coordinated by a cysteine and a histidine and the two bridging acid-labile sulfur atoms, in the deprotonated and protonated states, respectively. These values agree with literature available for [2Fe-2S] clusters[63,189] with 3 Cys and 1 His coordination, in general and as described for IscR by Fleischhacker and coworkers[71]. Upon pH change, the relative contribution of components 2 and 3 varies, but remain at a summed contribution of 50%. At lower pH values such as 5.7 and 6.4, where no deprotonation of the histidine residue is observed, the contribution of component 1 is 50%, component 2 contributes 0% and component 3 contributes 50%. At pH values higher than 10 no protonation is observed, so component 1 remains the same, while component 2 contributes 50% and component 3 contributes 0%. Thus, the proportion of components 2 and 3 directly reflects the proportion of deprotonated or protonated cluster-coordinating histidine.

It is important to note that at a pH below 7, and at pH above 9, cluster breakdown starts to play a role in Mössbauer spectra as non-specifically bound iron atoms show up in the spectra. The non-specifically bound iron atoms were also simulated. At low pH values (pH 5.7 and 6.4), component 3, simulated with a δ of 1.35 mm/s, a ΔE_Q of 3.04-3.23 mm/s, and a line width of 0.50-0.53 mm/s, visible in the spectra, corresponds to non-specific bound Fe^{2+}. At high pH values (above pH 10), component 3, simulated with a δ of 0.40-0.48 mm/s, a ΔE_Q of 0.67-0.70 mm/s, and a line width of 0.27-0.52 mm/s corresponds to non-specifically bound Fe^{3+} is seen.

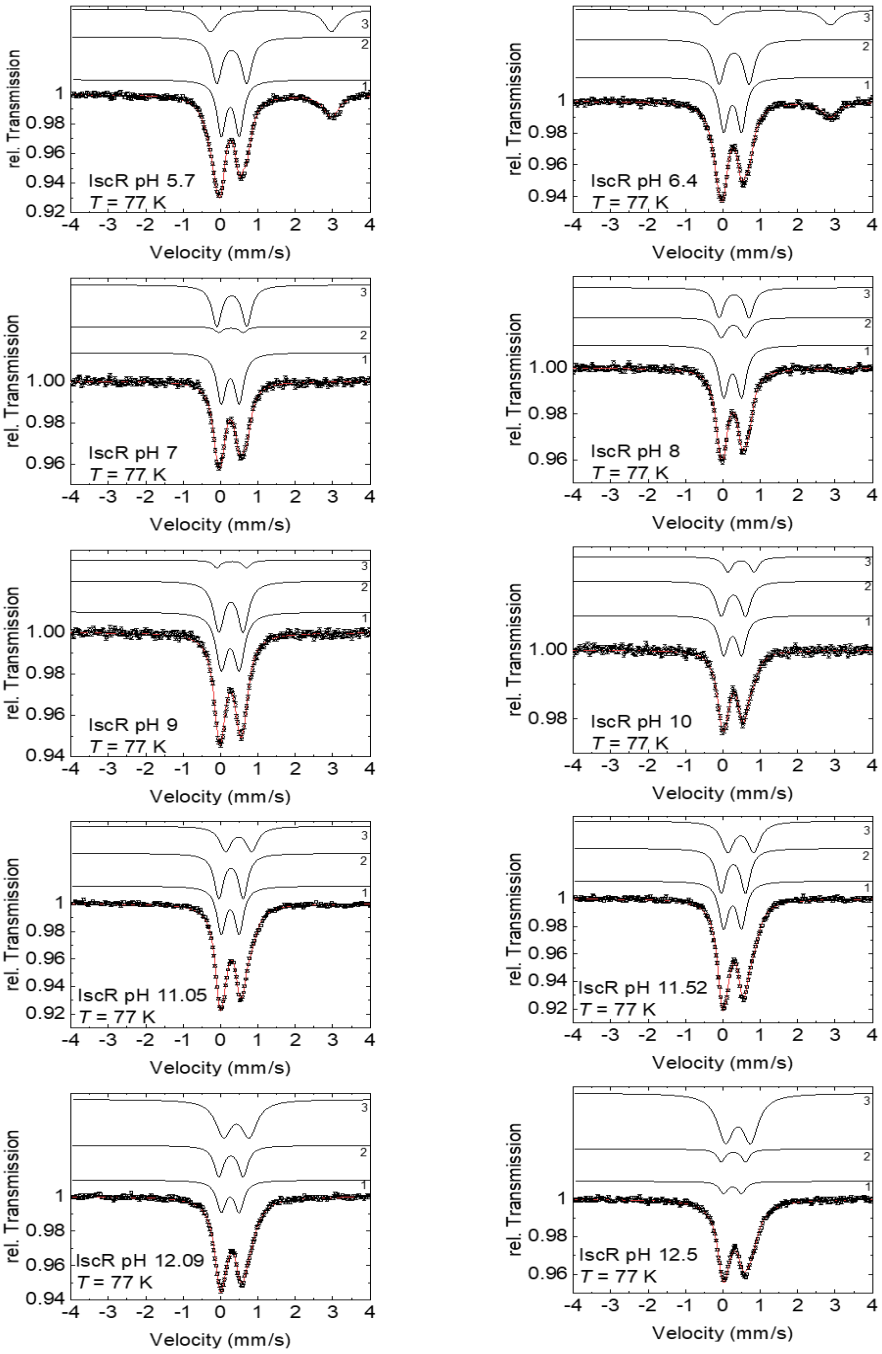

Figure 51. Mössbauer spectra of oxidized IscR at several pH values. Temperature 77 K, without external field applied. Figure and data treatment by Lukas Knauer.

Field measurements were carried out for the sample at pH 8, at 7 K, 0.1 and 5 T, to assess whether there was cluster breakdown, whether the sample was diamagnetic and to quantify any free/non-specifically bound Fe^{3+} in solution due to spectral overlap at zero field. Additionally, field measurements were conducted for the sample at pH 11.05 to determine the contribution of free Fe^{3+} in solution at high pH values. All four spectra (pH 8.00 and pH 11.05, 0.1 and 5 T) are shown in Figure

52. A certain extent of cluster breakdown was expected for the sample at pH 11.05, but not as much for the sample at pH 8.00.

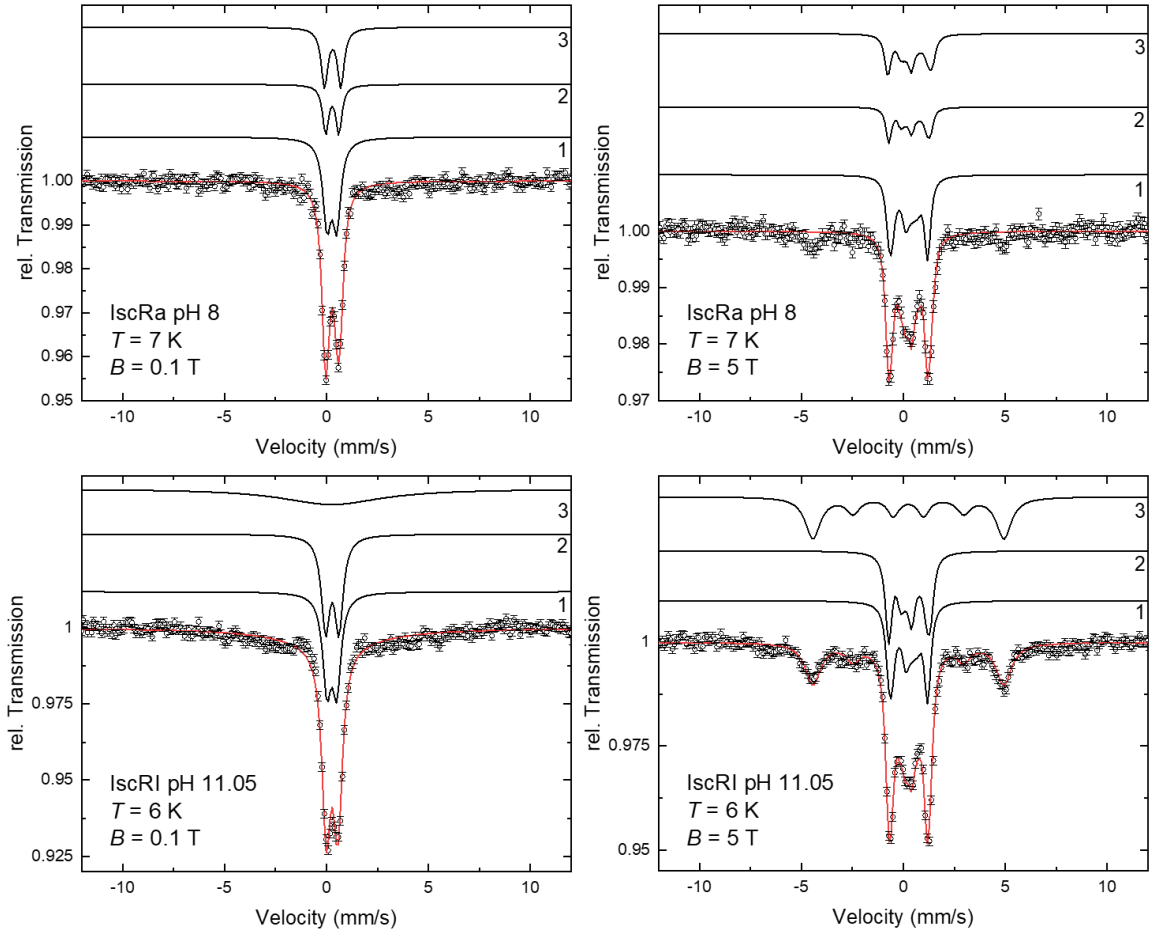

Figure 52. Mössbauer spectra of IscR at pH 8.00 (top) and pH 11.05 (bottom) under an applied field of 0.1 (left) and 5 T (right). Temperature 7 K, pH 8 and 6 K, pH 11.05. Figure and data treatment by Lukas Knauer.

In the spectra of IscR pH 8 under 5 T magnetic field, it is possible to see a symmetrical signal at -5 and 5 mm/s that were attributed to free Fe^{3+} in the sample at pH 11.05 where it is also visible. However, in the sample at pH 8 this signal does not seem to contribute as much as it does for the sample at pH 11.05, where it was calculated to correspond to 34% of the signal area. It is also not possible to clearly observe the neighboring splitting as it is in the sample at pH 11.05. At 0.1 T it is possible to observe a baseline broadening in the sample at pH 11.05 attributed to Fe^{3+}, not clear in the sample at pH 8. These results appear to indicate that cluster breakdown plays a role independently of the pH value, possibly due to protein handling and the necessity to concentrate the sample, but it is more pronounced at high pH values, as expected. The parameters used to simulate the spectra can be found in the supplementary information (S.7.).

A careful analysis of the contribution of the protonated and deprotonated species through a range of pH values allowed the estimation of the pK_a of histidine ligand in the [2Fe-2S] cluster of IscR in the

oxidized state. Plotting the normalized fraction of protonated histidine versus the pH value allowed the estimation of the histidine's pK_a in the oxidized state, which is represented in Figure 53.

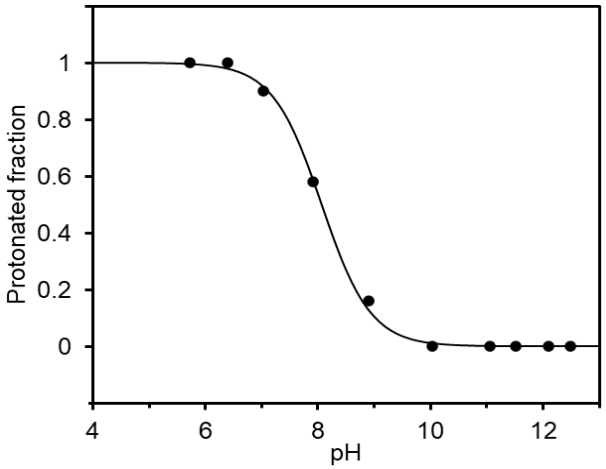

Figure 53. Protonated fraction as a function of the pH value determined by Mössbauer spectroscopy of oxidized IscR.

The pK_a in the oxidized state, determined by Mössbauer spectroscopy, was 8.1. This agrees with those determined for IscR in the oxidized state using CD and UV-Vis spectroscopy in this work. The value is consistent with other clusters of the same type, such as MitoNEET[51], as well as those with double histidinyl coordination, like Rieske[60] and Apd1[63].

2.8. X-ray crystallography

The XRC performed for IscR in collaboration with Dr. Berta Martins from the Humboldt University, Berlin yielded a few small crystals. However, upon measurement in the Bessy synchrotron, in Berlin, no diffraction pattern was obtained.

2.9. Site-directed mutagenesis of IscR

This study included a brief examination of some IscR mutants. In this section, the experimental results obtained for these mutants will be presented and discussed. These mutants, specifically IscR H107C, H107D, H107E, L136*, H143*, D146*, and R149*, were created using site-directed mutagenesis. Due to time constraints, not all experiments conducted on wild-type IscR were performed on the mutants. Most of these results were generated through Bachelor/ Master projects and practical courses conducted under my supervision.

2.9.1. IscR H107C

IscR H107C was perhaps the most relevant and studied mutant. Part of the work on this mutant was conducted by the master student Gian Franco Bellagamba in 2022, under my direct supervision. IscR H107C was initially produced and purified as described in Section 2 of Chapter II and the main purification steps are shown in Figure 54.

A clear color difference between wild-type and H107C IscR can be observed even during the purification process. Wild-type IscR presented a reddish, almost even purple, color whereas H107C mutant showed a clear brown color. A further difference that could be detected during the purification process was that IscR H107C was extremely cold-labile. In Figure 54, panel C, it is possible to observe the turbidity of a solution even after filtration because it was kept at 4 ºC. As soon as the solution was kept at room temperature protein and cluster seemed to have gained a higher stability. Such instability at cold temperatures was not detected for wild-type IscR

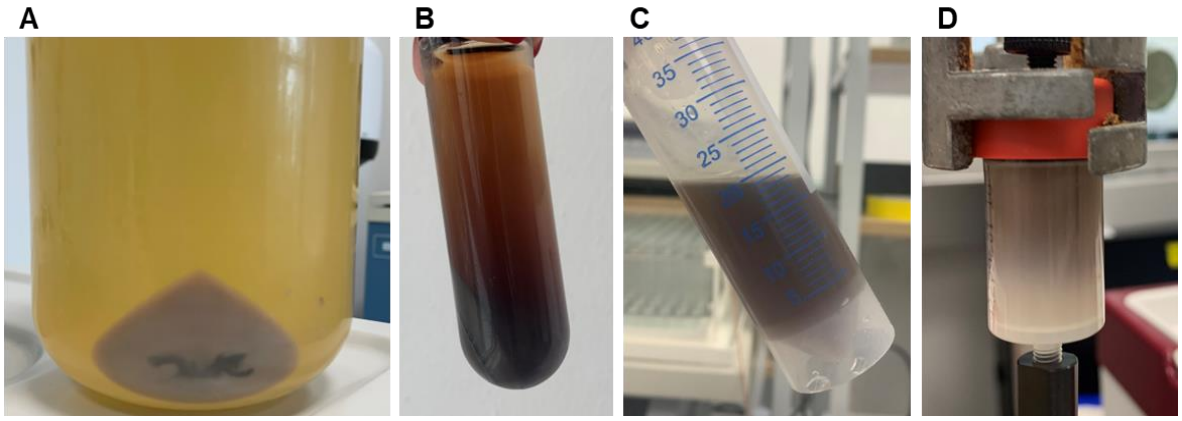

Figure 54. Purification of the H107C IscR mutant. (A) cells after harvesting; (B) ultra centrifuge tube after centrifugation to separate pellet and soluble fraction; (C) Soluble fraction; (D) column after loading the soluble fraction.

A UV-Vis spectrum of IscR H107C was recorded and compared to the spectrum of the wild-type protein (Figure 55). These spectroscopic data revealed the presence of three maxima at 331, 418 and 461 nm that, as discussed in the UV-Vis section of wild type IscR, are characteristic of a 4-Cys coordinated system. Additionally, in the UV-Vis spectra, even though absorbance at 280 nm is almost the same in both spectra, absorbance at 420 and 460 is almost half of the observed for the wild-type protein, indicating a lower cluster content in the mutant.

Comparing the protein color at the same protein concentration in Figure 55, Panel B, it is also observed that wild type IscR color is more intense than the mutants color. Observing protein color at the same cluster concentration, Panel C, it is possible to observe a faint but noticeable color difference between a more reddish (wild type) and a slightly more brownish (H107C) protein.

Protein, iron and acid-labile sulfur quantification confirmed that cluster incorporation was not as high as observed for wild type IscR, as shown by UV-Vis. One colorimetric quantification was performed for IscR H107C showing similar protein yields (0.69 mM dimer IscR), but a reduced amount of iron and acid-labile sulfur (0.53 mM and 0.86 mM, respectively). These results correspond to ~0.8 Fe ions/dimer and ~1.2 acid-labile sulfur/dimer.

Despite being known for being more stable than non-cysteinyl coordinated clusters, the His107Cys variant of IscR turned out to be more unstable. This substitution in IscR may cause cluster distortion

to have all cysteine residues coordinating the cluster and possibly lead to disruptions of non-covalent, but relevant, molecular interactions.

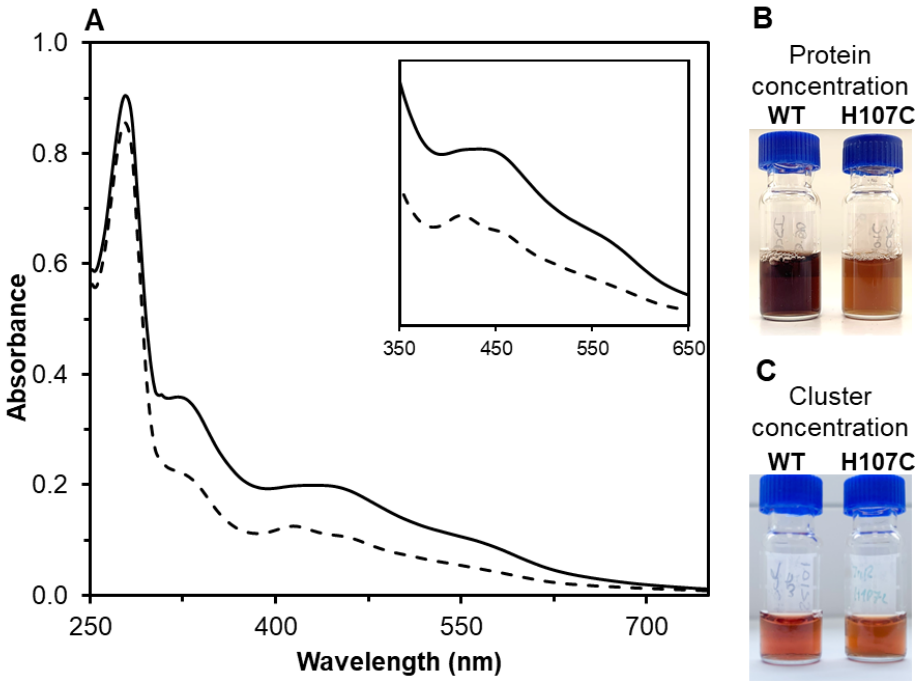

Figure 55. UV-Vis spectra and direct color comparison of wild type and H107C IscR. (A) UV -Visible spectra of wild-type (full) and H107C (dashed) IscR. Color comparison between wild-type and H107C IscR at the same protein concentration (B) and same cluster concentration (C).

A 15% SDS-PAGE comparing the purified wild type and mutant proteins is shown in Figure 56. In this SDS-PAGE gel, it is interesting to note that, even though both proteins seem to be relatively pure, presenting only some minor high molecular mass contaminants, a second band can be observed

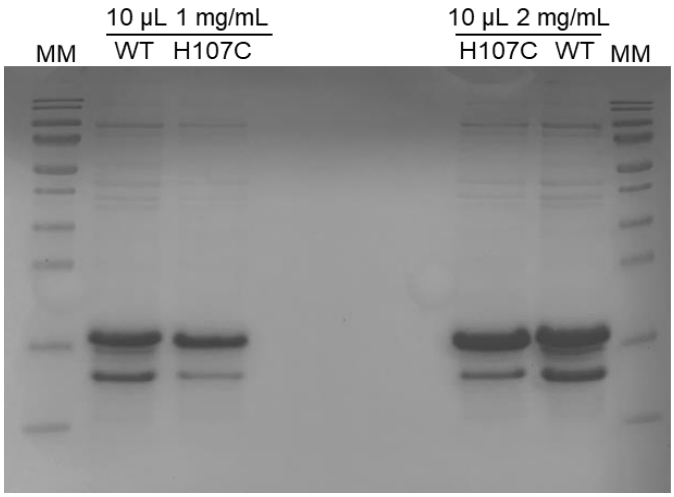

Figure 56. Coomassie stained 15% SDS-PAGE of the wild type (WT) and H107C IscR.

below the ~16 kDa IscR band. This second band could be a product of C-terminus proteolysis, and it seems to impact both wild type IscR and the His107Cys variant.

The DNA binding ability of the mutant H107C was also assessed. For this, EMSA assays were run together with wild type IscR. These gels, represented as a cut version in Figures 22, 23 and 25 will now be fully shown in this section. During the assessment of protein's migration pattern in a native PAGE, shown in Figure 57 (full Figure 22), IscR H107C seemed to have a slightly higher mobility than IscR wild type, however, presented a similar band spreading behavior. Upon addition of *hya* DNA the mutant presents the same bands and pattern as observed for the wild type but presented stronger bands indicating that DNA binding might be slightly improved.

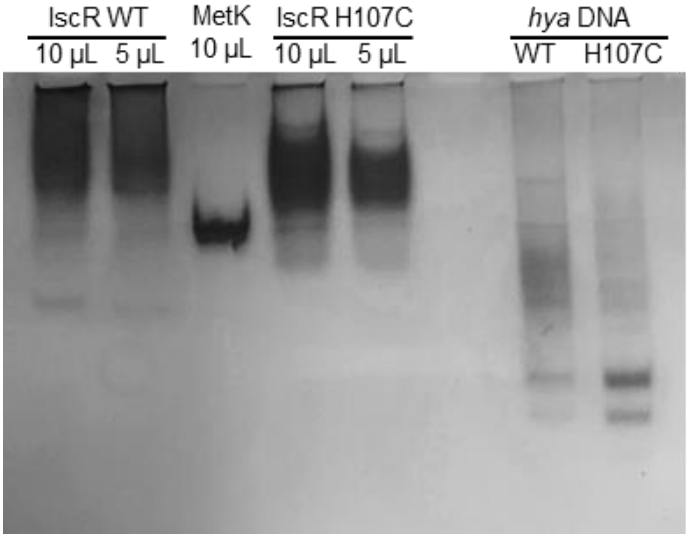

Figure 57. Coomassie Blue stained 6% native PAGE of IscR wild type and H107C with and without *hya* promoter DNA.

The EMSA assay, shown in Figure 58 (correspondent to the full Figure 23), shows the difference in patterns observed between wild type and H107C IscR upon DNA addition. Surprisingly, it appears that mutant IscR forms DNA complexes that are better resolved in EMSA assays than the ones formed with wild-type IscR. Nonetheless, both proteins seem to roughly form complexes with a similar quaternary structure organization. It is not clear, however, the reason behind the difference in band resolution between the two proteins.

Another EMSA assay was run to determine the best ratio of binding of protein to *hya* promoter DNA. This EMSA gel is shown in Figure 59, and it shows that between 1:1 and 4:1, protein to DNA ratio, binding is observed as two clear bands. This agrees with the data obtained for wild type IscR that showed two resolved bands up to a ratio of 5:1, protein to DNA. However, contrary to the observed previously in Figure 58, in this gel it is not possible to observe the clear and resolved top two bands.

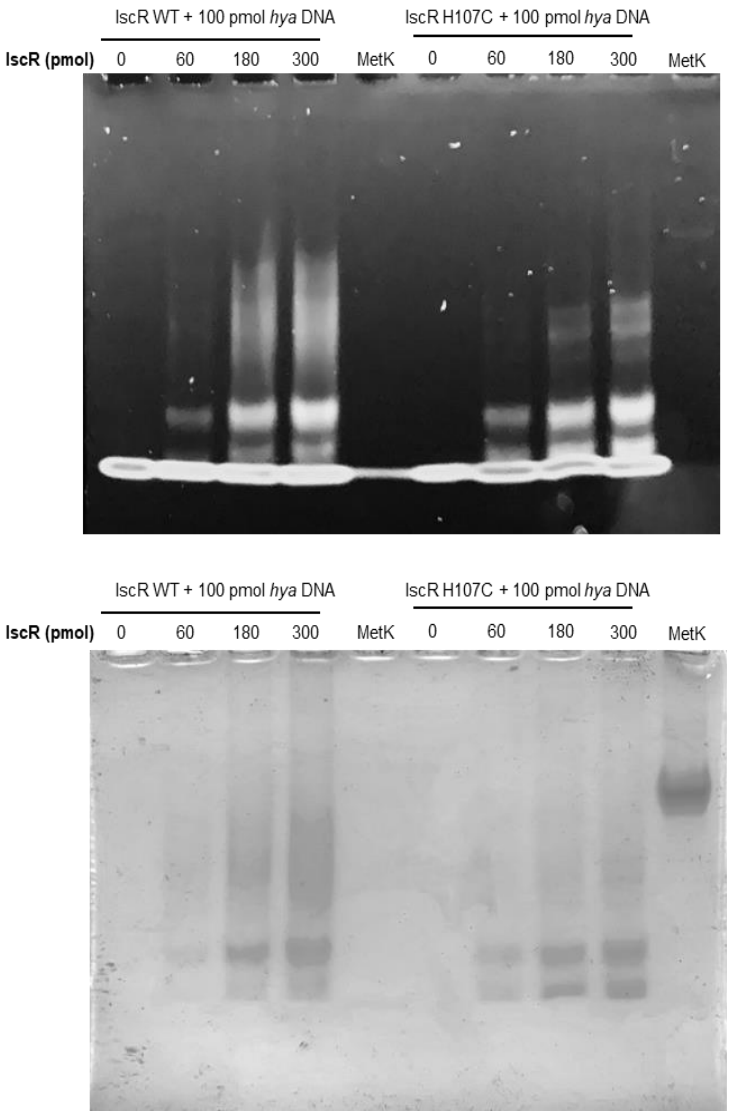

Figure 58. EMSA assay of the wild type and H107C IscR binding to the *hya* promoter DNA. Top gel is observed under UV irradiation in the presence of Gel red, revealing DNA by fluorescence and bottom gel is stained with Coomassie Blue for protein visualization.

The binding of IscR's mutant to *iscrb* promoter DNA was also assessed by EMSA. This assay is shown in Figure 60 and corresponds to the full version of Figure 25. In this assay, the results obtained for IscR H107C are not consistent. While for wild type IscR binding started around a ratio of 2:1 protein to DNA both in the top and bottom gel, for H107C binding is observed in the top gel from approximately 1:1 ratio, but this result is not reproduced in the bottom gel, that only starts to show possible binding from a ratio of 3:1 protein to DNA. Nevertheless, the mutation neither seems to impact the ability of the protein to bind to a Type 1 nor to a Type 2 DNA binding site.

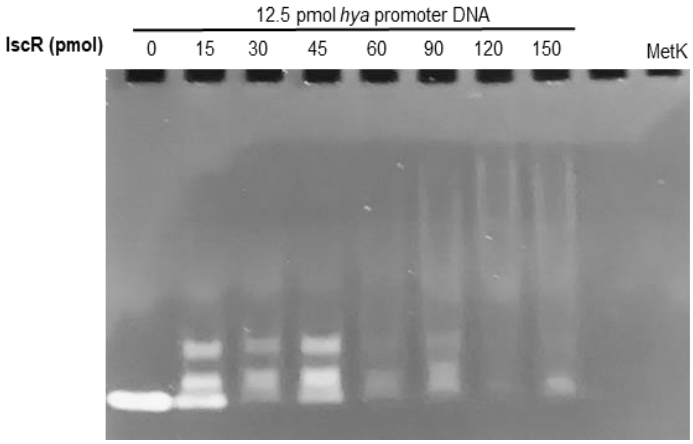

Figure 59. EMSA assay of H107C IscR binding to the *hya* promoter DNA. UV irradiation in the presence of Gel red, revealed DNA by fluorescence.

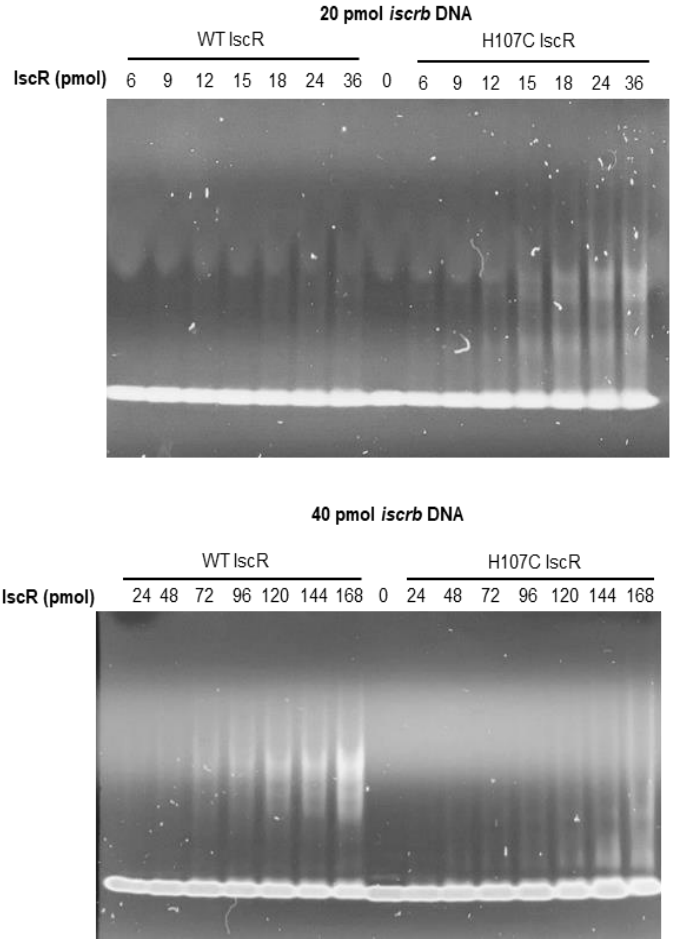

Figure 60. EMSA assay for H107C IscR protein binding to *iscrb* promoter DNA. DNA concentrations were 20 (top gel) and 40 (bottom gel) pmol. UV irradiation in the presence of Gel red, revealed DNA by fluorescence.

Further EMSA assays and DNA binding assays, such as isothermal titration calorimetry (ITC), would be necessary to assess whether the differences observed between the wild type and H107C protein are an indicator of a possible influence of the cluster in DNA binding.

The mutant IscR protein was also analyzed by EPR spectroscopy at several pH values. The sample preparation was as described for the wild-type protein in the methodology section. This experiment aimed to assess whether spectral changes would occur upon pH shift. H107C IscR EPR spectra are shown in Figure 61.

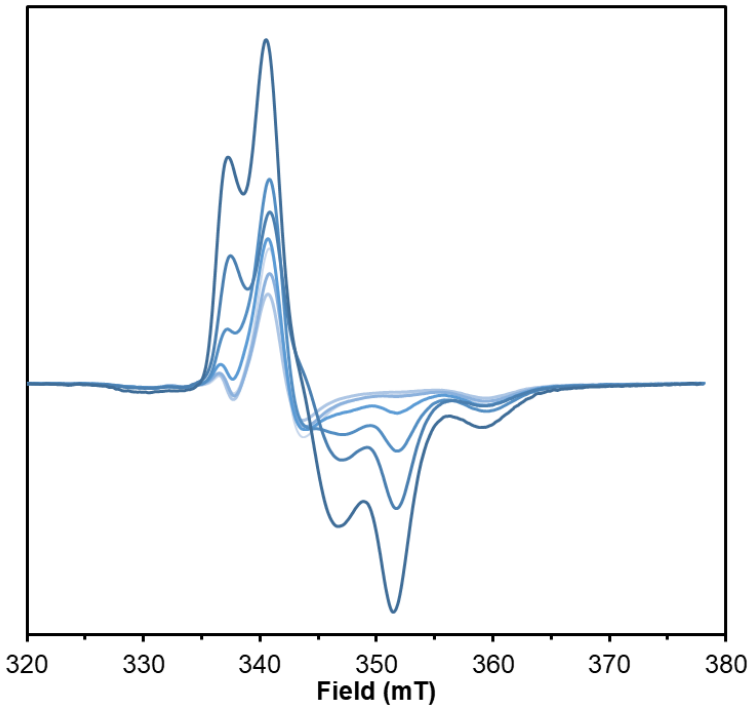

Figure 61. X-Band EPR spectra of H107C IscR at several pH values. pH values are between pH 6 (light blue) and pH 9 (dark blue). EPR conditions: Frequency: 9.4 GHz, T: 77 K, microwave power: 2 mW, modulation amplitude: 10 G, modulation frequency: 100 kHz.

Upon inspection of the EPR spectra obtained for H107C IscR protein, it was possible to observe a significant change in spectral features upon pH shift. Due to the lack of a protonable group in the direct vicinity of the cluster, spectral changes were not expected. It is not clear what these spectral changes might indicate, the best hypothesis is that the lability of the cluster is extremely pH dependent and that in part multiple breakdown products of the cluster are observed. For *g*-value determination, and initial determination of possible species mixture, four field values were chosen. These are (A) the first maximum, around 338 mT, with a *g*-value of 1.98; (B) the zero crossing of the high pH samples, around 343 mT, with a *g*-value of 1.95; the minimum of the high pH samples, around 351 mT with a *g*-value of 1.90; and (D) the minima of the low pH samples, at 360 mT, corresponding to a *g*-value of 1.85. Upon comparison with literature, it was noted that very few FeS clusters have all *g*-values below 2, with IscR as rare exception. However, no FeS cluster with three of those four values was found.

2.9.2. IscR H107D and H107E

Due to the complexity of the results obtained for the H107C mutant, it was attempted define His107 as ligand by generation of two other mutants, H107D and H107E, by site-directed mutagenesis. Aspartate and glutamate were chosen based on the premise that cluster instability and the appearance of inhomogeneous coordination of the His107Cys variant related to the difference in stereochemical constraints, hydrogen bonding and amino acid volume, when comparing histidine to cysteine. Again, cells were grown under the same conditions used for the wild type and H107C mutant. The appearance of the cells overexpressing the His107Asp and His107Glu mutants after harvesting and SDS-PAGE of cell extracts is shown in Figure 62.

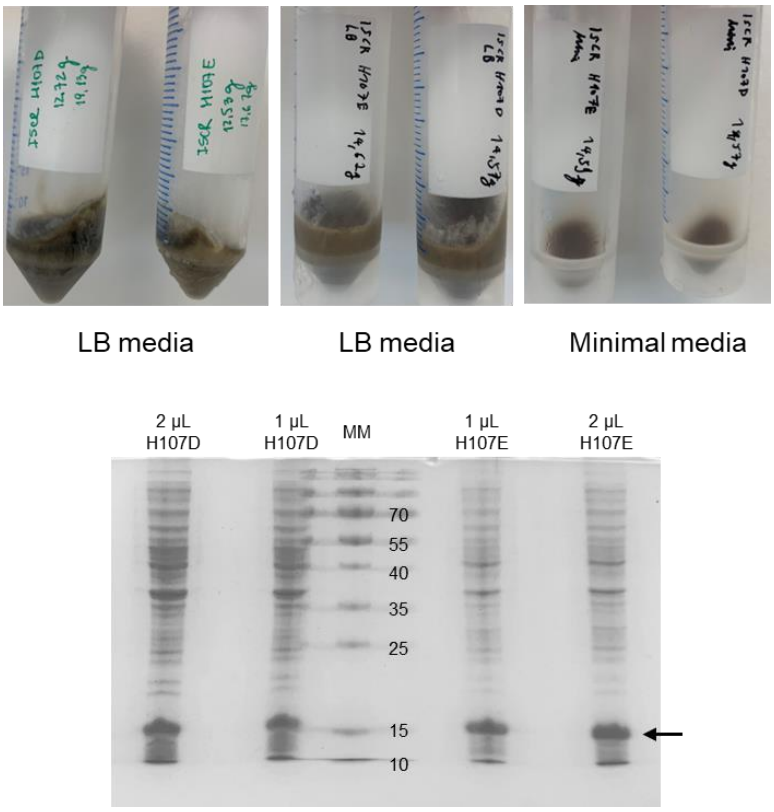

Figure 62. Cells containing overexpressed H107D and H107E IscR mutants (top) and corresponding Coomassie stained 15% SDS-PAGE gel (bottom) with LB media grown IscR mutants.

Both mutant proteins were successfully overexpressed by me and the PhD student Lukas Knauer, based on the presence of a thick characteristic band in the cell samples, slightly above 15 kDa, as observed previously for wild type and H107C proteins. However, upon three purification trails each time using a different batch of cells, no protein was obtained upon elution of the Heparin column with 650 mM KCl, neither in the holo nor in the apo state. Either the protein did not bind to the heparin column, or it rapidly denatured and remained on the column, or it was highly unstable and as misfolded protein degraded by proteolysis. The presence of aspartate or glutamate (negatively

charged ligand) at a position at which in wild type IscR histidine (neutral or positively charged ligand) is naturally present, could not only affect cluster binding but also lead to the disruption of hydrogen bonds and other local interactions that are necessary for the correct structure of the protein.

2.9.3. L136*, H143*, D146*, and R149*

SDS-PAGE gels of wild type and H107C IscR proteins occasionally exhibited two bands. It was then hypothesized that the band with the higher electrophoretic mobility derived from proteolysis of the flexible or intrinsically disordered C-terminus. Such C-terminal proteolysis is common if in the crystal structure of proteins, the electron density of termini is not defined. Rajagopalan and colleagues[70] as well as Santos and colleagues[177] were unable to observe the complete C-terminus of IscR in their four crystal structures. This observation is puzzling if one considers that IscR was purified via a C-terminal His-tag. Thus, it is most likely that the C-terminus is unstructured, or that the hexahistidine tag prevented binding to the structured core of the IscR dimer.

Alphafold3 predictions show that, starting from Glu128, the subsequent 34 amino acids could form a single alpha helix that ends in a disordered region extending beyond the protein's main globular shape. These helices, one from each monomer, extend in opposite directions, towards the outer side of the protein, and perpendicular to the direction of DNA binding. The production of truncated versions of IscR was targeted to improve the homogeneity and assess whether the C-terminus truncation influenced the biophysical properties of IscR. Truncations are also of interest for experiments with DEPC modification. Producing a mutant with the same overall stability and properties but containing one single histidine, His107 (the cluster ligand) and lacking the C-terminal His143 and His145 residues would exclude that spectral changes obtained by DEPC modification relate to the modification of these residues. Considering that IscR possesses three histidine residues in its primary structure, generation of a mutant (H143*) in which the His codon is replaced by a stop codon (*) would eliminate the two histidine residues.

Not only the H143* but also other truncated versions of IscR in which an amino acid was substituted by a stop codon were made, such as L136*, D146* and R149*. Mutants were made by site-directed mutagenesis by the technical assistant Doreen Knochenhauer. The purification and partial characterization of these IscR mutants was conducted by the Bachelor student Nicole Ultes in 2023, under my direct supervision. Due to time constraints, she could not purify the mutant L136*. Cell growth and protein overexpression was successfully achieved for the mutants D146*, R149* and H143*. In Figure 63 a first impression of the protein in the heparin column can be gathered.

SDS-PAGE gels were run to follow the purification of these mutant proteins (Figure 64). The analysis indicated that the expression and purification was successful for the D146* and R149* mutant proteins (Figure 64, top and middle gels) due to the presence of clear bands at ~15 kDa in the lanes corresponding to cell extracts and purified protein.

Figure 63. Heparin affinity purification of truncated IscR versions, IscR R149* (left), IscR D146* (middle) and IscR H143* (right). Reproduced from Nicole Ultes Bachelor thesis.

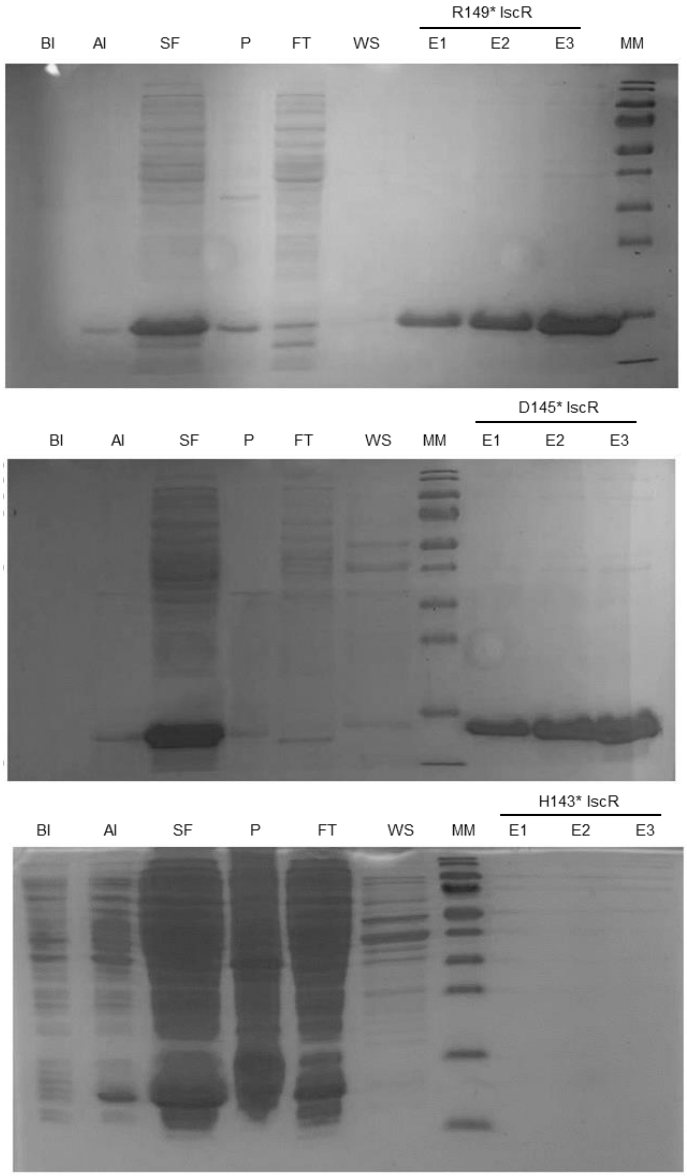

Figure 64. 15% SDS-PAGE analysis of the purification process of mutants R149* (top), D146* (middle) and H143* (bottom). Adapted from Nicole Ultes Bachelor thesis.

However, for the His143* IscR mutant, even though a ~15 kDa band was observed at the position corresponding to IscR in the cell extract, no soluble protein could be collected after elution with 650 mM KCl (Figure 64, bottom).

Interestingly, the R149* and D146*mutants showed very little protein in the flowthrough, but H143* showed a considerable amount of protein in this lane. Very little protein was also present in the wash step for the three mutants. Both R149* and D146* mutants showed single bands for IscR after purification; for the H143* mutant, however, only a very low amount of protein seemed to be recovered after elution, at least at the normal loading volume employed for wildtype IscR and the other two mutants. Thus, the amount of protein was much lower than obtained for the other two mutants. This might be because IscR's C-terminus contains many positively charged residues that could contribute to an efficient binding to the negatively charged heparin column. Since the heparin column mimics the negative charges found in the DNA, the H143* truncated protein's inability to bind the column could indicate a role for the C-terminus in DNA binding in the cell. The weaker binding of the H143* mutant agrees with the presence of some 15 kDa protein in the flowthrough.

To study the cluster of the C-terminally truncated mutant proteins, R149*, the least truncated protein, was chosen to be analyzed by CD spectroscopy due to its more robust behavior when compared to the other mutants. CD spectra were recorded at three pH values (Figure 65). However, due to the lower yields obtained, protein concentrations were lower when compared to IscR wildtype. This led to CD spectra with a low signal to noise ratio and, consequently, difficult data analysis.

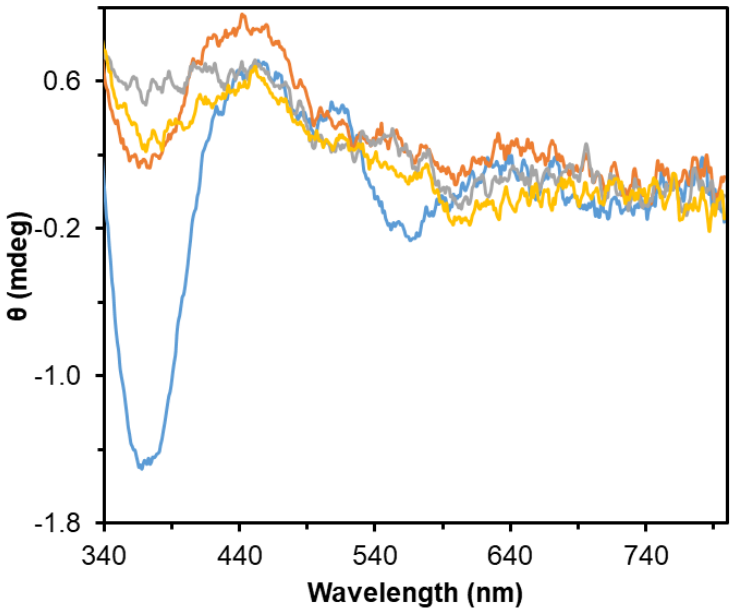

Figure 65. CD spectra of R149* IscR at different pH values. Samples analyzed had pH values of 7.4 (light blue), 8.4 (orange), 9.5 (gray) and 10.5 (yellow). Adapted from Nicole Ultes Bachelor thesis.

At pH 7.4 the R149* mutant shows a CD spectrum with reasonably well-defined spectral features. From the spectra recorded at pH 9.5 and 10.5 it appears that this mutant is less stable than wild type IscR. At all pH values, this mutant shows a minimum at 366 nm, but this minimum is more prominent in the spectrum at pH 7.4. At pH 7.4 two maxima, at 454 nm as well as 517, and another minimum at 568 nm are detected. The minimum at 568 nm at pH 7.4 is absent at other pH values or is shifted to around 600 nm. This experiment needs to be repeated with a higher protein concentration to accurately determine the pK_{ox} value.

Finally, some preliminary studies were made with the Leu136* mutant. Though it could be purified this mutant was the most unstable amongst all mutants. Figure 66 shows some of the purification steps. After cell disruption and ultracentrifugation, the soluble fraction (Figure 66, A and B) did not present the characteristic brown color already indicating a very low yield of protein or cluster content.

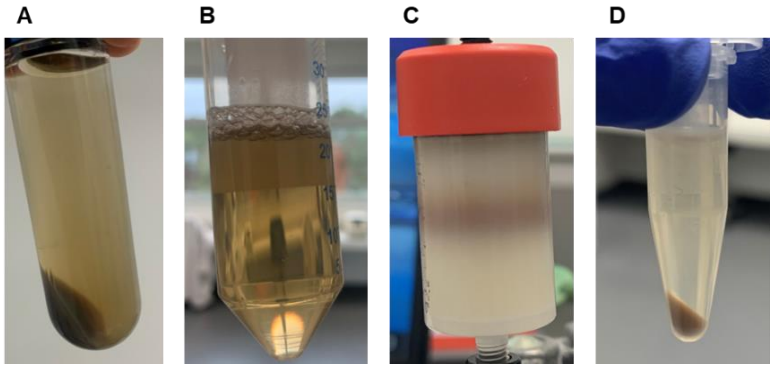

Figure 66. L136* IscR purification process. In this figure represented the ultracentrifuge tube after cell disruption and centrifugation (A) and the corresponding soluble fraction after filtration (B), as well as the protein in the column during elution (C) and the protein solution (D) after centrifugation to remove precipitated protein and broken-down cluster.

During elution (Figure 66, C), the protein looked brownish/reddish as expected. However, shortly after emerging from the column, the protein solution became turbid. A small brown precipitate was removed by centrifugation, and the clear soluble fraction was transferred to another Eppendorf tube. Further precipitation occurred in the following minutes. After a second centrifugation step, a large and brownish pellet was observed (Figure 66, D). Upon addition of 100 µL of 3 M KCl directly in the Eppendorf tube (total volume of 1050 µL) and mixing, the solution became translucid, and the pellet dissolved. This indicates a change in the protein's solubility due to a change in isoelectric point to a value close to the pH value used for purification, which could be counteracted by a higher ion strength. These properties were not suitable for further studies, and, except for UV-Vis spectroscopy, no further experiments were carried out with the mutant.

2.9.4. UV-visible characterization of all IscR variants

UV-Vis spectra were recorded for all mutants and compared with wild-type IscR (Figure 67). The inset shows an enlarged view of the visible region. Spectra were normalized to the protein peak at 280 nm. Wild type and R149* IscR appeared to have practically the same cluster content, but the spectral shape of the R149* was slightly different, resembling the one observed for IscR at high pH values. H143*, D145*, and L136* mutants had a progressively lower cluster content. The L136* mutant presented a very low absorbance in the visible range, which in part might be an artifact from light scattering. It appears that progressive truncation of C-terminal amino acids lowers the cluster content and the protein stability.

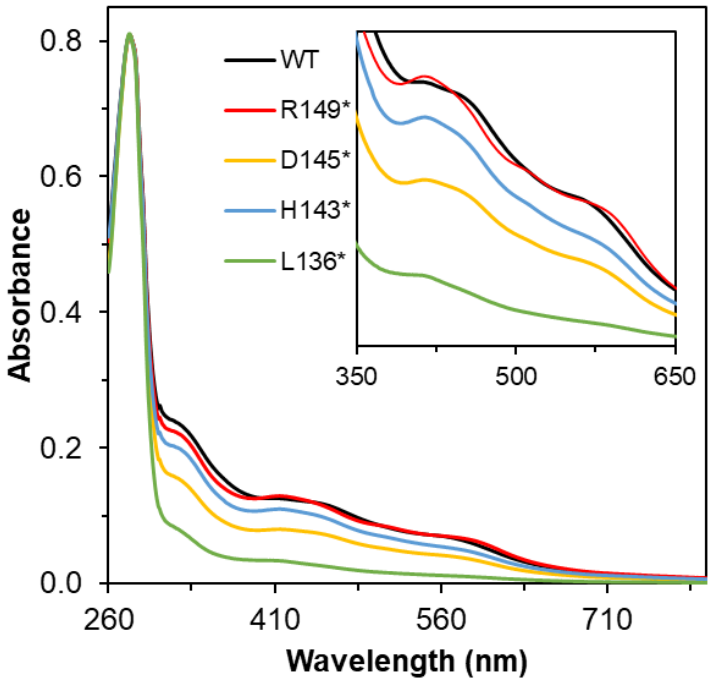

Figure 67. UV-Vis spectra of wild type (black), R149* (red), H143* (light blue), D145* (yellow) and L136* (green) IscR. The inset shows an enlarged view between 350 and 650 nm.

Additionally, it is interesting to note that for some mutants, as R149* and H143*, band shape and maxima appear to shift. Upon comparison with the UV-Vis spectra of wild-type IscR (Figure 18, section 2.2.2) these two mutants present UV-Vis features that match the ones shown by the alkaline version of wild-type IscR. This could indicate a shift in pK_a in the oxidized state in the mutant proteins and that the C-terminus might be more than a protruding flexible tail, perhaps even interacting with the cluster region. In summary, the study of truncated mutants was complicated by the low protein yield and stability. CD, EPR and Mössbauer spectroscopic studies as well as EMSA experiments were thus not feasible.

Chapter IV. The [3Fe-4S]$^{0/1+}$ cluster of the *E. coli* YjdI protein and its conversion to a [4Fe-4S]$^{1+}$ cluster

1. Introduction

E. coli YjdI is a small protein composed entirely of a so-called Domain of unknown Function 1271 (DUF1271). Very little research has been published on this protein. Most of the available information is present in Daniel Bak's PhD thesis, conducted under the supervision of Prof. Sean Elliott at Boston University[202]. Two Chapters of his thesis described cyclic voltammetry and stability studies of the MitoNEET protein, which were published in 2013[203]. But Bak also bioinformatically explored the connection between CDGSH-containing proteins, to which MitoNEET belongs, and the DUF1271. *E. coli* YjdI. Along with it, the Alvin0680 protein from *Allochromatium vinosum*, a complex protein with one DUF1271 and two CDGSH motifs, was also characterized. The *E. coli* YjdI *g*=2.02 EPR signal in the oxidized state was interpreted as evidence for a $[3Fe\text{-}4S]^{1+}$ cluster. Intriguingly, the electrochemistry of the *E. coli* YjdI protein yielded a redox potential of -762 mV. Such low potential could be from the transition between the reduced (0) and the super reduced (-2 net charge, all-ferrous cluster) form, as previously described by Duff and coworkers in 1996[204]. Though in the dithionite reduced state a broad *g*=1.92 EPR signal was observed, this signal was not taken as evidence for a $[4Fe\text{-}4S]^{1+}$ cluster. Various questions remained, but these were not followed up by further studies, nor by publication.

DUF1271 is annotated in databases such as Pfam and InterPro as a divergent [4Fe-4S] mono-cluster containing domain. The domain is currently described as a protein domain family called Fer4_19 (Pfam: PF06902) matching over 5000 proteins in the database. In the Pfam database, 52 domain architectures are found. The main architecture, found for slightly less than half of the matches, only contains a single PF06902 domain, as is the case for *E. coli* YjdI. Around 18% of the proteins, the second most common architecture, have one PF06902 domain and one PF09360 domain (CDGSH, likely binding a MitoNEET like [2Fe-2S] cluster). Around 30% of the proteins consist of one PF06902 domain and two PF09360 domains, as described by Bak in Chapter 4 of his thesis. However, this architecture is equally divided between two different sequential arrangements – A, B, B or B, A, B, where A is the PF06902 domain and B is the PF09360 domain binding a MitoNEET like [2Fe-2S] cluster. This equal division causes each of these to become the third most common architecture.

In total, these four architectures of domain organization in nature comprise almost all the, so far, described PF06902 domains in nature. Other much less common architectures worth mentioning are the fusions of the PF06902 domain with ferritin-like, osmotically inducible protein, and bacterial globin domains. An interesting fusion with a “beta lactamase” domain is also in the domain architecture database. It is predicted to contain a diiron center, along with a flavodoxin domain. In their review of the various classes of flavodiiron proteins (FDP) Folgosa *et al.*[205] already described this architecture as class E FDPs. They noted that in FDPs of *Syntrophomonadaceae* the YjdI-like domain had a $CXHXXXCX_{33}CP$ consensus motif and could possibly bind a [3Fe-4S] or [4Fe-4S] center. Recently, follow up studies by the same group on a class E FDP from *Syntrophomonas wolfei* were deposited

on BioRxiv by Maria C. Martins and coworkers[206]. The analysis of the most common distribution of Fer4_19, including a Class E FDP and their relative occurrence is shown in Figure 68.

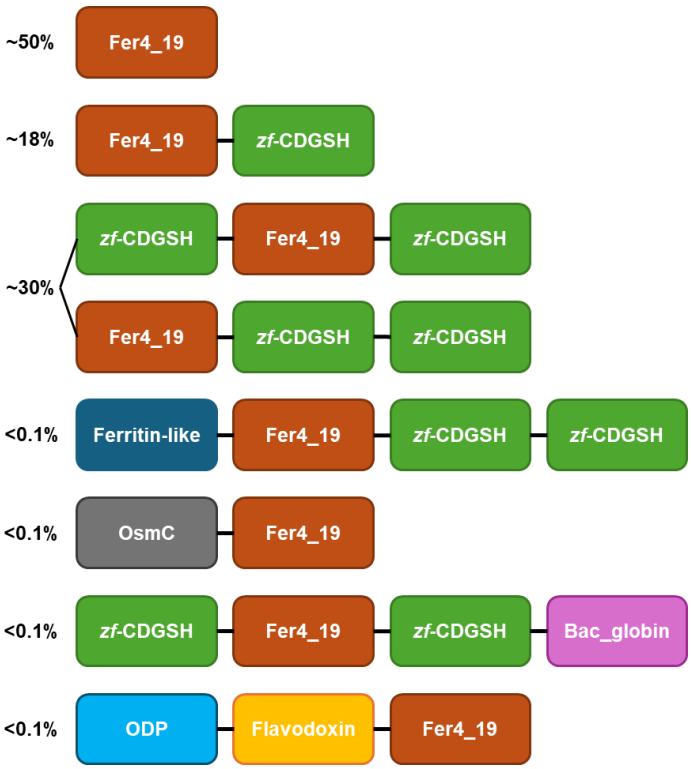

Figure 68. Cartoon representation of some protein architectures containing the Fer4_19 domain. The size of each domain is not to scale with their real size. Fer4_19 - Divergent 4Fe-4S mono-cluster; *zf*-CDGSH - Iron-binding zinc finger CDGSH type; OsmC- Osmotically inducible protein C-like domain; Bac_globin- Bacterial-like globin; ODP - ODP family beta lactamase.

AlphaFold predictions (available in the AlphaFold website with the UniProt code P0AF59, https://alphafold.ebi.ac.uk/entry/P0AF59, on November 4th, 2024) for the structure of *E. coli* YjdI show that Cys12 is not spatially close (16 Å) to the putative cluster binding Cys27, Cys33, and Cys66, indicating that this domain could either bind a [3Fe-4S] cluster, as described by Bak, or harbor a [4Fe-4S] cluster with a non-cysteinyl coordination, possible the conserved His29. A biochemical and spectroscopic characterization was performed to better understand the physical properties and perhaps elucidate the *in vivo* function of YjdI. The practical work was performed in part by Alissa Agovic as part of her Bachelor thesis under my direct supervision. Without exception these data were acquired together and are here summarized and, in several cases, reanalyzed and reinterpreted in paragraph 2.1. to supply an introduction to the EPR spectroscopic studies. Acquisition of all EPR spectroscopic data and the spectroscopic analysis was carried out by me.

2. Results and discussion

2.1. Expression, purification, UV-Vis and CD spectroscopic characterization

By cloning of the *E. coli yjdI* gene into pPR-IBA101 expression of C-terminally Twin-Strep-tagged was pursued. Below the encoded amino acid sequence is shown, with the cysteine residues highlighted in blue, the N-terminal extension from cloning highlighted in pink, the linker highlighted in green, and the Twin-Strep tag underlined.

MGDRGPEFMNQALLDGGYRCYTGEKIDVYFNTAICQHSGNCVRGNGKLFNLKRKPWIMPDEVDV
ATVVKVIDTCPSGALKYRHKLQGDHGLSAWSHPQFEKGGGSGGGSGGGSWSHPQFEK

Without the tag YjdI is composed of 76 amino acids and has a molecular mass of 8.55 kDa, while the construct used here has 121 amino acids with a corresponding mass of 13.17 kDa. Its estimated isoelectric point is 8.4 with the tag and 6.5 without it. Plasmid transformation was performed in BL21(DE3) with and without the pRKISC plasmid. After transformation and plating, the cells harboring the pRKISC plasmid were chosen for overexpression due to the number and size of the colonies present on the plate. Growth before induction appeared to be normal but slowed down after induction. After growth and harvesting a yield of ~ 2 g of cells per liter was obtained. After disruption with a French Press and ultracentrifugation of the lysate, the soluble fraction presented a dark brown color. This color was likely due to a successful overexpression process and the presence of protein with an efficient cluster incorporation. The soluble fraction was then anaerobically loaded in a Strep Tactin XT 4-FLOW previously equilibrated with anaerobic buffer, and the protein purification carried out using a Twin-Strep-tag present at the protein's C-terminus. Figure 69 shows the purification steps of loading, column washing and elution of the protein.

During the wash step (Figure 69, Panel B), it was possible to observe that the column was completely saturated with protein, indicating that some protein was lost in the flowthrough and/or wash step. Elution yielded a dark brown solution. By looking at the solution against light (Figure 69, Panel E) it became clear that the solution was translucid without indication of protein precipitation.

SDS-PAGE was carried out and showed that after induction a band increased, which had the same apparent mass of approx. 12 kDa as the YjdI protein after elution with biotin (see Alissa Agovic's Bachelor thesis)[207]. Thus, the purification process was successful.

Protein quantification was performed twice for the two batches of YjdI protein isolated from two separate batches of *E. coli* cells, one with and the other without ^{57}Fe labelling. The average concentrations as well as the cluster incorporation are presented in Table 25.

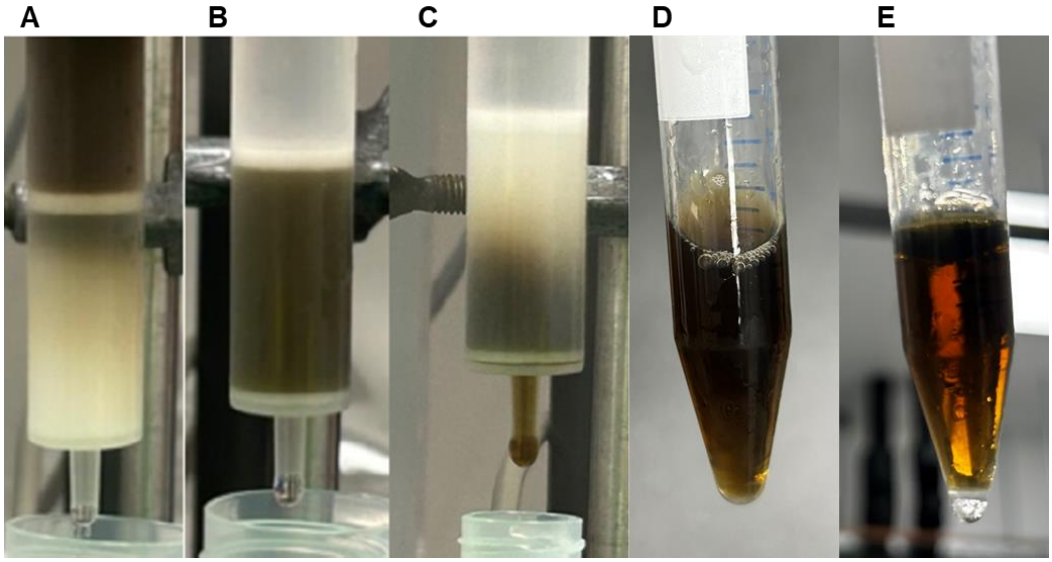

Figure 69. YjdI purification process. (A) soluble fraction loading; (B) wash step; (C) protein elution; (D) YjdI after purification and (E) YjdI after purification against light. Adapted from Alissa Agovic's practical report.

Table 25. Protein, iron and acid-labile sulfide determination for *E. coli* YjdI.

	Preparation 1: ^{57}Fe	**Preparation 2: naturally abundant Fe**
Protein (mM)	0.162	0.295
Iron (mM)	0.426	0.400
S^{2-} (mM)	0.261	0.280
Fe/protein	2.6	1.4
S^{2-}/protein	1.6	1.0

According to these results, there are approximately 1.0 to 1.6 acid-labile sulfur atoms per polypeptide chain, while 1.4 to 2.6 atoms of iron were observed. Considering that for 100% incorporation 4 sulfur atoms and 3 Fe atoms, for a [3Fe-4S] cluster, or 4 Fe atoms, for a [4Fe-4S] cluster, would be observed, the cluster incorporation was calculated. According to the acid-labile sulfur quantification, 25-40% of the protein molecules contained a cluster. But this method is known to be less reliable than the Fe determination by the Ferene method. For iron quantification the incorporation was calculated to be between 47-87% for [3Fe-4S] or 35-65% for [4Fe-4S]. These data do not allow the determination of the type of cluster present in YjdI but indicate that the cluster incorporation is below 100%. Though protein determination was carried out with the Microbiuret/TCA method, it seemed appropriate to employ UV/visible spectroscopy to independently assess the cluster content.

The UV-Visible spectrum of as isolated YjdI was recorded between 250 and 800 nm with a dilution of 1:20 and is represented in Figure 70. This spectrum shows two maxima at approximately 420 and 670 nm, besides the protein peak centered at 280 nm. These features can be characteristic of [4Fe-4S]$^{2+}$ clusters, but such features are also seen for [3Fe-4S]$^{1+}$, or a mixture of these clusters. UV-Vis spectra of [3Fe-4S]$^{1+}$ typically show a maximum at around 412 nm with less intense features at 320 and 455 nm, whereas [4Fe-4S]$^{2+}$ clusters usually exhibit a peak with a maximum centered between 380 and 420 nm and a shoulder at approximately 305 nm. These interactions result from LMCT from the sulfides to the iron ions[10,130,208]. A small artifact can be seen at around 310 nm caused by the lamp switch in the spectrophotometer. In the same spectrum, it is possible to observe a small and broad peak centered around 670 nm. This could possibly be attributed to electronic transitions between iron ions with different oxidation states, usually observed in the near infrared range of the spectrum.

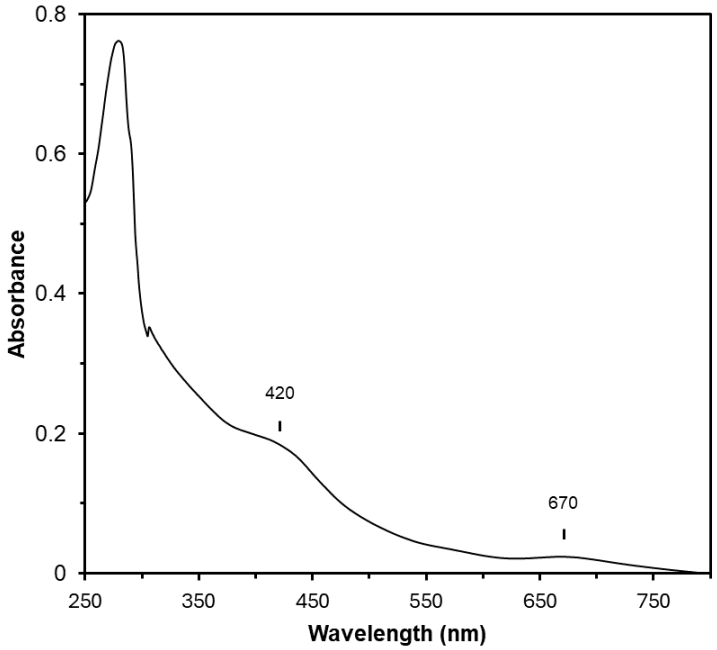

Figure 70. UV-Vis spectrum of YjdI, diluted 1:20. Adapted from Alissa Agovic's practical report.

The predicted extinction coefficient of YjdI based on tryptophan/tyrosine content is 22460 $M^{-1}cm^{-1}$ at 280 nm. With this information, a protein concentration of 0.68 mM was calculated. A clear disparity is observed upon comparison with the results obtained by colorimetric protein determination. It is worth noting that not only [2Fe-2S]$^{2+}$ clusters absorb around 280 nm, but also [3Fe-4S] and [4Fe-4S] clusters[209]. This causes an overestimation of the protein concentration based on 280 nm absorbance. The primary structure of YjdI contains four tyrosine, three tryptophan, and five phenylalanine residues, a high number for a small protein. However, two tryptophan and two phenylalanine residues were introduced with the Twin-Strep-tag. A final concentration of protein of 0.41 mM can be calculated

considering the same contribution of the FeS cluster at 280 nm as at 420 nm, as done for IscR in Chapter III. This value is slightly higher when compared to the obtained by the colorimetric method.

Determination of FeS cluster concentration is also possible with UV-Vis. But $[4Fe\text{-}4S]^{2+}$ and $[3Fe\text{-}4S]^{1+}$ clusters have very similar spectra and extinction coefficients at 420 nm. For $[4Fe\text{-}4S]^{2+}$ clusters extinction coefficients of 15000 to 17000 M^{-1} cm^{-1} are reported, resulting in an extinction coefficient of 4000 M^{-1} cm^{-1} per iron atom in ferredoxins and model compounds[184,209], while $[3Fe\text{-}4S]^{1+}$ typically present a slightly lower extinction coefficient of 14000 M^{-1} cm^{-1} [210], so the per iron extinction coefficient is similar. Calculating the cluster concentration with an extinction coefficient of 15000 M^{-1} cm^{-1} YjdI would present 0.25 mM cluster, assuming that the cluster is oxidized. If the amount of $[3Fe\text{-}4S]^{0}$ cluster is substantial, the cluster content might have been underestimated.

If a cluster has a sufficiently high redox potential, an anaerobically purified protein can contain reduced FeS clusters. This does not apply to $[4Fe\text{-}4S]^{2+/1+}$ clusters, which have a very low redox potential. But for IscR[71] (Chapter III), the [3Fe-4S] form of aconitase[211] and ferredoxins with a $[3Fe\text{-}4S]^{1+/0}$ cluster[212] proteins can be isolated with the cluster (partially) in the reduced state. Therefore, a titration with potassium ferricyanide was performed to obtain evidence for the presence of $[3Fe\text{-}4S]^{0}$ clusters. However, because potassium ferricyanide absorbs in the visible range ($\varepsilon_{420\ nm}$ =1020 $M^{-1}cm^{-1}$)[213] small volumes were added stepwise to carefully oxidize and avoid the unwanted contribution of an excess of ferricyanide. In this titration, shown in Figure 71, nine additions of 10 µM ferricyanide were performed, but only the first four, that led to cluster oxidation are represented in this figure. The remaining six additions did not significantly change the spectrum. Contarily, a steady decrease in absorbance, possibly due to cluster breakdown was observed.

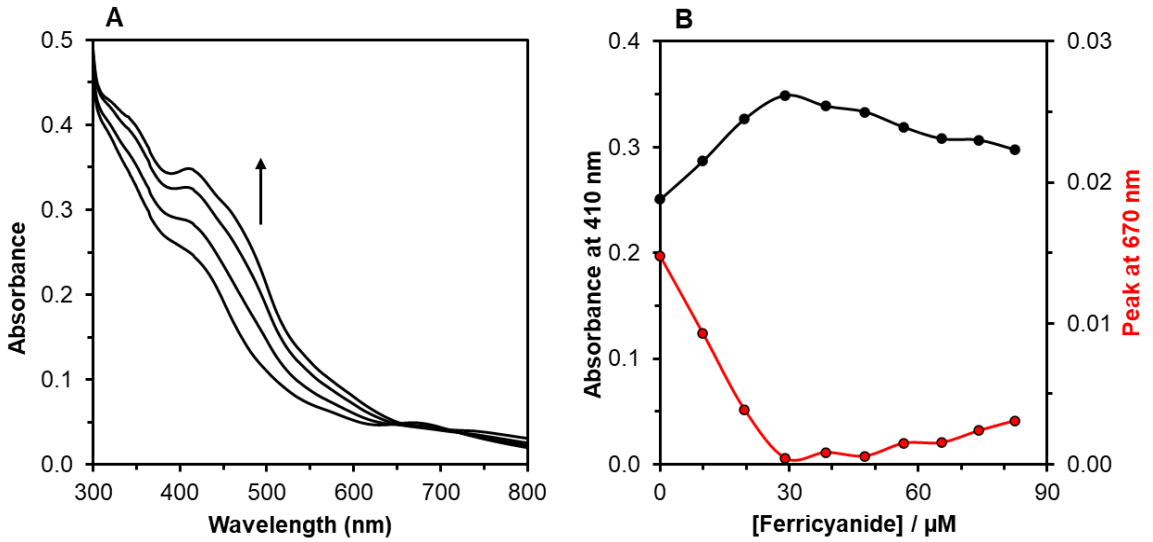

Figure 71. First four spectra of the UV-Vis titration of YjdI with potassium ferricyanide (A). UV-Vis spectra from Alissa Agovic. Reanalysis of absorbance at selected wavelengths (B). The netto absorbance at 670 nm was calculated by subtracted the average absorbance at 670 nm.

After addition of 30 µM ferricyanide the 670 nm band disappeared, and the spectra show features that were not present in the spectra of YjdI as isolated. Namely the very broad 400 nm shoulder changed into a peak at 410 nm and a shoulder at 460 nm. Besides that, the shoulders at 330 nm became more pronounced in these spectra. These results seem to indicate that a significant proportion of the as isolated YjdI contains a $[3Fe\text{-}4S]^{0}$ cluster, which has a 670 nm band, that converts to $[3Fe\text{-}4S]^{1+}$ as previously observed for aconitase in the inactive state[211] and *Mycobacterium tuberculosis* ferredoxin[212]. But it cannot be excluded that a population with a $[4Fe\text{-}4S]^{2+}$ cluster was present. After further addition of ferricyanide (up to a final concentration of 83 µM) a decrease of visible absorbance is detected, which possibly results from cluster breakdown combined with reduction of the added ferricyanide by the released sulfide ions.

UV-Visible spectroscopy was also used to assess cluster stability with time. Based on the ferricyanide oxidation experiment the spectra recorded are initially for the $[3Fe\text{-}4S]^{0}$ species. In the experiment, 75 consecutive 3-minute scans were recorded. The result is shown in Figure 72.

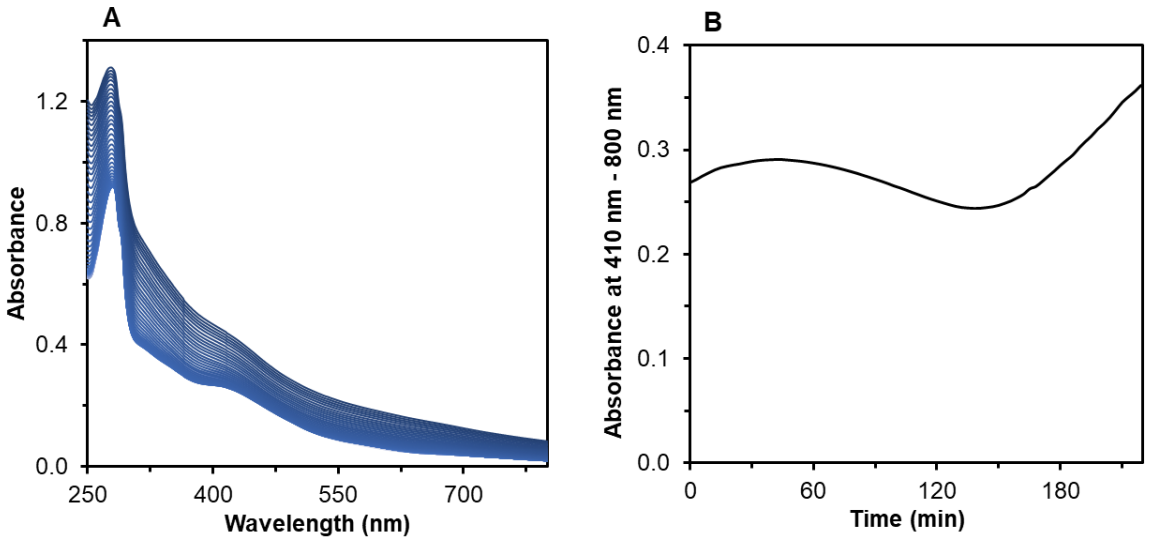

Figure 72. UV-Vis stability study of YjdI. A series of 75 scans of 3 minutes was measured. (A) Reanalysis of data from Alissa Agovic. (B) Analysis of the three phases of the conversion.

In this experiment three different phases were identified. To optimally discriminate between these phases the absorbance at 410 nm minus 800 nm was monitored as a function of time. Up to 45 minutes, a minor increase of the visible absorbance in the range between 300 and 550 nm occurs (Figure 72, Panel B). This increase might indicate partial oxidation of the [3Fe-4S] cluster to the $[3Fe\text{-}4S]^{1+}$ state, but not as extensive as in the ferricyanide experiment. Between 45 and 140 minutes, the absorbance between 300 and 500 nm slowly decreases with time, which might indicate cluster breakdown or re-reduction. After 140 minutes, however, there is a strong increase in absorption over the whole 250-800 nm range, indicating protein precipitation (Figure 72, Panel A).

Additionally, CD spectroscopy was used to study the secondary structural elements of YjdI. The spectra of YjdI between 200 and 280 nm over time, 30 scans of approximately 2 minutes each, are shown in Figure 73. In its CD spectrum YjdI has one minimum at 207 nm and a shoulder at approximately 215 nm. These spectral features are characteristic of α-helices. However, in contrast to IscR, YjdI does not show a true minimum between 220 and 223 nm, which could be due to contributions of the cluster in the UV region. Instead, a shoulder in this position could indicate a mixture between α-helices and β-sheets. It is also worth noting that, even though a 7 % decrease in ellipticity is observed over time (Figure 73, Panel B), no shape changes or shift of the minima are observed. This might indicate a mild rearrangement in secondary structure over time, or a contribution of the cluster in the UV region of the CD spectrum, changing due to cluster conversion.

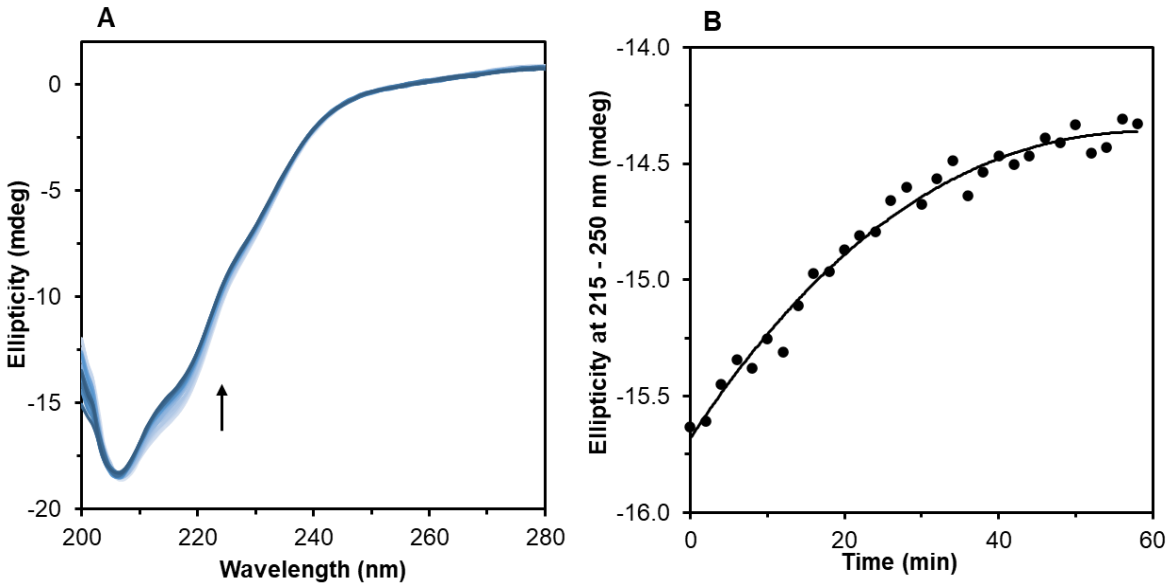

Figure 73. UV CD spectroscopy of YjdI in phosphate buffer. 30 2-minutes scans are shown where light blue indicates shorter and dark blue longer times. Adapted from Alissa Agovic's practical report.

2.2. EPR spectroscopy

2.2.1. Oxidized, as isolated and reduced YjdI

EPR spectroscopy was used to identify and determine the oxidation state of YjdI's cluster after purification. The X-Band EPR spectra are represented in Figure 74. In this experiment it is possible to identify the very pronounced spectral features of a $[3Fe\text{-}4S]^{1+}$ cluster in the oxidized sample. The intense quasi-isotropic S=1/2 signal at g= 2.013 is a typical signal found for this type of cluster[10,214,215]. The same signal is found in the sample as isolated although the signal amplitude is significantly less intense (Figure 74, Panel D). Comparison of signal intensity between the oxidized and as isolated sample, under the assumption that oxidation did not convert $[4Fe\text{-}4S]^{2+}$ to $[3Fe\text{-}4S]^{1+}$, indicated that YjdI contains only 3.8± 0.2% of cluster in the oxidized state after purification. The signal obtained for the sample in the dithionite reduced state in the g=2 area is merely background from the EPR cavity,

showing that dithionite completely reduced the 3.8 % $[3Fe\text{-}4S]^{1+}$ cluster of the as isolated state (Figure 74, Panel C).

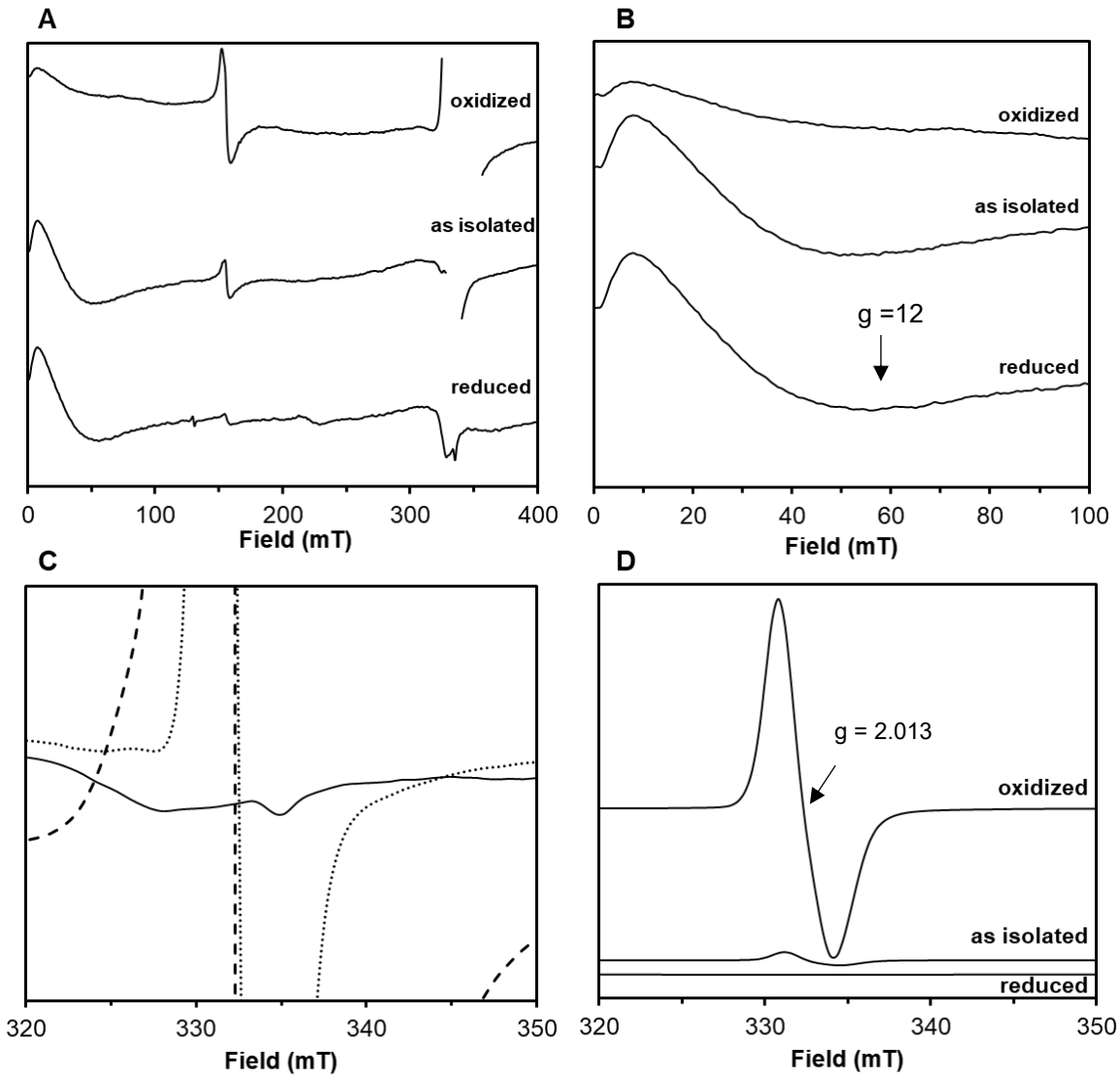

Figure 74. EPR spectra of oxidized, as isolated and reduced *E.coli* YjdI. (A) Stack plot of full EPR spectra from 0-400 mT where intense signals at *g*=2 were omitted for better signal visualization. (B) Zoomed in version of (A) between 0-100 mT. (C) Zoomed in version of the g=2 region between 320-350 mT. (D) stack plot of the *g*=2 region showing real amplitudes of the *S*=1/2 signal. Adapted from Alissa Agovic's practical report. EPR conditions: Frequency: 9.4 GHz, T: 10 K, microwave power: 2 mW, modulation amplitude: 10 G, modulation frequency: 100 kHz.

A broad signal at low field values with a minimum at *g*=12 is revealed, that is typical for an *S*=2 spin system[216,217] (Figure 74, Panel A). This signal is observed both in the reduced and in the as isolated sample, but not in the fully oxidized sample (Figure 74, Panels A and B). Comparing the intensity of the *S*=2 signal through a subtraction of the amplitudes at the minimum and maximum, it can be estimated that YjdI as isolated contained approximately 95 ± 3% of reduced [3Fe-4S] cluster. These values agree with the obtained for the *S*=1/2 signal.

2.2.2. Dye-mediated redox titration of YjdI

To determine the cluster's redox potential a reductive and an oxidative dye-mediated redox titrations were carried out. In these titrations, the variation of the *S*=1/2 and *S*=2 signals was monitored as an indicator of the presence of $[3Fe\text{-}4S]^{1+}$ and $[3Fe\text{-}4S]^{0}$ species. Figure 75 shows stack plots of EPR spectra of the reductive, between -481 and +114 mV versus S.H.E, and oxidative, between +3 and +207 mV, titrations and original data can be found in the supplementary data. All spectra were measured at 2 mW and at 10 K, except for the spectra relating to temperature dependence of the signal where the temperature is indicated.

Analyzing the lower field region of the spectra (Figure 75, Panel A) one observes that the amplitude of the *g*=12 signal increases from +114 mV to +13 mV but remains roughly constant below that potential. This indicates that the redox potential is more positive than +13 mV. This is uncommon for [3Fe-4S] clusters that usually present negative midpoint potentials of -450 to -150 mV[50], though in some proteins like *E. coli* fumarate reductase -70 mV)[218] and NiFe hydrogenases (+60 and +65 mV) higher midpoint potentials have been found[219,220]. In the *g*=2 region (Figure 62,B), the same signal observed for the oxidized sample in Figure 56 is seen in the sample with a redox potential of +114 mV, which agrees with the results obtained for the reduced *S*=2 species. It should be noted that the signal belonging to the $[3Fe\text{-}4S]^{1+}$ cluster (*g*=2.013) observed in the sample poised at +114 mV is different from signals at *g*=2.000 that appear at low redox potentials from the mediators methyl- and benzylviologen that upon one-electron reduction are radicals.

The oxidative titration (Figure 75, C) yielded similar results for the *g*=2.013 signal appearing above +127 mV and presenting a similar amplitude at +166 mV and 207 mV. In comparison with the reductive titration sample at + 114 mV, the signal obtained in the sample +127 mV is less intense, which can be attributed to differences in equilibration time in the two experiments.

The intensities of the *S*=2 and *S*=1/2 EPR signals as function of the redox potential could be fitted to the Nernst curve. The fitting obtained for the reductive titration, measuring the intensities of the *S*=2 signal yielded a redox potential of +184 mV. The fitting of the oxidized fraction from the amplitude of the *S*=1/2 signal yielded a midpoint potential of +153 mV. Neither data set has the precision required to accurately determine the midpoint potential, but they indicate that the redox potential is positive and between +100 and +200 mV. It is likely that breakdown of the cluster or conversion between [3Fe-4S] and [4Fe-4S] forms has complicated the titrations. To precisely determine the midpoint potential of the $[3Fe\text{-}4S]^{0/1+}$ cluster it is necessary to perform redox titrations with smaller reduction/oxidation steps, between 0 and 300 mV.

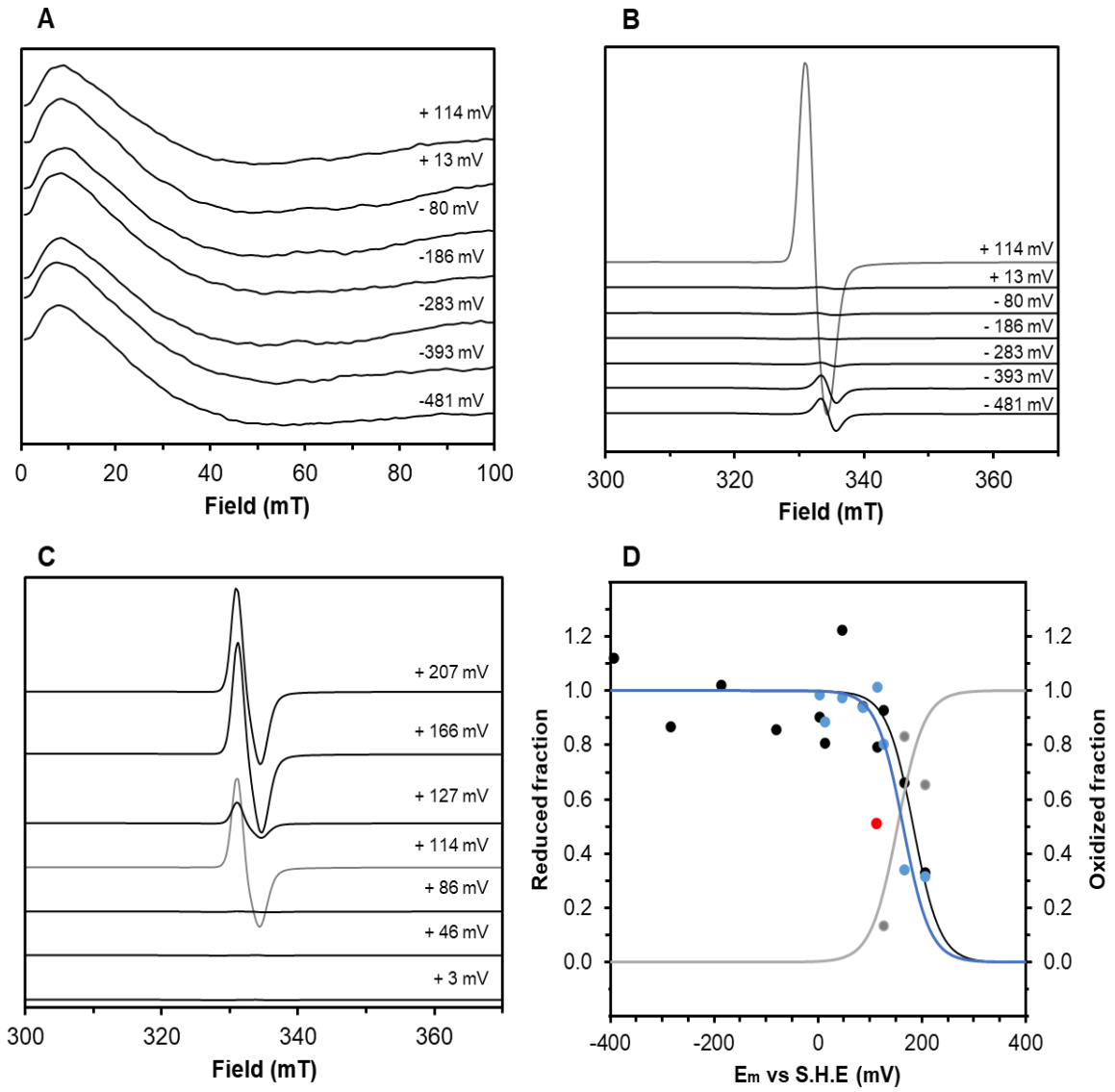

Figure 75. Oxidative and reductive dye-mediated redox titrations of YjdI measured by EPR. (A) *S*=2 signal and (B) *S*=1/2 observed in the reductive titration; (C) *S*=1/2 signal observed in the oxidative titration plus signal at +114 mV from the reductive titration; (D) reduced (black, *S*=2) and oxidized (blue, *S*=2, and gray, *S*=1/2) fractions obtained from the normalization of the signal amplitude peak to peak. Red point represents the amplitude of the *S*=1/2 signal of sample +114 mV. Adapted from Alissa Agovic's practical report. EPR conditions: Frequency: 9.4 GHz, T: 10 K, microwave power: 2 mW, modulation amplitude: 10 G, modulation frequency: 100 kHz.

2.2.3. Cluster reconstitution

Following the finding that YjdI mainly contained a [3Fe-4S] cluster, reconstitution was attempted to generate a [4Fe-4S] cluster. The protein was incubated with Mohr's salt (ammonium iron(II) sulfate) for 4 and 30 min and then fully reduced with dithionite for 3 minutes. The results are shown in Figure 76.

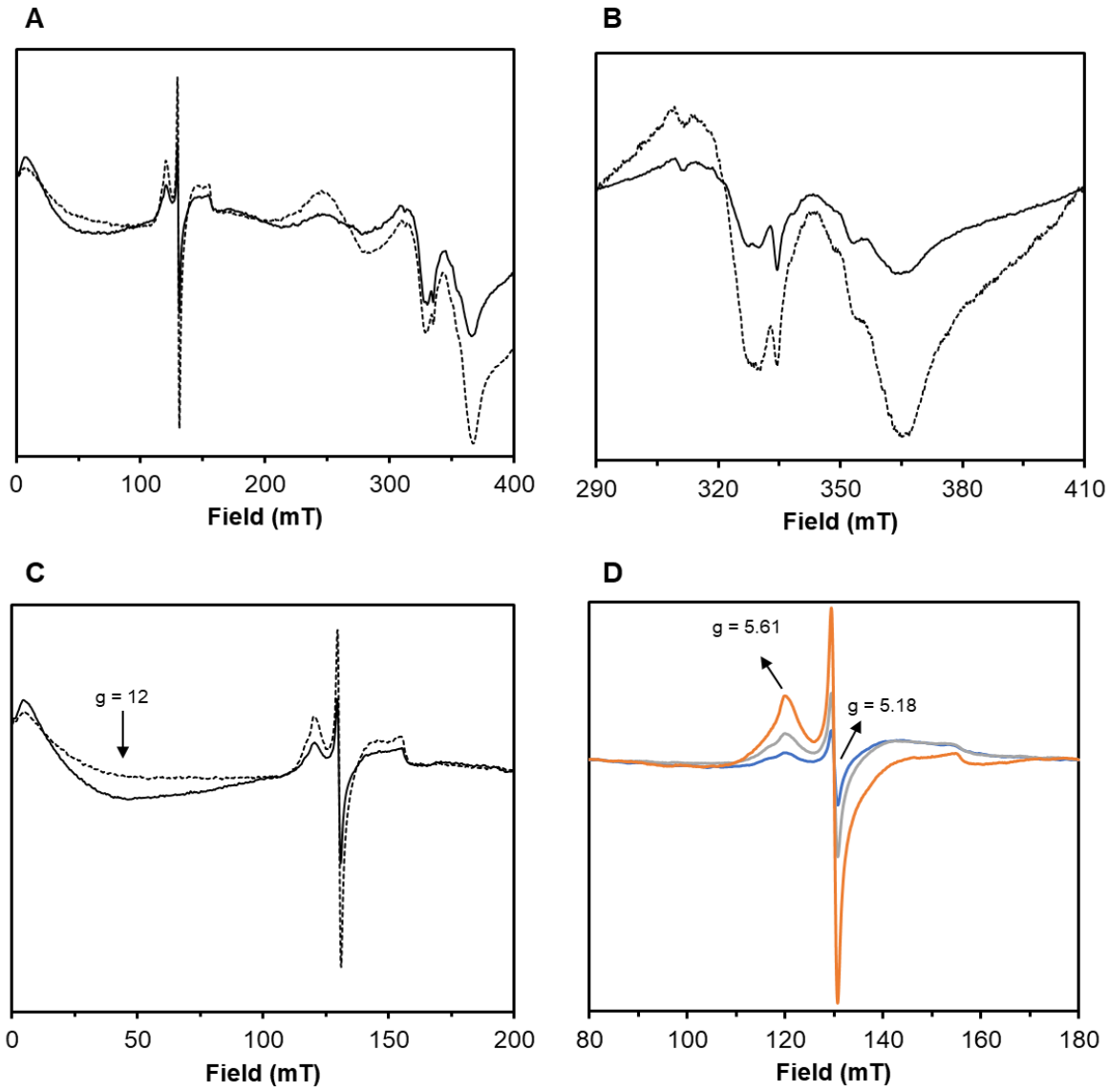

Figure 76. EPR spectra of YjdI after reconstitution for 4 and 30 minutes with Fe^{2+}. (A) Whole spectrum 0 to 400 mT; (B) Spectra of the sample incubated for 4 minutes between 290 and 410 mT and (C) between 0-200 mT. Full and dashed line indicate sample incubated for 4 and 30 minutes, respectively; except on Panel B, where it corresponds to 0.2 and 2 mW microwave power. (D) Temperature dependence of the signal in the sample incubated for 30 min. Spectra were multiplied by their temperature. Orange represents 20 K, grey 10 K and blue 7 K. Adapted from Alissa Agovic's practical report. EPR conditions: Frequency: 9.4 GHz, T: 10 K, microwave power: 2 mW, modulation amplitude: 10 G, modulation frequency: 100 kHz.

In this experiment the signal at *g*=12 corresponding to the *S*=2 state of the $[3Fe\text{-}4S]^0$ form can be seen in both 4- and 30-minutes samples (Figure 76, Panels A and C). The signal amplitude however is lower in the sample incubated with ferrous ions for 30 minutes indicating that a longer incubation led to the decrease of the $[3Fe\text{-}4S]^0$ cluster species. New signals not observed in the previous experiments can be seen at a magnetic field between 100 and 175 mT (Figure 76, Panels A and C). These signals are present both in the 4- and 30-minutes samples but presenting a higher amplitude in the sample incubated for 30 minutes. There is a sharp derivative-shaped but not completely

isotropic *g*=5.18 EPR signal and an absorption-shaped signal at *g*=5.61, which due to their *g*-values >>2 are attributed to a high spin species, possibly of a $[4Fe\text{-}4S]^{1+}$ cluster formed by insertion of a ferrous ion into the $[3Fe\text{-}4S]^{0}$ cluster[221].

A further signal, also not observed in the previous experiments, can be seen in the *g*=2 region (Figure 76, Panels A and B). This signal can be attributed to a low spin $[4Fe\text{-}4S]^{1+}$ cluster with a derivative shaped feature at *g*~1.89. The signal assigned to the $[3Fe\text{-}4S]^{1+}$ is not observed in these samples as expected, since the protein was reduced with sodium dithionite. Comparing the amplitude of the *S*=1/2 signal in both samples (4 and 30 min) it is possible to observe that incubation with iron for a longer time leads to a simultaneous 2-fold increase of both high and low spin EPR signals.

The sample incubated with ferrous ions for 30 min was measured at three different temperatures – 7, 10 and 20 K – to determine the nature of the signals observed in the $g \approx 5$ region. All three spectra were multiplied by their corresponding temperatures to correct for the general Curie-law temperature dependence. These three spectra are depicted in Figure 76, Panel D. It is observed that the intensity of both EPR features at *g*= 5.61 and *g*= 5.18 increases with temperature. This indicates that these two signals derive from an excited state and possibly belong to the same species. These data, combined with the asymmetry of the signal at *g*= 5.18, seem to indicate an axial symmetry with g_z= 5.61 and g_{xy}= 5.18. Looking closely, a small shoulder is present around 115 mT (*g*= 5.76). This shoulder is present at low temperatures but disappears at 20 K, which would assign it to a transition within a lower energetic level or a ground state of the same spin system as the g_z= 5.61 and g_{xy}= 5.18 signals.

In case these three signals belong to the same species it would be necessary to simulate the spectra and compare them with rhombograms. This would allow the determination of the rhombicity and the Kramers' doublets to which these species belong to. The data obtained so far indicates that the axial EPR signal is from the $|\pm 3/2\rangle$ Kramers' doublet of an *S*=7/2 or *S*=9/2 spin system (the corresponding rhombogram can be found in the supplementary information S.8.). Since the intensity only increases at T > 10 K, the D value is presumably negative.

In a second reconstitution experiment the number of equivalents of iron used was tested. Samples were prepared by incubation of YjdI with zero, two and four equivalents of ferrous ions for 30 minutes after which they were reduced with sodium dithionite, incubated for 30 more minutes and shock-frozen in EPR tubes. The results shown in Figure 77 indicate that no reconstitution occurred in the sample without added iron ions since the signals obtained are very similar to the ones observed in Figure 74.

However, for the samples reconstituted with two and four equivalents of iron ions, the presence of the same signals as observed in Figure 76 as well as the decrease of the intensity of the signal at *g*=12 corresponding to the $[3Fe\text{-}4S]^{0}$ cluster indicate a successful reconstitution. A small and barely

significant increase in signal intensity was observed from two to four equivalents, as reconstituting the cluster with two equivalents Fe^{2+} yielded 95 ± 5 % of the signal obtained for a reconstitution with four equivalents. This indicates that time was the limiting factor, but not the amount of Fe^{2+} available for reconstitution.

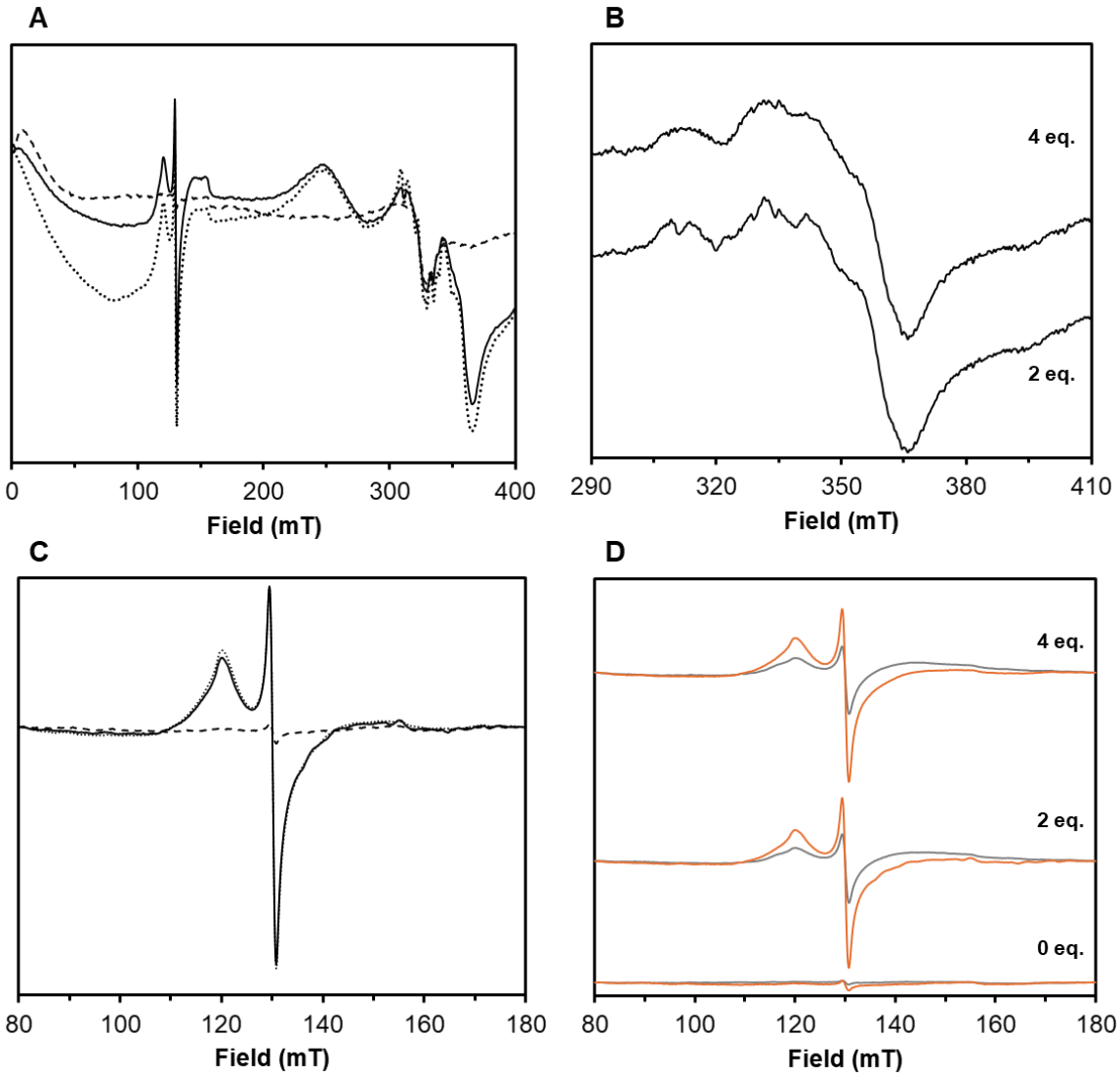

Figure 77. EPR spectra of YjdI after reconstitution with zero, two and four equivalents of Fe^{2+}. (A) Whole spectrum 0 to 400 mT; (B). Zoomed in spectra between 290 and 410 mT and (C) between 80-180 mT at 20 K. (D) Temperature dependence of the signals' amplitude at 10 (grey) and 20 K (orange) where the spectra were multiplied by their temperature. Orange represents 20 K, grey 10 K and blue 7 K. Dashed, full and dotted lines indicate samples reconstituted with zero, two and four equivalents, respectively. Adapted from Alissa Agovic's practical report. EPR conditions: Frequency: 9.4 GHz, T: 10 K, microwave power: 2 mW, modulation amplitude: 10 G, modulation frequency: 100 kHz.

Besides an almost equal amount of reconstituted cluster, when the protein was incubated with four equivalents of iron ions it is possible to observe another signal in the *g*=12 region. The sharper signal corresponding to a system with *S*=2 of the reduced [3Fe-4S] cluster loses intensity and is replaced by a much broader and not well-resolved signal. This new signal can possibly be attributed to free

Fe^{2+} in solution since the [3Fe-4S] cluster cannot bind the excess of iron ions. In agreement with this interpretation the broad *S*=2 signal from ferrous ions in solution is more intense in the sample treated with 4 equivalents. In the spectrum of the sample reconstituted with two equivalents there is still a slight rise of the signal between 0 and 15 mT, which could be from a small population of $[3Fe\text{-}4S]^0$ clusters remaining in solution.

In the *g*=2 region there are two complex signals for the samples reconstituted with two and four equivalents. The sharp signals (Figure 77, Panel A) are most pronounced in the sample reconstituted with four equivalents and were attributed to a Mn^{2+} contaminant possibly present in the Mohr's salt used for the reconstitution. By subtraction of spectra a clear six line spectrum was obtained, typical for the hyperfine splitting by the *I*=5/2 nucleus of Mn^{2+}. With this difference spectrum the Mn^{2+} contribution could be removed from the *g*=2 region and a derivative shaped feature could be detected around *g*=1.89 for the $[4Fe\text{-}4S]^{1+}$ cluster (Figure 77, Panel B).

The signal at *g*= 5.18 (Figure 77, C) has similar intensities in samples reconstituted with two and four equivalents and is absent in the sample lacking added ferrous ions. The temperature dependence of this signal (10 vs. 20 K) showed a behavior that is similar to that observed in Figure 76, Panel D.

These results indicate that reconstitution is possible, but do not determine whether this is physiologically relevant: does YjdI *in vivo* have a [4Fe-4S] cluster that breaks down to a [3Fe-4S] cluster during opening of the cells and sample handling for purification or does YjdI *in vivo* bind a [3Fe-4S] cluster. EPR and Mössbauer spectroscopy of whole cells or rapidly permeabilized cells are necessary to obtain insights into this matter.

Finally, AlphaFold3 structures were generated, both for YjdI with and without the Twin-Strep-tag due to the large size of the tag in comparison to the protein itself. The structure predicted for YjdI clearly identifies a cluster binding site. However, even though four cysteine residues are present in its primary structure, only three cysteine residues are spatially close enough to ligate an FeS cluster in its tertiary structure, both for untagged natural YjdI and for YjdI as produced here with Twin-Strep-tag. The AlphaFold3 structures of YjdI are represented in Figure 78. No significant differences were observed for the untagged and tagged structural predictions. In both predictions cysteines 27, 33 and 66 are the most likely ligands in case the protein harbors a [3Fe-4S] cluster. The histidine residue mutated by Martins *et al*[222] appears to be facing away from the cluster binding pocket, whereas serine 68 occupies what appears to be the place a fourth cluster ligand would take.

A serine ligand fits the observed in this practical work: a cluster that could potentially be a [4Fe-4S] cluster, due to the chemical similarities between cysteine and serine residues. However, in case the serine residue decreases cluster stability, this could relate to a tuning mechanism for protein function under different Fe availability, for example, shifting between a $[3Fe\text{-}4S]^{0/1+}$ and a $[4Fe\text{-}4S]^{1+/2+}$.

AlphaFold3 prediction for *E. coli* YjdI shows a similar overall structure when compared to the prediction for the C-terminal domain of the Class E FDP [206]. The predictions share exterior α-helices that surround a central β-sheet. These results agree with the UV CD data obtained here, which indicated a mixture of α-helices and β-sheets.

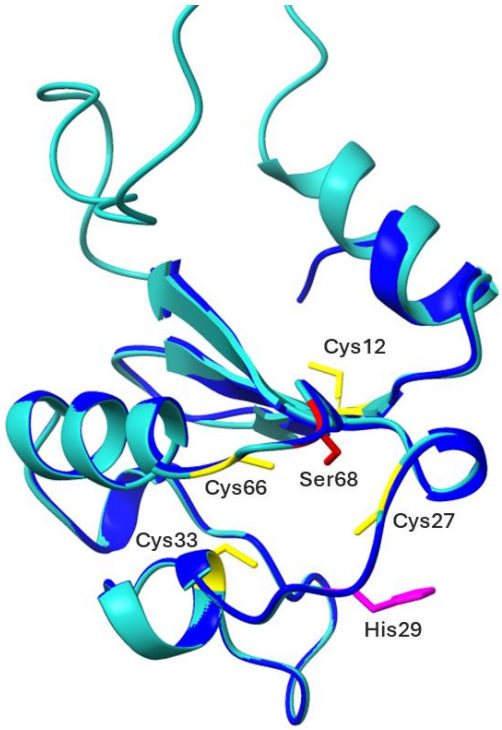

Figure 78. AlphaFold3 structure of the tagged (light blue) and untagged (dark blue) YjdI from *E. coli*. The main polypeptide chain is represented in blue, cysteine residues in pink, serine is green and histidine in orange

Chapter V. EPR spectroscopic identification of the monoprotonated state of the *Thermus thermophilus* reduced Rieske protein

1. Introduction

Rieske proteins are one of the best studied iron sulfur proteins in the field of Biochemistry. First discovered by John S. Rieske and coworkers in 1964[223], (multiple) genes encoding Rieske proteins have been found in numerous prokaryotes and eukaryotes[61]. As mentioned in Chapter I, these proteins are divided into two main classes – the low and the high potential Rieske proteins[60,61]. Low potential Rieske clusters are found as a domain in the Rieske oxygenase proteins transferring electrons to the non-heme iron center and having a midpoint potential between -200 and +100 mV[224]. The high potential "classical" Rieske clusters are found in cytochromes bc_1 and b_6f complexes, present in mitochondrial, bacterial, archaeal and photosynthetic electron transfer chains showing midpoint potentials in the range of +200 to +500 mV[60,225,226]

The high potential Rieske proteins are composed of a soluble and a hydrophobic domain. Its soluble domain contains a [2Fe-2S] cluster and is in the mitochondrial intermembrane space in eukaryotes and in the periplasm in prokaryotes and Archea[227,228]. The hydrophobic domain is inserted in the mitochondrial inner membrane or the inner membrane, in eukaryotes and prokaryotes, respectively. The structure of the yeast cytochrome bc_1 complex[227,229] is shown in Figure 79, which was adapted from Hunte and coworkers[227] by omission of the antibodies used for crystallization for better visualization.

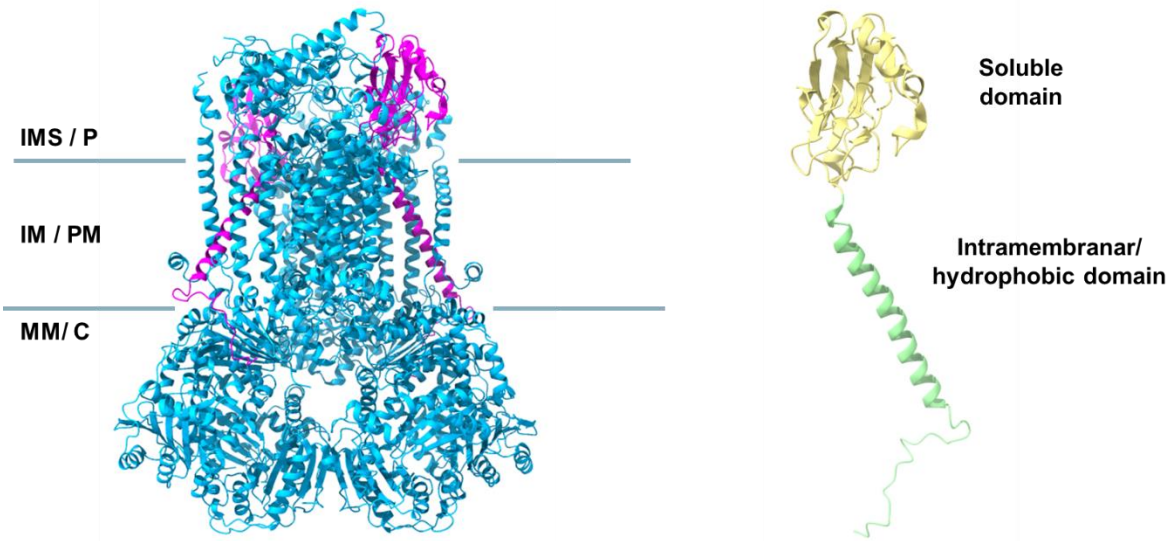

Figure 79. Yeast cytochrome bc1 complex (blue) with its Rieske domains highlighted (pink). The Rieske domain with its soluble (yellow) and intramembrane (light green) component shown in detail on the right. PDB code: 1P84. IMS- mitochondrial intermembrane space; P-periplasm; IM- mitochondrial inner membrane; PM- inner plasmic membrane; MM- mitochondrial matrix; C- cytosol. Figure made with ChimeraX.

Rieske clusters are [2Fe-2S] clusters coordinated by two cysteine and two histidine residues, located in the proteins' soluble domain[228]. The ligand conservation in Rieske clusters with different functions among species seems to be related to a specific function performed by these ligands and indicates that the cluster evolution might have a common ancestor from which it diverged, indicating

homology[61,230]. Thus far no natural Rieske proteins with a different cluster coordination have been discovered. The Rieske clusters are of paramount importance as they show specific properties resulting from this type of coordination. The structure of the soluble component of the Rieske protein from *Thermus thermophilus*, deposited on PDB in 2003 by Hunsicker-Wang[231] and colleagues, is shown in Figure 80.

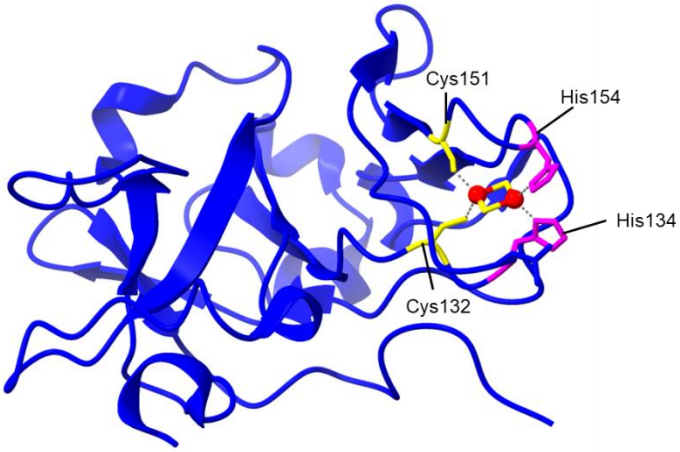

Figure 80. Soluble component of the Rieske protein from *Thermus thermophilus* with the histidine (pink) and cysteine (yellow) ligands to its [2Fe-2S] cluster. Fe ions shown in red. PDB code: 1NYK. Figure made with ChimeraX.

High potential Rieske proteins have been characterized by a wide range of spectroscopic methods in several groups. In EPR spectroscopy, the reduced protein shows a rhombic signal characteristic of an S=1/2 species, resulting from a Fe^{3+} (S= 5/2) antiferromagnetically coupled to a Fe^{2+} (S= 2), with g-values usually around 2.01, 1.90 and 1.79, under physiological conditions[232]. The presence of two histidine residues as cluster ligands has been extensively linked to the process of PCET and the cluster's midpoint potentials are known to be pH dependent[60]. However, a full characterization of the redox chemistry of these proteins has been a challenge due to the high pK_a values associated with the coordinating histidine residues for the reduced cluster.

Very interestingly, a study by Oliveira and coworkers in 2004[233] characterized the Rieske cluster from *Thermus thermophilus* (TtRp) in its reduced and deprotonated state, at pH 14, and compared it with pH 7. The EPR spectrum at pH 14 showed significant differences when compared to the spectrum obtained at a physiological pH value. The novel spectrum showed broad features and g-values of 2.14, 1.94 and 1.81, which are uncommon and had not been seen before. These signals were attributed by the authors to an asymmetric, also known as Dzyaloshinskii-Moriya, D-M, exchange coupling between the iron ions of the Rieske protein at pH 14 contrary to the usual Heisenberg interaction.

This study was followed by the analysis of the Rieske protein from the archaeon *Sulfolobus tokodaii* by Iwasaki and coworkers in 2006[232]. They performed HYSCORE spectroscopy at pH 7 and 13.3 and concluded that though the main characteristics, including its geometry and ligands, are similar a redistribution of the spin density occurs changing the mixed-valence state of the cluster.

These changes, associated with the deprotonation of Nε atoms of the two histidine ligands in the reduced cluster, raised a question of whether an intermediate state could be obtained and whether it might be possible to determine two separate pK_a values for each histidine residue. That has not been possible by protein film voltammetry: in the benchmark article by Zu and coworkers[60] equal pK_{red} values were assumed as it was impossible to determine individual pK_{red} values, Recently, a study of the UV-Vis and CD spectroscopic properties of the deprotonated reduced Rieske protein from *Thermus thermophilus* was conducted by the Master student Erik Matonia, supervised by the PhD student Lukas Knauer. This small chapter corresponds to the EPR spectroscopic measurements of TtRp at defined alkaline pH values. This is part of a collaborative effort between me, Lukas Knauer and Erik Matonia and the EPR data acquisition and analyses, conducted by me, are here described.

2. Results and discussion

2.1. TtRp spectral analysis by EPR spectroscopy

The EPR spectra of the dithionite reduced Rieske protein from *Thermus thermophilus* (TtRp) at pH 10.6 present EPR spectral features that are identical those published for the *S*=1/2 $[2Fe\text{-}2S]^{1+}$ cluster with antiferromagnetic coupling between a ferrous (Fe^{2+}) and a ferric (Fe^{3+}) iron ion at pH 7. The *g*-values obtained, g_z=2.011, g_y= 1.898, g_x= 1.776 and the low $g_{average}$ (g_{av}= 1.895) at pH 10.6, are indicative of non-cysteinyl ligation[232].

The EPR spectrum at pH 13.9 revealed the broad signal with g_z=2.129, g_y=1.938, and g_z=1.793, g_{av}= 1.953[232,233]. Both spectra, at pH 10.6 and 13.9 are shown in Figure 81. These values fully agree with those published by de Oliveira and coworkers as well as Iwasaki and colleagues[232,234], which are summarized in Table 26.

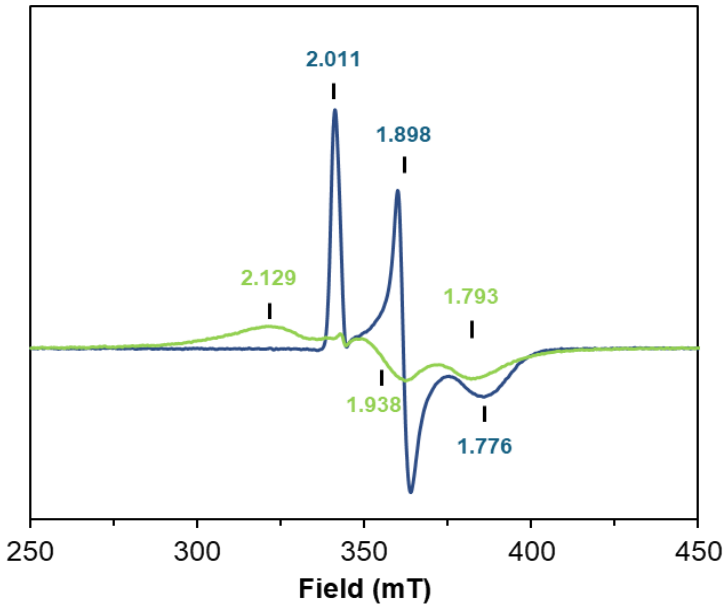

Figure 81. EPR spectra of dithionite reduced the Rieske protein from *Thermus thermophilus* at pH 10.6 (blue) and 13.9 (green). The *g* values calculated at the maxima, zero crossing and minima are shown in the same color as the spectrum to which they belong. EPR conditions: Microwave frequency 9.62 GHz, T: 18 K, microwave power 2 mW, modulation amplitude 10 G and modulation frequency 100 kHz.

Minor differences compared to literature are observed for the *g*-values with broad linewidths. It is interesting to note that no or little cluster breakdown occurred even at extreme pH values. The decrease in amplitude relates to the broad even more anisotropic nature of the species resulting after deprotonation of the histidine ligands. The double integral of spectra of the sample at pH 10.6 has a 10% lower area than the one at pH 13.9. This is likely caused by minor saturation of the sharp and easier to saturate pH 10.6 spectrum at the microwave power necessary to obtain a reasonable signal-

to-noise of the broad spectrum at pH 13.9, which did not saturate. These spectra correspond to the samples at lowest and highest pH value of the pH titration.

Table 26. Comparison of *g*-values obtained for TtRp with the results published by Tiago de Oliveira and colleagues, in 2004, and for the *Sulfolobus tokadii* Rieske protein by Iwasaki and coworkers, in 1996 and 2006.

	pH	g_z	g_y	g_x
This work	10.6	2.011	1.898	1.776
	Int. species	2.034	1.899	1.776
	13.9	2.129	1.938	1.793
Oliveira *et al*.[233]	7.0	2.02	1.90	1.80
	14.0	2.14	1.94	1.81
Iwasaki *et al.*[232,234]	6.8	2.01	1.91	1.79
	13.3	2.13	1.92	1.78

2.2. TtRp pH titration monitored by EPR spectroscopy

To obtain insights into the transitions and spectral features occurring upon consecutive deprotonation of the histidine ligands a pH titration of dithionite reduced TtRp between pH 10.6 and 13.9 was performed. Additionally, this titration aimed to determine the pK_a values of the histidine ligands. The EPR spectra of the pH titration samples are represented in Figure 82. The EPR spectra of the Rieske cluster at different pH values shows that up to pH 11.6, shown in blue in Figure 82, Panel A, the spectral features of the signal are like those previously reported at physiological pH values. Sharp features are present at *g*-values 2.011, 1.898, and 1.776 which are associated with the di-protonated species. However, with a further increase of the pH value, a different peak-shaped feature appears in the low field shoulder of the highest *g-value*, indicating a possible conversion to an intermediate associated with a monoprotonated species between the known pH 10.6 and pH 13.9 species.

Various changes of amplitudes and *g*-values accompany the transition to the fully deprotonated species. Importantly, though the signal amplitude drastically decreases the double integral remains almost constant confirming that the decrease in amplitude is explained by signal broadening and higher anisotropy.

Above pH 12.6, shown in green in Figure 82, Panel A, broad EPR spectra are observed which are similar to that reported by Oliveira and coworkers at pH 14. These spectra show *g*-values of 2.129, 1.938, and 1.793 that are attributed to the fully deprotonated species. In this titration it was not possible to obtain a signal that corresponded to 100% monoprotonated species.

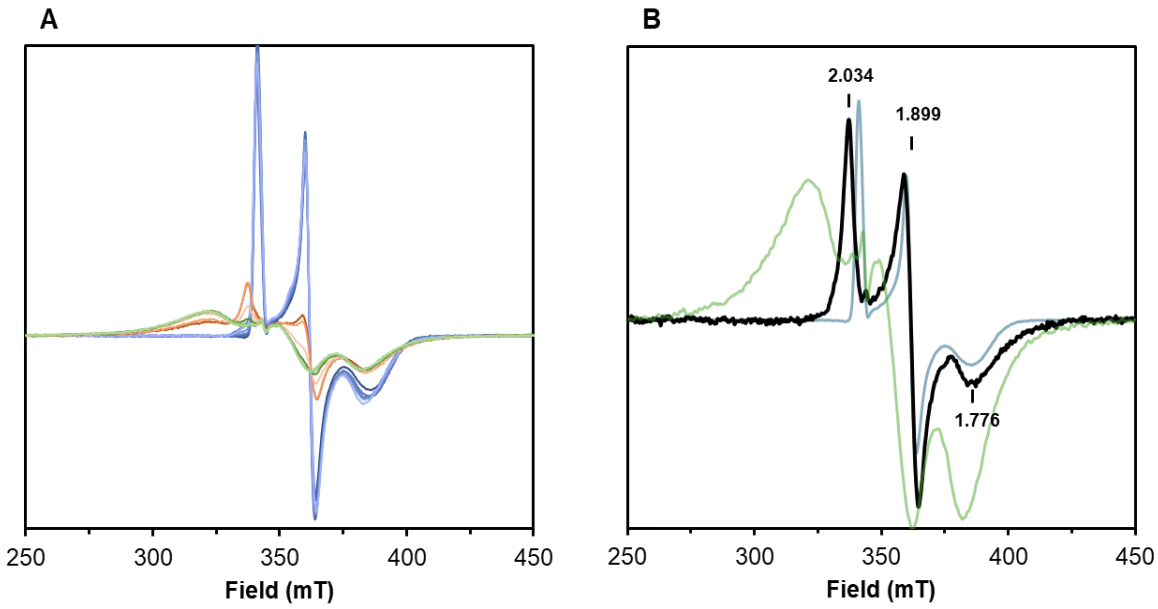

Figure 82. pH titration of the Rieske protein from *Thermus thermophilus*. (A) EPR spectra of Rieske protein at several pH values. The fully protonated species are shown in blue (pH 10.6- 11.6), the intermediate species in orange (pH 11.8-12.6) and the fully deprotonated in green (pH above 12.6).(B) Monoprotonated intermediate species spectrum (black) determined by subtraction of 55% of the spectrum at pH 13.9 (green) and 2% of the spectrum at pH 10.6 (blue) from the spectrum at pH 11.8. Measurement conditions: microwave frequency 9.62 GHz, T: 18 K, microwave power 2 mW, modulation amplitude 10 G, and modulation frequency 100 kHz.

Therefore, difference spectra, shown in Figure 82, Panel B, were calculated to deconvolute the spectra and extract the EPR spectral characteristics of the intermediate species. It was necessary to subtract 4% of the doubly protonated low pH spectrum (pH 10.6) and 55% of the fully deprotonated species (pH 12.6) from the spectrum with highest intermediate species content (pH 11.8) to obtain the spectrum of the intermediate species. The difference spectrum revealed well defined features, with linewidth slightly larger than for the fully protonated species, but much sharper than for the fully deprotonated cluster. For the intermediate species *g*-values of 2.034, 1.899 and 1.776 were determined.

The difficulty of obtaining a sample which exclusively contains the intermediate species could indicate that the pK_a values that so close that the second deprotonation begins before the first step is complete. This is demonstrated by the high contribution (55%) of the doubly deprotonated species to spectra with the highest content of the intermediate species. It could even be that the first deprotonation step might have a higher pK_a than the second step: once the first proton is released it becomes energetically more favorable for the second proton to be removed.

The spectra for the three protonation states of TtRp were simulated with the program Geestrain5 (Table 27) and are shown in Figure 83. Even though the simulation of the fully and mono protonated species matched the experimental spectra extremely well, it was not possible to simulate fully deprotonated species to complete satisfaction. This could indicate some residual content of the intermediate species or be caused by a mixture of species.

Table 27. Simulation parameters used for the fully protonated, monoprotonated and fully deprotonation species of TtRp. Simulations were performed in GeeStrain5. Due to the application of moderate *g*-strain in the simulation of the high pH spectrum, the *g*-values obtained do not entirely match the ones measured and calculated from the field in the spectrum.

Simulation parameter	Fully protonated	Monoprotonated	Fully deprotonated
Residual broadening (w-0)	0.005	0.005	0.025
***g*-values (x,y and z)**	1.773, 1.899, 2.015	1.757, 1.899, 2.042	1.790, 1.955, 2.190
Linewidth (W-xx,yy,zz)	0.032, 0.008, 0.007	0.045, 0.013, 0.017	0.07, 0.07, 0.11
***g*-strain (w-xy, xz,yz)**	0.0, 0.01, 0.01	0.02, 0.03, 0.013	0.09, 0.12, 0.04

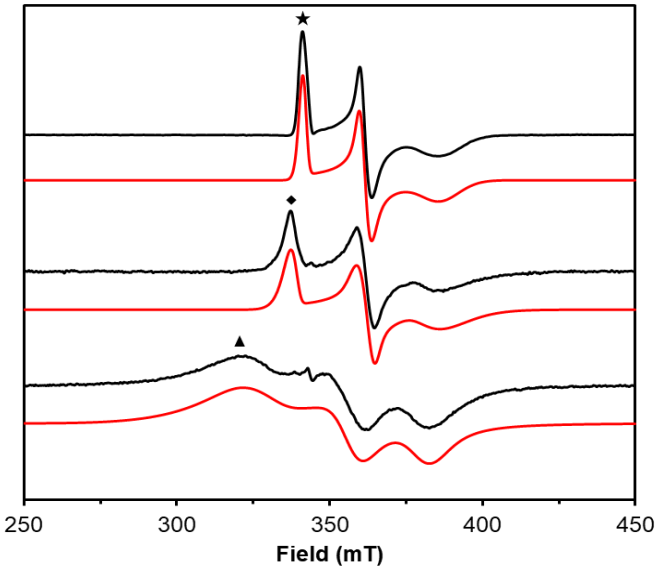

Figure 83. Experimental (black) and simulation (red) spectra of the TtRp in the fully protonated (top), monoprotonated (middle) and fully deprotonated (bottom) forms. The star, diamond and triangle represent the field at which each species evolution with the increase of the pH value was estimated.

To determine the fraction of fully protonated, monoprotonated and fully deprotonated species the spectral shifts were analyzed at specific *g*-values. At high pH values a direct measurement of the increase of signal intensity at g_z (shown in Figure 83 as a triangle) allowed a convenient quantification of the fully deprotonated species. The intermediate and the fully protonated species do not contribute at all to the EPR spectral intensity at that *g-value*. For the intermediate and fully protonated species, the signal amplitude at the maximum of the spectra between 340 and 343 mT, represented in Figure 83 by a diamond and a star, respectively, was used to follow the variation of these species as a function of the pH value. Even though there is a minor overlap of these two species at these field values, these seemed to be the most appropriate spectral positions to obtain insights on the relative intensity of species as the overlap in this region contrary to the rest of the spectrum appears to be the smallest.

For the intermediate species, however, it was difficult to obtain a flat baseline at low and high pH monitoring this signal by its amplitude only. A different approach was therefore applied in which the spectrum obtained by deconvolution for the intermediate species was partially subtracted from the spectrum of each sample until a shape of a pure fully protonated (for pH values lower than 12.2) and fully deprotonated (for pH values higher than 12.2) was obtained. The variation of the percentage subtracted, which corresponded to the fraction of intermediate species, was plotted against the pH value. This procedure resulted in a well-defined baseline at low and high pH values. The overall shape of the amplitude of the intermediate as a function of pH was maintained. With the amplitudes of the three species derived as described and shown in Figure 84, it was possible to estimate pK values.

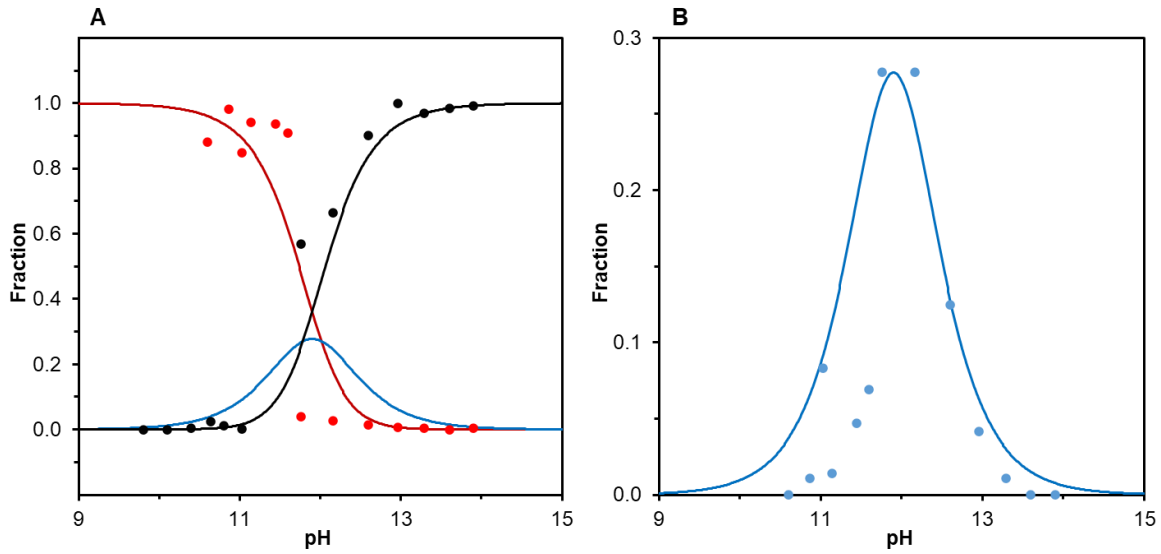

Figure 84. Variation of species in solution with the variation of the pH value and theoretical fit. (A) Fully protonated species is shown in red, intermediate species in blue and fully deprotonated in black. (B) Enlarged version of the intermediate species with experimental points shown. Data were fitted using an adapted version of the Henderson-Hasselbalch equation for double protonation/ deprotonation.

The double integral of the calculated intermediate species (from the species shown in Figure 82, Panel B, black) and of the average of the samples at the three highest pH (13.3, 13.6 and 13.9) was used to determine the maximum fraction of intermediate species present in the samples. The maximal ratio was almost identical (0.28) for two of the samples. This indicates that the intermediate species maximally accounts for 28% of the species present in the sample. This value was then used to determine the separation of pK_a values since the maximal occupancy of the intermediate is a function of the separation of the two pK values. Based on the equations that describe a system with two pK_a, equations 5-7[235], a maximum of 28% of intermediate species corresponds to a pK_a separation of -0.23. In this scenario, the first pK_a is higher than the second pK_a by 0.23 pH units only. The data were fitted with an average pK_a of 11.95, being pK_a 1 and 2 approximately 12.07 and 11.84, respectively. Figure 85 shows the variation of the maximum fraction of intermediate species and the broadness of the peak based on the separation of the pK_a values.

$$f_{H2A} = \frac{[H^+]^2}{[H^+]^2 + K_{a1}[H^+] + K_{a1}K_{a2}}$$ Equation 5

$$f_{HA-} = \frac{K_{a1}[H^+]}{[H^+]^2 + K_{a1}[H^+] + K_{a1}K_{a2}}$$ Equation 6

$$f_{A2-} = \frac{K_{a1}K_{a2}}{[H^+]^2 + K_{a1}[H^+] + K_{a1}K_{a2}}$$ Equation 7

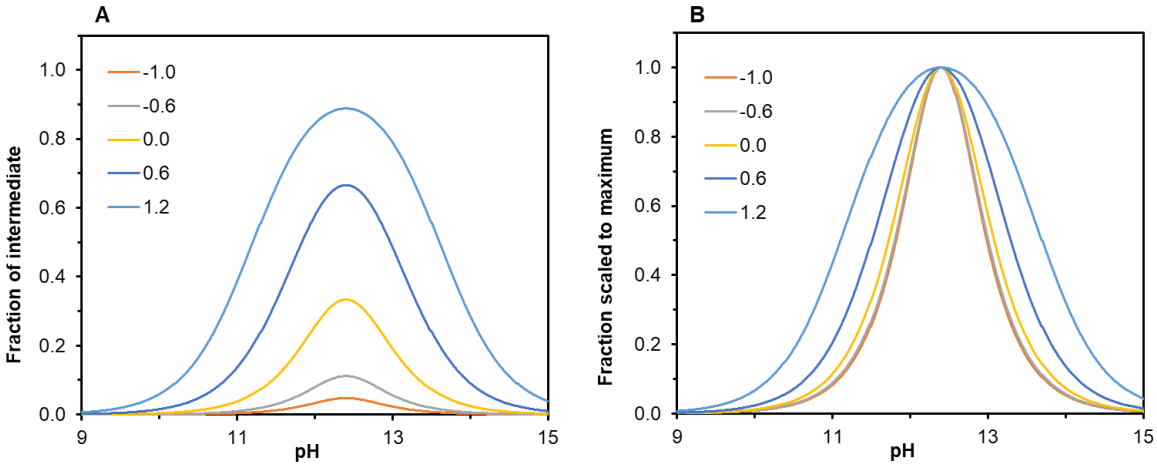

Figure 85. Influence of the separation between two pK_a values in the maximum fraction of intermediate (A) and in the broadness of the intermediate curve (B).

It was noticed that, even though the calculated curves fit most experimental points within reasonable error, a set of low pH samples (10.6, 10.9, 11.1, 11.4 and 11.6) did not seem to fit well. This is in the pH region corresponding to the first deprotonation step. However, the sample pH 11.0, a pH value in the same interval, appears to agree well with calculated fit. Upon closer inspection, it was noticed that the difference between pH 11.0 sample and the others is, as described in Chapter II, 4, Table 21, the buffer system. While all pH 10.6 to 11.6 samples were prepared in CAPS buffer, the pH 11.0 sample that agrees with the fit was prepared in NaOH only. This indicates that a possible buffer pH shift upon freezing could have occurred in the samples prepared in CAPS buffer. An estimation based on the theoretical curve showed that these experimental points would perfectly match the calculated curve in case the buffer pH would drop by 0.8 pH unit upon freezing.

Little reference data was found on the properties of CAPS pH shift upon freezing. A $\Delta pH/\Delta t$ of -0.028 for CAPS buffer is reported by Reach Devices website (consulted on November 4th, 2024, available at https://www.reachdevices.com/Protein/BiologicalBuffers.html), calculated with the Van't Hoff equation considering an enthalpy variation (ΔH^0) of 48.1 kJ/mol. This variation would then lead to an increase in pH value upon freezing instead of a decrease as observed. Another study by Fukada and measured the pH variation with the increase of temperature in the presence of 0.1 M KCl observing a pH increase of 0.77 pH units upon temperature change from 25 to 0 ºC, with a similar $\Delta pH/\Delta t$ as described previously. A qualitative article by Orii and Morita, 1976[236], states that of all Good's buffers

tested, CAPS was the only one that did not show a typical 1 pH unit increase upon freezing. It is not mentioned though whether the general behavior of CAPS is a pH decrease or a smaller than 1 pH unit increase. Interactions between buffers and the cluster or cluster ligands, especially the ones containing amine groups as is CAPS, could also potentially have some effect on the spectral properties of the iron ions by EPR.

Chapter VI. Discussion and conclusions

1. IscR

IscR is an important regulator of DNA transcription, and particularly relevant for the regulation of the transcription of the ISC and Suf pathways in *E. coli*. Understanding the mechanism and function of this protein is of paramount importance for the study of FeS clusters in bacteria. The study of IscR's redox potential and its pH dependence, as well as the process of protonation and deprotonation of the histidine ligand has yielded new information that could change our view of the regulatory processes in the cell.

According to the NMR spectroscopic data in Fleischacker *et al*.[71], the pK_a of the histidine while the cluster is in the reduced state is approximately 7.1. Literature on similar clusters, such as MitoNEET[51] and the doubly histidine coordinated sites as in Rieske[60] or Apd1[63], compiled in Table 28, shows that deprotonation of the histidine while the [2Fe-2S] cluster is in the reduced state is not favorable at physiological pH value. The higher pK in comparison to the oxidized state is likely due to the increased electron density at the reducible iron ion of the cluster. Thus, it would require an unusual cluster environment of IscR to have such a low pK_a in the reduced state. This work showed through pK determinations by UV-Vis, EPR, CD and Mössbauer spectroscopies that, when the cluster is in the reduced state and at physiological relevant pH values, it appears that the histidine ligand is fully protonated and not in a mixture of deprotonated and protonated as a pK_a of 7.1 would indicate. The data allowed to estimate a pK_a of 8.1±0.2 in the oxidized state and of approximately 11.2 in the reduced state, which is in accordance with experimental data on similar clusters.

Table 28. Literature data on proteins with a [2Fe-2S] cluster with single and double histidinyl coordination. Red corresponds to parameters determined in this work.

Protein	pK_{ox1}	pK_{ox2}	pK_{red1}	pK_{red2}	$\Delta pK_{(red1-ox1)}$	Em_{acid} (mV)	Em_{alk} (mV)	ΔE_m (mV)
RsRp[60]	7.6	9.6	12.4	12.4	4.8	308	-134	442
TtRp[60]	7.9	9.7	12.5* **12.07**	12.5* **11.84**	4.6	161	-275	436
BphF[60]	9.8	11.5	13.3	13.3	3.5	-135	-441	306
Apd1[63]	7.9	9.7	>12.0	>12.0	4.1	161	**n.d.**	**n.d.**
MitoNEET[51]	6.7	-	12.4	-	5.7	25	**n.d.**	**n.d.**
IscR	**8.1± 0.2**	-	**11.2 ± 0.2**	-	**3.1 ± 0.2**	**-49**	**-221**	**172**

* determined in reference 60.

Regarding redox potentials of [2Fe-2S] proteins, it is known that the substitution of a cysteine by a histidine in nature, as observed in IscR, allows to tune the redox potential. Though the redox potential obtained for IscR was pH dependent above pH 7, at physiological pH its potential was -50 mV (at least for the first redox transition). Substitution of a cysteine residue by a histidine increases the redox potential of the $[2Fe\text{-}2S]^{2+/1+}$ cluster. This was thus far only experimentally shown for MitoNEET[51] and Apd1[63]. The experimental data in this thesis expands our knowledge to another protein.

The spectroscopic determination of the pK_a in the oxidized and reduced states as well as the determination of the redox potential at several pH values by mediated EPR-followed titrations allowed a full characterization of the pH dependence of the redox potential, as shown in Figure 86.

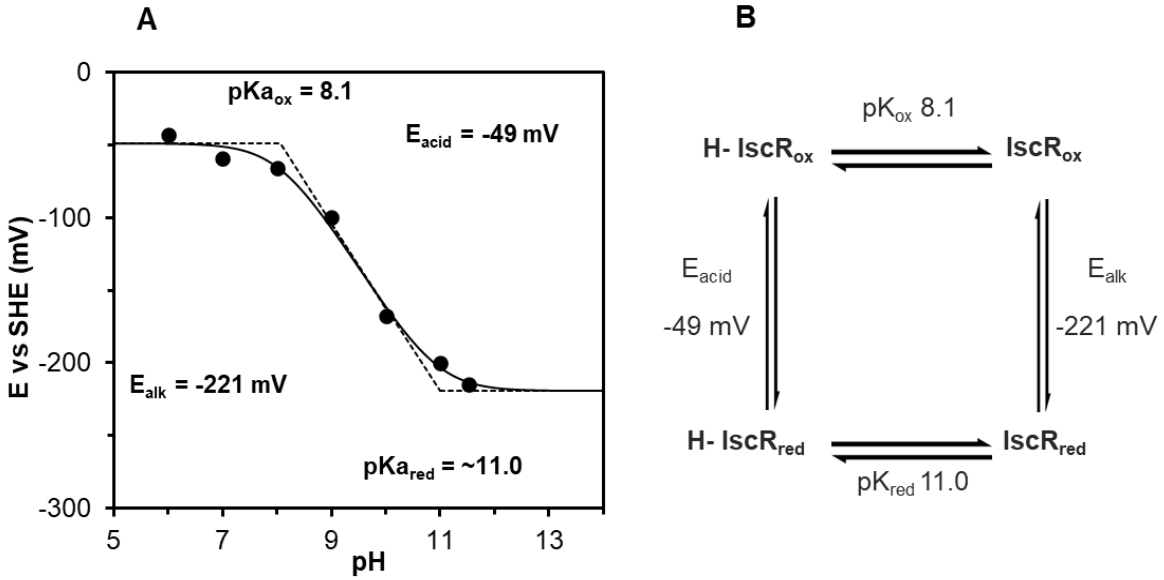

Figure 86. Histidine protonation and its relationship with the cluster redox state. (A) pH dependence of the redox midpoint potential for wild type IscR by dye-mediated redox titrations. Fit with a $pK_{a\ ox}$ of 8.1, $pK_{a\ red}$ of 11.0, $E_{m,acid}$ of -49 mV and $E_{m,alk}$ of -221 mV.(B) Square scheme for the redox and protonation events in wild type IscR.

The redox titrations indicate that below pH 7, IscR's redox potential is barely pH dependent varying between -40 and -63 mV, pH 6 and 7, respectively. However, upon increase of the pH value the redox midpoint potential decreases to -215 mV, at pH 11.5. Fitting the midpoint potentials measured as a function of pH allowed the determination of the four parameters of interest: $E_{m,acid}$ and $_{alk}$ were -49 and -221 mV, respectively, $pK_{a\ ox}$ of 8.1 and $pK_{a\ red}$ of 11.0. The latter pK values necessary to explain the pH dependency of the redox potential in the dye-mediated redox titrations, fully agreed with the values obtained by spectroscopic determinations.

Dividing the ΔE_m ($E_{m,alk}$ - $E_{m,acid}$) by the ΔpK_a ($pK_{a,\ red}$ – $pK_{a,\ ox}$), an average slope of -55 mV per pH unit is obtained. This is almost identical to the -59 mV per pH unit slope observed when proton coupled electron transfer of one proton per electron occurs[237]. The summary of pK_a values spectroscopically obtained in this work is shown in Table 29.

The cellular redox potential of *E. coli* is reported to be between -200 and -300 mV considering that the ratio of redox active pairs, such as GSSG/GSH and NAD^+/ NADH, determine the cellular redox potential[180,238,239]. The variation in the redox potential in the cell is usually related to oxidative stress. Logically, in case of an oxidative event, redox active molecules will have their ratio altered in response to it. One of the main targets of oxidative stress in the cell are the molecules of GSH that will be converted into GSSG. The conversion of GSH in GSSG increases the ratio GSSG/GSH leading to an increase in the cellular redox potential. The same is observed for the pair NAD^+/NADH with a more

pronounced effect, due to the 1 to 1 ratio of conversion as opposed to the 1 to 2 ratio for GSSG and GSH.

Table 29. Summary of the pK_a determination and electrochemistry of *E. coli* IscR through different spectroscopies.

Technique	$pK_{a\ ox}$	$pK_{a\ red}$	E_m acid	E_m alk
UV-Vis	7.9	-	-	-
CD	8.1	11.3	-	-
EPR	-	11.2	-	-
Mössbauer	8.1	-	-	-
pH dependence of the redox potential	8.1	11.0	-49 mV	-221 mV
ΔE (mV)	-172			
mV/pH unit	-57 ± 5			

As discussed before, IscR is present *in vivo* in the reduced and with a protonated histidine ligand. Initially, it was hypothesized that an increase in redox potentials caused by a potential oxidative stress could lead to oxidation of IscR's cluster that, coupled with the deprotonation of the histidine residue, would lead to a faster cluster dissociation rate and consequently to the controlled increase in the amount of apo IscR. The extent of oxidative stress and consequent increase of the redox potential would then determine the extent of cluster breakdown. Although the system would tend to equilibrate towards the oxidized IscR form upon an increase in cellular redox potential, such an increase of approximately +100 mV needed for the partial oxidation of IscR seems only possible *in vivo* if a dramatic oxidative event occurs.

However, the recent full range dye-mediated redox titration at pH 8 (shown in Chapter III, section 2.5.2, Figure 39) showed the presence of two reduction steps, indicating that IscR is present in solution in the apo, semi-holo (cluster 1) or bis-holo (clusters 1 and 2) forms, containing zero, one and two $[2Fe\text{-}2S]^{1+/2+}$ clusters per dimer, respectively. Further analysis of these results suggest they can be explained in two different ways. In the first hypothesis, cluster 1, representative of the semi-holo species and half of the bis-holo species, corresponds to the first reduction step (-67 mV), while the second reduction step (-245 mV) corresponds to cluster 2 from the bis-holo species. This hypothesis does not seem to fully explain what is known about IscR though. IscR is a homodimer in solution, indicating that both monomers would presumably have the same structure and both clusters 1 and 2 would exist in an identical, or at least similar, chemical environment. Such a difference in redox potentials could only be explained by a major change in the chemical environment surrounding one of the clusters. Additionally, no cluster coupling is expected since X- and Q-Band EPR spectra do not show cluster interaction and AlphaFold predictions for bis-holo IscR show a distance of approximately 30 Å between the closest iron ions in clusters 1 and 2 (Figure 87).

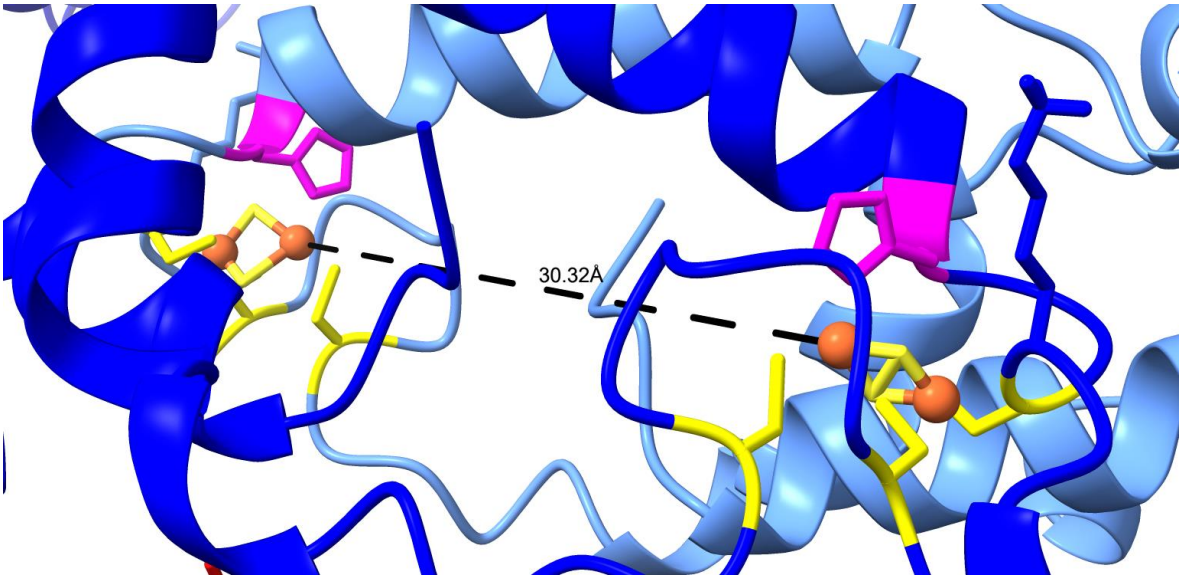

Figure 87. Distance between the Fe ions in the AlphaFold structure of wild type *E. coli* IscR. AlphaFold structure with [2Fe-2S] cluster made by the PhD student Lukas Knauer. Figure made with ChimeraX.

An alternative hypothesis could be that though a mix of semi- and bis-holo is still present in solution, upon binding of cluster 2 to a semi-holo protein, generating a bis-holo protein, conformational changes lead to a decrease in the redox potential of both clusters. Thus, both equivalent clusters 1 and 2 in the bis-holo form would have a midpoint potential of -245 mV, while the single cluster 1 in the semi-holo would have a higher midpoint potential of -67 mV. This would indicate that 36% of the protein would be in the bis-holo form, showing a preference for this form instead of the semi-holo one. With a midpoint potential of -245 mV, it would be more likely that the fraction of oxidized cluster increased upon oxidative stress, since this midpoint potential is close to the *in vivo* redox potential. It was also speculated that DNA binding (see Chapter III, section 2.3) could differ based on cluster composition and that iron homeostasis mechanisms could also contribute for a finely controlled mechanism of regulation. In addition, a recent study on IscR from *Caulobacter crescentus* by dos Santos *et al.* [240] provides evidence that IscR is not regulated by oxidative stress but, instead, by iron availability in the cell.

These findings require further investigation as they possibly unravel different functions for bis- and semi-holo, as well as apo IscR. They also shed light on mechanisms of action and their triggers *in vivo*. Future efforts should focus on the chromatographic separation of the three forms of IscR, though this imposes the risk of further cluster loss. The determination of the structure of holo IscR as well as the study of the second redox transition here observed (-245 mV) are key points to better understand the function of IscR. Mössbauer spectroscopy of IscR in the reduced state could provide additional information on the pK_a coordinating histidine.

2. YjdI

The DUF1271 or Fer4_19 is a small *E. coli* protein domain that is part of several protein architectures, of which 50% corresponds to this domain alone and almost all the remaining 50% corresponds to a fusion with either one or two zinc finger-CDGSH motif(s). Although it has been annotated as a divergent [4Fe-4S] mono-cluster containing domain, little studies were conducted on this protein, either on *E. coli* YjdI by Bak in his PhD thesis or by Martins and coworkers in a recently published preprint on the Class E FDPs. These two studies could only find evidence for [3Fe-4S] cluster binding.

In this work, the overproduction of YjdI in *E. coli* BL21 (DE3) pRK-ISC cells yielded protein with 1.4 to 2.6 Fe/monomer consistent with what was described by Bak (1.34 and 2.29 Fe/polypeptide chain) but inconsistent with the C-terminal of the Class E FDP (FDP_E_Cter) described by Martins and coworkers (1.1 Fe/protein). The UV-Vis spectrum shows an overall similar shape with a maximum between 420 and 450 nm, but here a small peak was also observed at 670 nm, not visible in the YjdI UV-Vis spectrum shown in Bak's thesis. This could be due to different redox ratios in both preparations. The UV-Vis spectrum of the FDP_E_Cter did not present clear absorption bands between 420 and 450 nm, possibly due to the low iron content in the protein. CD spectroscopy in the UV range showed that the overall secondary structure of the protein is composed of a mixture of α-helices and β-sheets, consistent with the structure obtained by AlphaFold3.

EPR spectroscopy showed that the protein is purified mainly in the reduced state (~95%) and contains a $[3Fe\text{-}4S]^{0}$ cluster, characterized by a broad signal with g=12. Residual amounts of $[3Fe\text{-}4S]^{1+}$ cluster were observed in the as isolated sample, characterized by a quasi-isotropic signal at g=2.013. Upon oxidation with ferricyanide, an intense signal with the same g-value appears indicating the conversion of a $[3Fe\text{-}4S]^{0}$ to a $[3Fe\text{-}4S]^{1+}$. These results are consistent with the observations by Bak for YjdI in the oxidized state (quasi-isotropic signal with g= 2.02, 10 K), but differ from the rhombic signal (g-values: 2.028, 2.015 and 1.999, 7 K) observed by Martins *et al*. It appears that there are some structural differences between the [3Fe-4S] cluster in YjdI and in Fer4_19 as a domain in Class E FDPs.

A reductive and an oxidative dye-mediated redox titration were carried out between -481 and +207 mV with the oxidized species appearing only above +86 mV. This indicates that the midpoint potential of the $[3Fe\text{-}4S]^{0/1+}$ is higher than +86 mV. Since the lowest potential reached in the redox titrations carried out in this work was -481 mV no conclusions can be drawn in comparison to the value reported by Bak of -762 mV. It is likely that the redox transition observed by Bak could correspond to the transition between a reduced and super reduced [3Fe-4S] cluster in YjdI. In agreement with the redox titration carried out in this work (approximately +150 mV), a slightly positive midpoint potential of ~70 mV was obtained by Martins and colleagues and attributed to a [3Fe-4S].

Further experiments were carried out to reconstitute the [3Fe-4S] cluster under different conditions, such as incubation time and equivalents of iron per protein. YjdI could be successfully reconstituted with the most promising results achieved by 30 minutes incubation time with iron (II). Incubation with 2 equivalents of iron showed residual signals of $[3Fe\text{-}4S]^0$ in solution whereas incubation with 4 equivalents of iron showed free iron (II) in solution. The reconstituted protein showed a broad derivative-like signal around g~1.89 and a high spin signal in the g=5 region originating from an excited state possibly belonging to the Kramer's doublets of an S=7/2 or S=9/2 spin system.

Mössbauer spectroscopy combined with EPR of whole cells are necessary to infer on the ligands of the [4Fe-4S] cluster and determine cluster form and its redox state *in vivo*. Even though the data seem to indicate that YjdI exists *in vivo* as a [3Fe-4S] cluster, the presence of non-cysteinyl ligands can be linked to a lower stability of the cluster leading to the loss of an iron ion upon handling.

The AlphFold3 structure prediction suggests that serine 68 could be the fourth ligand of a [4Fe-4S] and that histidine 29 faces the opposite direction, preventing cluster coordination unless environmental distortion occurs. Protein structure determination is of paramount importance to verify whether this is the first reported naturally occurring FeS cluster with a serine coordination and the role played by this amino acid in protein function.

3. Rieske

Rieske proteins are amongst the most studied proteins due to their high relevance for vital processes such as the oxidative phosphorylation and the mono and dioxygenation of substrates. Known for its typical [2Fe-2S] cluster with a bis-histidinyl coordination, it has been extensively characterized. However, a complete characterization of its redox chemistry associated with proton transfer has been difficult to achieve as the pK_a values for histidine deprotonation when the cluster is in the reduced state are often in a pH range that is incompatible with life. The extremely pH stable soluble domain of the Rieske protein from *Thermus thermophilus* was used in our lab to determine the two pK_a values of the coordinating histidine residues when the cluster is in the reduced state by EPR spectroscopy, following up on the work of Tiago de Oliveira and coworkers.

The pH titration between pH 10.6 and 13.9 showed features that are identical to the known EPR signals observed by de Oliveira *et al.*[233]: at lower pH values the typical Rieske EPR spectra showed sharp features with *g*-values of 2.011, 1.898, and 1.776, at higher pH values, the spectral features broadened and shifted to *g*-values of 2.129, 1.938, and 1.793. The change was explained by de Oliveira[233] *et al*. by an antisymmetric exchange coupling between spins.

An intermediate species (monoprotonated) could be observed at intermediate pH values. This species has not been previously described and could thus far not be observed individually. It was rather observed as a mixture, mostly with the fully deprotonated species. Difference spectroscopy allowed removal of the fully protonated and deprotonated species from the spectrum with the highest content of the intermediate species. This resulted in a well-defined spectrum with *g*-values of 2.034, 1.899 and 1.776.

The determination of the fraction of the monoprotonated intermediate revealed a maximum of 28%, which allowed to calculate the separation of -0.23 pH units between the pK_a values of 12.1 and 11.8 for the first and second deprotonation step, respectively. Interestingly, Zu and coworkers[60] specifically state that their data “exclude the possibility that pK_{red1} is significantly lower than pK_{red2} but do not exclude the possibility that pK_{red1} is higher than pK_{red2} (implying that the two protons bind cooperatively in the reduced state)”. But follow-up studies to investigate this puzzling statement have not appeared in literature. It is interesting to note that, the phenomenon observed for the pK_a values in this work (a cooperativity in a protonation and deprotonation process) has a parallel in systems in which two redox transitions occur in an inverted order with respect to their redox potential. For redox chemistry this is described as disproportionation. It occurs in many systems such as flavins and dinuclear iron centers, as reported by Abdulaziz and coworkers[241].

TtRp appeared to be very stable at high pH values, which was demonstrated by the constant double integral at elevated pH values. A decrease in the double integral could be observed for the samples at lower pH values, which was attributed to a mild saturation of the sharp EPR signal. This was

necessary to measure all samples under the same conditions and still observe spectral features of the very broad EPR signals observed for the high pH samples.

Besides the high pH values, the impact of buffer pH shift upon freezing presented a serious challenge to precisely determine the pK_a values as it appears that samples containing CAPS experienced a 0.8 unit pH downward shift upon freezing. More efforts towards reliable buffer systems for the future study of proteins at cryogenic temperatures should be made. Additionally, the identification of Rieske proteins with a larger difference between the two pK_a values from other organisms, could improve the isolation and characterization of the intermediate species.

References

(1) Malmström, B. G.; Neilands, J. B. Metalloproteins. *Annu. Rev.* **1963**, 331–354.

(2) Waldron, K. J.; Robinson, N. J. How Do Bacterial Cells Ensure That Metalloproteins Get the Correct Metal? *Nat. Rev. Microbiol.* **2009**, *7* (1), 25–35.

(3) Lu, Y.; Chakraborty, S.; Miner, K. D.; Wilson, T. D.; Mukherjee, A.; Yu, Y.; Liu, J.; Marshall, N. M. Metalloprotein Design. *Compr. Inorg. Chem. II* **2013**, *3*, 565–593..

(4) Van Stappen, C.; Decamps, L.; Cutsail, G. E.; Bjornsson, R.; Henthorn, J. T.; Birrell, J. A.; Debeer, S. The Spectroscopy of Nitrogenases. *Chem. Rev.* **2020**, *120* (12), 5005–5081.

(5) Peters, J. W.; Schut, G. J.; Boyd, E. S.; Mulder, D. W.; Shepard, E. M.; Broderick, J. B.; King, P. W.; Adams, M. W. W. [FeFe]- and [NiFe]-Hydrogenase Diversity, Mechanism, and Maturation. *Biochim. Biophys. Acta - Mol. Cell Res.* **2015**, *1853* (6), 1350–1369.

(6) Waldron, K. J.; Rutherford, J. C.; Ford, D.; Robinson, N. J. Metalloproteins and Metal Sensing. *Nature* **2009**, *460* (7257), 823–830.

(7) Foster, A. W.; Osman, D.; Robinson, N. J. Metal Preferences and Metallation. *J. Biol. Chem.* **2014**, *289* (41), 28095–28103.

(8) Poulos, T. L. Heme Enzyme Structure and Function. *Chem. Rev.* **2014**, *114* (7), 3919–3962.

(9) Fontecave, M. Iron-Sulfur Clusters : Ever-Expanding Roles. **2006**, *2* (4), 171–174.

(10) Quist, T.; Chen, J.; MacNeil, A.; Pandelia, M. E. The Cryptic Nature of Fe-S Clusters: A Case Study of the Hepatitis B HBx Oncoprotein. *Inorganics* **2023**, *11* (475), 1–21.

(11) Fontecave, M.; Ménage, S.; Duboc-Toia, C. Functional Models of Non-Heme Diiron Enzymes. *Coord. Chem. Rev.* **1998**, *178–180*, 1555–1572.

(12) Martins, M. C.; Romão, C. V.; Folgosa, F.; Borges, P. T.; Frazão, C.; Teixeira, M. How Superoxide Reductases and Flavodiiron Proteins Combat Oxidative Stress in Anaerobes. *Free Radic. Biol. Med.* **2019**, *140* (January), 36–60.

(13) Felg, A. L.; Lippard, S. J. Reactions of Non-Heme Iron(II) Centers with Dioxygen in Biology and Chemistry. *Chem. Rev.* **1994**, *94*, 759–805.

(14) Beinert, H.; Holm, R. H.; Munck, E. Iron-Sulfur Clusters: Nature's Modular, Multipurpose Structures. *Science.* **1997**, *277*, 653–659.

(15) Ayala-Castro, C.; Saini, A.; Outten, F. W. Fe-S Cluster Assembly Pathways in Bacteria. *Microbiol. Mol. Biol. Rev.* **2008**, *72* (1), 110–125.

(16) Lill, R. Function and Biogenesis of Iron-Sulphur Proteins. *Nature* **2009**, *460* (7257), 831–838.

(17) Rouault, T. A.; Tong, W. H. Iron-Sulfur Cluster Biogenesis and Human Disease. *Trends Genet.* **2008**, *24* (8), 398–407.

(18) Meyer, J.; Moulis, J. Rubredoxin. *Handb. Met.* **2004**, 1–13.

(19) Chung, C.; Blank, M. A.; Fay, A. W.; Yoshizawa, J. M.; Hu, Y.; Hodgson, K. O.; Hedman, B.; Ribbe, M. W. Stepwise Formation of P-Cluster in Nitrogenase MoFe Protein. *PNAS* **2009**, *106* (11), 18474–18478.

(20) Rupnik, K.; Tanifuji, K.; Rettberg, L.; Ribbe, M. W.; Hu, Y. Electron Paramagnetic Resonance and Magnetic Circular Dichroism Spectra of the Nitrogenase M Cluster Precursor Suggest Sulfur Migration upon Oxidation : A Proposal for Substrate and Inhibitor Binding. *ChemBioChem* **2020**, *21*, 1767–1772.

(21) Jeoung, J. H.; Dobbek, H. ATP-Dependent Substrate Reduction at an [Fe8S9] Double-Cubane Cluster. *Proc. Natl. Acad. Sci. U. S. A.* **2018**, *115* (12), 2994–2999.

(22) Fritsch, J.; Scheerer, P.; Frielingsdorf, S.; Kroschinsky, S.; Friedrich, B.; Lenz, O.; Spahn, C. M. T. The Crystal Structure of an Oxygen-Tolerant Hydrogenase Uncovers a Novel Iron-Sulphur Centre. *Nature* **2011**, *479* (7372), 249–253.

(23) Zhou, J.; Pecqueur, L.; Aučynaitė, A.; Fuchs, J.; Rutkienė, R.; Vaitekūnas, J.; Meškys, R.; Boll, M.; Fontecave, M.; Urbonavičius, J.; Golinelli-Pimpaneau, B. Structural Evidence for a [4Fe-5S] Intermediate in the Non-Redox Desulfuration of Thiouracil. *Angew. Chemie - Int. Ed.* **2021**, *60* (1), 424–431.

(24) Wagner, T.; Koch, J.; Ermler, U.; Shima, S. Methanogenic Heterodisulfide Reductase (HdrABC-MvhAGD) Uses Two Noncubane [4Fe-4S] Clusters for Reduction. *Science.* **2017**, *357* (6352), 699–703.

(25) Nicolet, Y.; Fontecilla-Camps, J. C. Fe – S Clusters: Biogenesis and Redox, Catalytic, and Regulatory Properties. In *Bioinspired Catalysis: Metal-Sulfur Complexes*; Weigant, W., Schollhammer, P., Eds.; 2015; pp 21–48.

(26) Crack, J. C.; Green, J.; Thomson, A. J.; Brun, N. E. L. Iron-Sulfur Clusters as Biological Sensors: The Chemistry of Reactions with Molecular Oxygen and Nitric Oxide. *Acc. Chem. Res.* **2014**, *47* (10), 3196–3205.

(27) Boyd, E. S.; Thomas, K. M.; Dai, Y.; Boyd, J. M.; Outten, F. W. Interplay between Oxygen and Fe-S Cluster Biogenesis: Insights from the Suf Pathway. *Biochemistry* **2014**, *53* (37), 5834–5847.

(28) Imlay, J. A. Iron-Sulphur Clusters and the Problem with Oxygen. *Mol. Microbiol.* **2006**, *59* (4), 1073–1082.

(29) Aron, A. T.; Reeves, A. G.; Chang, C. J. Activity-Based Sensing Fluorescent Probes for Iron in Biological Systems. *Curr. Opin. Chem. Biol.* **2018**, *43*, 113–118.

(30) Jang, S.; Imlay, J. A. Hydrogen Peroxide Inactivates the *Escherichia coli* Isc Iron-Sulphur Assembly System, and OxyR Induces the Suf System to Compensate. *Mol. Microbiol.* **2010**, *78* (6), 1448–1467.

(31) Jafari, S.; Tavares Santos, Y. A.; Bergmann, J.; Irani, M.; Ryde, U. Benchmark Study of Redox Potential Calculations for Iron-Sulfur Clusters in Proteins. *Inorg. Chem.* **2022**, *61* (16), 5991–6007.

(32) Maiocco, S. J.; Walker, L. M.; Elliott, S. J. Determining Redox Potentials of the Iron–Sulfur Clusters of the AdoMet Radical Enzyme Superfamily. In *Methods in Enzymology*; Elsevier Inc., 2018; Vol. 606, pp 319–339.

(33) Page, C. C.; Moser, C. C.; Dutton, P. L. Mechanism for Electron Transfer within and between Proteins. *Curr. Opin. Chem. Biol.* **2003**, *7* (5), 551–556.

(34) Agip, A. N. A.; Blaza, J. N.; Bridges, H. R.; Viscomi, C.; Rawson, S.; Muench, S. P.; Hirst, J. Cryo-EM Structures of Complex I from Mouse Heart Mitochondria in Two Biochemically Defined States. *Nat. Struct. Mol. Biol.* **2018**, *25* (7), 548–556.

(35) Volbeda, A.; Charon, M.-H.; Piras, C.; Hatchikian, E. C.; Frey, M.; Fontecilla-Camps, J. C. Crystal Structure of the Nickel-Iron Hydrogenase from *Desulfovibrio gigas*. *Nature* **1995**, *373* (16), 580–587.

(36) Dias, J. M.; Than, M. E.; Humm, A.; Huber, R.; Bourenkov, G. P.; Bartunik, H. D.; Bursakov, S.; Calvete, J.; Caldeira, J.; Carneiro, C.; Moura, J. J. G.; Moura, I.; Romão, M. J. Crystal Structure of the First Dissimilatory Nitrate Reductase at 1.9 Å Solved by MAD Methods. *Structure* **1999**, *7* (1), 65–79.

(37) Johansson, C.; Kavanagh, K. L.; Gileadi, O.; Oppermann, U. Reversible Sequestration of Active Site Cysteines in a 2Fe-2S-Bridged Dimer Provides a Mechanism for Glutaredoxin 2 Regulation in Human Mitochondria. *J. Biol. Chem.* **2007**, *282* (5), 3077–3082.

(38) Gaudu, P.; Moon, N.; Weiss, B. Regulation of the SoxRS Oxidative Stress Regulon: Reversible Oxidation of the Fe-S Centers of SoxR in Vivo. *J. Biol. Chem.* **1997**, *272* (8), 5082–5086.

(39) Gaudu, P.; Weiss, B. SoxR, a [2Fe-2S] Transcription Factor, Is Active Only in Its Oxidized Form. *Proc. Natl. Acad. Sci. U. S. A.* **1996**, *93* (19), 10094–10098.

(40) Fujikawa, M.; Kobayashi, K.; Kozawa, T. Direct Oxidation of the [2Fe-2S] Cluster in SoxR Protein by Superoxide: Distinct Differential Sensitivity to Superoxide-Mediated Signal Transduction. *J. Biol. Chem.* **2012**, *287* (42), 35702–35708.

(41) Liochev, S. I.; Benov, L.; Touati, D.; Fridovich, I. Induction of the SoxRS Regulon of *Escherichia coli* by Superoxide. *J. Biol. Chem.* **1999**, *274* (14), 9479–9481.

(42) Kobayashi, K.; Mizuno, M.; Fujikawa, M.; Mizutani, Y. Protein Conformational Changes of the Oxidative Stress Sensor, SoxR, upon Redox Changes of the [2Fe-2S] Cluster Probed with Ultraviolet Resonance Raman Spectroscopy. *Biochemistry* **2011**, *50* (44), 9468–9474.

(43) Kobayashi, K.; Fujikawa, M.; Kozawa, T. Binding of Promoter DNA to SoxR Protein Decreases the Reduction Potential of the [2Fe-2S] Cluster. *Biochemistry* **2015**, *54* (2), 334–339.

(44) Watanabe, S.; Kita, A.; Kobayashi, K.; Miki, K. Crystal Structure of the [2Fe-2S] Oxidative-Stress Sensor SoxR Bound to DNA. *Proc. Natl. Acad. Sci. U. S. A.* **2008**, *105* (11), 4121–4126.

(45) Fujikawa, M.; Kobayashi, K.; Tsutsui, Y.; Tanaka, T.; Kozawa, T. Rational Tuning of Superoxide Sensitivity in SoxR, the [2Fe-2S] Transcription Factor: Implications of Species-Specific Lysine Residues. *Biochemistry* **2017**, *56* (2), 403–410.

(46) Harris, D. F.; Lukoyanov, D. A.; Kallas, H.; Trncik, C.; Yang, Z. Y.; Compton, P.; Kelleher, N.; Einsle, O.; Dean, D. R.; Hoffman, B. M.; Seefeldt, L. C. Mo-, V-, and Fe-Nitrogenases Use a Universal Eight-Electron Reductive-Elimination Mechanism to Achieve N2 Reduction. *Biochemistry* **2019**, *58* (30), 3293–3301.

(47) Flint, D. H.; Allen, R. M. Iron − Sulfur Proteins with Nonredox Functions. *Chem. Rev.* **1996**, *96* (7), 2315–2334.

(48) Beinert, H.; Kennedy, M. C.; Stout, C. D. Aconitase as Iron−Sulfur Protein, Enzyme, and Iron-Regulatory Protein. *Chem. Rev.* **1996**, *96* (7), 2335–2373.

(49) Lauble, H.; Kennedy, M. C.; Beinert, H.; Stout, C. D. Crystal Structures of Aconitase with Isocitrate and Nitroisocitrate. *Biochemistry* **1992**, *31*, 2735–2748.

(50) Bak, D. W.; Elliott, S. J. Alternative Fes Cluster Ligands: Tuning Redox Potentials and Chemistry. *Curr. Opin. Chem. Biol.* **2014**, *19* (1), 50–58.

(51) Zuris, J. A.; Halim, D. A.; Conlan, A. R.; Abresch, E. C.; Nechushtai, R.; Paddock, M. L.; Jennings, P. A. Engineering the Redox Potential over a Wide Range within a New Class of FeS Proteins. *J. Am. Chem. Soc.* **2010**, *132* (38), 13120–13122.

(52) Moulis, J.-M.; Davasse, V.; Meyer, J.; Golinelli, M.; Quinkal, I. The Coordination Sphere of Iron-Sulfur Clusters : Lessons from Site-Directed Mutagenesis Experiments. *J. Biol. Inorg. Chem.* **1996**, No. 1, 2–14.

(53) Kubas, A.; Maszota, P. Theoretical Insights into the Unique Ligation of [Fe4S4] Iron–Sulfur Clusters. *Eur. J. Inorg. Chem.* **2018**, *2018* (20), 2419–2428.

(54) Albers, A.; Demeshko, S.; Dechert, S.; Saouma, C. T.; Mayer, J. M.; Meyer, F. Fast Proton-Coupled Electron Transfer Observed for a High-Fidelity Structural and Functional [2Fe-2S] Rieske Model. *J. Am. Chem. Soc.* **2014**, *136* (10), 3946–3954.

(55) Saouma, C. T.; Morris, W. D.; Darcy, J. W.; Mayer, J. M. Protonation and Proton-Coupled Electron Transfer at S-Ligated [4Fe-4S] Clusters. *Chem. - A Eur. J.* **2015**, *21* (25), 9256–9260.

(56) Chang, C. J.; Chang, M. C. Y.; Damrauer, N. H.; Nocera, D. G. Proton-Coupled Electron Transfer: A Unifying Mechanism for Biological Charge Transport, Amino Acid Radical Initiation and Propagation, and Bond Making/Breaking Reactions of Water and Oxygen. *BBA - Biochim. Biophys. Acta* **2004**, *1655*, 13–28.

(57) Wiley, S. E.; Paddock, M. L.; Abresch, E. C.; Gross, L.; Van Der Geer, P.; Nechushtai, R.; Murphy, A. N.; Jennings, P. A.; Dixon, J. E. The Outer Mitochondrial Membrane Protein MitoNEET Contains a Novel Redox-Active 2Fe-2S Cluster. *J. Biol. Chem.* **2007**, *282* (33), 23745–23749.

(58) Kurisu, G.; Zhang, H.; Smith, J. L.; Cramer, W. A. Structure of the Cytochrome b_6f Complex of Oxygenic Photosynthesis: Tuning the Cavity. *Science.* **2003**, *302* (5647), 1009–1014.

(59) Link, T. A. The Structures of Rieske and Rieske-Type Proteins. *Adv. Inorg. Chem.* **1999**, *47*, 83–157.

(60) Zu, Y.; Couture, M. M. J.; Kolling, D. R. J.; Crofts, A. R.; Eltis, L. D.; Fee, J. A.; Hirst, J. Reduction Potentials of Rieske Clusters: Importance of the Coupling between Oxidation State and Histidine Protonation State. *Biochemistry* **2003**, *42* (42), 12400–12408.

(61) Schneider, D.; Schmidt, C. L. Multiple Rieske Proteins in Prokaryotes: Where and Why? *Biochim. Biophys. Acta - Bioenerg.* **2005**, *1710* (1), 1–12.

(62) Roret, T.; Tsan, P.; Couturier, J.; Zhang, B.; Johnson, M. K.; Rouhier, N.; Didierjean, C. Structural and Spectroscopic Insights into BolA-Glutaredoxin Complexes. *J. Biol. Chem.* **2014**, *289* (35), 24588–24598.

(63) Stegmaier, K.; Blinn, C. M.; Bechtel, D. F.; Greth, C.; Auerbach, H.; Müller, C. S.; Jakob, V.; Reijerse, E. J.; Netz, D. J. A.; Schünemann, V.; Pierik, A. J. Apd1 and Aim32 Are Prototypes of Bishistidinyl-Coordinated Non-Rieske [2Fe-2S] Proteins. *J. Am. Chem. Soc.* **2019**, *141* (14), 5753–5765.

(64) Blinn, C. M.; Pierik, A. J. In Vivo Und in Vitro Untersuchungen Neuer, Thioredoxin-Artiger [2Fe-2S]-Proteine, 2023.

(65) Volbeda, A.; Martinez, M. T. P.; Crack, J. C.; Amara, P.; Gigarel, O.; Munnoch, J. T.; Hutchings, M. I.; Darnault, C.; Le Brun, N. E.; Fontecilla-Camps, J. C. Crystal Structure of the Transcription Regulator RsrR Reveals a [2Fe-2S] Cluster Coordinated by Cys, Glu, and His Residues. *J. Am. Chem. Soc.* **2019**, *141* (6), 2367–2375.

(66) Geldenhuys, W. J.; Long, T. E.; Saralkar, P.; Iwasaki, T.; Nuñez, R. A. A.; Nair, R. R.; Konkle, M. E.; Menze, M. A.; Pinti, M. V.; Hollander, J. M.; Hazlehurst, L. A.; Robart, A. R. Crystal Structure of the Mitochondrial Protein MitoNEET Bound to a Benze-Sulfonide Ligand. *Commun. Chem.* **2019**, *2* (1), 1–9.

(67) Wiley, S. E.; Murphy, A. N.; Ross, S. A.; Van Der Geer, P.; Dixon, J. E. MitoNEET Is an Iron-Containing Outer Mitochondrial Membrane Protein That Regulates Oxidative Capacity. *Proc. Natl. Acad. Sci. U. S. A.* **2007**, *104* (13), 5318–5323.

(68) Geldenhuys, W. J.; Piktel, D.; Moore, J. C.; Rellick, S. L.; Meadows, E.; Pinti, M. V.; Hollander, J. M.; Ammer, A. G.; Martin, K. H.; Gibson, L. F. Loss of the Redox Mitochondrial Protein MitoNEET Leads to Mitochondrial Dysfunction in B-Cell Acute Lymphoblastic Leukemia. *Free Radic. Biol. Med.* **2021**, *175* (August), 226–235.

(69) Schwartz, C. J.; Giel, J. L.; Patschkowski, T.; Luther, C.; Ruzicka, F. J.; Beinert, H.; Kiley, P. J. IscR, an Fe-S Cluster-Containing Transcription Factor, Represses Expression of *Escherichia coli* Genes Encoding Fe-S Cluster Assembly Proteins. *Proc. Natl. Acad. Sci. U. S. A.* **2001**, *98* (26), 14895–14900.

(70) Rajagopalan, S.; Teter, S. J.; Zwart, P. H.; Brennan, R. G.; Phillips, K. J.; Kiley, P. J. Studies of IscR Reveal a Unique Mechanism for Metal-Dependent Regulation of DNA Binding Specificity. *Nat. Struct. Mol. Biol.* **2013**, *20* (6), 740–747.

(71) Fleischhacker, A. S.; Stubna, A.; Hsueh, K. L.; Guo, Y.; Teter, S. J.; Rose, J. C.; Brunold, T. C.; Markley, J. L.; Münck, E.; Kiley, P. J. Characterization of the [2Fe-2S] Cluster of *Escherichia coli* Transcription Factor IscR. *Biochemistry* **2012**, *51* (22), 4453–4462.

(72) Shimomura, Y.; Wada, K.; Fukuyama, K.; Takahashi, Y. The Asymmetric Trimeric Architecture of [2Fe-2S] IscU: Implications for Its Scaffolding during Iron-Sulfur Cluster Biosynthesis. *J. Mol. Biol.* **2008**, *383* (1), 133–143.

(73) Kounosu, A.; Li, Z.; Cosper, N. J.; Shokes, J. E.; Scott, R. A.; Imai, T.; Urushiyama, A.; Iwasaki, T. Engineering a Three-Cysteine, One-Histidine Ligand Environment into a New Hyperthermophilic Archaeal Rieske-Type [2Fe-2S] Ferredoxin from *Sulfolobus solfataricus*. *J. Biol. Chem.* **2004**, *279* (13), 12519–12528.

(74) Li, H.; Mapolelo, D. T.; Dingra, N. N.; Naik, S. G.; Lees, N. S.; Hoffman, B. M.; Riggs-Gelasco, P. J.; Boi, H. H.; Johnson, M. K.; Outten, C. E. The Yeast Iron Regulatory Proteins Grx3/4 and Fra2 Form Heterodimeric Complexes Containing a [2Fe-2S] Cluster with Cysteinyl and Histidyl Ligation. *Biochemistry* **2009**, *48* (40), 9569–9581.

(75) Li, H.; Mapolelo, D. T.; Randeniya, S.; Johnson, M. K.; Outten, C. E. Human Glutaredoxin 3 Forms [2Fe-2S]-Bridged Complexes with Human BolA2. *Biochemistry* **2012**, *51* (8), 1687–1696.

(76) Broach, R. B.; Jarrett, J. T. Role of the [2Fe-2S]2+ Cluster in Biotin Synthase: Mutagenesis of the Atypical Metal Ligand Arginine 260. *Biochemistry* **2006**, *45* (47), 14166–14174.

(77) Yankovskaya, V.; Horsefield, R.; Törnroth, S.; Luna-Chavez, C.; Miyoshi, H.; Léger, C.; Byrne, B.; Cecchini, G.; Iwata, S. Architecture of Succinate Dehydrogenase and Reactive Oxygen Species Generation. *Science.* **2003**, *299* (5607), 700–704.

(78) Sun, F.; Huo, X.; Zhai, Y.; Wang, A.; Xu, J.; Su, D.; Bartlam, M.; Rao, Z. Crystal Structure of Mitochondrial Respiratory Membrane Protein Complex II. *Cell* **2005**, *121* (7), 1043–1057.

(79) Demmer, J. K.; Huang, H.; Wang, S.; Demmer, U.; Thauer, R. K.; Ermler, U. Insights into Flavin-Based Electron Bifurcation via the NADH-Dependent Reduced Ferredoxin:NADP Oxidoreductase Structure. *J. Biol. Chem.* **2015**, *290* (36), 21985–21995.

(80) Xia, B.; Cheng, H.; Bandarian, V.; Reed, G. H.; Markley, J. L. Human Ferredoxin: Overproduction in *Escherichia coli*, Reconstitution in Vitro, and Spectroscopic Studies of Iron-Sulfur Cluster Ligand Cysteine-to- Serine Mutants. *Biochemistry* **1996**, *35* (29), 9488–9495.

(81) Cheng, H.; Xia, B.; Markley, J. L.; Reed, G. H. Optical, EPR, and 1H NMR Spectroscopy of Serine-Ligated [2Fe-2S] Ferredoxins Produced by Site-Directed Mutagenesis of Cysteine Residues in Recombinant *Anabaena* 7120 Vegetative Ferredoxin. *Biochemistry* **1994**, *33* (11), 3155–3164.

(82) Meyer, J.; Fujinaga, J.; Gaillard, J.; Lutz, M. Mutated Forms of the [2Fe-2S] Ferredoxin from *Clostridium pasteurianum* with Noncysteinyl Ligands to the Iron—Sulfur Cluster. *Biochemistry* **1994**, *33* (46), 13642–13650.

(83) Volbeda, A.; Darnault, C.; Renoux, O.; Nicolet, Y.; Fontecilla-camps, J. C. The Crystal Structure of the Global Anaerobic Transcriptional Regulator FNR Explains Its Extremely Fine-

Tuned Monomer-Dimer Equilibrium. *Sci. Adv.* **2015**, *1* (e1501086), 2–6.

(84) Gruner, I.; Frädrich, C.; Böttger, L. H.; Trautwein, A. X.; Jahn, D.; Härtig, E. Aspartate 141 Is the Fourth Ligand of the Oxygen-Sensing [4Fe-4S] 2+ Cluster of *Bacillus subtilis* Transcriptional Regulator Fnr. *J. Biol. Chem.* **2011**, *286* (3), 2017–2021.

(85) Volbeda, A.; Dodd, E. L.; Darnault, C.; Crack, J. C.; Renoux, O.; Hutchings, M. I.; Le Brun, N. E.; Fontecilla-Camps, J. C. Crystal Structures of the NO Sensor NsrR Reveal How Its Iron-Sulfur Cluster Modulates DNA Binding. *Nat. Commun.* **2017**, *8* (15052), 1–10.

(86) Bröcker, M. J.; Schomburg, S.; Heinz, D. W.; Jahn, D.; Schubert, W.-D.; Moser, J. Crystal Structure of the Nitrogenase-like Dark Operative Protochlorophyllide Oxidoreductase Catalytic Complex (ChlN/ChlB)2. *J. Biol. Chem.* **2010**, *285* (35), 27336–27345.

(87) Vitt, S.; Ma, K.; Warkentin, E.; Moll, J.; Pierik, A. J.; Shima, S.; Ermler, U. The F420-Reducing [NiFe]-Hydrogenase Complex from *Methanothermobacter marburgensis*, the First X-Ray Structure of a Group 3 Family Member. *J. Mol. Biol.* **2014**, *426* (15), 2813–2826.

(88) Lee, M.; Gräwert, T.; Quitterer, F.; Rohdich, F.; Eppinger, J.; Eisenreich, W.; Bacher, A.; Groll, M. Biosynthesis of Isoprenoids: Crystal Structure of the [4Fe-4S] Cluster Protein IspG. *J. Mol. Biol.* **2010**, *404* (4), 600–610.

(89) Dobritzsch, D.; Schneider, G.; Schnackerz, K. D.; Lindqvist, Y. Crystal Structure of Dihydropyrimidine Dehydrogenase, a Major Determinant of the Pharmacokinetics of the Anti-Cancer Drug 5-Fluorouracil. *EMBO J.* **2001**, *20* (4), 650–660.

(90) Peters, J. W.; Lanzilotta, W. N.; Lemon, B. J.; Seefeldt, L. C. X-Ray Crystal Structure of the Fe-Only Hydrogenase (CpI) from *Clostridium pasteurianum* to 1.8 Angstrom Resolution. *Science.* **1998**, *282* (5395), 1853–1858.

(91) Guigliarelli, B.; More, C.; Foumel, A.; Asso, M.; Bertrand, P.; Claude Hatchikian, E.; Williams, R.; Cammack, R. Structural Organization of the Ni and (4Fe-4S) Centers in the Active Form of *Desulfovibrio gigas* Hydrogenase. Analysis of the Magnetic Interactions by Electron Paramagnetic Resonance Spectroscopy. *Biochemistry* **1995**, *34* (14), 4781–4790.

(92) Garcin, E.; Vernede, X.; Hatchikian, E. C.; Volbeda, A.; Frey, M.; Fontecilla-Camps, J. C. The Crystal Structure of a Reduced [NiFeSe] Hydrogenase Provides an Image of the Activated Catalytic Center. *Structure* **1999**, *7* (5), 557–566.

(93) Magalon, A.; Asso, M.; Guigliarelli, B.; Rothery, R. A.; Bertrand, P.; Giordano, G.; Blasco, F. Molybdenum Cofactor Properties and [Fe-S] Cluster Coordination in *Escherichia coli* Nitrate Reductase A: Investigation by Site-Directed Mutagenesis of the Conserved His-50 Residue in the NarG Subunit. *Biochemistry* **1998**, *37* (20), 7363–7370.

(94) Bertero, M. G.; Rothery, R. A.; Palak, M.; Hou, C.; Lim, D.; Blasco, F.; Weiner, J. H.; Strynadka, N. C. J. Insights into the Respiratory Electron Transfer Pathway from the Structure of Nitrate Reductase A. *Nat. Struct. Biol.* **2003**, *10* (9), 681–687.

(95) Sazanov, L. A.; Hinchliffe, P. Structure of the Hydrophilic Domain of Respiratory Complex I from *Thermus thermophilus*. *Science.* **2006**, *311* (5766), 1430–1436.

(96) Martins, B. M.; Dobbek, H.; Çinkaya, I.; Buckel, W.; Messerschmidt, A. Crystal Structure of 4-Hydroxybutyryl-CoA Dehydratase: Radical Catalysis Involving a [4Fe-4S] Cluster and Flavin. *Proc. Natl. Acad. Sci. U. S. A.* **2004**, *101* (44), 15645–15649.

(97) Schiffer, A.; Parey, K.; Warkentin, E.; Diederichs, K.; Huber, H.; Stetter, K. O.; Kroneck, P. M. H.; Ermler, U. Structure of the Dissimilatory Sulfite Reductase from the Hyperthermophilic Archaeon *Archaeoglobus fulgidus*. *J. Mol. Biol.* **2008**, *379* (5), 1063–1074.

(98) Babini, E.; Bertini, I.; Borsari, M.; Capozzi, F.; Dikiy, A.; Eltis, L. D.; Luchinat, C. A Serine to Cysteine Ligand Mutation in the High Potential Iron - Sulfur Protein from *Chromatium vinosum*

Provides Insight into the Electronic Structure of the [4Fe-4S] Cluster. *J. Am. Chem. Soc.* **1996**, *118*, 75–80.

(99) Brereton, P. S.; Verhagen, M. F. J. M.; Zhou, Z. H.; Adams, M. W. W. Effect of Iron-Sulfur Cluster Environment in Modulating the Thermodynamic Properties and Biological Function of Ferredoxin from *Pyrococcus furiosus*. *Biochemistry* **1998**, *37* (20), 7351–7362.

(100) Brereton, P. S.; Duderstadt, R. E.; Staples, C. R.; Johnson, M. K.; Adams, M. W. W. Effect of Serinate Ligation at Each of the Iron Sites of the [Fe4S4] Cluster of *Pyrococcus furiosus* Ferredoxin on the Redox, Spectroscopic, and Biological Properties. *Biochemistry* **1999**, *38* (32), 10594–10605.

(101) Zheng, L.; Whitet, R. H.; Cash, V. L.; Jack, R. F.; Dean, D. R. Cysteine Desulfurase Activity Indicates a Role for NIFS in Metallocluster Biosynthesis. *Biochemistry* **1993**, *90*, 2754–2758.

(102) Nakamura, M.; Saeki, K.; Takahashi, Y. Hyperproduction of Recombinant Ferredoxins in *Escherichia coli* by Coexpression of the ORF1-ORF2-IscS-IscU-IscA-HscB-HscA-Fdx-ORF3 Gene Cluster. *J. Biochem.* **1999**, *126* (1), 10–18.

(103) Patzer, S. I.; Hantke, K. Sufs Is a NifS-Like Protein, and SufD Is Necessary for Stability of the [2Fe-2S] FhuF Protein in *Escherichia coli*. *J. Bacteriol.* **1999**, *181* (10), 3307–3309.

(104) Qi, W.; Cowan, J. A. Structural, Mechanistic and Coordination Chemistry of Relevance to the Biosynthesis of Iron-Sulfur and Related Iron Cofactors. *Coord. Chem. Rev.* **2011**, *255*, 688–699.

(105) Schilke, B.; Voisine, C.; Beinert, H.; Craig, E. Evidence for a Conserved System for Iron Metabolism in the Mitochondria of *Saccharomyces cerevisiae*. *Cell Biol.* **1999**, *96*, 10206–10211.

(106) Jacobson, M. R.; Brigle, K. E.; Bennett, L. T.; Setterquist, R. A.; Wilson, M. S.; Cash, V. L.; Beynon, J.; Newton, W. E.; Dean, D. R. Physical and Genetic Map of the Major Nif Gene Cluster from *Azotobacter vinelandii*. *J. Bacteriol.* **1989**, *171* (2), 1017–1027.

(107) Santos, P. C. Dos; Dean, D. R. FeS Cluster Assembly: NIF System in Nitrogen-Fixing Bacteria . *Encycl. Inorg. Bioinorg. Chem.* **2017**, 1–13.

(108) Mao, Z.; Liou, S. H.; Khadka, N.; Jenney, F. E.; Goodin, D. B.; Seefeldt, L. C.; Adams, M. W. W.; Cramer, S. P.; Larsen, D. S. Cluster-Dependent Charge-Transfer Dynamics in Iron-Sulfur Proteins. *Biochemistry* **2018**, *57* (6), 978–990.

(109) Blanc, B.; Gerez, C.; Ollagnier de Choudens, S. Assembly of Fe/S Proteins in Bacterial Systems. Biochemistry of the Bacterial ISC System. *Biochim. Biophys. Acta - Mol. Cell Res.* **2015**, *1853* (6), 1436–1447.

(110) Zheng, L.; Cash, V. L.; Flint, D. H.; Dean, D. R. Assembly of Iron-Sulfur Clusters. Identification of an IscSUA-HscBA-Fdx Gene Cluster from *Azotobacter vinelandii*. *J. Biol. Chem.* **1998**, *273* (21), 13264–13272.

(111) Romsang, A.; Dubbs, J. M.; Mongkolsuk, S. The Iron-Sulfur Cluster Biosynthesis Regulator IscR Contributes to Iron Homeostasis and Resistance to Oxidants in *Pseudomonas aeruginosa*. In *Stress and Environmental Regulation of Gene Expression and Adaptation in Bacteria*; 2016; Vol. 1, pp 1090–1102.

(112) Giel, J. L.; Rodionov, D.; Liu, M.; Blattner, F. R.; Kiley, P. J. IscR-Dependent Gene Expression Links Iron-Sulphur Cluster Assembly to the Control of O2-Regulated Genes in *Escherichia coli*. *Mol. Microbiol.* **2006**, *60* (4), 1058–1075.

(113) Mettert, E. L.; Kiley, P. J. How Is Fe-S Cluster Formation Regulated? *Annu. Rev. Microbiol.* **2015**, *69* (1), 505–526.

(114) Schwartz, C. J.; Djaman, O.; Imlay, J. A.; Kiley, P. J. The Cysteine Desulfurase, IscS, Has a Major Role in in Vivo Fe-S Cluster Formation in *Escherichia coli*. *Proc. Natl. Acad. Sci. U. S. A.* **2000**, *97* (16), 9009–9014.

(115) Agar, J. N.; Krebs, C.; Frazzon, J.; Huynh, B. H.; Dean, D. R.; Johnson, M. K. IscU as a Scaffold for Iron-Sulfur Cluster Biosynthesis: Sequential Assembly of [2Fe-2S] and [4Fe-4S] Clusters in IscU. *Biochemistry* **2000**, *39* (27), 7856–7862.

(116) Hoff, K. G.; Silberg, J. J.; Vickery, L. E. Interaction of the Iron-Sulfur Cluster Assembly Protein Iscu with the Hsc66/Hsc20 Molecular Chaperone System of *Escherichia coli*. *Proc. Natl. Acad. Sci. U. S. A.* **2000**, *97* (14), 7790–7795.

(117) Esquilin-Lebron, K.; Dubrac, S.; Barras, F.; Boyd, J. Bacterial Approaches for Assembling Iron-Sulfur Proteins. *MBio* **2022**, *12: e02425*, 1–17.

(118) Ollagnier-De-Choudens, S.; Mattioli, T.; Takahashi, Y.; Fontecave, M. Iron-Sulfur Cluster Assembly. Characterization of IscA and Evidence for a Specific and Functional Complex with Ferredoxin. *J. Biol. Chem.* **2001**, *276* (25), 22604–22607.

(119) Shimomura, Y.; Takahashi, Y.; Kakuta, Y.; Fukuyama, K. Crystal Structure of *Escherichia coli* YfhJ Protein, a Member of the ISC Machinery Involved in Assembly of Iron-Sulfur Clusters. *Proteins Struct. Funct. Genet.* **2005**, *60* (3), 566–569.

(120) Yokoyama, N.; Nonaka, C.; Ohashi, Y.; Shioda, M.; Terahata, T.; Chen, W.; Sakamoto, K.; Maruyama, C.; Saito, T.; Yuda, E.; Tanaka, N.; Fujishiro, T.; Kuzuyama, T.; Asai, K.; Takahashi, Y. Distinct Roles for U-Type Proteins in Iron–Sulfur Cluster Biosynthesis Revealed by Genetic Analysis of the Bacillus Subtilis SufCDSUB Operon. *Mol. Microbiol.* **2018**, *107* (6), 688–703.

(121) Blahut, M.; Sanchez, E.; Fisher, C. E.; Outten, F. W. Fe-S Cluster Biogenesis by the Bacterial Suf Pathway. *Biochim. Biophys. Acta - Mol. Cell Res.* **2020**, *1867* (118829), 1–12.

(122) Mettert, E. L.; Kiley, P. J. Coordinate Regulation of the Suf and Isc Fe-S Cluster Biogenesis Pathways by IscR Is Essential for Viability of *Escherichia coli*. *J. Bacteriol.* **2014**, *196* (24), 4315–4323.

(123) Johnson, D. C.; Dean, D. R.; Smith, A. D.; Johnson, M. K. Structure, Function, and Formation of Biological Iron-Sulfur Clusters. *Annu. Rev. Biochem.* **2005**, *74*, 247–281.

(124) Gao, F. Iron–Sulfur Cluster Biogenesis and Iron Homeostasis in Cyanobacteria. *Front. Microbiol.* **2020**, *11*, 1–11.

(125) Yeo, W. S.; Lee, J. H.; Lee, K. C.; Roe, J. H. IscR Acts as an Activator in Response to Oxidative Stress for the Suf Operon Encoding Fe-S Assembly Proteins. *Mol. Microbiol.* **2006**, *61* (1), 206–218.

(126) Sharma, A. K.; Pallesen, L. J.; Spang, R. J.; Walden, W. E. Cytosolic Iron-Sulfur Cluster Assembly (CIA) System: Factors, Mechanism, and Relevance to Cellular Iron Regulation. *J. Biol. Chem.* **2010**, *285* (35), 26745–26751.

(127) Lill, R.; Dutkiewicz, R.; Freibert, S. A.; Heidenreich, T.; Mascarenhas, J.; Netz, D. J.; Paul, V. D.; Pierik, A. J.; Richter, N.; Stümpfig, M.; Srinivasan, V.; Stehling, O.; Mühlenhoff, U. The Role of Mitochondria and the CIA Machinery in the Maturation of Cytosolic and Nuclear Iron-Sulfur Proteins. *Eur. J. Cell Biol.* **2015**, *94*, 280–291.

(128) Lill, R.; Mühlenhoff, U. Iron-Sulfur-Protein Biogenesis in Eukaryotes. *Trends Biochem. Sci.* **2005**, *30* (3), 133–141.

(129) Paul, V. D.; Lill, R. Biogenesis of Cytosolic and Nuclear Iron – Sulfur Proteins and Their Role in Genome Stability. *BBA - Mol. Cell Res.* **2015**, *1853* (6), 1528–1539.

(130) Picollo, M.; Aceto, M.; Vitorino, T. UV-Vis Spectroscopy. *Phys. Sci. Rev.* **2019**, *4* (4), 1–14.

(131) Malinin, D. R.; Yoe, J. H. Development of the Laws of Colorimetry a Historical Sketch. *J. Chem. Educ.* **1961**, *38* (3), 129–131.

(132) Jee, K. A Short Review on Ultraviolet and Visible Spectroscopy. *Int. J. Sci. Dev. Res.* **2023**, *7* (12), 683–687.

(133) *Circular Dichroism and the Conformational Analysis of Biomolecules*; Fasman, G. D., Ed.; 1996.

(134) Iametti, S.; Bonomi, F.; Barbiroli, A. Circular Dichroism to Probe the Synthesis, Transfer, and Stability of Fe-S Clusters. In *Fe-S Proteins: Methods and Protocols*; 2021; Vol. 2353, pp 209–229.

(135) Greenfield, N. J. Using Circular Dichroism Spectra to Estimate Protein Secondary Structure. *Nat. Protoc.* **2007**, *1* (6), 2876–2890.

(136) Klewpatinond, M.; Viles, J. H. Empirical Rules for Rationalising Visible Circular Dichroism of Cu2+ and Ni2+ Histidine Complexes: Applications to the Prion Protein. *FEBS Lett.* **2007**, *581* (7), 1430–1434.

(137) Conlan, A. R.; Paddock, M. L.; Homer, C.; Axelrod, H. L.; Cohen, A. E.; Abresch, E. C.; Zuris, J. A.; Nechushtai, R.; Jennings, P. A. Mutation of the His Ligand in MitoNEET Stabilizes the 2Fe-2S Cluster despite Conformational Heterogeneity in the Ligand Environment. *Acta Crystallogr. Sect. D Biol. Crystallogr.* **2011**, *67* (6), 516–523.

(138) Webert, H.; Freibert, S.; Gallo, A.; Heidenreich, T.; Linne, U.; Banci, L.; Lill, R.; Amlacher, S.; Hurt, E.; Mu, U. Functional Reconstitution of Mitochondrial Fe/S Cluster Synthesis on Isu1 Reveals the Involvement of Ferredoxin. *Nat. Commun.* **2014**, *5* (5013), 1–12.

(139) Freibert, S.; Weiler, B. D.; Bill, E.; Lill, R.; Pierik, A. J.; Ulrich, M. Biochemical Reconstitution and Spectroscopic Analysis of Iron – Sulfur Proteins. **2018**, *599*, 197–226.

(140) Miles, A. J.; Janes, R. W.; Wallace, B. A. Tools and Methods for Circular Dichroism Spectroscopy of Proteins: A Tutorial Review. *Chem. Soc. Rev.* **2021**, *50* (15), 8400–8413.

(141) *Practical Approaches to Biological Inorganic Chemistry*, 2nd ed.; Crichton, R., Louro, R. O., Eds.; 2020.

(142) Roessler, M. M.; Salvadori, E. Principles and Applications of EPR Spectroscopy in the Chemical Sciences. *Chem. Soc. Rev.* **2018**, *47* (8), 2534–2553.

(143) Hagen, W. R. *Biomolecular EPR Spectroscopy*; 2008.

(144) Wili, N. A Primer in Pulse EPR-Based Hyperfine Spectroscopy for NMR Spectroscopists. *J. Magn. Reson. Open* **2023**, *16–17* (100108), 1–13.

(145) Bianchi, C. L.; Djellabi, R.; Ponti, A.; Patience, G. S.; Falletta, E. Experimental Methods in Chemical Engineering: Mössbauer Spectroscopy. *Can. J. Chem. Eng.* **2021**, *99* (10), 2105–2114.

(146) Ameh, E. S. A Review of Basic Crystallography and X-Ray Diffraction Applications. *Int. J. Adv. Manuf. Technol.* **2019**, *105*, 3289–3302.

(147) Smyth, M. S.; Martin, J. H. J. X-Ray Crystallography. *J Clin Pathol Mol Pathol* **2000**, *53*, 8–14.

(148) Khoury, Y. El; Hellwig, P. A Combined Far-Infrared Spectroscopic and Electrochemical Approach for the Study of Iron – Sulfur Proteins. *ChemPhysChem* **2011**, *12*, 2669–2674.

(149) Trindade, I. B.; Coelho, A.; Cantini, F.; Piccioli, M.; Louro, R. O. NMR of Paramagnetic Metalloproteins in Solution: Ubi Venire, Quo Vadis? *J. Inorg. Biochem.* **2022**, *234* (111871),

1–15.

(150) Mack, J.; Stillman, M. J. Magnetic Circular Dichroism (MCD) Spectroscopy. In *Encyclopedia of Inorganic and Bioinorganic Chemistry*; 2011; pp 1–16.

(151) Caserta, G.; Zuccarello, L.; Barbosa, C.; Silveira, C. M.; Moe, E.; Katz, S.; Hildebrandt, P.; Zebger, I.; Todorovic, S. Unusual Structures and Unknown Roles of FeS Clusters in Metalloenzymes Seen from a Resonance Raman Spectroscopic Perspective. *Coord. Chem. Rev.* **2022**, *452*, 214287.

(152) Todorovic, S.; Teixeira, M. Resonance Raman Spectroscopy of Fe – S Proteins and Their Redox Properties. *JBIC J. Biol. Inorg. Chem.* **2018**, *23* (4), 647–661.

(153) Stoll, S.; Schweiger, A. EasySpin, a Comprehensive Software Package for Spectral Simulation and Analysis in EPR. *J. Magn. Reson.* **2006**, *178*, 42–55.

(154) Gunnlaugsson, H. P. Spreadsheet Based Analysis of Mössbauer Spectra. *Hyperfine Interact.* **2016**, *237* (1), 13–18.

(155) Fakruddin, M.; Mohammad Mazumdar, R.; Bin Mannan, K. S.; Chowdhury, A.; Hossain, M. N. Critical Factors Affecting the Success of Cloning, Expression, and Mass Production of Enzymes by Recombinant *E. coli*. *ISRN Biotechnol.* **2013**, *2013*, 1–7.

(156) Desjardins, P.; Conklin, D. NanoDrop Microvolume Quantitation of Nucleic Acids. *J. Vis. Exp.* **2010**, No. 45, e2565, 1–5.

(157) Carter, P. Site-Directed Mutagenesis. *Biochem. J.* **1986**, *237* (1), 1–7.

(158) Li, J.; Li, C.; Xiao, W.; Yuan, D.; Wan, G.; Ma, L. Site-Directed Mutagenesis by Combination of Homologous Recombination and Dpn I Digestion of the Plasmid Template in *Escherichia coli*. *Anal. Biochem.* **2008**, *373*, 389–391.

(159) Goa, J. A Micro Biuret Method for Protein Determination Determination of Total Protein in Cerebrospinal Fluid. *Scand. J. Clin. Lab. Invest.* **1953**, *5* (3), 218–222.

(160) Westley, J.; Lambeth, J. Protein Determination on the Basis of Copper-Binding Capacity. *BBA - Biochim. Biophys. Acta* **1960**, *40*, 364–366.

(161) Itzhaki, R. F.; Gill, D. M. A Micro-Biuret Method for Estimating Proteins. *Anal. Biochem.* **1964**, *410* (8), 401–410.

(162) Lovenberg, W.; Buchanan, B. B.; Rabinowitz, J. C. Studies on the Chemical Nature of Clostridial Ferredoxin. *J. Biol. Chem.* **1963**, *238* (12), 3899–3913.

(163) Fogo, J. K.; Popowsky, M. Spectrophotometric Determination of Hydrogen Sulfide. *Anal. Chem.* **1948**, *21* (6), 732–734.

(164) Manns, J. M. SDS-Polyacrylamide Gel Electrophoresis (SDS-PAGE) of Proteins. In *Current Protocols in Microbiology*; 2011; p A.3M.1-A.3M.13.

(165) Hellman, L. M.; Fried, M. G. Electrophoretic Mobility Shift Assay (EMSA) for Detecting Protein-Nucleic Acid Interactions. *Nat. Protoc.* **2007**, *2* (8), 1849–1861.

(166) Begic, T.; Pierik, A. J. Synthesis and Isolation of β-Lysine by Lysine 2,3-Aminomutase, 2022.

(167) Hansen, K.; Pierik, A. J. Expression, Reinigung Und Charakterisierung von Fünf Potenziellen Fe- Oder Fe/S-Proteinen Der Bäckerhefe, 2023.

(168) Wilson, G. S. Determination of Oxidation-Reduction Potentials. *Methods Enzymol.* **1978**, *54*, 396–410.

(169) Halaka, F. G.; Babcock, G. T.; Dye, J. L. Properties of 5-Methylphenazinium Methyl Sulfate.

J. Biol. Chem. **1982**, *257* (3), 1458–1461.

(170) Hagedoorn, P.; Weel, L. Van Der; Hagen, W. R. EPR Monitored Redox Titration of the Cofactors of *Saccharomyces cerevisiae* Nar1. *J. Vis. Exp.* **2014**, No. 93, e51611, 1–7.

(171) Le Breton, N.; Wright, J. J.; Jones, A. J. Y.; Salvadori, E.; Bridges, H. R.; Hirst, J.; Roessler, M. M. Using Hyperfine Electron Paramagnetic Resonance Spectroscopy to Define the Proton-Coupled Electron Transfer Reaction at Fe-S Cluster N2 in Respiratory Complex I. *J. Am. Chem. Soc.* **2017**, *139* (45), 16319–16326.

(172) Trautwein, A. X.; Bill, E.; Bominaar, E. L.; Winkler, H. Iron-Containing Proteins and Related Analogs — Complementary Mössbauer, EPR and Magnetic Susceptibility Studies. In *Structure and Bonding*; 1991; pp 1–95.

(173) Ohnishi, T.; Meinhardt, S. W.; von Jagow, G.; Yagi, T.; Hatefi, Y. Effect of Ethoxyformic Anhydride on the Rieske Iron-Sulfur Protein of Bovine Heart Ubiquinol: Cytochrome c Oxidoreductase. *FEBS Lett.* **1994**, *353* (1), 103–107.

(174) Fontecave, M.; Ollagnier-de-Choudens, S. Iron-Sulfur Cluster Biosynthesis in Bacteria: Mechanisms of Cluster Assembly and Transfer. *Arch. Biochem. Biophys.* **2008**, *474* (2), 226–237.

(175) Giel, J. L.; Nesbit, A. D.; Mettert, E. L.; Fleischhacker, A. S.; Wanta, B. T.; Kiley, P. J. Regulation of Iron-Sulphur Cluster Homeostasis through Transcriptional Control of the Isc Pathway by [2Fe-2S]-IscR in *Escherichia coli*. *Mol. Microbiol.* **2013**, *87* (3), 478–492.

(176) Nesbit, A. D.; Giel, J. L.; Rose, J. C.; Kiley, P. J. Sequence-Specific Binding to a Subset of IscR-Regulated Promoters Does Not Require IscR Fe-S Cluster Ligation. *J. Mol. Biol.* **2009**, *387* (1), 28–41.

(177) Santos, J. A.; Alonso-Garciá, N.; Macedo-Ribeiro, S.; Barbosa Pereira, P. J. The Unique Regulation of Iron-Sulfur Cluster Biogenesis in a Gram-Positive Bacterium. *Proc. Natl. Acad. Sci. U. S. A.* **2014**, *111* (22), E2251–E2260.

(178) Bergner, M.; Dechert, S.; Demeshko, S.; Kupper, C.; Mayer, J. M.; Meyer, F. Model of the MitoNEET [2Fe-2S] Cluster Shows Proton Coupled Electron Transfer. *J. Am. Chem. Soc.* **2017**, *139* (2), 701–707.

(179) Koone, J. C.; Simmang, M.; Saenger, D. L.; Hunsicker-Wang, L. M.; Shaw, B. F. Charge Regulation in a Rieske Proton Pump Pinpoints Zero, One, and Two Proton-Coupled Electron Transfer. *J. Am. Chem. Soc.* **2023**, *145* (30), 16488–16497.

(180) Reuter, W. H.; Masuch, T.; Ke, N.; Lenon, M.; Radzinski, M.; Van Loi, V.; Ren, G.; Riggs, P.; Antelmann, H.; Reichmann, D.; Leichert, L. I.; Berkmen, M. Utilizing Redox-Sensitive GFP Fusions to Detect in Vivo Redox Changes in a Genetically Engineered Prokaryote. *Redox Biol.* **2019**, *26* (101280), 1–9.

(181) Gadgil, H.; Oak, S. A.; Jarrett, H. W. Affinity Purification of DNA-Binding Proteins. *J. Biochem. Biophys. Methods* **2001**, *49*, 607–624.

(182) Voet, D.; Gratzer, W. B.; Cox, R. A.; Doty, P. Absorption Spectra of Nucleotides, Polynucleotides, and Nucleic Acids in the Far Ultraviolet. *Biopolymers* **1963**, *1* (3), 193–208.

(183) Prasad, S.; Mandal, I.; Singh, S.; Paul, A.; Mandal, B.; Venkatramani, R.; Swaminathan, R. Near UV-Visible Electronic Absorption Originating from Charged Amino Acids in a Monomeric Protein. *Chem. Sci.* **2017**, *8* (8), 5416–5433.

(184) Valer, L.; Rossetto, D.; Scintilla, S.; Hu, Y. J.; Tomar, A.; Nader, S.; Betinol, I. O.; Mansy, S. S. Methods to Identify and Characterize Iron–Sulfur Oligopeptides in Water. *Can. J. Chem.* **2022**, *100* (7), 475–483.

(185) Gasteiger, E.; Hoogland, C.; Gattiker, A.; Duvaud, S.; Wilkins, M. R.; Appel, R. D.; Bairoch, A. Protein Identification and Analysis Tools on the ExPASy Server. In *The Proteomics Protocols Handbook*; 2005; pp 571–607.

(186) Motomura, T.; Zuccarello, L.; Sétif, P.; Boussac, A.; Umena, Y.; Lemaire, D.; Tripathy, J. N.; Sugiura, M.; Hienerwadel, R.; Shen, J. R.; Berthomieu, C. An Alternative Plant-like Cyanobacterial Ferredoxin with Unprecedented Structural and Functional Properties. *Biochim. Biophys. Acta - Bioenerg.* **2019**, *1860* (11), 148084.

(187) Orme-Johnson, W. H.; Orme-Johnson, N. R. Overview of Iron-Sulfur Proteins. *Methods Enzymol.* **1978**, *53*, 259–268.

(188) Hurley, J. K.; Weber-Main, A. M.; Hodges, A. E.; Stankovich, M. T.; Benning, M. M.; Holden, H. M.; Cheng, H.; Xia, B.; Markley, J. L.; Genzor, C.; Gomez-Moreno, C.; Hafezi, R.; Tollin, G. Iron-Sulfur Cluster Cysteine-to-Serine Mutants of Anabaena [2Fe-2S] Ferredoxin Exhibit Unexpected Redox Properties and Are Competent in Electron Transfer to Ferredoxin:NADP+ Reductase. *Biochemistry* **1997**, *36* (49), 15109–15117.

(189) Camponeschi, F.; Piccioli, M.; Banci, L. The Intriguing MitoNEET: Functional and Spectroscopic Properties of a Unique [2Fe-2S] Cluster Coordination Geometry. *Molecules* **2022**, *27* (23).

(190) Noodleman, L.; Norman, J. G.; Osborne, J. H.; Aizman, A.; Case, D. A. Models for Ferredoxins: Electronic Structures of Iron-Sulfur Clusters with One, Two, and Four Iron Atoms. *J. Am. Chem. Soc.* **1985**, *107* (12), 3418–3426.

(191) Konkle, M. E.; Muellner, S. K.; Schwander, A. L.; Dicus, M. M.; Pokhrel, R.; Britt, R. D.; Taylor, A. B.; Hunsicker-Wang, L. M. Effects of PH on the Rieske Protein from *Thermus thermophilus*: A Spectroscopic and Structural Analysis. *Biochemistry* **2009**, *48*, 9848–9857.

(192) Iwasaki, T.; Samoilova, R. I.; Kounosu, A.; Ohmori, D.; Dikanov, S. A. Continuous-Wave and Pulsed EPR Characterization of the [2Fe-2S](Cys) 3(His)1 Cluster in Rat MitoNEET. *J. Am. Chem. Soc.* **2009**, *131* (38), 13659–13667.

(193) Brown, E. N.; Friemann, R.; Karlsson, A.; Parales, J. V.; Couture, M. M. J.; Eltis, L. D.; Ramaswamy, S. Determining Rieske Cluster Reduction Potentials. *J. Biol. Inorg. Chem.* **2008**, *13* (8), 1301–1313.

(194) Konkle, M. E.; Elsenheimer, K. N.; Hakala, K.; Robicheaux, J. C.; Weintraub, S. T.; Hunsicker-Wang, L. M. Chemical Modification of the Rieske Protein from *Thermus thermophilus* Using Diethyl Pyrocarbonate Modifies Ligating Histidine 154 and Reduces the [2Fe-2S] Cluster. *Biochemistry* **2010**, *49* (34), 7272–7281.

(195) Karagas, N. E.; Jones, C. N.; Osborn, D. J.; Dzierlenga, A. L.; Oyala, P.; Konkle, M. E.; Whitney, E. M.; David Britt, R.; Hunsicker-Wang, L. M. The Reduction Rates of DEPC-Modified Mutant *Thermus thermophilus* Rieske Proteins Differ When There Is a Negative Charge Proximal to the Cluster. *J. Biol. Inorg. Chem.* **2014**, *19* (7), 1121–1135.

(196) Davies, E. R. A New Pulse Endor Technique. *Phys. Lett. A* **1974**, *47* (1), 1–2.

(197) Hoffman, B. M. ENDOR of Metalloenzymes. *Acc. Chem. Res.* **2003**, *36* (7), 522–529.

(198) Tait, C. E.; Stoll, S. ENDOR with Band-Selective Shaped Inversion Pulses. *J. Magn. Reson.* **2017**, *277*, 36–44.

(199) Mims, W. B. Pulsed Endor Experiments. *R. Soc.* **1965**, *283* (1395), 452–457.

(200) Doan, P. E.; Lees, N. S.; Shanmugam, M.; Hoffman, B. M. Simulating Suppression Effects in Pulsed ENDOR, and the “hole in the Middle” of Mims and Davies ENDOR Spectra. *Appl. Magn. Reson.* **2010**, *37* (1), 763–779.

(201) Doan, P. E.; Hoffman, B. M. Making Hyperfine Selection in Mims ENDOR Independent of Deadtime. *Chem. Phys. Lett.* **1997**, *269*, 208–214.

(202) Bak, D. W.; Elliott, S. J. A Study of the CDGSH Protein Family: Biophysical and Bioinformatic Analysis of the [2FE-2S] Cluster Protein Mitoneet, 2006.

(203) Bak, D. W.; Elliott, S. J. Conserved Hydrogen Bonding Networks of MitoNEET Tune Fe-S Cluster Binding and Structural Stability. *Biochemistry* **2013**, *52*, 4687–4696.

(204) Duff, J. L. C.; Breton, J. L. J.; Butt, J. N.; Armstrong, F. A.; Thomson, A. J. Novel Redox Chemistry of [3Fe-4S] Clusters: Electrochemical Characterization of the All-Fe(II) Form of the [3Fe-4S] Cluster Generated Reversibly in Various Proteins and Its Spectroscopic Investigation in *Sulfolobus acidocaldarius* Ferredoxin. *J. Am. Chem. Soc.* **1996**, *118* (36), 8593–8603.

(205) Folgosa, F.; Martins, M. C.; Teixeira, M. Diversity and Complexity of Flavodiiron NO/O2 Reductases. *FEMS Microbiol. Lett.* **2018**, *365* (3), 1–8.

(206) Martins, M. C.; Silveira, C. M.; Morgado, L.; Teixeira, M.; Folgosa, F. An Iron-Sulfur Cluster as a New Metal Centre in a Flavodiiron Protein. *bioRxiv* **2024**, 2024.04.03.587993.

(207) Agovic, A.; Pierik, A. J. Biochemische Charakterisierung Des DUF1271-Enthaltenden YjdI-Proteins, Ein Ferredoxin Aus *E. coli*, 2023.

(208) Hill, C. L.; Renaud, J.; Holm, R. H.; Mortenson, L. E. Synthetic Analogues of the Active Sites of Iron-Sulfur Proteins. 15.1 Comparative Polarographic Potentials of the [Fe4S4(SR)4]2-,3- and *Clostridium pasteurianum* Ferredoxin Redox Couples. *J. Am. Chem. Soc.* **1976**, *4*, 2549–2557.

(209) Yang, S. S.; Ljungdahl, L. G.; LeGall, J. A Four-Iron, Four-Sulfide Ferredoxin with High Thermostability from *Clostridium thermoaceticum*. *J. Bacteriol.* **1977**, *130* (3), 1084–1090.

(210) Hoppe, A.; Pandelia, M. E.; Gärtner, W.; Lubitz, W. [Fe4S4]- and [Fe3S4]-Cluster Formation in Synthetic Peptides. *Biochim. Biophys. Acta - Bioenerg.* **2011**, *1807* (11), 1414–1422.

(211) Emptage, M. H.; Dreyers, J. L.; Kennedy, M. C.; Beinert, H. Optical and EPR Characterization of Different Species of Active and Inactive Aconitase. *J. Biol. Chem.* **1983**, *258* (18), 11106–11111.

(212) Müller, C. S.; Bechtel, D. F.; Auerbach, H.; Wolny, J. A.; Pierik, A. J.; Schünemann, V. Characterization of *Mycobacterium tuberculosis* Ferredoxin with Mössbauer Spectroscopy. *Hyperfine Interact.* **2019**, *240* (1), 1–8.

(213) Sakuradani, E.; Kobayashi, M.; Shimizu, S. Identification of an NADH-Cytochrome B5 Reductase Gene from an Arachidonic Acid-Producing Fungus, *Mortierella alpina* 1S-4, by Sequencing of the Encoding CDNA and Heterologous Expression in a Fungus, Aspergillus Oryzae. *Appl. Environ. Microbiol.* **1999**, *65* (9), 3873–3879.

(214) Liu, Y.; Vinyard, D. J.; Reesbeck, M. E.; Suzuki, T.; Manakongtreecheep, K.; Holland, P. L.; Brudvig, G. W.; Söll, D. A [3Fe-4S] Cluster Is Required for TRNA Thiolation in Archaea and Eukaryotes. *Proc. Natl. Acad. Sci. U. S. A.* **2016**, *113* (45), 12703–12708.

(215) Knaff, D. B.; Hirasawa, M.; Ameyibor, E.; Fu, W.; Johnson, M. K. Spectroscopic Evidence for a [3Fe-4S] Cluster in Spinach Glutamate Synthase. *J. Biol. Chem.* **1991**, *266* (23), 15080–15084.

(216) Teixeira, M.; Moura, I.; Xavier, A. V; Moura, J. J.; LeGall, J.; DerVartanian, D. V; Peck, H. D.; Huynh, B. H. Redox Intermediates of *Desulfovibrio gigas* [NiFe] Hydrogenase Generated Under Hydrogen. *J. Biol. Chem.* **1989**, *264* (28), 16435–16450.

(217) Papaefthymiou, V.; Girerd, J. J.; Moura, I.; Moura G, J.; Mtinck, E. Mossbauer Study of *D. gigas* Ferredoxin II and Spin-Coupling Model for the Fe3S4 Cluster with Valence

Delocalization. *J. Am. Chem. Soc.* **1987**, *109* (15), 4703–4710.

(218) Manodori, A.; Cecchini, G.; Schroder, I.; Gunsalus, R. P.; Werth, M. T.; Johnson, M. K. [3Fe-4S] to [4Fe-4S] Cluster Conversion in *Escherichia coli* Fumarate Reductase by Site-Directed Mutagenesis. *Biochemistry* **1992**, *31* (10), 2703–2712.

(219) Bingemann, R.; Klein, A. Conversion of the Central [4Fe-4S] Cluster into a [3Fe-4S] Cluster Leads to Reduced Hydrogen-Uptake Activity of the F420-Reducing Hydrogenase of *Methanococcus voltae*. *Eur. J. Biochem.* **2000**, *267* (22), 6612–6618.

(220) Rousset, M.; Montet, Y.; Guigliarelli, B.; Forget, N.; Asso, M.; Bertrand, P.; Fontecilla-Camps, J. C.; Hatchikian, E. C. [3Fe-4S] to [4Fe-4S] Cluster Conversion in *Desulfovibrio fructosovorans* [NiFe] Hydrogenase by Site-Directed Mutagenesis. *Proc. Natl. Acad. Sci. U. S. A.* **1998**, *95* (20), 11625–11630.

(221) Thomson, A. J.; Breton, J.; N. Butt, J.; A. Armstrong, F.; Hatchikian, E. C. Iron-Sulphur Clusters with Labile Metal Ions. *J. Inorg. Biochem.* **1992**, *47* (1), 197–207.

(222) Martins, M. C.; Silveira, C. M.; Morgado, L.; Teixeira, M.; Folgosa, F. *An Iron-Sulfur Cluster as a New Metal Centre in a Flavodiiron Protein*; 2024. https://www.biorxiv.org/content/10.1101/2024.04.03.587993v1?rss=1&utm_source=researcher_app&utm_medium=referral&utm_campaign=RESR_MRKT_Researcher_inbound.

(223) Rieske, J. S.; Hansen, R. E.; Zaugg, W. S. Studies on the Electron Transfer System. *J. Biol. Chem.* **1964**, *239* (9), 3017–3022.

(224) Colbert, C. L.; Couture, M. M.-J.; Eltis, L. D.; Bolin, J. T. A Cluster Exposed: Structure of the Rieske Ferredoxin from Biphenyl Dioxygenase and the Redox Properties of Rieske Fe-S Proteins. *Structure* **2000**, *8* (12), 1267–1278.

(225) Ding, H.; Robertson, D. E.; Daldal, F.; Dutton, L. Cytochrome Bc1 Complex [2Fe-2S] Cluster and Its Interaction with Ubiquinone at the Q0 Site: A Double-Occupancy Q0 Site Model. *Biochemistry* **1992**, No. 31, 3144–3158.

(226) Fee, J. A.; Findling, K. L.; Yoshida, T.; Hille, R.; Tarr, G. E.; Hearshen, D. O.; Dunham, W. R.; Day, E. P.; Kent, T. A.; Münck, E. Purification and Characterization of the Rieske Iron-Sulfur Protein from *Thermus thermophilus*. Evidence for a [2Fe-2S] Cluster Having Non-Cysteine Ligands. *J. Biol. Chem.* **1984**, *259* (1), 124–133.

(227) Hunte, C.; Koepke, J.; Lange, C.; Roßmanith, T.; Michel, H. Structure at 2.3 Å Resolution of the Cytochrome Bc1 Complex from the Yeast *Saccharomyces cerevisiae* Co-Crystallized with an Antibody Fv Fragment. *Structure* **2000**, *8* (6), 669–684.

(228) Conte, L.; Zara, V. The Rieske Iron-Sulfur Protein: Import and Assembly into the Cytochrome bc_1 Complex of Yeast Mitochondria. *Bioinorg. Chem. Appl.* **2011**, *2011*, 1–9.

(229) Palsdottir, H.; Lojero, C. G.; Trumpower, B. L.; Hunte, C. Structure of the Yeast Cytochrome bc_1 Complex with a Hydroxyquinone Anion Qo Site Inhibitor Bound. *J. Biol. Chem.* **2003**, *278* (33), 31303–31311.

(230) Schmidt, C. L.; Shaw, L. A Comprehensive Phylogenetic Analysis of Rieske and Rieske-Type Iron-Sulfur Proteins. *J. Bioenerg. Biomembr.* **2001**, *33* (1), 9–26.

(231) Hunsicker-Wang, L. M.; Heine, A.; Chen, Y.; Luna, E. P.; Todaro, T.; Zhang, Y. M.; Williams, P. A.; McRee, D. E.; Hirst, J.; Stout, C. D.; Fee, J. A. High-Resolution Structure of the Soluble, Respiratory-Type Rieske Protein from *Thermus thermophilus*: Analysis and Comparison. *Biochemistry* **2003**, *42* (24), 7303–7317.

(232) Iwasaki, T.; Kounosu, A.; Samoilova, R. I.; Dikanov, S. A. 15N HYSCORE Characterization of the Fully Deprotonated, Reduced Form of the Archaeal Rieske [2Fe-2S] Center. *J. Am. Chem. Soc.* **2006**, *128* (7), 2170–2171.

(233) De Oliveira, F. T.; Bominaar, E. L.; Hirst, J.; Fee, J. A.; Münck, E. Antisymmetric Exchange in [2Fe-2S]1+ Clusters: EPR of the Rieske Protein from *Thermus thermophilus* at PH 14. *J. Am. Chem. Soc.* **2004**, *126* (17), 5338–5339.

(234) Iwasaki, T.; Isogai, Y.; Iizuka, T.; Oshima, T. Sulredoxin: A Novel Iron-Sulfur Protein of the Thermoacidophilic *Archaeon sulfolobus* Sp. Strain 7 with a Rieske-Type [2Fe-2S] Center. *J. Bacteriol.* **1996**, *177* (9), 2726–2582.

(235) Thuy, N. T. H.; Kongkaew, A.; Flood, A.; Boontawan, A. Fermentation and Crystallization of Succinic Acid from *Actinobacillus succinogenes* ATCC55618 Using Fresh Cassava Root as the Main Substrate. *Bioresour. Technol.* **2017**, *233*, 342–352.

(236) Orii, Y.; Morita, M. Measurement of the PH of Frozen Buffer Solutions by Using pH Indicators. *J. Biochem.* **1977**, *81* (1), 163–168.

(237) Warren, J. J.; Tronic, T. A.; Mayer, J. M. Thermochemistry of Proton-Coupled Electron Transfer Reagents and Its Implications. *Chem. Rev.* **2010**, *110* (12), 6961–7001.

(238) Schafer, F. Q.; Buettner, G. R. Redox Environment of the Cell as Viewed Through the Redox State of the Glutathione Disulfide/Glutathione Couple. *Free Radic. Biol. Med.* **2001**, *30* (11), 1191–1212.

(239) Bagramyan, K.; Galstyan, A.; Trchounian, A. Redox Potential Is a Determinant in the *Escherichia coli* Anaerobic Fermentative Growth and Survival: Effects of Impermeable Oxidant. *Bioelectrochemistry* **2000**, *51*, 151–156.

(240) dos Santos, N. M.; Picinato, B. A.; Santos, L. S.; de Araújo, H. L.; Balan, A.; Koide, T.; Marques, M. V. Mapping the IscR Regulon Sheds Light on the Regulation of Iron Homeostasis in Caulobacter. *Front. Microbiol.* **2024**, *15* (1463854), 1–18.

(241) Abdulaziz, E. N.; Bell, T. A.; Rashid, B.; Heacock, M. L.; Begic, T.; Skinner, O. S.; Yaseen, M. A.; Chao, L. H.; Mootha, V. K.; Pierik, A. J.; Cracan, V. A Natural Fusion of Flavodiiron, Rubredoxin, and Rubredoxin Oxidoreductase Domains Is a Self-Sufficient Water-Forming Oxidase of *Trichomonas vaginalis*. *J. Biol. Chem.* **2022**, *298* (8), 102210.

Supplementary information

S.1. Vector pET-Duet1 and pET29 b (+) maps

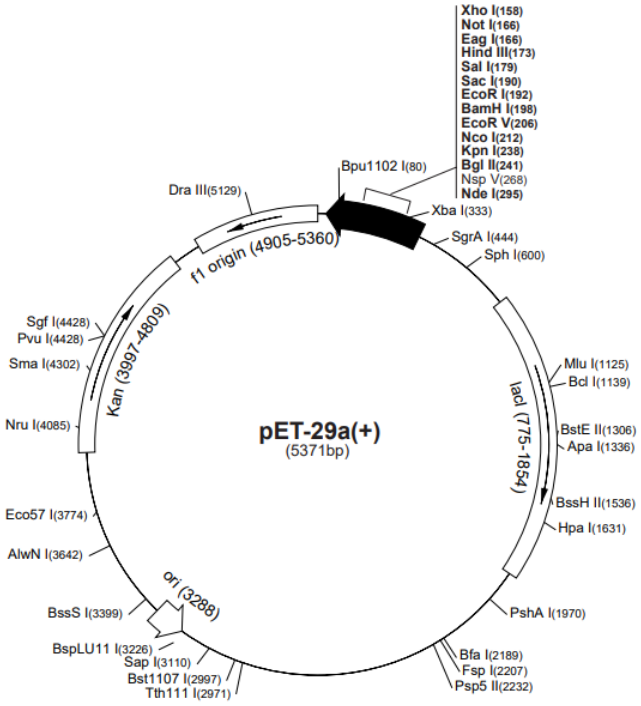

S. 1. pET-29a(+) vector map. pET-29b(+) is the same as pET-29a(+), except pET-29b(+) is a 5370bp plasmid; subtract 1bp from each site beyond BamH I at 198. Reproduced from Novagen plasmid information sheet.

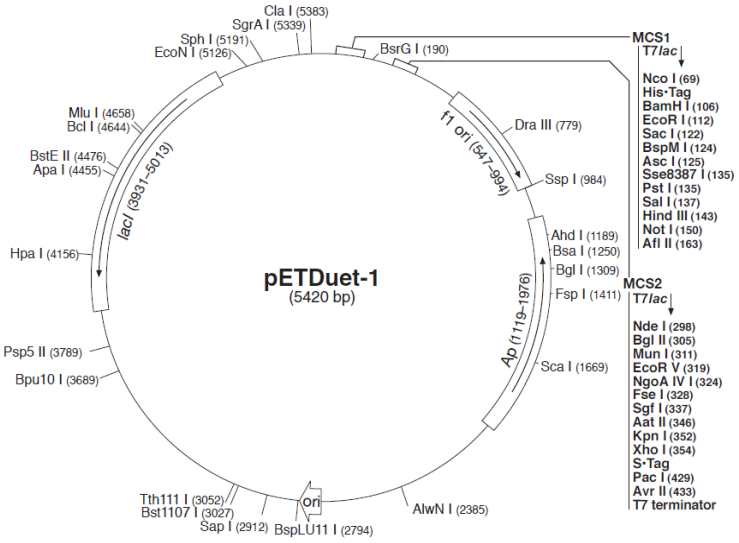

S. 2. pET-Duet1 vector map. Reproduced from Novagen plasmid information sheet.

S.2. Miniprep low copy plasmids protocol

Reproduced from the manufacturer's (Macherey-Nagel) book of protocols.

Isolation of low-copy plasmids, P1 constructs, or cosmids

Processing of larger culture volumes requires increased lysis buffer volumes. The buffer volumes provided with the kit are calculated for high-copy plasmid purification only. Thus, if this support protocol is to be used frequently, an additional NucleoSpin® Buffer Set can be ordered separately (see ordering information).

Before starting the preparation:

• Check if Wash Buffer A4 was prepared according to section 3.

1. Cultivate and harvest bacterial cells

Use 5–10 mL of a saturated *E. coli* LB culture, pellet cells in a standard benchtop microcentrifuge for 30 s at 11,000 x *g*. Discard the supernatant and remove as much of the liquid as possible.

2. Cell lysis

Add 500 µL Buffer A1. Resuspend the cell pellet completely by vortexing or pipetting up and down. Make sure no cell clumps remain before addition of Buffer A2!

Attention: Check Buffer A2 for precipitated SDS prior to use. If a white precipitate is visible, warm the buffer for several minutes at 30–40 °C until precipitate is dissolved completely. Cool buffer down to room temperature (18–25 °C).

Add 500 µL Buffer A2. Mix gently by inverting the tube 6–8 times. Do not vortex to avoid shearing of genomic DNA. Incubate at room temperature for up to 5 min or until lysate appears clear.

Add 600 µL Buffer A3. Mix thoroughly by inverting the tube 6–8 times. Do not vortex to avoid shearing of genomic DNA!

3. Clarification of lysate

Centrifuge for 10 min at 11,000 x *g* at room temperature.

4. Bind DNA

Place a NucleoSpin® Plasmid / Plasmid (NoLid) Column in a Collection Tube (2 mL) and decant the supernatant from step 3 or pipette a maximum of 750 µL of the supernatant onto the column. Centrifuge for 1 min at 11,000 x *g*. Discard flow-through and place the NucleoSpin® Plasmid Column back into the collection tube. Repeat this step to load the remaining lysate.

5. **Wash silica membrane**

Recommended: Add 500 µL Buffer AW, optionally preheated to 50 °C, and centrifuge for 1 min at 11,000 x g. *Discard flow-through and place the NucleoSpin® Plasmid / Plasmid (NoLid) Column back into the* collection tube*.*

Add 600 µL Buffer A4 (supplemented with ethanol, see section 3). Centrifuge for 1 min at 11,000 x *g*. Discard flow-through and place the NucleoSpin® Plasmid / Plasmid (NoLid) Column back into the empty collection tube.

6. **Dry silica membrane**

Centrifuge for 2 min at 11,000 x *g* and discard the collection tube.

Note: Residual ethanolic wash buffer might inhibit enzymatic reactions.

7. **Elute DNA**

Place the NucleoSpin® Plasmid / Plasmid (NoLid) Column in a 1.5 mL microcentrifuge tube (not provided) and add 50 µL Buffer AE preheated to 70 °C. Incubate for 2 min at 70 °C. Centrifuge for 1 min at 11,000 x *g*.

Note: For more efficient elution procedures and alternative elution buffer (e.g., TE buffer or water) see section 2.4.

S.3. PCR-Clean-Up-Kit protocol

Reproduced from the manufacturer's (Macherey-Nagel) book of protocols.

The following protocol is suitable for PCR clean-up as well as DNA concentration and removal of salts, enzymes, etc. from enzymatic reactions (SDS < 0.1 %).

Before starting the preparation:

Check if Wash Buffer NT3 was prepared according to section 3.

1. **Adjust DNA binding condition**

For very small sample volumes < 30 µL adjust the volume of the reaction mixture to 50–100 µL with water. It is not necessary to remove mineral oil. Mix 1 volume of sample with 2 volumes of Buffer NTI (e.g., mix 100 µL PCR reaction and 200 µL Buffer NTI). Note: For removal of small fragments like primer dimers dilutions of Buffer NTI can be used instead of 100 % Buffer NTI. Please refer to section 2.3.

2. Bind DNA

Place a NucleoSpin® Gel and PCR Clean-up Column into a Collection Tube (2 mL) and load up to 700 µL sample. Centrifuge for 30 s at 11,000 x g. Discard flow-through and place the column back into the collection tube. Load remaining sample if necessary and repeat the centrifugation step.

3. Wash silica membrane

Add 700 µL Buffer NT3 to the NucleoSpin® Gel and PCR Clean-up Column. Centrifuge for 30 s at 11,000 x g. Discard flow-through and place the column back into the collection tube.

Recommended: Repeat previous washing step to minimize chaotropic salt carry-over and improve A260/A230 values (see section 2.7 for detailed information).

4. Dry silica membrane

Centrifuge for 1 min at 11,000 x g to remove Buffer NT3 completely. Make sure the spin column does not come in contact with the flow-through while removing it from the centrifuge and the collection tube.

Note: Residual ethanol from Buffer NT3 might inhibit enzymatic reactions. Total removal of ethanol can be achieved by incubating the columns for 2–5 min at 70 °C prior to elution.

5. Elute DNA

Place the NucleoSpin® Gel and PCR Clean-up Column into a new 1.5 mL microcentrifuge tube (not provided). Add 15–30 µL Buffer NE and incubate at room temperature (15–25 °C) for 1 min. Centrifuge for 1 min at 11,000 x g.

Note: DNA recovery of larger fragments (> 1000 bp) can be increased by multiple elution steps with fresh buffer, heating to 70 °C and incubation for 5 min. See section 2.6 for detailed information.

S.4. Iron, protein and acid labile sulfur determination

All iron, protein and acid labile determination conducted in this work were done according to the following pipetting schemes. These protocols are based on the manual of the Metals in Biology course, made by Prof. Dr. Antonio J. Pierik.

Iron determination													
Reagent (µL)	Blank	Iron standard						undiluted protein			10 x diluted protein		
Iron standard 0.2 mg/mL	0	10	20	40	60	80	100	10	20	40	10	20	40
ddH_2O	200	190	180	160	140	120	100	190	180	160	190	180	160

HCl 1% (v/v)	100	100	100	100	100	100	100	100	100	100	100	100	100
Mix and incubate for 10 minutes at 80ºC and let the vial cool down													
Ammonium acetate 7.5% (w/v)	500	500	500	500	500	500	500	500	500	500	500	500	500
Mix by vortexing													
Ascorbic acid 4% (w/v)	100	100	100	100	100	100	100	100	100	100	100	100	100
Mix by vortexing													
SDS 2.5 % (w/v)	100	100	100	100	100	100	100	100	100	100	100	100	100
Ferene 1.5 % (w/v)	100	100	100	100	100	100	100	100	100	100	100	100	100
Centrifuge at 13000 xg for 7 minutes													
Measure the absorption at 593 nm against water													
Absorbance	Blank	Iron standard						undiluted protein			10 x diluted protein		

Protein determination												
Reagent (µL)	Blank	BSA standard					Undiluted protein			10-fold diluted protein		
BSA 2 mg/mL	0	50	100	150	200	300	10	20	30	10	20	30
ddH_2O	1000	950	900	850	800	700	990	980	970	990	980	970
DOC 0.15%	100	100	100	100	100	100	100	100	100	100	100	100
Mix and incubate for 5 minutes at room temperature												
TCA 70%	100	100	100	100	100	100	100	100	100	100	100	100
Mix and centrifuge at 13000 *xg* for 10 minutes and remove the supernatant carefully												
NaOH 3%	950	950	950	950	950	950	950	950	950	950	950	950
Mix by vortexing to dissolve the protein precipitate												
Microbiuret reagent	50	50	50	50	50	50	50	50	50	50	50	50
Incubate in the dark for 15 minutes												
Measure the absorption at 545 nm against water												
Absorbance	Blank	BSA standard					undiluted protein			10 x diluted protein		

Acid labile sulfur determination												
Reagent (µL)	Blank	Sulfur standard					undiluted protein			10 x diluted protein		
Li_2S 2 mM	0	5	10	15	20	25	10	20	30	10	20	30
ddH_2O	200	195	190	185	180	175	190	180	170	190	180	170
Zinc acetate 1%	600	600	600	600	600	600	600	600	600	600	600	600
NaOH 7%	50	50	50	50	50	50	50	50	50	50	50	50
Invert once and incubate for 15 minutes at room temperature												
Spin down for a few seconds at low speed and perform steps 7,8 and 9 consecutively for each vial												
DMPD 0.1%	150	150	150	150	150	150	150	150	150	150	150	150
$FeCl_3$ 10 mM	150	150	150	150	150	150	150	150	150	150	150	150
Immediately close the vial and vortex vigorously fo 30 seconds												
Centrifuge at 13000 xg for 10 minutes												
Transfer the supernatant to a plastic cuvette and measure the absorption at 670 nm against water												
Absorbance	Blank	Sulfur standard					undiluted protein			10 x diluted protein		

S.5. SDS-PAGE and EMSA

Several buffers and reagents were used in the preparation of SDS-PAGE and EMSA gels. They are described below. All buffers and components used for EMSA were prepared like the ones used in the SDS-PAGE experiments, except they did not contain SDS and β-mercaptoethanol.

S.5.1. Running buffer

Running buffer was used in this work as the buffer the gel was immersed in during gel run. It was always used as a 1x concentrated solution.

	Reagent	Mass/Volume
10-fold SDS-PAGE running buffer	Tris	30.3 g
	Glycine	144 g
	ddH_2O	up to 1 L
10% SDS	SDS	25 g
	ddH_2O	up to 250 mL
1 x Running buffer	10 x SDS	10 mL
	10 x SDS-PAGE running buffer	100 mL
	ddH_2O	up to 1 L

S.5.2. Stacking and separating buffers

Buffers used in gel preparation.

	Reagent	Mass/Volume
4 x stacking buffer	0.5 M Tris-HCl, pH 6.8	15.5 g
	0.4% (w/v) SDS	1 g
	ddH_2O	up to 250 mL
4 x separating buffer	1.5 M Tris-HCl, pH 8.8	45.5 g
	0.4% (w/v) SDS	1 g
	ddH_2O	up to 250 mL

S.5.3. Sample buffer

Sample buffer was used in this work for sample preparation and to follow sample migration during the run. The sample buffer was always diluted to 1x final concentration.

	Reagent	Mass/Volume
5 x Sample buffer (loading buffer)	Glycerol	6.3 g
	2 M Tris-HCl, pH 6.8	1.56 mL
	SDS	1 g
	Bromophenol Blue	50 mg
	ddH_2O	up to 10 mL

S.5.4. SDS-PAGE gel preparation

SDS-PAGE gels used in this experimental work consisted of a 4% stacking gel and a 15% separating gel, prepared according to the table below. EMSA gels had no stacking gel and were entirely made of a 6% resolving gel, also prepared according to the table but with SDS- and β-mercaptoethanol-free buffers. Each preparation yields enough for two gels.

Stacking gel	
Reagent	**Volume**
4 x Stacking gel buffer	0.6 mL
30% acrylamide/bisacrylamide	1.125 mL
ddH_2O	2.73 mL

Resolving gel						
Reagent	16.50%	15%	12.50%	10%	8%	6%
30% acrylamide/bisacrylamide	6.6 mL	6 mL	5 mL	4 mL	3.2 mL	2.4 mL
4 x Separating gel buffer	3 mL					
ddH_2O	2.3 mL	2.9 mL	3.9 mL	4.9 mL	5.7 mL	6.5 mL

S.6. Crystallographic screens

S.6.1. ProPlex HT-96 screen

HT-96 Well	Salt	Buffer	pH	Precipitant	Additive
A1	None	0.1 M Tris	8.0	25 % v/v PEG 350 MME	None
A2	0.1 M calcium acetate	0.1 M MES	6.0	15 % v/v PEG 400	None
A3	0.1 M lithium Chloride	0.1 M Na HEPES	7.5	20 % v/v PEG 400	None
A4	None	0.1 M Tris	8.0	25 % v/v PEG 400	None
A5	None	0.1 M MES	6.5	15 % v/v PEG 550 MME	None
A6	0.2 M sodium chloride	0.1 M Na/K phosphate	6.5	25 % w/v PEG 1000	None
A7	0.1 M ammonium sulfate	0.1 M Tris	7.5	20 % w/v PEG 1500	None
A8	0.2 M ammonium sulfate	0.1 M sodium acetate	5.5	10 % w/v PEG 2000 MME	None
A9	0.2 M sodium chloride	0.1 M MES	6.0	20 % w/v PEG 2000 MME	None
A10	0.1 M potassium chloride	0.1 M Tris	8.0	15 % w/v PEG 2000 MME	None
A11	None	0.1 M Na HEPES	7.5	25 % w/v PEG 2000 MME	None
A12	0.2 M sodium acetate	0.1 M sodium citrate	5.5	5 % w/v PEG 4000	None
B1	0.2 M lithium sulfate	0.1 M Tris	7.5	5 % w/v PEG 4000	None
B2	0.1 M calcium acetate	0.1 M sodium acetate	4.5	10 % w/v PEG 4000	None
B3	0.2 M sodium acetate	0.1 M sodium citrate	5.5	10 % w/v PEG 4000	None
B4	0.2 M sodium chloride	0.1 M MES	6.5	10 % w/v PEG 4000	None
B5	0.1 M magnesium chloride	0.1 M Na HEPES	7.5	10 % w/v PEG 4000	None
B6	None	0.1 M Na HEPES	7.0	10 % w/v PEG 4000	10 % v/v 2-propanol
B7	0.2 M ammonium acetate	0.1 M sodium acetate	4.0	15 % w/v PEG 4000	None
B8	0.1 M magnesium chloride	0.1 M sodium citrate	5.0	15 % w/v PEG 4000	None
B9	None	0.1 M sodium cacodylate	6.0	15 % w/v PEG 4000	None
B10	0.15 M ammonium sulfate	0.1 M MES	6.0	15 % w/v PEG 4000	None
B11	None	0.1 M Na HEPES	7.0	15 % w/v PEG 4000	None
B12	0.1 M magnesium chloride	0.1 M Na HEPES	7.0	15 % w/v PEG 4000	None
C1	0.15 M ammonium sulfate	0.1 M Tris	8.0	15 % w/v PEG 4000	None
C2	None	0.1 M sodium citrate	4.5	20 % w/v PEG 4000	None
C3	0.2 M ammonium acetate	0.1 M sodium acetate	5.0	20 % w/v PEG 4000	None
C4	0.2 M lithium sulfate	0.1 M MES	6.0	20 % w/v PEG 4000	None
C5	None	0.1 M Tris	8.0	20 % w/v PEG 4000	None
C6	0.15 M ammonium sulfate	0.1 M Na HEPES	7.0	20 % w/v PEG 4000	None
C7	None	0.1 M sodium citrate	5.6	20 % w/v PEG 4000	20 % v/v 2-propanol
C8	0.2 M sodium chloride	0.1 M Tris	8.0	20 % w/v PEG 4000	None
C9	None	0.1 M sodium cacodylate	5.5	25 % w/v PEG 4000	None
C10	0.15 M ammonium sulfate	0.1 M MES	5.5	25 % w/v PEG 4000	None
C11	None	0.1 M sodium cacodylate	6.5	25 % w/v PEG 4000	None
C12	0.2 M potassium iodide	0.1 M MES	6.5	25 % w/v PEG 4000	None
D1	0.2 M sodium chloride	0.1 M Na HEPES	7.5	25 % w/v PEG 4000	None
D2	None	0.1 M MES	6.5	10 % w/v PEG 5000 MME	12 % v/v 1-propanol
D3	0.1 M potassium chloride	0.1 M Na HEPES	7.0	15 % w/v PEG 5000 MME	None
D4	0.2 M ammonium sulfate	0.1 M Tris	7.5	20 % w/v PEG 5000 MME	None
D5	0.1 M magnesium chloride	0.1 M MES	6.0	8 % w/v PEG 6000	None
D6	0.15 M sodium chloride	0.1 M Tris	8.0	8 % w/v PEG 6000	None
D7	None	0.1 M sodium citrate	5.5	15 % w/v PEG 6000	None
D8	0.1 M magnesium acetate	0.1 M sodium cacodylate	6.5	15 % w/v PEG 6000	None
D9	None	0.1 M MES	6.5	15 % w/v PEG 6000	5 % v/v MPD
D10	0.1 M potassium chloride	0.1 M Na HEPES	7.5	15 % w/v PEG 6000	None
D11	None	0.1 M Tris	8.5	15 % w/v PEG 6000	None
D12	None	0.1 M Tris	8.5	20 % w/v PEG 6000	None

HT-96 Well	Salt	Buffer	pH	Precipitant	Additive
E1	0.1 M magnesium acetate	0.1 M sodium acetate	4.5	8 % w/v PEG 8000	None
E2	None	0.1 M sodium citrate	5.0	8 % w/v PEG 8000	None
E3	0.2 M sodium chloride	0.1 M sodium cacodylate	6.0	8 % w/v PEG 8000	None
E4	None	0.1 M Na HEPES	7.0	8 % w/v PEG 8000	None
E5	None	0.1 M Tris	8.0	8 % w/v PEG 8000	None
E6	0.1 M calcium acetate	0.1 M sodium cacodylate	5.5	12 % w/v PEG 8000	None
E7	None	0.1 M sodium phosphate	6.5	12 % w/v PEG 8000	None
E8	0.1 M magnesium acetate	0.1 M MOPS	7.5	12 % w/v PEG 8000	None
E9	0.2 M sodium chloride	0.1 M Na HEPES	7.5	12 % w/v PEG 8000	None
E10	**0.2 M ammonium sulfate**	0.1 M Tris	8.5	12 % w/v PEG 8000	None
E11	None	0.1 M sodium citrate	5.0	20 % w/v PEG 8000	None
E12	0.2 M ammonium sulfate	0.1 M MES	6.5	20 % w/v PEG 8000	None
F1	None	0.1 M Na HEPES	7.0	20 % w/v PEG 8000	None
F2	0.2 M lithium chloride	0.1 M Tris	8.0	20 % w/v PEG 8000	None
F3	0.1 M magnesium acetate	0.1 M MES	6.5	10 % w/v PEG 10 000	None
F4	None	0.1 M Na HEPES	7.0	18 % w/v PEG 12 000	None
F5	0.1 M sodium chloride	0.1 M Tris	8.0	8 % w/v PEG 20 000	None
F6	None	0.1 M Na HEPES	7.0	15 % w/v PEG 20 000	None
F7	None	0.1 M MES	6.5	0.5 M ammonium sulfate	None
F8	None	0.1 M sodium acetate	5.0	1 M ammonium sulfate	None
F9	None	0.1 M MES	6.5	1 M ammonium sulfate	None
F10	None	0.1 M Tris	8.0	1 M ammonium sulfate	None
F11	None	0.1 M sodium acetate	5.0	1.5 M ammonium sulfate	None
F12	None	0.1 M Na HEPES	7.0	1.5 M ammonium sulfate	None
G1	None	0.1 M Tris	8.0	1.5 M ammonium sulfate	None
G2	None	0.1 M sodium acetate	5.0	2 M ammonium sulfate	None
G3	None	0.1 M Na HEPES	7.0	2 M ammonium sulfate	None
G4	None	0.1 M Tris	8.0	2 M ammonium sulfate	None
G5	1 M potassium chloride	0.1 M Na HEPES	7.0	1 M ammonium sulfate	None
G6	None	0.1 M sodium acetate	5.0	2 M sodium formate	None
G7	None	0.1 M Tris	7.5	3 M sodium formate	None
G8	None	None	7.5	0.8 M Na/K hydrogen phosphate	None
G9	None	None	7.0	1.3 M Na/K hydrogen phosphate	None
G10	None	None	6.5	1.6 M Na/K hydrogen phosphate	None
G11	None	0.1 M Na HEPES	7.5	1 M sodium acetate	None
G12	None	0.1 M Na HEPES	7.0	1 M sodium citrate	None
H1	None	0.1 M sodium citrate	6.0	2 M sodium chloride	None
H2	None	0.1 M MES	6.5	1 M lithium sulfate	None
H3	None	0.1 M Tris	8.0	1.6 M lithium sulfate	None
H4	None	None	6.0	1.4 M sodium malonate	None
H5	None	0.1 M Tris	8.0	1.2 M Na/K tartrate	None
H6	None	0.1 M MES	6.5	1.6 M magnesium sulfate	None
H7	None	0.1 M sodium acetate	5.0	15 % v/v MPD	2 % w/v PEG 4000
H8	0.05 M calcium acetate	0.1 M sodium cacodylate	6.0	25 % v/v MPD	None
H9	None	0.1 M imidazole	7.0	50 % v/v MPD	None
H10	0.05 M magnesium Chloride	0.1 M MES	6.5	10 % v/v 2-propanol	5 % w/v PEG 4000
H11	0.2 M ammonium acetate	0.1 M Na HEPES	7.5	25 % v/v 2-propanol	None
H12	0.1 M sodium chloride	0.1 M Tris	8.0	15 % v/v ethanol	5 % v/v MPD

Table reproduced from Molecular Dimensions ProPlex HT-96 information sheet.

S.6.2. MemGold™ HT-96 Eco Screen

Well #	Conc.	Units	Salt	Conc.	Units	Buffer	pH	Conc.	Units	Precipitant
A1	2.2	M	Ammonium sulfate	0.08	M	Sodium citrate	5.2			
A2	1.2	M	Sodium citrate tribasic dihydrate	0.01	M	Tris	8.0			
A3				0.015	M	Tricine	8.5	24	% w/v	PEG 4000
A4	0.36	M	Sodium chloride	0.015	M	Sodium phosphate	7.0	9.9	% w/v	PEG 4000
A5	0.3	M	Sodium chloride	0.01	M	Tris	8.0	27.5	% w/v	PEG 4000
A6				0.225	M	MES/Bis-Tris	6.6	6.6	% w/v	PEG 6000
A7	0.1	M	Ammonium sulfate	0.1	M	HEPES	7.5	12	% w/v	PEG 4000
								22	% v/v	Glycerol
A8	0.01	M	Magnesium sulfate heptahydrate	0.02	M	MES	6.5	7.7	% w/v	PEG 1500
	0.02	M	Sodium chloride							
	0.02	M	Calcium chloride dihydrate							
A9	2.5	M	Ammonium sulfate	0.05	M	HEPES	7.5			
A10	1.1	M	Sodium citrate tribasic dihydrate	0.0665	M	HEPES	7.5			
A11	3.3	M	Ammonium sulfate	0.15	M	Potassium phosphate	6.5			
A12	0.1	M	Magnesium acetate tetrahydrate	0.1	M	Sodium citrate	5.8	14	% w/v	PEG 5000 MME
B1	0.1	M	Soduim chloride	0.02	M	Sodium citrate	5.6	11	% w/v	PEG 3350
B2	0.1	M	Sodium chloride	0.02	M	Sodium citrate	5.6	5.5	% w/v	PEG 3350
B3	0.05	M	Calcium chloride dihydrate	0.1	M	Tris	8.2	32	% v/v	PEG 400
	0.05	M	Barium chloride dihydrate							
B4	0.05	M	Sodium chloride	0.1	M	Sodium phosphate	6.2	16	% w/v	PEG 4000
B5	0.1	M	Magnesium chloride hexahydrate	0.03	M	Tris-HCl	8.2	19	% w/v	PEG 4000
B6	0.2	M	Sodium chloride	0.025	M	HEPES	7.5	13	% w/v	PEG 4000
B7				0.1	M	HEPES	7.5	11	% w/v	PEG 3350
B8	0.1	M	Sodium chloride	0.02	M	KMES	6.7	6.6	% w/v	PEG 4000
B9	0.1	M	Potassium chloride	0.02	M	Tris	7.0	20	% w/v	PEG 4000
B10	0.05	M	Magnesium chloride hexahydrate	0.1	M	MES	6.7	6.6	% w/v	PEG 3350
B11	0.2	M	Potassium chloride	0.1	M	Sodium citrate	5.5	37	% v/v	Pentaerythritol propoxylate (5/4 PO/OH)
B12				0.1	M	Tris	8.0	5.5	% w/v	PEG 4000
C1	0.1	M	Sodium chloride	0.02	M	Tris	7.0	7.7	% w/v	PEG 4000
C2	0.1	M	Magnesium chloride hexahydrate	0.1	M	Tris	7.5	22	% v/v	PEG 400
C3	0.04	M	Sodium chloride	0.04	M	Tris	8.0	27	% v/v	PEG 350 MME
C4	0.05	M	Sodium chloride	0.1	M	Sodium citrate	6.0	22	% v/v	PEG 400
	0.02	M	Magnesium chloride hexahydrate							
C5				0.1	M	Sodium acetate	5.5	8.8	% w/v	PEG 2000 MME
C6				0.4	M	Ammonium acetate	8.0	13	% w/v	PEG 2000 MME
C7				0.02	M	Bis-Tris	7.0	15	% w/v	PEG 2000
C8	0.1	M	Sodium chloride	0.02	M	Tris	7.5	11	% w/v	PEG 1500
	0.1	M	Magnesium chloride hexahydrate							
C9	0.1	M	Sodium chloride	0.1	M	HEPES	8.0	11	% w/v	PEG 1500
	0.1	M	Magnesium chloride hexahydrate							
C10	0.2	M	Sodium acetate trihydrate	0.1	M	HEPES	7.0	22	% w/v	PEG 3000
	0.2	M	Potassium chloride							
C11	0.02	M	Nickel(II) sulfate hexahydrate	0.01	M	HEPES	7.0	33	% v/v	Jeffamine® M-600
C12	0.15	M	Sodium chloride	0.1	M	Tris	8.0	13	% w/v	PEG 6000
D1	0.2	M	Calcium chloride dihydrate	0.1	M	HEPES	7.5	53	% v/v	PEG 400
D2	0.05	M	Magnesium acetate tetrahydrate	0.05	M	Sodium acetate	5.0	28	% v/v	PEG 400
D3				0.05	M	HEPES	7.5	22	% w/v	PEG 4000
D4	0.2	M	Calcium chloride dihydrate	0.1	M	Tris-HCl	8.0	44	% v/v	PEG 400
D5	0.05	M	Magnesium acetate tetrahydrate	0.05	M	Sodium acetate	5.4	24	% v/v	PEG 400
D6	0.2	M	Calcium chloride dihydrate	0.1	M	MES	6.5	26	% v/v	PEG 350 MME
D7	0.1	M	Potassium chloride	0.1	M	Tris	8.5	39	% v/v	PEG 400
D8	0.05	M	Magnesium chloride hexahydrate	0.1	M	Glycine	9.0	22	% v/v	PEG 400
D9	0.1	M	Ammonium sulfate	0.1	M	Glycine	3.8	28	% v/v	Triethylene glycol (TEG)
D10	0.15	M	Sodium formate	0.1	M	HEPES	7.2	18	% w/v	PEG 3350
D11				0.2	M	Sodium acetate	6.8	8.8	% w/v	PEG 6000
D12	0.2	M	Potassium chloride	0.1	M	MES	6.5	18	% w/v	PEG 6000

Well #	Conc.	Units	Salt	Conc.	Units	Buffer	pH	Conc.	Units	Precipitant
E1	0.22	M	Sodium citrate tribasic dihydrate	0.1	M	Tris	8.0	35	% v/v	PEG 400
E2				0.1	M	Sodium acetate	4.5	17	% v/v	PEG 400
E3	1.0	M	Lithium sulfate	0.02	M	Tris	8.5	1.8	% w/v	PEG 8000
E4				0.02	M	Tris	7.5	22	% v/v	PEG 500 MME
E5	0.05	M	Sodium chloride	0.02	M	Glycine	10.0	33	% w/v	PEG 1000
E6	0.2	M	Magnesium chloride hexahydrate	0.1	M	Tris	8.5	25	% w/v	PEG 4000
E7	0.2	M	Magnesium chloride hexahydrate	0.1	M	MES	6.5	31	% w/v	PEG 2000
E8				0.64	M	Sodium acetate	4.6	18	% w/v	PEG 3350
E9	0.1	M	Sodium chloride	0.1	M	Tris-HCl	8.0	33	% v/v	PEG 400
	0.1	M	Cadmium chloride hemi(pentahydrate)							
E10				0.1	M	BICINE	8.9	31	% w/v	PEG 2000
E11	0.05	M	Sodium sulfate	0.05	M	Tris	8.5	35	% v/v	PEG 400
	0.05	M	Lithium sulfate							
E12	0.1	M	Sodium chloride	0.05	M	Glycine	9.5	33	% v/v	PEG 300
F1	0.3	M	Magnesium nitrate hexahydrate	0.1	M	Tris	8.0	23	% w/v	PEG 2000
F2	0.12	M	Lithium sulfate	0.02	M	Tris	7.5	20	% v/v	PEG 300
				0.1	M	Sodium citrate	5.0			
F3	0.1	M	Sodium chloride	0.12	M	Tris	9.4	20	% v/v	PEG 400
F4	0.2	M	Sodium chloride	0.1	M	HEPES	7.0	22	% v/v	PEG 500 MME
F5	0.1	M	Sodium chloride	0.1	M	Tris	8.0	21	% v/v	PEG 400
	0.325	M	Sodium acetate trihydrate							
F6	0.02	M	Sodium citrate tribasic dihydrate	0.08	M	Sodium phosphate	6.2	18	% w/v	PEG 2000
F7	0.02	M	Potassium nitrate	0.03	M	Potassium citrate	6.5	7.7	% w/v	PEG 4000
F8	0.1	M	Sodium chloride	0.1	M	Tris	8.5	30	% w/v	PEG 2000 MME
	0.005	M	Magnesium chloride hexahydrate							
F9	0.2	M	Calcium chloride dihydrate	0.1	M	HEPES	7.0	33	% v/v	PEG 400
F10	0.1	M	Calcium chloride dihydrate	0.1	M	Tris	6.5	13	% w/v	PEG 2000 MME
F11	0.2	M	Ammonium sulfate	0.02	M	Sodium acetate	4.0	33	% v/v	PEG 200
	0.02	M	Sodium chloride							
F12	0.07	M	Sodium chloride	0.05	M	Sodium citrate	4.5	22	% v/v	PEG 400
G1	0.2	M	Ammonium sulfate	0.1	M	Sodium acetate	4.6	28	% v/v	PEG 500 MME
G2				0.05	M	Glycine	9.0	55	% v/v	PEG 400
G3	0.1	M	Magnesium chloride hexahydrate	0.1	M	Tris	8.5	33	% v/v	PEG 400
	0.1	M	Sodium chloride							
G4	0.05	M	Citric acid					19	% w/v	PEG 1000
	0.1	M	Lithium sulfate							
	0.05	M	Sodium phosphate dibasic dihydrate							
G5	0.2	M	Magnesium chloride hexahydrate	0.025	M	Sodium citrate	4.0	33	% v/v	PEG 400
	0.1	M	Potassium chloride							
G6	0.05	M	Zinc acetate dihydrate	0.05	M	MES	6.1	11	% w/v	PEG 8000
G7	0.3	M	Magnesium nitrate hexahydrate	0.1	M	Tris	8.0	22	% w/v	PEG 8000
G8	0.1	M	Sodium chloride	0.1	M	MES	6.5	33	% v/v	PEG 400
								4	% v/v	Ethylene glycol
G9	0.05	M	Sodium chloride	0.1	M	Sodium citrate	5.5	26	% v/v	PEG 400
G10	0.1	M	Lithium sulfate	0.1	M	Glycine	9.3	30	% v/v	PEG 400
G11	0.15	M	Potassium citrate tribasic monohydrate					22	% w/v	PEG 6000
	0.05	M	Lithium citrate tribasic tetrahydrate							
	0.1	M	Sodium phosphate monobasic monohydrate							
G12	0.001	M	Zinc sulfate heptahydrate	0.05	M	HEPES	7.8	28	% v/v	PEG 600
H1	0.1	M	Sodium chloride	0.1	M	Sodium phosphate	7.0	33	% v/v	PEG 300
H2	0.1	M	Sodium chloride	0.05	M	BICINE	9.0	33	% v/v	PEG 300
H3	0.05	M	Zinc acetate dihydrate	0.1	M	MES	6.0	6.6	% w/v	PEG 8000
								6	% v/v	Ethylene glycol
H4	0.2	M	Lithium sulfate	0.1	M	Sodium citrate	3.5	28	% v/v	PEG 400
H5	0.1	M	Sodium chloride	0.1	M	Tris	7.5	11	% w/v	PEG 4000
H6	0.05	M	Lithium sulfate	0.1	M	Tricine	7.4	7	% w/v	PEG 3000
H7	0.2	M	Calcium chloride dihydrate	0.1	M	MES	6.5	33	% v/v	PEG 400
H8	1.0	M	Sodium chloride	0.1	M	Sodium citrate	6.0	28	% w/v	PEG 4000
H9				0.1	M	HEPES	7.5	11	% w/v	PEG 4000
H10	0.002	M	Zinc sulfate heptahydrate	0.08	M	HEPES	7.0	25	% v/v	Jeffamine® ED-2003
H11	0.001	M	Cadmium chloride hemi(pentahydrate)	0.1	M	MES	6.5	30	% v/v	PEG 400
	0.03	M	Magnesium chloride hexahydrate							
H12	3.0	M	Sodium chloride	0.1	M	Bis-Tris propane	7.0			

Table reproduced from Molecular Dimensions MemGold™ HT-96 Eco Screen information sheet.

S.6.3. MemGold2™ HT-96 Eco Screen

Tube #	Conc.	Salt	Conc.	Salt2	Conc.	Buffer	pH	Conc.	Precipitant
A1	0.2 M	Magnesium chloride hexahydrate	0.005 M	Cadmium chloride hemi(pentahydrate)	0.1 M	Tris	7.5	14 % v/v	PEG 500 MME
A2	0.1 M	Potassium acetate	0.01 M	Potassium chloride	0.02 M	Tris	7.0	44 % w/v	PEG 3000
A3	0.08 M	Magnesium sulfate heptahydrate	0.02 M	Sodium chloride	0.02 M	MES	6.0	10 % w/v	PEG 1450
A4	0.04 M	Magnesium sulfate heptahydrate	0.02 M	Sodium chloride	0.02 M	MES	6.5	8 % w/v	PEG 1450
A5	0.05 M	Sodium sulfate	0.05 M	Lithium chloride	0.05 M	Tris	8.5	32 % v/v	PEG 400
A6	0.1 M	Sodium phosphate monobasic monohydrate	0.1 M	Potassium phosphate dibasic	0.1 M	Bis-Tris propane	7.5	10 % w/v	PEG 3350
A7	0.1 M	Sodium chloride	0.1 M	Lithium sulfate	0.1 M	ADA	6.5	11.5 % w/v	PEG 4000
A8	0.1 M	Lithium chloride	0.1 M	Cadmium chloride hemi(pentahydrate)	0.1 M	Sodium acetate	4.5	30 % v/v	PEG 400
A9	0.2 M	Ammonium sulfate	0.1 M	Sodium chloride	0.1 M	Sodium citrate	6.0	20 % w/v	PEG 2000
A10	0.2 M	Lithium sulfate	0.1 M	Sodium chloride	0.1 M	HEPES	7.0	31 % v/v	PEG 400
A11	0.2 M	Ammonium phosphate monobasic	0.1 M	Ammonium sulfate	0.1 M	Sodium citrate	4.5	32 % v/v	PEG 400
A12	0.05 M	Sodium citrate tribasic dihydrate	0.12 M	Potassium chloride	0.08 M	Bis-Tris	6.0	14 % w/v	PEG 4000
B1	0.1 M	Sodium chloride	0.15 M	Ammonium sulfate	0.01 M	MES	6.5	19 % w/v	PEG 1000
B2	0.01 M	Nickel(II) sulfate hexahydrate			0.1 M	Sodium citrate	6.0	18 % w/v	PEG 2000 MME
B3	0.02 M	Magnesium chloride hexahydrate			0.02 M	MES	6.0	3.5 % w/v	PEG 3350
B4	0.02 M	Sodium chloride			0.05 M	MES	5.5	14 % v/v	PEG 350 MME
B5	0.025 M	Magnesium chloride hexahydrate			0.02 M	MOPS	7.0	35 % v/v	PEG 500 MME
B6	0.03 M	Magnesium chloride hexahydrate			0.1 M	MES	6.5	28 % v/v	PEG 400
B7	0.04 M	Sodium chloride			0.04 M	Tris	8.0	25 % v/v	PEG 350 MME
B8	0.04 M	Magnesium acetate tetrahydrate			0.1 M	MES	6.0	36 % v/v	MPD
B9	0.05 M	Zinc acetate dihydrate			0.05 M	ADA	6.3	11 % w/v	PEG 8000
B10	0.05 M	Magnesium acetate tetrahydrate			0.1 M	MES	6.5	26 % v/v	PEG 400
B11	0.05 M	Magnesium acetate tetrahydrate			0.1 M	Glycine	9.5	32 % v/v	PEG 400
B12	0.066 M	Sodium chloride			0.02 M	Tris	7.5	3 % w/v	PEG 4000
C1	0.075 M	Magnesium chloride hexahydrate			0.1 M	MES	6.5	30 % w/v	PEG 2000 MME
C2	0.08 M	Magnesium acetate tetrahydrate			0.1 M	Sodium citrate	6.0	14 % w/v	PEG 5000 MME
C3	0.01 M	Zinc acetate dihydrate	1.5 M	Ammonium sulfate	0.1 M	MES	6.0		
C4	0.087 M	Ammonium sulfate			0.05 M	Tris	7.0	22 % v/v	PEG 250 DME
C5	0.1 M	Magnesium chloride hexahydrate			0.1 M	Tris	7.5	13 % w/v	PEG 8000
C6	0.1 M	Magnesium formate dihydrate			0.1 M	MOPS	7.0	17 % w/v	PEG 3350
C7	0.1 M	Potassium chloride			0.1 M	Bis-Tris	6.0	18 % w/v	PEG 4000
C8	0.1 M	Potassium chloride			0.1 M	Potassium phosphate	7.5	18 % v/v	PEG 200
C9	0.1 M	Magnesium acetate tetrahydrate			0.1 M	MES	6.0	22 % w/v	PEG 4000
C10	0.1 M	Calcium acetate hydrate			0.1 M	MES	6.0	22 % w/v	PEG 8000
C11	0.1 M	Ammonium sulfate			0.1 M	HEPES	8.5	23 % w/v	PEG 3350
C12	0.1 M	Potassium chloride			0.1 M	MES	6.0	32 % v/v	PEG 400
D1	0.1 M	Sodium chloride			0.1 M	MES	6.5	36 % v/v	PEG 300
D2	0.1 M	Sodium chloride			0.1 M	BICINE	9.0	45 % v/v	PEG 500 MME
D3	0.15 M	Calcium chloride dihydrate			0.1 M	Glycine	9.0	35 % v/v	PEG 400
D4	0.2 M	Ammonium sulfate			0.05 M	ADA	6.5	13 % w/v	PEG 4000
D5	0.2 M	Choline chloride			0.1 M	Tris	7.5	14 % w/v	PEG 2000 MME
D6	0.2 M	Sodium chloride			0.05 M	MOPS	7.0	19 % w/v	PEG 6000
D7	0.05 M	Sodium chloride			0.05 M	MOPS	7.0	19 % w/v	PEG 6000
D8	0.2 M	Magnesium formate dihydrate			0.05 M	Tris	8.0	19 % w/v	PEG 3350
D9	0.2 M	Calcium chloride dihydrate			0.1 M	MES	5.0	20 % v/v	PEG 350 MME
D10	0.2 M	Ammonium nitrate			0.05 M	HEPES	7.0	20 % w/v	PEG 3350
D11	0.02 M	Lithium chloride	0.05 M	Magnesium chloride hexahydrate	0.02 M	Glycine	10.0	33 % w/v	PEG 1000
D12	0.2 M	Calcium acetate hydrate			0.1 M	HEPES	7.0	24 % v/v	PEG 400

Tube #	Conc.	Salt	Conc.	Salt2	Conc.	Buffer	pH	Conc.	Precipitant
E1	0.2 M	Sodium acetate trihydrate			0.1 M	MES	6.5	28 % v/v	PEG 400
E2	0.2 M	Sodium chloride			0.05 M	Calcium acetate	5.0	29 % v/v	PEG 400
E3	0.2 M	Sodium chloride			0.1 M	HEPES	7.0	29 % v/v	PEG 400
E4	0.2 M	Ammonium formate			0.1 M	Tris	7.0	31 % v/v	Pentaerythritole ethoxylate (15/4 EO/OH)
E5	0.2 M	Ammonium sulfate			0.1 M	Tris	8.5	35 % w/v	PEG 3350
E6	0.2 M	Calcium acetate hydrate			0.1 M	Sodium acetate	5.0	38 % v/v	PEG 400
E7	0.2 M	Sodium chloride			0.1 M	MOPS	7.5	38 % v/v	PEG 400
E8	2.0 M	Ammonium sulfate	0.2 M	Sodium chloride	0.1 M	MES	6.5		
E9	0.225 M	Ammonium sulfate			0.05 M	Sodium acetate	4.0	12 % w/v	PEG 4000
E10	0.23 M	Sodium chloride			0.05 M	Sodium acetate	4.5	33 % v/v	PEG 400
E11	0.25 M	Magnesium formate dihydrate			0.1 M	MES	6.5	22 % w/v	PEG 3000
E12	0.25 M	Magnesium chloride hexahydrate			0.1 M	Tris	8.5	40 % w/v	PEG 1000
F1	0.3 M	Lithium sulfate			0.1 M	MES	6.5	25 % v/v	PEG 400
F2	0.3 M	Ammonium formate			0.05 M	Tris	9.0	33 % v/v	PEG 500 MME
F3	0.3 M	Barium chloride dihydrate			0.1 M	MES	6.0	34 % v/v	PEG 400
F4	0.32 M	Lithium chloride			0.1 M	Sodium citrate	5.5	14 % w/v	PEG 4000
F5	0.34 M	Ammonium sulfate			0.1 M	Sodium citrate	5.5	12 % w/v	PEG 4000
F6	0.35 M	Lithium sulfate			0.1 M	Sodium acetate	4.0	11 % v/v	PEG 600
F7	0.37 M	Potassium nitrate			0.1 M	MES	6.5	22 % v/v	PEG 400
F8	0.4 M	Ammonium sulfate			0.1 M	MES	6.5	10 % w/v	PEG 3350
F9	0.04 M	Magnesium chloride hexahydrate	0.05 M	Sodium chloride	0.1 M	HEPES	7.5	32 % v/v	PEG 400
F10	0.4 M	Potassium chloride			0.05 M	HEPES	7.5	12 % v/v	PEG 400
F11	0.4 M	Ammonium thiocyanate			0.1 M	Sodium acetate	4.5	15 % w/v	PEG 4000
F12	0.4 M	Sodium thiocyanate			0.1 M	Sodium acetate	4.0	16 % w/v	PEG 4000
G1	0.5 M	Potassium chloride			0.05 M	HEPES	6.5	20 % v/v	PEG 400
G2	0.5 M	Magnesium chloride hexahydrate			0.05 M	Tris	7.5	21 % v/v	PEG 350 MME
G3	0.8 M	Potassium formate			0.1 M	Sodium acetate	5.0	11 % w/v	PEG 4000
G4		none			0.1 M	MOPS	7.0	9 % w/v	PEG 8000
G5		none			0.1 M	MES	6.0	11 % w/v	PEG 20,000
G6		none			0.1 M	MES	6.5	13 % v/v	PEG 400
G7		none			0.1 M	ADA	5.5	14 % w/v	PEG 6000
G8		none			0.05 M	Tris	7.5	17 % v/v	PEG 350 MME
G9		none			0.07 M	Sodium citrate	4.5	22 % v/v	PEG 300
G10		none			0.05 M	ADA	6.5	24 % v/v	PEG 400
G11		none			0.1 M	MES	6.5	24 % w/v	PEG 1500
G12		none			0.1 M	HEPES	7.5	28 % v/v	PEG 600
H1		none			0.05 M	Tris	8.5	28 % v/v	PEG 400
H2		none			0.1 M	BICINE	9.0	30 % v/v	PEG 400
H3		none			0.1 M	ADA	7.0	31 % v/v	PEG 600
H4		none			0.1 M	Tris	8.5	32 % v/v	PEG 500 MME
H5		none			0.1 M	HEPES	7.5	33 % v/v	PEG 400
H6		none			0.18 M	Sodium citrate	4.0	34 % w/v	PEG 3350
H7		none			0.1 M	Tris	8.5	44 % v/v	PEG 200
H8		none			0.1 M	Tris	8.0	65 % v/v	MPD
H9	2.75 M	Ammonium chloride			0.025 M	Bis-Tris	7.0		
H10	2.8 M	Ammonium chloride			0.075 M	HEPES	7.5		
H11	3.0 M	Ammonium sulfate			0.1 M	MES	5.5		
H12					0.01 M	HEPES	7.5	3.25 M	1,6-Hexanediol

Table reproduced from Molecular Dimensions MemGold2™ HT-96 Eco Screen information sheet .

S.6.4. JBScreen B1/C1/B4/C10

The JBScreen B1/C1/B4/C10 is composed of four screens, each containing 24 precipitating agents. Two of these four screens are the JBScreen Basic 1 (B1), JBScreen Classic 1 (C1), having as main components glycerol, MPD and PEGs. The remaining two are the JBScreen Basic 4 (B4) e JBScreen Classic 10 (C10) that have as main components different salts.

The 96-well plate was then divided in four having B1 solutions from wells A1 to B12, C1 solutions from C1 to D12, B4 solutions from E1 to F12 and, finally, C10 solutions from G1 to H12.

JBScreen Basic 1 (B1) – Jena Bioscience (Cat.-No.:CS-121)

No.	Precipitant	Precipitant 2	Buffer	Additive
A1	25 % v/v Ethylene glycol	none	none	none
A2	12 % v/v Glycerol	1.5 M Ammonium sulfate	100 mM TRIS; pH 8.5	none
A3	1 M 1,6-Hexanediol	none	100 mM Sodium acetate; pH 4.6	10 mM Cobalt (II) chloride
A4	2.5 M 1,6-Hexanediol	none	100 mM tri-Sodium citrate; pH 5.6	none
A5	3.4 M 1,6-Hexanediol	none	100 mM TRIS; pH 8.5	200 mM Magnesium chloride
A6	30 % v/v 2-Methyl-2,4-pentanediol	none	100 mM Sodium acetate; pH 4.6	200 mM Sodium chloride
A7	30 % v/v 2-Methyl-2,4-pentanediol	none	100 mM tri-Sodium citrate; pH 5.6	200 mM Ammonium acetate
A8	30 % v/v 2-Methyl-2,4-pentanediol	none	100 mM Sodium acetate; pH 4.6	20 mM Calcium chloride
A9	30 % v/v 2-Methyl-2,4-pentanediol	500 mM Ammonium sulfate	100 mM HEPES; pH 7.5	none
A10	30 % v/v 2-Methyl-2,4-pentanediol	none	100 mM HEPES; pH 7.5	200 mM tri-Sodium citrate
A11	50 % v/v 2-Methyl-2,4-pentanediol	none	100 mM TRIS; pH 8.5	200 mM Ammonium di-hydrogen phosphate
A12	70 % v/v 2-Methyl-2,4-pentanediol	none	100 mM HEPES; pH 7.5	none
B1	2 % w/v Ethylene imine polymer	none	100 mM tri-Sodium citrate; pH 5.6	500 mM Sodium chloride
B2	2 % v/v Polyethylene glycol 400	2 M Ammonium sulfate	100 mM HEPES; pH 7.5	none
B3	28 % v/v Polyethylene glycol 400	none	100 mM HEPES; pH 7.5	200 mM Calcium chloride
B4	30 % v/v Polyethylene glycol 400	none	100 mM TRIS; pH 8.5	200 mM tri-Sodium citrate
B5	30 % v/v Polyethylene glycol 400	none	100 mM HEPES; pH 7.5	200 mM Magnesium chloride
B6	30 % v/v Polyethylene glycol 400	none	100 mM Sodium acetate; pH 4.6	100 mM Calcium chloride
B7	20 % v/v Polyethylene glycol monomethyl ether 550	none	100 mM BICINE; pH 9.5	100 mM Sodium chloride
B8	25 % v/v Polyethylene glycol monomethyl ether 550	none	100 mM MES; pH 6.5	10 mM Zinc sulfate
B9	10 % w/v Polyethylene glycol 1,000	10 % w/v Polyethylene glycol 8,000	none	none
B10	30 % w/v Polyethylene glycol 1,500	none	none	none
B11	20 % w/v Polyethylene glycol monomethyl ether 2,000	none	100 mM TRIS; pH 8.5	10 mM Nickel (II) chloride
B12	30 % w/v Polyethylene glycol monomethyl ether 2,000	none	100 mM Sodium acetate; pH 4.6	200 mM Ammonium sulfate

*pH values indicated are those of the 1.0 M buffer stock solution prior to dilution with other components

Table reproduced from Jena Bioscience JBScreen Basic 1 (B1) information sheet.

JBScreen Classic 1 (C1) – Jena Bioscience (Cat.-No.:CS-101L)

No.	Precipitant	Buffer	Additive
1/A1	15 % w/v Polyethylene glycol 400	100 mM Sodium acetate; pH 4.6	100 mM Calcium chloride
1/A2	15 % w/v Polyethylene glycol 400	100 mM MES; pH 6.5	none
1/A3	15 % w/v Polyethylene glycol 400	100 mM HEPES; pH 7.5	200 mM Magnesium chloride
1/A4	15 % w/v Polyethylene glycol 400	100 mM TRIS; pH 8.5	200 mM tri-Sodium citrate
1/A5	25 % w/v Polyethylene glycol 400	100 mM Sodium acetate; pH 4.6	100 mM Magnesium chloride
1/A6	25 % w/v Polyethylene glycol 400	100 mM TRIS; pH 8.5	200 mM Lithium sulfate
1/B1	28 % w/v Polyethylene glycol 400	100 mM HEPES; pH 7.5	200 mM Calcium chloride
1/B2	30 % w/v Polyethylene glycol 400	100 mM Sodium acetate; pH 4.6	100 mM Calcium chloride
1/B3	30 % w/v Polyethylene glycol 400	100 mM MES; pH 6.5	100 mM Sodium acetate
1/B4	30 % w/v Polyethylene glycol 400	100 mM MES; pH 6.5	100 mM Magnesium chloride
1/B5	30 % w/v Polyethylene glycol 400	100 mM HEPES; pH 7.5	200 mM Magnesium chloride
1/B6	30 % w/v Polyethylene glycol 400	100 mM TRIS; pH 8.5	200 mM tri-Sodium citrate
1/C1	30 % w/v Polyethylene glycol monomethyl ether 550	100 mM BICINE; pH 9.0	100 mM Sodium chloride
1/C2	25 % w/v Polyethylene glycol monomethyl ether 550	100 mM MES; pH 6.5	10 mM Zinc sulfate
1/C3	25 % w/v Polyethylene glycol 1,000	100 mM HEPES; pH 7.5	none
1/C4	30 % w/v Polyethylene glycol 1,000	100 mM TRIS; pH 8.5	none
1/C5	15 % w/v Polyethylene glycol 1,500	none	none
1/C6	20 % w/v Polyethylene glycol 1,500	100 mM HEPES; pH 7.5	none
1/D1	30 % w/v Polyethylene glycol 1,500	none	none
1/D2	20 % w/v Polyethylene glycol monomethyl ether 2,000	100 mM TRIS; pH 8.5	10 mM Nickel (II) chloride
1/D3	25 % w/v Polyethylene glycol monomethyl ether 2,000	none	none
1/D4	30 % w/v Polyethylene glycol monomethyl ether 2,000	100 mM MES; pH 6.5	100 mM Sodium acetate
1/D5	20 % w/v Polyethylene glycol 3,000	100 mM HEPES; pH 7.5	200 mM Sodium acetate
1/D6	30 % w/v Polyethylene glycol 3,000	100 mM TRIS; pH 8.5	200 mM Lithium sulfate

*pH values indicated are those of the 1.0 M buffer stock solution prior to dilution with other components

Table reproduced from Jena Bioscience JBScreen Classic 1 (C1) information sheet.

JBScreen Basic 4 (B4) – Jena Bioscience (Cat.-No.:CS-124)

No.	Precipitant 1	Precipitant 2	Buffer	Additive
G1	800 mM Potassium di-hydrogen phosphate	800 mM Sodium di-hydrogen phosphate	100 mM HEPES; pH 7.5	none
G2	400 mM Ammonium di-hydrogen phosphate	none	none	none
G3	1 M Ammonium di-hydrogen phosphate	none	100 mM tri-Sodium citrate; pH 5.6	none
G4	2 M Ammonium di-hydrogen phosphate	none	100 mM TRIS; pH 8.5	none
G5	2 M Ammonium formate	none	100 mM Sodium acetate; pH 4.6	none
G6	4 M Ammonium formate	none	100 mM HEPES; pH 7.5	none
G7	2 M Ammonium formate	none	none	none
G8	500 mM Ammonium sulfate	1 M Lithium sulfate	100 mM tri-Sodium citrate; pH 5.6	none
G9	1.6 M Ammonium sulfate	none	100 mM HEPES; pH 7.5	100 mM Sodium chloride
G10	1.8 M Ammonium sulfate	none	100 mM MES; pH 6.5	10 mM Cobalt (II) chloride
G11	2 M Ammonium sulfate	none	100 mM TRIS; pH 8.5	none
G12	2 M Ammonium sulfate	none	none	none
H1	2 M Ammonium sulfate	none	100 mM Sodium acetate; pH 4.6	none
H2	2 M Ammonium sulfate	none	100 mM tri-Sodium citrate; pH 5.6	200 mM Potassium Sodium tartrate
H3	200 mM Magnesium formate	none	none	none
H4	1.6 M Magnesium sulfate	none	100 mM MES; pH 6.5	none
H5	2 M Magnesium chloride	none	100 mM BICINE; pH 9.5	none
H6	1 M Sodium acetate	none	100 mM Imidazole; pH 6.5	none
H7	1 M Sodium acetate	none	100 mM HEPES; pH 7.5	50 mM Cadmium sulfate
H8	1.4 M Sodium acetate	none	100 mM MES; pH 6.5	none
H9	500 mM Sodium chloride	10 mM Magnesium chloride	none	10 mM Cetyltrimethylammonium bromide
H10	2 M Sodium chloride	none	100 mM Sodium acetate; pH 4.6	none
H11	2 M Sodium chloride	none	100 mM MES; pH 6.5	100 mM Sodium di-hydrogen phosphate, 100 mM Potassium di-hydrogen phosphate
H12	4.3 M Sodium chloride	none	100 mM HEPES; pH 7.5	none

*pH values indicated are those of the 1.0 M buffer stock solution prior to dilution with other components

Table reproduced from Jena Bioscience JBScreen Basic 4 (B4) information sheet.

JBScreen Classic 10 (B10) – Jena Bioscience (Cat.-No.:CS-110L)

No.	Precipitant 1	Precipitant 2	Buffer	Additive
10/A1	500 mM Sodium acetate	none	100 mM Imidazole; pH 8.0	none
10/A2	700 mM tri-Sodium citrate	none	100 mM HEPES; pH 7.5	none
10/A3	700 mM Lithium sulfate	none	100 mM TRIS; pH 8.5	none
10/A4	800 mM Potassium Sodium tartrate	none	100 mM HEPES; pH 7.5	none
10/A5	1 M Ammonium di-hydrogen phosphate	none	100 mM tri-Sodium citrate; pH 5.6	none
10/A6	1 M Ammonium di-hydrogen phosphate	none	100 mM TRIS; pH 8.5	none
10/B1	1 M Lithium sulfate	none	100 mM TRIS; pH 8.5	10 mM Nickel (II) chloride
10/B2	1 M Sodium acetate	none	100 mM Imidazole; pH 8.0	none
10/B3	1 M Sodium formate	none	100 mM Sodium acetate; pH 4.6	none
10/B4	1.4 M Sodium acetate	none	100 mM MES; pH 6.5	none
10/B5	1.4 M tri-Sodium citrate	none	100 mM HEPES; pH 7.5	none
10/B6	1.5 M Lithium sulfate	none	100 mM TRIS; pH 8.5	none
10/C1	1.5 M tri-Sodium citrate; pH 6.5	none	none	none
10/C2	1.6 M Magnesium sulfate	none	100 mM MES; pH 6.5	none
10/C3	1.6 M Potassium Sodium tartrate	none	100 mM MES; pH 6.5	none
10/C4	2 M Ammonium formate	none	100 mM MES; pH 6.5	none
10/C5	2 M Ammonium di-hydrogen phosphate	none	100 mM TRIS; pH 8.5	none
10/C6	2 M Sodium formate	none	none	none
10/D1	2 M Magnesium chloride	none	100 mM TRIS; pH 8.5	none
10/D2	2 M Sodium chloride	none	100 mM MES; pH 6.5	200 mM Sodium acetate
10/D3	2 M Sodium formate	none	100 mM Sodium acetate; pH 4.6	none
10/D4	1 M Ammonium di-hydrogen phosphate	30 % w/v Glycerol	100 mM TRIS; pH 8.5	none
10/D5	4 M Sodium chloride	none	100 mM HEPES; pH 7.5	none
10/D6	3 M Sodium formate	none	none	none

*pH values indicated are those of the 1.0 M buffer stock solution prior to dilution with other components

Table reproduced from Jena Bioscience JBScreen Classic 10 (C10) information sheet.

S.7. Mössbauer simulation parameters

All calculations used in this work referred to the components corresponding to the Fe ion ligated by a histidine in the protonated or deprotonated states. In the samples in which the sum of the three components shown below is not 100%, contribution of either Fe^{2+} or Fe^{3+} could be observed. Due to the high complexity of a table including all parameters, these values are not shown.

- Oxidized wild type IscR samples at zero magnetic field:

		Fe_{Cys}	$Fe_{His\ prot}$	$Fe_{His\ deprot}$
δ (mm/s)				
ΔE_Q (mm/s)		0.48	0.8	0.65
Γ (mm/s)	5.73	0.29	0.34	-
	6.4	0.29	0.35	-
	7.03	0.29	0.31	0.25
	7.91	0.31	0.3	0.33
	8.9	0.35	0.25	0.34
	10.03	0.3	-	0.33
	11.05	0.29	-	0.3
	11.52	0.3	-	0.31
	12.09	0.3	-	0.3
	12.48	0.27	-	0.25
Area (%)	5.73	36.5	36.5	-
	6.4	39.5	39.5	-
	7.03	50	45	5
	7.91	50	29	21
	8.9	50	5	45
	10.03	42	-	42
	11.05	37	-	37
	11.52	34.5	-	34.5
	12.09	25	-	25
	12.48	10.5	-	10.5

- Oxidized wild type IscR samples at 0.1 T:

IscR pH 8 0.1 T	Fe_{Cys}	$Fe_{His\ deprot}$	$Fe_{His\ prot}$
δ(mm/s)	0.26	0.28	0.30
ΔE_Q(mm/s)	-0.48	0.65	0.80
Γ (mm/s)	0.48	0.35	0.39
Area (%)	50	21	29
ETA	0.3	0	0
Chi^2		1.24	

IscR pH 11.05 0.1 T	Fe_{Cys}	$Fe_{His\ deprot}$	Fe?
δ(mm/s)	0.26	0.28	0.26
ΔE_Q(mm/s)	-0.48	0.65	0
Γ (mm/s)	0.50	0.50	6
Area (%)	33	33	34
ETA	0.3	0	0
Chi^2		1.82	

- Oxidized wild type IscR samples at 5 T:

IscR pH 8 5 T	Fe_{Cys}	$Fe_{His\ deprot}$	$Fe_{His\ prot}$
δ(mm/s)	0.26	0.28	0.30
ΔE_Q(mm/s)	-0.48	0.65	0.80
Γ (mm/s)	0.32	0.29	0.34
Area (%)	50	21	29
ETA	0.3	0	0
Chi^2		1.19	

IscR pH 11.05 5 T	Fe_{Cys}	$Fe_{His\ deprot}$	Fe?
δ(mm/s)	0.26	0.28	0.24
ΔE_Q(mm/s)	-0.48	0.65	0
Γ (mm/s)	0.35	0.36	0.90 0.80 0.69
Area (%)	33	33	34
ETA	0.3	0	0
Bhf [T]	-	-	29
Chi^2		1.46	

S.8. *S*=7/2 |±3/2> Kramers doublets rhombogram

Image reproduced from Wilfred R. Hagen (1992) Adv. Inorg. Chem. 38, 165-222. EPR Spectroscopy of Iron-Sulfur Proteins. The dashed line shows the presumed rhombicity of the high spin signal around *g*= 5.2.

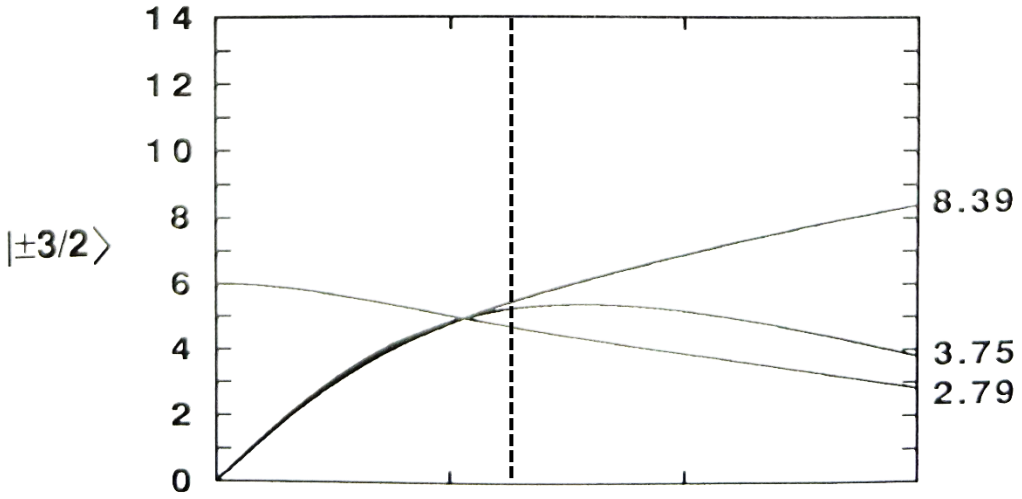

Publication list

1. Ana Lago-Maciel, **Jessica C. Soares**, Jan Zarzycki, Charles J. Buchanan, Tristan Reif Trauttmansdorff, Frederik V. Schmidt, Stefano Lometto, Nicole Paczia, Jan M. Schuller, D. Flemming Hansen, Gabriella T. Heller, Simone Prinz, Georg K. A. Hochberg, Antonio J. Pierik and Johannes G. Rebelein **(2024).** S*ubmitted to Nat. Catal*. Methylthio-alkane reductases use nitrogenase metalloclusters for 2 carbon-sulfur bond cleavage. Available in: Biorxiv, https://www.biorxiv.org/content/10.1101/2024.10.19.619033v1.full.pdf.

2. Nicola Sekularac, **Jessica C. Soares**, Antonio J. Pierik, Eugenio Pérez Patallo, Susanne Zehner, and Nicole Frankenberg-Dinkel **(2024).** *To be submitted.* Viral take-over of host photosynthetic electron transport: Biochemical analysis of cyanophage plastocyanin.

3. Özge Efendi, Lukas Knauer, Jason Crack, Jonathan Oltmanns, Melanie Heghmanns, **Jessica C. Soares**, Nick E. Le Brun, Volker Schünemann, Müge Kasanmascheff and Joseph J. Braymer **(2024).** *To be submitted to Angew. Chem. Int. Ed.* Yeast [FeFe]-hydrogenase-like protein Nar1 can bind not only two [4Fe-4S] clusters but also a [2Fe-2S] cluster

4. Maria C. Martins, Susana F. Fernandes, Bruno A. Salgueiro, **Jessica C. Soares**, Célia V. Romão, Cláudio M. Soares, Diana Lousa, Filipe Folgosa and Miguel Teixeira **(2021).** *Catalysts.* The Amino Acids Motif -32GSSYN36- in the Catalytic Domain of *E coli* Flavorubredoxin no Reductase is Essential for Its Activity. DOI: https://doi.org/10.3390/catal11080926

5. Nuno Coelho, João P. Jacinto, Rodrigo Silva, **Jessica C. Soares**, Alice S. Pereira and Pedro Tavares **(2023).** *Coatings.* Green Synthesis and Antibacterial Activity of Silver Nanoparticles Obtained from *Moringa oleifera* Seed Cake. DOI: https://doi.org/10.3390/coatings13081439

Scientific presentations

Soares, J. C.*, Knauer, L., Schünemann, V., Pierik, A.J. – Non-cysteinyl coordination of [2Fe-2S] clusters: redox properties of the *E. coli* IscR protein. * Presenting author.

Talks

- August 2024 - EuroBIC, Münster, Germany. Flash talk.
- January 2024 - GRS Bioinorganic Chemistry – Ventura, California.

Posters

- August 2024 - EuroBIC, Münster, Germany.
- June 2024 - FEBS Advanced Course - Metals in biology: their importance and tools to study them, Lisbon, Portugal.
- April 2024 - Cost Action – Iron-Sulfur Clusters, from Microbes to Immune System, Prague, Czech Republic.
- January 2024 - GRC Metals in Biology – Ventura, California.
- September 2023 - EPR Summer school, EFEPR – Geneva, Switzerland.

JESSICA CANDIDO SOARES

M.Sc. Biochemistry

jsoares@rptu.de

Lab Competences

• CW-EPR X-Band of IscR, MitoNEET, Rieske proteins, Type I copper centers. Perpendicular and parallel modes.

• Heterologous expression of proteins (FlRd, CpI, IscR)

• Redox titrations

• Circular Dichroism

References

Prof. Dr. Antonio J. Pierik

Head of the lab and full professor, RPTU.

Pierik Group –

Iron-Sulfur clusters for Life

Prof. Dr. Miguel Teixeira

Head of the lab and full professor, ITQB-UNL.

Metalloenzymes and Molecular Bioenergetics – Metalloproteins and Bioenergetics Unit

Lab. Experience

PhD Candidate • Pierik Group, RPTU, Kaiserslautern, Germany • 3 years (2021 - 2024)

Master Thesis • Metalloenzymes and Molecular Bioenergetics laboratory, ITQB-UNL, Lisbon, Portugal • 1 year (2019 -2020)

Biochemistry Project • Molecular Biophysics, UCBIO-REQUIMTE, FCT -NOVA, Lisbon, Portugal • 2 months (2018)

Education

PhD Candidate Biochemistry• 2021-Now • RPTU, Kaiserslautern, Germany

M. Sc. Biochemistry for Health • 2018-2020 • FCT-NOVA/ITQB-UNL, Lisbon, Portugal. Final Grade 18/20.

B. Sc. Biochemistry • 2015-2018 • FCT-NOVA, Lisbon, Portugal. Final Grade 16/20.

Scientific Output

Scientific talks

2024 – Soares, J. C.*, Knauer, L., Schünemann, V., Pierik, A.J. – Non-cysteinyl coordination of [2Fe-2S] clusters: redox properties of the *E. coli* IscR protein – GRS Bioinorganic Chemistry – Ventura, California. * Presenting author.

Posters

2024 – Soares, J. C.*, Knauer, L., Schünemann, V., Pierik, A.J. – Non-cysteinyl coordination of [2Fe-2S] clusters: redox properties of the *E. coli* IscR protein – GRC Metals in Biology – Ventura, California. * Presenting author.

Publications

2023 – Coelho, N., Jacinto, J., Soares, J.C., Pereira, A.S., Tavares, P. – Green Synthesis and Antibacterial Activity of Silver Nanoparticles Obtained from *Moringa oleifera* Seed Cake – Coatings.

2021 – Martins, M. C., Fernandes, S. F., Salgueiro, B., Soares, J. C., Romão, C. V., Soares, C., Lousa, D., Folgosa, F., Teixeira, M. - The Amino Acids Motif -32GSSYN36- in the Catalytic Domain of *E coli* Flavorubredoxin no Reductase is Essential for Its Activity – Catalysts.